From Conventional to Superlens-assisted Laser Manufacturing for Micro & Nano Device Applications

PRIFYSGOL
BANGOR
UNIVERSITY

Yiduo Chen

Supervisor: Prof. Zengbo Wang

School of Computer Science and Electronic Engineering

Bangor University

A thesis submitted in partial fulfilment for the degree of

Doctor of Philosophy

2024

Declaration

I hereby declare that this thesis is the results of my own investigations, except where otherwise stated. All other sources are acknowledged by bibliographic references. This work has not previously been accepted in substance for any degree and is not being concurrently submitted in candidature for any degree unless, as agreed by the University, for approved dual awards.

Yr wyf drwy hyn yn datgan mai canlyniad fy ymchwil fy hun yw'r thesis hwn, ac eithrio lle nodir yn wahanol. Caiff ffynonellau eraill eu cydnabod gan droednodiadau yn rhoi cyfeiriadau eglur. Nid yw sylwedd y gwaith hwn wedi cael ei dderbyn o'r blaen ar gyfer unrhyw radd, ac nid yw'n cael ei gyflwyno ar yr un pryd mewn ymgeisiaeth am unrhyw radd oni bai ei fod, fel y cytunwyd gan y Brifysgol, am gymwysterau deuol cymeradwy.

Acknowledgements

First and foremost, I owe a profound debt of gratitude to Professor Zengbo (James) Wang, my PhD supervisor, for not only introducing me to such a captivating area of research but also for his constant support and expert guidance throughout my PhD journey. His insightful feedback and thoughtful mentorship have been instrumental in shaping every aspect of my research and thesis. I am immensely grateful for his dedication and feel privileged to have had him as my mentor.

Additionally, I extend my sincere appreciation to the Smart Efficiency Energy Centre (SEEC) project and its leaders, Dr. Iestyn Pierce and Dr. Xianfeng Chen, for their substantial financial support. Their contributions have been crucial in facilitating the advancements of my research, allowing me to focus deeply on my work.

I am also thankful to my colleagues at Bangor University for their steadfast support. Special thanks to Dr. Bing Yan, Dr. Liyang Yue, Dr. Yanhua Hong, Dr. Charlotte Baxter, and Mr. Ben Assinder. Their camaraderie and collaborative spirit have greatly enhanced both my professional growth and personal well-being during my time here. I cherish the friendships I've formed with my fellow PhD students—Baidong Wu, Jiaxiang He, Shuanglin Li, Zhenzhe Han and Jiapei Zhang. Their companionship and encouragement have been a consistent source of strength and motivation throughout this academic journey.

My parents deserve a special mention for their immeasurable contributions to my life. Their emotional and financial support has been unwavering, and it has been the cornerstone of my success. I owe them everything and am forever grateful for all the sacrifices they have made for me.

Finally, my deepest gratitude goes to my wife, Mrs Mengxuan Liu. Throughout our long-distance relationship, we have faced numerous challenges together and have always emerged stronger. You have been my pillar of support, helping me navigate through the ups and downs and standing by me during both challenging and joyful times. I am endlessly thankful for your steadfast presence in my life.

Abstract

This thesis explores the transition from conventional-lens-based to superlens-assisted laser manufacturing techniques, addressing key challenges in the fabrication of micro and nano devices. Initially, a novel laser direct writing technique was developed for creating graphene patterns on polybenzimidazole (PBI) thin films and glass substrates. This method, using a cost-effective UV laser system, produces high-quality graphene without the need for metallic precursors or causing thermal damage, offering a scalable and economical solution for graphene production. Additionally, the research introduces a high-precision method for fabricating micro-Fresnel Zone Plates (FZP) lenses on thin films, which effectively compensates for design-sample discrepancies, resulting in highly accurate micro lenses.

Advancing beyond conventional-lens-based methods, the research applies superlens-assisted techniques to enhance refractive index sensing using Long Period Optical Fiber Gratings (LPGs). By creating nanostructures on LPG surfaces, the sensitivity of these sensors is significantly improved, demonstrating the potential for more responsive and durable sensors. The thesis also introduces the SuperNANO system, an innovative dual-function instrument capable of super-resolution imaging and nano-fabrication. This system proves versatile in applications such as anti-counterfeiting security markings and the precise cutting of nanowires.

In summary, this thesis not only refines conventional-lens-based laser manufacturing techniques but also pioneers superlens-assisted methods, contributing significantly to the fields of manufacturing, sensing, and patterning in micro and nano device applications. The findings highlight the potential for scalable, cost-effective, and highly precise fabrication techniques, promising substantial improvements across various industrial and scientific domains.

Table of Contents

Nomenclature

F	Laser energy fluence, focal length
E	Laser pulse energy, electric field
A	Beam area
P	Average laser power
f	Pulse repetition rate
z_0	Axial distance
b	Aperture size, Normalized effective index
λ	Wavelength
d	Resolution limit
$N.A.$	Numerical aperture
n	Refractive index, zone number
α	Half-angle of the maximum cone of light, Fine structure constant
Δp_x	Momentum vector
Δx	Position vector
h	Planck constant
k_i	Wave vector
$D_{Rayleigh}$	Rayleigh criterion
H	Magnetic field
$\|E\|^2$	Electric field intensity
ω	Angular frequency
ε	Dielectric constant
c	Speed of light
a	Particle radius

q_0	Fundamental size parameter
r, θ, φ	Spherical coordinates
P_ℓ	Legendre function
$\zeta,\ \psi$	Spherical Bessel functions
$a_\ell,\ b_\ell$	Scattering waves
$c_\ell,\ d_\ell$	Internal waves
z	Z axis component
θ_1	Angle of incident light wave
θ_2	Angle of diffracted wave
m	Diffraction order
Λ	Grating period
β	Wave propagation
k	Wave mode number
$R,\ S$	Complex amplitudes
$A,\ B$	Complex amplitudes of unperturbed modes
κ	Cross-coupling coefficient
$\hat{\sigma}$	Self-coupling coefficient
δ	Wave detuning
T	Transmission spectrum
γ	$\sqrt{\kappa^2 - \delta^2}$
R	Reflectivity
L	Grating length
J	First Bessel function
K	Second Bessel function, Enhancement factor
a_1	Radius of fiber core
a_2	Radius of fiber cladding

$\zeta_0,\ \zeta_0'$	Field expressions
Z_0	Free space electromagnetic impedance
l	Azimuthal number
N	Bessel function of the second kind, Layer of graphene
κ_{co-co}	Coupling coefficient of core-core mode
κ_{co-cl}	Coupling coefficient of core-cladding mode
$\sigma(z)$	Slowly varying envelope
Δ	Index modulation
E_{cl}	Normalization constant of the electric field for cladding
T_{max}	Maximum transmission
$\Delta\lambda$	Wavelength shift
$\Delta\varepsilon$	Longitudinal strain
ΔT	Temperature change
r	Radius
D_f	Primary focal point
D	Hole density

List of Figures

List of Tables

List of Publications

Journal Paper:

[1] **Chen, Y.**, Yue, L., Yang, X., Jones, C. L., & Wang, Z. (2024). Superlens-Assisted laser nanostructuring of Long Period optical fiber Gratings (LPGs) for enhanced refractive index sensing. Optics & Laser Technology, 176, 111001.

[2] **Chen, Y.**, Yan, B., Yue, L., Jones, C. L., & Wang, Z. (2024). SuperNANO: Enabling Nanoscale Laser Anti-Counterfeiting Marking and Precision Cutting with Super-Resolution Imaging. Photonics 2024, 11, 846.

[3] Yu, L., Wang, Z., Xu, L., Yue, L., Yan, B., Minin, I. V., ... & **Chen, Y.** (2022). Highly curved reflective W-shape and J-shape photonic hook induced by light interaction with partially coated microfluidic channels. arXiv preprint arXiv:2209.03220.

Conference:

[1] **Chen, Y.**, Wang, Z., Wu, B., Yan, B., Yue, L., & Joya, Y. (2022, October). A New Method for Micro Fresnel Zone Plates Lens Design and Low-cost Fabrication by Laser Direct Writing. In Frontiers in Optics (pp. JW5A-10). Optica Publishing Group.

[2] **Chen, Y.**, Kwok, W., & Wang, Z. J. (2023). Enhancing Security with Superlens-Enabled Laser Direct Marking of Anti-counterfeiting DotCode. In Laser Science 2023 (pp. JM7A-34). Optica Publishing Group.

[3] **Chen, Y.**, Yue, L., Wang, Z., (2024). Nanosecond UV Laser Direct Writing of Graphene on Polybenzimidazole Thin Film and Glass Substrates.” In Proceedings of the 1st International Online Conference on Photonics, 14–16 October 2024, Basel, Switzerland.

[4] Wu, B., Wang, Z., **Chen, Y.**, Yue, L., & Yan, B. (2022, October). Design of Silicon Nanosphere-based Wide-angle Shift-free Metamaterial Edge Filter. In Frontiers in

Optics (pp. JW5A-8). Optica Publishing Group.

[5] Yu, L., Wang, Z., Xu, L., Yue, L., Yan, B., Wu, B., & **Chen, Y.** (2022, October). Highly curved W-shape and J-shape photonic hook. In Laser Science (pp. JW5A-36). Optica Publishing Group.

Chapter 1.
Introduction

1.1 Introduction

In recent years, the demand for advanced manufacturing techniques has surged, driven by the rapid development of micro and nano devices across various industries. Laser manufacturing has emerged as a pivotal technology in this domain due to its precision, versatility, and efficiency[1–3]. This thesis explores the evolution from conventional-lens-based laser manufacturing, constrained by diffraction-limited resolutions, to superlens-based techniques that achieve subwavelength resolutions. By integrating microsphere superlenses, the research demonstrates enhanced precision in fabricating micro- and nano-devices, overcoming the limitations of traditional optical focusing methods.

Conventional-lens-based laser manufacturing typically use an optical lens to focus the laser beam, which is limited by optical diffraction, resulting in focus spot sizes ranging from several micrometers to tens of micrometers[4,5]. An example of traditional methods includes the development of graphene patterns on polybenzimidazole (PBI) thin films and glass substrates using a conventional femtosecond UV laser system. This technique achieves scalable and cost-effective graphene production without requiring metallic precursors or causing thermal damage, marking a significant advancement in material science[6]. Additionally, the fabrication of thin-film micro-Fresnel Zone Plates (FZP) lenses using laser marking systems demonstrates the capability of conventional-lens-based laser techniques in achieving high-precision optical components essential for various optical applications[7,8].

However, conventional-lens-based laser manufacturing techniques are limited in marking and patterning resolution[9]. There has been a significant push in recent years to develop advanced super-resolution laser patterning and marking techniques

beyond the diffraction limit[10,11]. With advancements in nanophotonics, plasmonics, and metamaterials, several new super-resolution microscopy/nanoscopy techniques have emerged, such as near-field scanning optical microscopy (NSOM)[12] and metamaterial superlenses[13]. More recently, the use of microspheres has been shown to produce extremely fine focusing beyond the diffraction limit through a phenomenon known as 'photonic nanojet'[14]. This method has proven to be a simple yet effective strategy for achieving sub-diffraction resolution. Distinct from other super-resolution techniques, this approach offers real-time visualization under white-light illumination and is both label-free and features low intrinsic loss at higher optical frequencies[15–18]. Microsphere superlens-assisted nanopatterning offers significant advantages, including low-cost fabrication and the capability to pattern large areas efficiently in parallel, making it a highly economical and versatile choice for advanced manufacturing processes[19,20]. The potential applications for microsphere superlenses are extensive, especially when combined with other optical elements like fiber gratings[21].

Microsphere superlens-assisted nanopatterning has been demonstrated mainly on flat surface samples, achieving patterning resolutions within the range of 80 nm to 500 nm[22,23]. Although some research has been conducted on the patterning of curved tube surfaces, the tube sizes are on the millimeter to centimeter scale[24,25]. There is no report in the literature on using microsphere superlenses to generate nanopatterns on fiber-based functional devices. This thesis introduces the superlens-assisted patterning technique applied to fiber-based optical sensor devices—the fiber Bragg grating (FBG) and Long Period Grating (LPG)—with fiber diameters of only 125 µm. For the first time, we demonstrate that large-area nanoholes can be generated by innovative superlens laser patterning techniques. This unique laser nanopatterning process increases surface areas for sensing, boosting the refractive index sensitivity of LPG sensors through direct laser nanostructuring of LPG surfaces, facilitated by microsphere superlenses coated onto these surfaces. This technique significantly improves the sensitivity and durability of LPGs, making them more effective for

sensing applications.

Despite the successful demonstration of microsphere superlens-based imaging systems and patterning systems separately by research groups worldwide[23,26], there has been no combined system with simultaneous nano-imaging and nano-fabrication/patterning capabilities. For the first time, we developed the SuperNANO system—an advanced super-resolution platform that integrates nanopatterning, nanofabrication, and simultaneous nano-imaging. The system operates in a label-free manner, meaning it does not require any external markers, dyes, or fluorescent labels to visualize nanoscale features. Instead, it relies on the intrinsic optical or structural properties of the sample itself. This eliminates the need for additional contrast agents and preserves the native state of the material, enabling accurate, high-resolution imaging and fabrication at the nanoscale. This system achieves resolutions from 50 to 320 nm, showcasing its versatility in creating anti-counterfeiting security markings and precise cutting of nanowires. The introduction of a simplified anti-counterfeiting laser marking system utilizing superlens-assisted nanoscale marking of 2D DotCode further enhances security measures, providing a secure alternative to traditional methods.

1.2 Project aim and objectives

This research is part of the £7M Smart Efficiency Energy Centre (SEEC) project, funded by the European Regional Development Fund through the Welsh Government. While the SEEC project aims to develop advanced sensors and networks for validation and verification in safety-critical environments, particularly focusing on ocean renewable energy, nuclear energy, and efficient energy utilization, this study homes in on specific aspects of laser manufacturing and its applications in micro and nano device fabrication.

Aim:

The primary aim of this research is to explore and develop innovative laser manufacturing techniques, particularly superlens-assisted methods, for the fabrication and enhancement of advanced micro and nano devices.

Objectives:

1. **Develop and Optimize Laser Manufacturing Techniques:**
    - Investigate and refine conventional-lens-based laser manufacturing methods for creating graphene patterns on polybenzimidazole (PBI) thin films and glass substrates.
    - Fabricate high-precision thin-film micro-FZP lenses using laser marking systems.
2. **Innovate Superlens-Assisted Laser Manufacturing:**
    - Demonstrate superlens-assisted laser patterning techniques for fiber-based optical devices, including FBG and LPG.
    - Enhance the refractive index sensitivity of LPG sensors through direct laser nanostructuring facilitated by microsphere superlenses.
3. **Develop Advanced Nanofabrication and Nanoimaging Systems:**
    - Design and construct the SuperNANO system, capable of label-free nanopatterning and nanofabrication while performing simultaneous nanoimaging.
    - Utilize the SuperNANO system for creating anti-counterfeiting security markings and precise nanowire cutting.
4. **Enhance Anti-Counterfeiting Measures:**

- Develop a simplified anti-counterfeiting laser marking system using superlens-assisted nanoscale marking of 2D DotCode, providing a secure alternative to traditional methods.

5. **Contribute to Theoretical Understanding:**

   - Study the fundamental theories and principles related to superlens focusing and its applications in laser manufacturing.

1.3 Thesis outline

Chapter 1 introduces laser manufacturing techniques utilizing microsphere superlens technology, focusing on safety enhancement and optical fiber grating integration. It also describes the project's aims and objectives.

Chapter 2 reviews existing laser techniques, microsphere superlens techniques, and optical fiber grating sensing techniques, along with principles of super-resolution and optical fiber waveguides.

Chapter 3 explores theoretical simulation methods for analyzing the optical performance of microspheres, Fresnel lenses, and fiber grating sensors, covering experimental laser systems and surface characterization techniques.

Chapter 4 examines advanced direct laser manufacturing techniques using superlens-enabled marking, including laser-induced graphene, 2D Fresnel lenses fabrication, and superlens-assisted DotCode marking.

Chapter 5 focuses on enhancing the performance of optical fiber grating sensors through superlens-based laser nanostructuring, detailing experiments and RI sensing enhancements.

Chapter 6 introduces the SuperNANO system for integrated super-resolution nanofabrication and nanoimaging, detailing its applications in security and precise nanowire cutting.

Chapter 7 summarizes the thesis results, highlighting key conclusions and breakthroughs, and suggests future research directions to advance the field.

Chapter 2.
Literature Review

2.1 Conventional-lens-based laser manufacturing

2.1.1 Principle of laser operating

The first laser system was introduced by Theodore Maiman on May 16, 1960. This groundbreaking invention took place at Hughes Research Laboratories in Malibu, California. Maiman's laser relied on a synthetic ruby crystal as its medium[27].

Lasers, based on the principle of "Light Amplification by Stimulated Emission of Radiation," operate through a finely tuned process. It emitted a pulse of deep red light at 694 nm, which was the result of the chromium atoms in the ruby being excited and then releasing a photon of light which is an effect known as stimulated emission, a principle first proposed by Albert Einstein in 1917[28]. As shown in figure 2.1-1, initially, an external energy source, often referred to as "pumping," excites the atoms within a chosen medium like gas, liquid, or solid. This energy causes the atoms' electrons to ascend to higher energy states, establishing a condition known as population inversion, where the number of electrons in excited states surpasses those in ground states. The next step is the stimulated emission, in which an excited electron encounters a matching-energy photon and is induced to fall to a lower energy state, concurrently emitting a second photon that is coherent with the first in phase, frequency, polarization, and direction. The optical cavity which consists of two mirrors, including a partially reflective one allows light to bounce back and forth, amplifying the coherent light with each pass. Eventually, some of this light escapes through the partially reflective mirror as a highly focused, monochromatic beam of light, retaining the unique properties of coherence and directionality that make lasers incredibly

versatile and effective for diverse applications, from cutting-edge surgical procedures to communication technology[29–31].

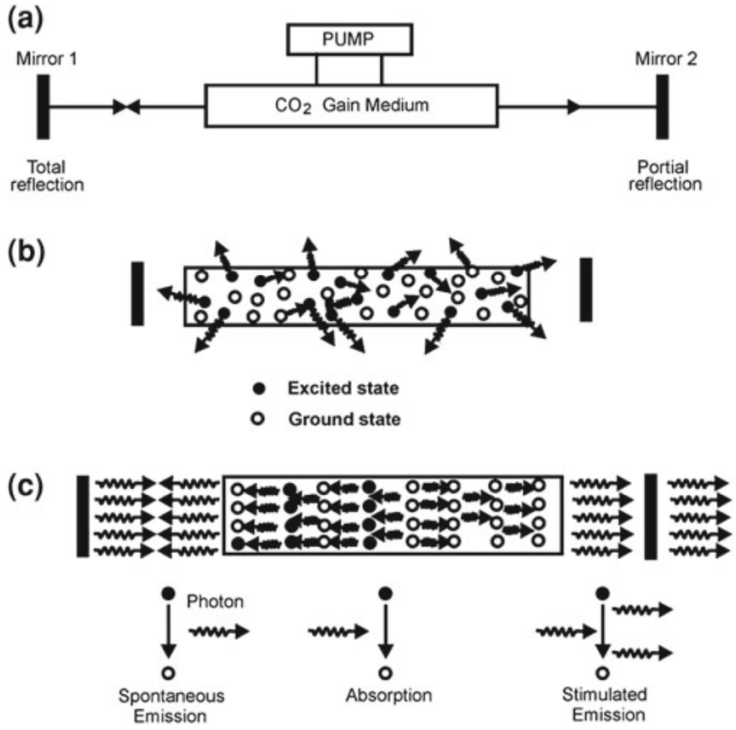

Figure 2.1-1 The schematic setup for generating a laser beam includes: (a) Machine components, showing the energy source, laser medium, and optical cavity with mirrors. (b) Atomic excitation, depicting the process where electrons in the medium are excited to higher energy states and then return to lower states. (c) Beam formation, illustrating stimulated emission as excited electrons emit coherent photons, leading to the amplification of a focused, monochromatic laser beam within the optical cavity and its partial escape through a reflective mirror[30].

The laser fluence F is the energy per unit area delivered by a laser pulse and is calculated as[32]:

$$F = \frac{E}{A} \tag{2.1-1}$$

where A is the beam area and E is the laser pulse energy defined by:

$$E = \frac{P}{f} \tag{2.1-2}$$

where P gives the average laser power and f is the pulse repetition rate.

2.1.2 Microscopic applications

Laser manufacturing and material processing in microscopic applications represent cutting-edge technologies that leverage laser beams for precise fabrication and manipulation at extremely small scales. This field integrates advanced laser systems with high-resolution imaging and control mechanisms to create intricate structures and modify materials with accuracy and efficiency. By harnessing the ability to focus intensely on tiny areas and deliver energy in controlled pulses, these technologies can achieve intricate patterning, surface modification, and even selective material removal, making laser processing a key technology in modern microscopic manufacturing environments[33]. With the capability to concentrate their beams down to fractions of a millimeter, lasers facilitate operations requiring high accuracy on an array of materials such as metals, fabrics, and composites[34]. The typical laser applications are shown in figure 2.1.2. While conventional-lens-based techniques are effective for macroscopic and microscopic applications like welding and cutting, they struggle with resolution limitations below the micrometer scale.

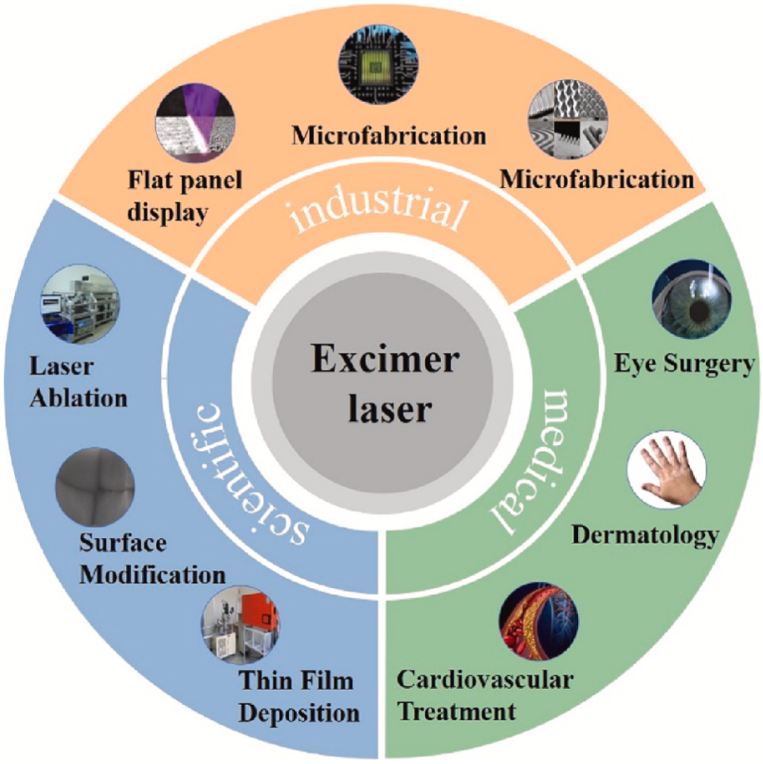

Figure 2.1-2 Typical microscopic applications of excimer lasers[35].

The most classic method is to control the laser beam through galvo to achieve microscopic processing. Hubeatir offers a comprehensive analysis of laser engraving and marking techniques with schematic of a galvo scanner shown in figure 2.1-3, focusing on the applications and optimizations of various laser types—CO_2, Nd: YAG, and fiber lasers—across different materials[36]. The review paper emphasizes the critical importance of optimizing laser parameters such as power, speed, and frequency to achieve high-quality engravings with minimal defects. It covers a range of applications, from industrial identification to aesthetic designs for consumer products.

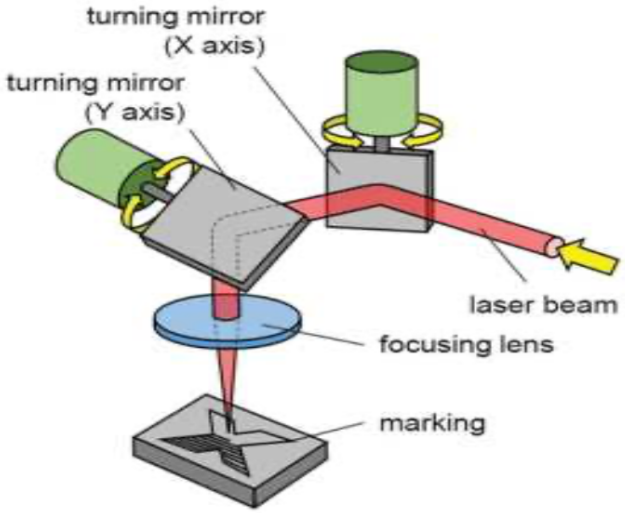

Figure 2.1-3 Schematic of a galvo scanner, showcasing a laser beam directed through turning mirror, focused by a lens onto a material for precise marking[36].

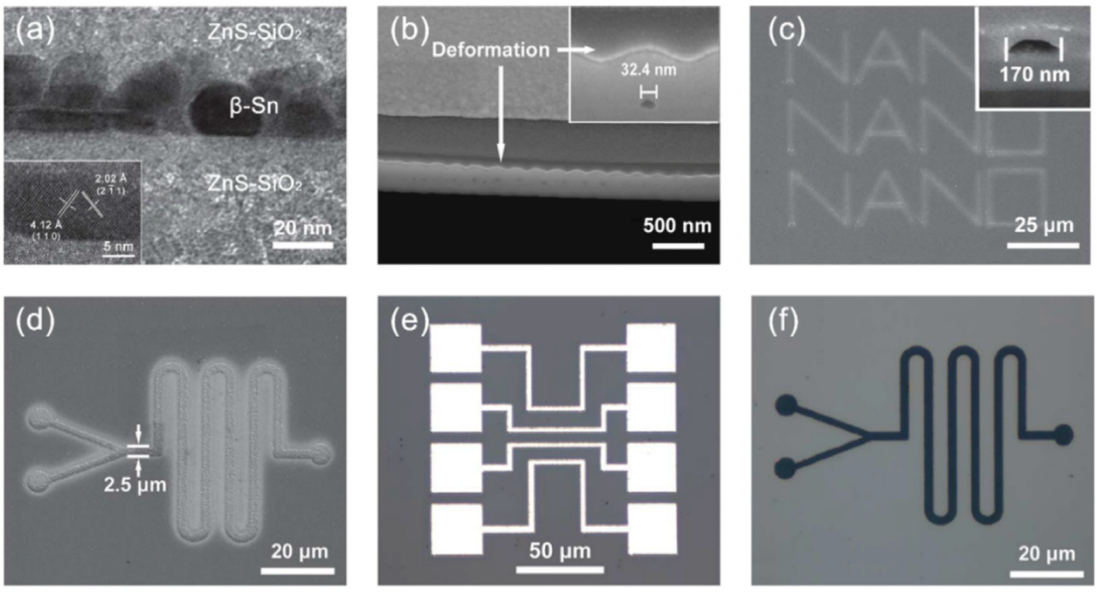

Figure 2.1-4 Examples of laser-marked patterns observed under SEM[37].

Additionally, a paper explores advancements in laser direct writing (LDW) technology, focusing on the contributions of new generation LDW systems. These innovations have significantly enhanced the precision of laser direct marking, allowing for the

creation of detailed micro- and nano-scale features, as depicted in figures 2.1-4. This progress facilitates more intricate and exact patterning capabilities, essential for modern applications in microfabrication and nanotechnology.

The review on laser surface treatment techniques detailed in the paper by Montealegre et al. offers a comprehensive overview of laser technologies used for hardening, melting, and cladding of various materials, demonstrated how these laser processes enhance the wear resistance and mechanical properties of treated surfaces[38]. It covers both thermal and thermo-chemical processes, emphasizing the flexibility and precision of laser treatment in targeting specific surface areas without affecting the whole component. Key findings include the improvement of surface hardness, microstructural refinements through controlled laser parameters, and the advantages of using high-power lasers for efficient surface modification. Laser surface treatment is a crucial technology for improving the performance and durability of materials in demanding industrial applications. A schematic of laser surface treatment is shown in figure 2.1-5.

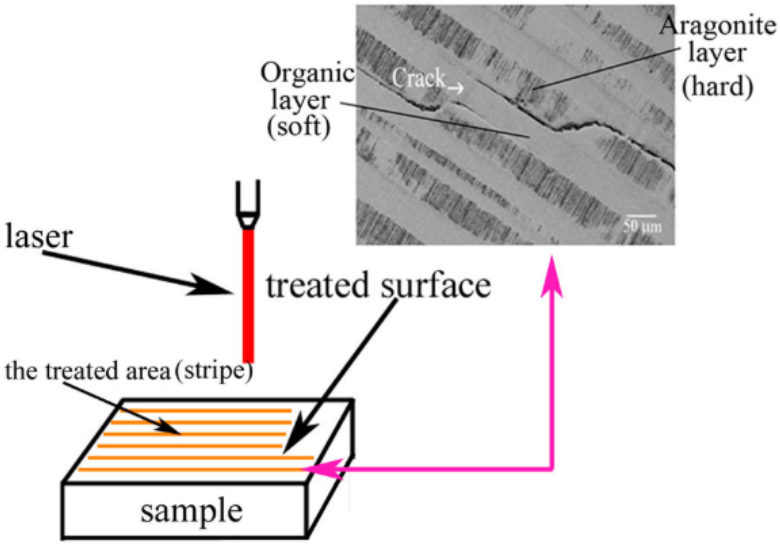

Figure 2.1-5 Schematic of laser surface treatment[39].

Another review paper on laser micromachining underscores the critical role this technology plays in the miniaturization of engineering materials. The paper explores the benefits and diverse applications of various laser types, including excimer, femtosecond, and nanosecond lasers, each selected for their unique microfabrication capabilities[40]. It highlights the precision and minimal thermal impact provided by ultrashort pulse lasers, essential for preserving the integrity of sensitive materials and components. The widespread applications of laser micromachining in producing intricate, high-precision components for industries such as biomedical devices, electronics, and aerospace were discussed. Laser micromachining emerges as a transformative technology that markedly improves manufacturing processes, facilitating the production of complex microscale features with high efficiency and accuracy. Examples of SEM micrographs that depict the fabrication of microstructures on metals using femtosecond laser micromachining are shown in figure 2.1-6.

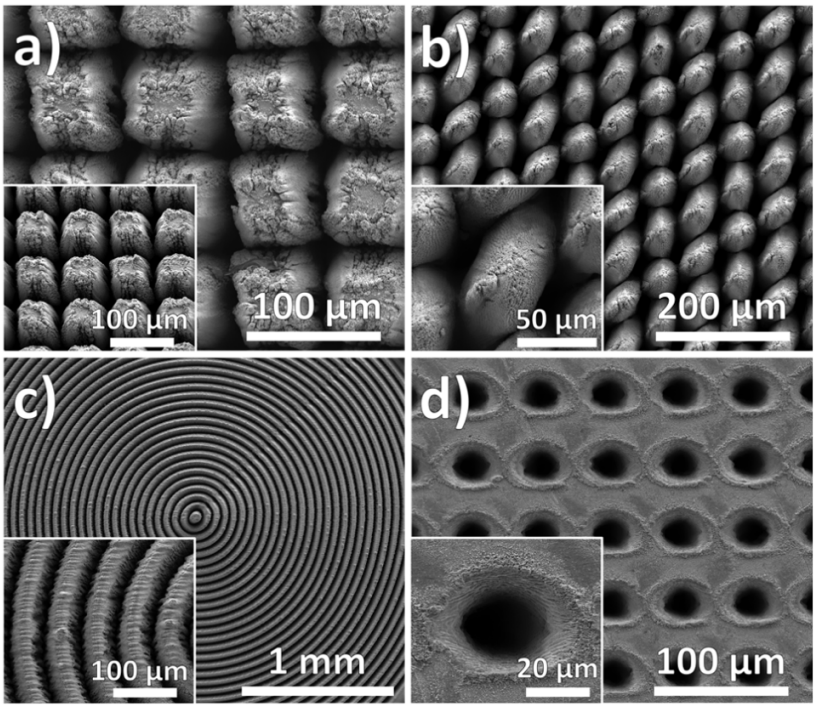

Figure 2.1-6 SEM of microstructures on metals by femtosecond laser micromachining[41].

Beyond the general laser manufacturing and material processing microscopic applications, laser technology significantly impacts manufacturing and material processing through advancements in laser-induced graphene and FZP.

2.1.2.1 Laser-induced graphene

Laser-induced graphene (LIG) represents a transformative approach in the field of material science, allowing for the direct conversion of certain carbon-based precursors into graphene through laser irradiation. This method, notable for its cost-effectiveness, speed, and environmental sustainability, has broadened the scope of graphene applications into areas like sensing, energy storage, and flexible electronics[42].

Graphene, which consists of a single layer of carbon atoms in a hexagonal structure, has garnered significant attention for its remarkable electrical, mechanical, and thermal characteristics. In 2014, researchers from Rice University pioneered the development of laser-induced graphene (LIG)[43]. They outlines the pioneering technique of producing laser-induced porous graphene films from commercial polymers through the application of CO_2 laser irradiation as shown in figure 2.1-7. Presented electrochemical analyses reveal that these graphene constructs demonstrate remarkable capacitance and power densities. This performance is attributed to their distinctive porous and polycrystalline characteristics.

LIG is typically produced by directing a CO_2 infrared laser onto a polyimide film, decomposing it into a porous graphene structure. This method allows for precise control by adjusting laser parameters like power, speed, number of passes, and the surrounding environment, impacting the quality and characteristics of the resultant graphene[44–46]. Recent research has investigated using alternative precursors and dopants to refine LIG's properties for specific uses[47]. Additionally, a novel UV laser direct writing method has been introduced for creating S- and N-doped graphene on substrates such as polyethylene terephthalate (PET) and glass, which avoids thermal

damage and eliminates the need for metallic precursors[6].

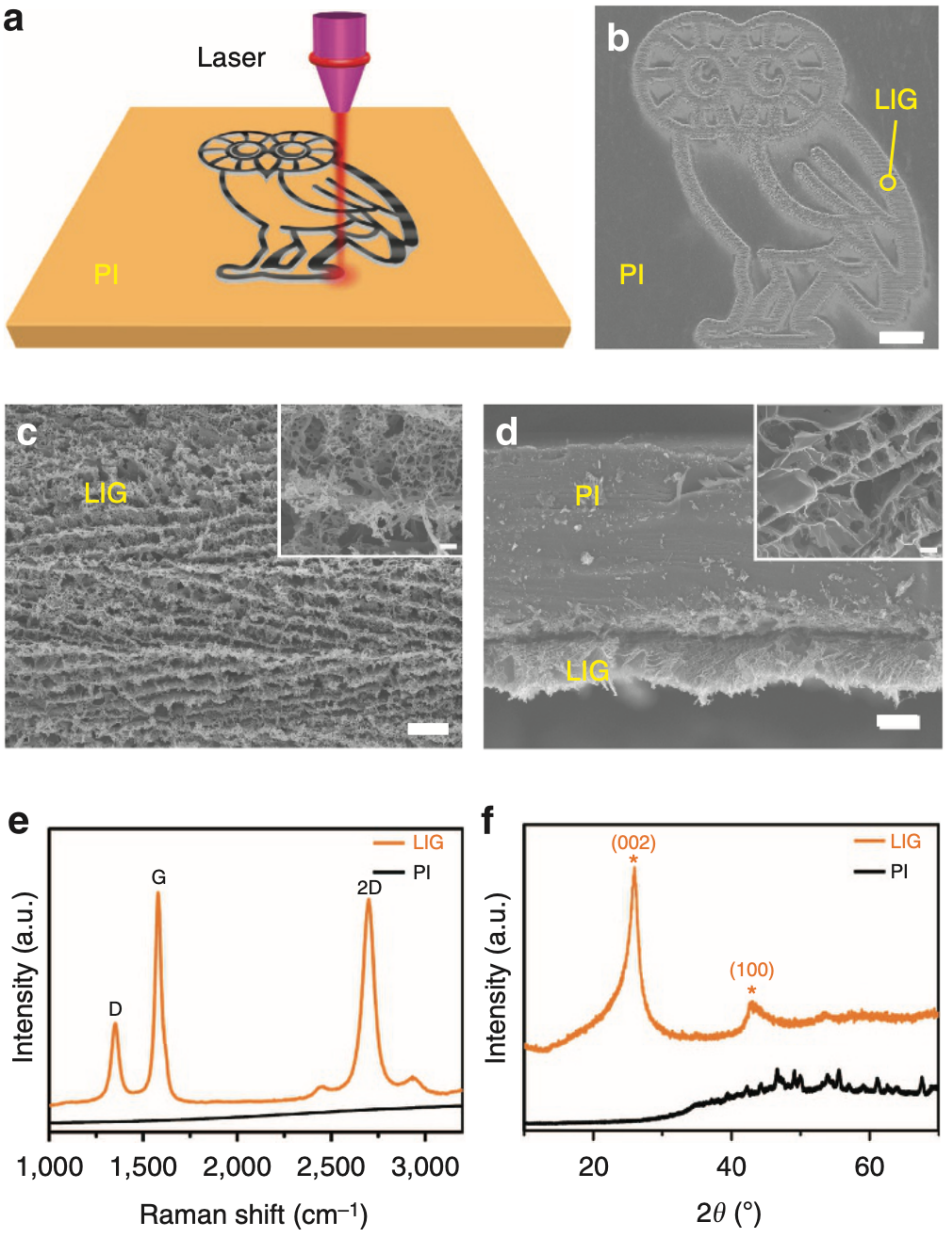

Figure 2.1-7 LIG created from commercial PI films using CO_2 laser patterning. (a) Diagram illustrating the LIG production method from PI. (b) SEM imagery showcasing LIG etched into an owl design, with a scale bar of 1 mm. (c) SEM image of a specific area of the LIG film highlighted in (b) Scale bar of 10 mm. An inset displays a zoomed-in SEM image, with a scale bar of 1 mm. (d) Cross-sectional SEM image of the LIG layer on the PI base, with a scale bar of 20 mm. An inset shows the porous structure of LIG with a scale bar of 1 mm. (e) Comparative Raman spectroscopy results of a LIG film versus the initial PI film. (f) XRD analysis of LIG powder removed from the PI film[43].

2.1.2.2 Fresnel Zone Plates

A key concept for understanding Fresnel lens diffraction is the FZP, which divides the wavefront into a series of concentric rings (zones). Each zone contributes either constructively or destructively to the intensity at a specific observation point, aiding in understanding how the amplitude and phase of light vary across the diffraction pattern[48]. FZP are diffractive optical elements that function similarly to lenses but use rings (zones) to focus light, each zone having a different optical path length to a common focal point. FZP can focus light or other waves and are used in various applications, including microscopy, imaging, and spectroscopy[49–51].

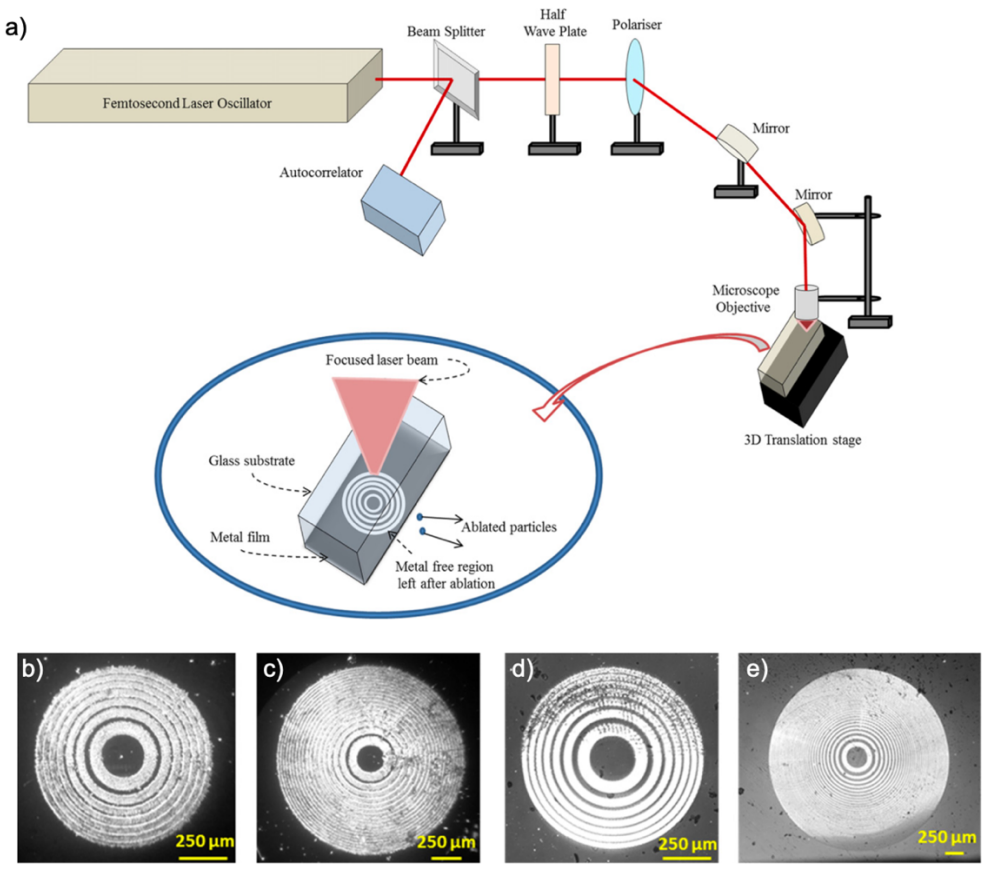

Figure 2.1-8 (a) Schematic of laser-induced solid ablation experiment set-up. The image of FZP: (b) Indium-coated 7 dark zones, (c) Indium-coated 16 dark zones, (d) Tungsten-coated 7 dark zones, (e) Tungsten-coated 50 dark zones[8].

Laser direct writing is a non-contact, maskless microfabrication method that enables the direct creation of customized designs on various substrates. Specifically for FZP, laser direct writing offers precise control over their geometrical dimensions and spatial arrangements, which are crucial for optimizing their optical functionality[7,52]. A research investigation has effectively confirmed that laser-induced solid ablation is a proficient, single-step approach for creating FZP on metal-coated transparent substrates[8]. As shown in figure 2.1-8, this method allows for the production of optical components without the necessity for masking or extensive post-processing, significantly simplifying the manufacturing process. This not only lowers costs but also makes the production method more environmentally friendly.

2.2 Fundamentals of optical super-resolution

2.2.1 Optical diffraction

Optical diffraction occurs when light waves meet an obstacle or pass through a slit of similar size to their wavelength. This causes the light to bend around the obstacle or spread after passing through the slit, creating a pattern of alternating dark and light bands, known as a diffraction pattern[53]. This pattern arises from the interference of light waves: in areas where the waves combine positively, bright bands are seen, and in areas where they negate each other, dark bands emerge[54]. Understanding diffraction is crucial for explaining various optical behaviours and underpins techniques in fields such as spectroscopy and microscopy, and the creation of optical instruments like diffraction gratings that divide light into its spectral components. Moreover, diffraction sets a limit on the resolution of optical imaging systems, as explained by the Rayleigh criterion, which defines the smallest distance between two distinguishable points in an optical system[55].

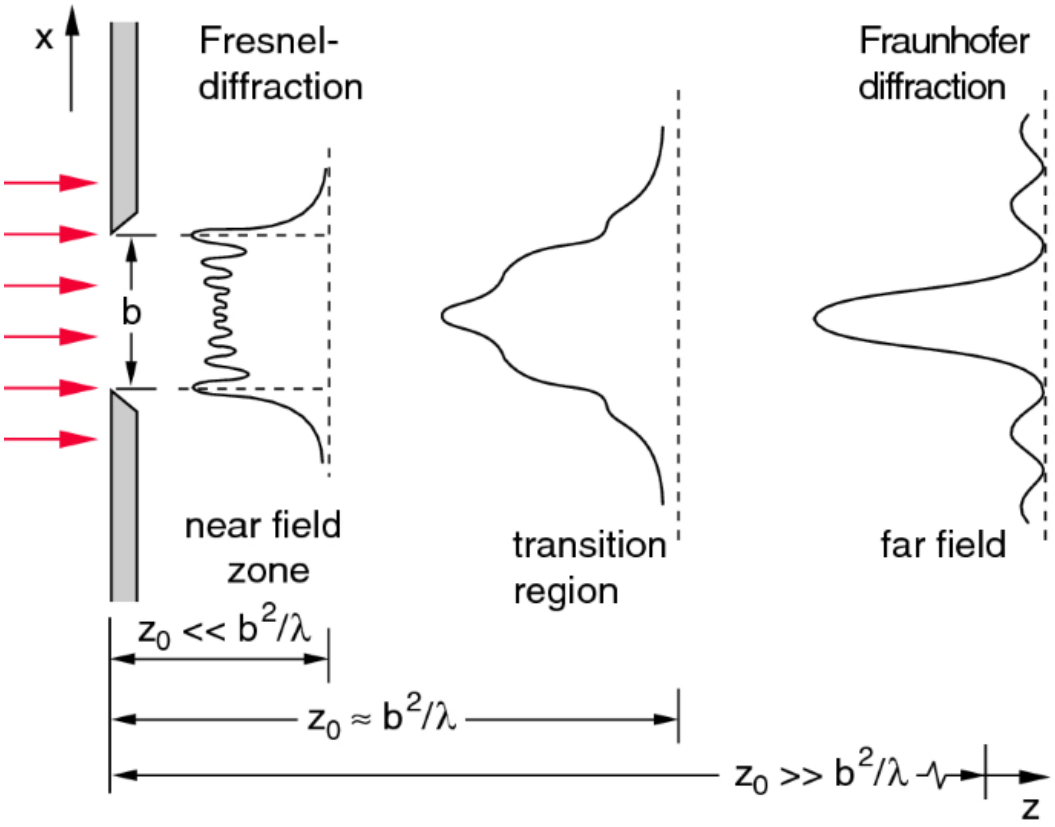

Figure 2.2-1 Diffraction with increasing axial distance z_0[56].

In the region immediately beyond the aperture opening, b, the irradiance pattern mirrors the shape of the aperture (near-field) as long as the axial distance is smaller than b^2/λ. When the axial distance z_0 exceeds b^2/λ, the far-field pattern becomes observable.

Different diffraction patterns can be observed depending on the distance from the aperture, generally characterized as near-field diffraction (Fresnel diffraction) and far-field diffraction[57]. Near-field diffraction, also known as Fresnel diffraction, occurs when the wavefront of light interacts with an obstacle or aperture at a distance not significantly greater than the light's wavelength. This type of diffraction is characterized by observing the diffraction pattern at relatively short distances from the diffracting object, where the curvature of the wavefronts and the angular spread of the waves are significant. The diffraction patterns in the Fresnel region can be

complex and highly dependent on the precise distance between the object and the observation screen[58,59]. Far-field diffraction, also known as Fraunhofer diffraction, involves the diffraction of waves, particularly light, under conditions where the wavefronts are far enough from the diffracting object or aperture that they appear essentially parallel. This typically occurs when the distance from the aperture to the observation point is much greater than both the aperture size and the wavelength of the light[60]. Far-field diffraction patterns are more predictable and exhibit less variability with changes in distance than those seen in near-field diffraction. The patterns themselves are primarily influenced by the aperture's shape and size. For example, a single slit produces a pattern of alternating bright and dark bands, while a circular aperture results in a central bright spot surrounded by concentric rings[61].

2.2.2 Resolution limit

The resolution limit refers to the smallest distinguishable distance between two points in a microscope image, fundamentally governed by the properties of light and the optical system of the microscope. This limit is determined by the wavelength of light and the numerical aperture of the microscope system. In 1873, the resolution limit of the microscope was first proposed by Ernst Abbe[62]. He defined that the formula to calculate the resolution limit of a microscope, as described in the paper, is derived from the wave nature of light and the geometry of the microscope optics. The resolution limit can be calculated using the formula:

$$d = \frac{\lambda}{2N.A.} \tag{2.2-1}$$

where d is the smallest resolvable feature size (the resolution limit), λ is the wavelength of the light used, $N.A.$ is the numerical aperture of the objective lens, which depends on the refractive index of the medium between the sample and the

lens and the sine of the half-angle (α) of the maximum cone of light that can enter the lens. The numerical aperture ($N.A.$) is given by:

$$N.A. = nsin(\alpha)$$

(2.2-2)

Here, n is the refractive index of the medium (air, water, oil, etc.) through which the light travels before entering the lens. This fundamental limit determines the resolution of images produced by optical systems and can be viewed as a specific application of Heisenberg's uncertainty principle, which relates the position (Δx) and momentum (Δp_x) of a photon. Thus, the optical diffraction limit represents a distinctive instance of quantum mechanical phenomena, employing Heisenberg's uncertainty principle concerning the position and momentum of a photon[63].

$$\Delta p_x \Delta x \geq h$$

(2.2-3)

Here, Δp_x and Δx pertain to any of the three components of the momentum and position vectors, respectively, signifying the uncertainties linked to these specific components of the position and momentum vectors. In medium i, the three components of the wavevector k_i must meet certain conditions:

$$k_i^2 = k_x^2 + k_y^2 + k_z^2$$

(2.2-4)

Here, the magnitude of the wavevector $|k_i|$ is defined as $2\pi/\lambda_i = n_i|k_o|$, where λ_i is the wavelength within medium i, and n_i is its refractive index, with k_o representing the wavevector in free space. In classical photonics, focusing effects are

primarily concerned with freely propagating photons. These photons exhibit wavevectors with three real-valued components k_x, k_y and k_z which, according to the relationship, must each be smaller than k_i. This condition is crucial as it pertains to the diffraction limit in the far-field region in classical optics, where the nature of free propagation is determined by these components. Thus, $|k_i|$ invariably exceeds each of the wavevector's individual components, reflecting its role in governing the characteristics of light's propagation. The spatial resolution of a freely propagating light beam is characterized by Δx, which denotes the minimum cross-section of the beam. Consequently, the minimum cross-section of a freely propagating beam is defined as:

$$\Delta x > \frac{1}{k_x} = \frac{\lambda_i}{2\pi} \tag{2.2-5}$$

This closely resembles the renowned Rayleigh criterion formula, which defines the smallest resolvable distance for a focusing objective as:

$$D_{Rayleigh} = 0.61 \frac{\lambda}{N.A.} \tag{2.2-6}$$

where λ represents the wavelength and $N.A.$ denotes the numerical aperture. This fundamental boundary constrains the resolution capabilities of optical systems like microscopes[64]. Thus, to attain resolutions beyond the diffraction limit (super-resolution), it is necessary to utilize evanescent waves in the near-field[65].

2.2.3 Near-field scanning optical microscope

Synge's initial proposal in 1928 described a technique for overcoming the diffraction

limit, involving a potent light source placed behind a thin metal film with a small aperture, with the sample positioned 100nm away from the light source, and scanned point-by-point[66]. This innovative concept was later actualized with the introduction of the Super-resolution Aperture Scanning Microscope, which was demonstrated by Ash and Nicholls[67].

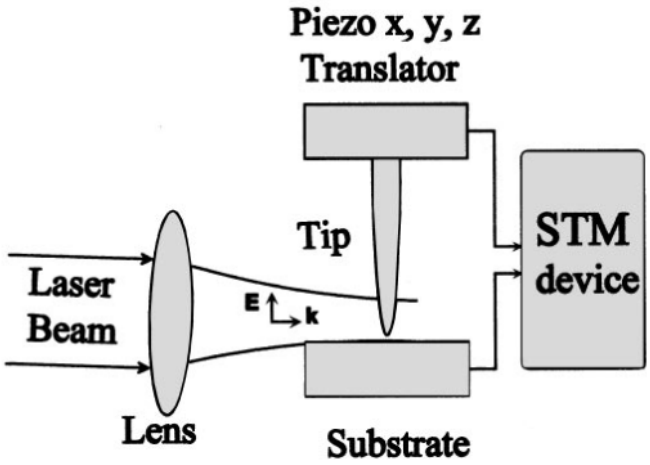

Figure 2.2-2 Schematic of the experimental setup for a scanning tunneling microscope tip with laser light[68].

A Scanning Tunneling Microscope (STM) is primarily employed for visualizing and altering conductive surfaces down to atomic and nanometer precision, as illustrated in figures 2.2-2. This instrument manipulates and modifies surfaces through various interactions including contact forces, electrical fields, and electron beam-induced effects[68]. Progress in nano-fabrication technology facilitated the production of sub-wavelength sized probe tips, and advances in computer image processing from technologies like STM and Atomic Force Microscopy (AFM) led to the unveiling of the first modern Near-field Scanning Optical Microscope (NSOM) in 1991 by Betzig et al. The development of NSOM represented a crucial breakthrough in super-resolution research, using a diminutive tip placed close to an object's surface to gather

evanescent waves from the near field. Scanning the sample produces a super-resolution image whose resolution is defined by the diameter of the tip's aperture rather than the incident light's wavelength. Although early efforts were constrained by the challenges of precise scanning within a wavelength's distance, advancements in nano-fabrication, control over probe tips, and image processing rejuvenated this imaging approach in the 1980s, culminating in Betzig's group demonstrating a sophisticated NSOM system capable of detecting single molecules[69].

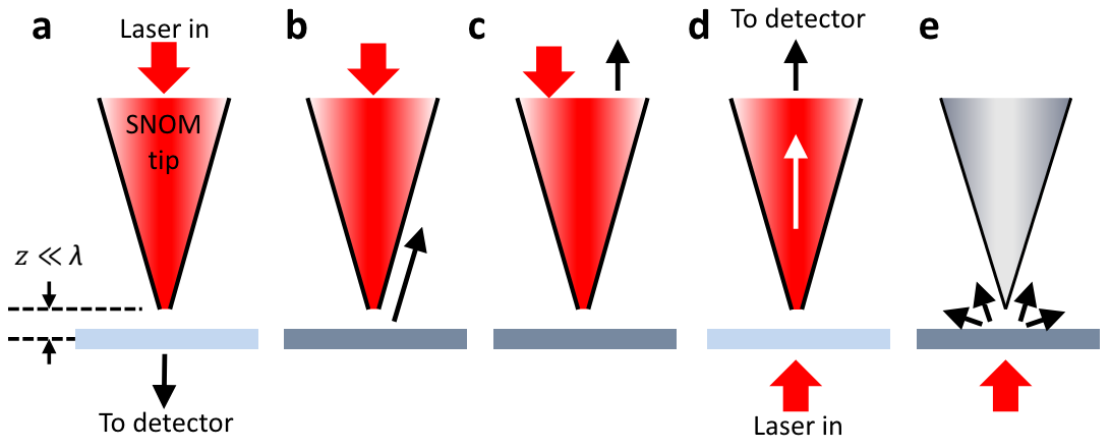

Figure 2.2-3 Modes of NSOM. (a-c) Illumination mode, including transmission illumination, scattering illumination and reflection illumination. (c-d) Collection mode, including reflected collection and transmitted collection. (e) Aperture-less mode[70].

The operation of an NSOM is segmented into three principal modes as illustrated in figure 2.2-3. Illumination mode uses the NSOM tip as a sub-wavelength point source to illuminate the sample. This mode has three variations: Transmission illumination (Fig. 2.2-3a), where light passing through the sample is captured by an external detector, scattering illumination (Fig. 2.2-3b), where light scattered from the sample's surface is collected by an external detector such as a microscope objective and reflection illumination (Fig. 2.2-3c), where reflected light is directly gathered by the NSOM tip itself. The second mode, known as collection mode, involves the NSOM tip collecting signals instead of emitting them. This includes reflected collection (Fig. 2.2-

3c), where the tip gathers reflected light, and transmitted collection (Fig. 2.2-3d), where it collects light transmitted through the sample. Lastly, the aperture-less mode (Fig. 2.2-3e) employs a sharp, metal tip without an aperture as a minor scatterer for light transmitted or reflected from the sample, with the scattered signal subsequently collected by a large external detector. Each mode operates with a sub-wavelength aperture, typically between 20 nm to 100 nm, positioned at the tip of a metal-coated tapered optical fiber. These diverse operational modes allow for detailed surface analysis at resolutions surpassing the traditional diffraction limit of light.

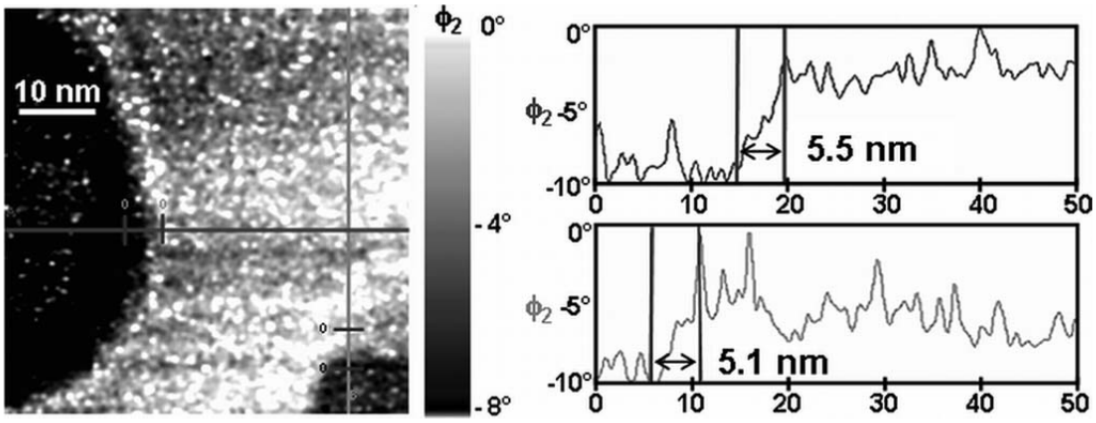

Figure 2.2-4 A optical phase image and line scan data belonging to the marked positions on the image[71].

Pohl's study marks a significant advancement in optical microscopy by achieving sub-wavelength resolution imaging. Utilizing a novel method akin to a medical stethoscope, this research bypasses the traditional diffraction limit, enabling the identification of features as tiny as 25 nm through a finely engineered aperture[72]. On the other hand, Bek's work centres on developing and deploying an aperture-less NSOM, which attains resolutions below 10 nm as shown in figure 2.2-4. This instrument is instrumental for detailed examinations of optical properties at surfaces and interfaces, effectively imaging both opaque and transparent substrates[71].

2.2.4 Photonic Nanojet

The concept of "photonic nanojet" (PNJ) refers to a distinct optical phenomenon where super-resolution focusing is achieved through the scattering of light by microscale dielectric spheres. This effect was first observed by Lu and Luk'yanchuk et al. in 2000, marking a significant breakthrough in optical science[14]. By 2004, Chen et al. formally introduced the term "photonic nanojet" into the optics community, highlighting its ability to produce highly concentrated, subwavelength beams of light at the shadow side of a dielectric particle[15].

PNJs result from the complex interplay of light interactions, including reflection, refraction, and interference, occurring at the surface of micro or nanoscale dielectric structures. These interactions lead to the formation of a sharply focused light beam that extends beyond the physical dimension of the particle, thus enabling imaging capabilities that surpass the conventional diffraction limit[73]. The remarkable properties of PNJs, particularly their intense light concentration and the ability to focus light to subwavelength scales make them extremely valuable in a variety of advanced optical applications. They are utilized in super-resolution imaging, which allows scientists to view details at the nanoscale that were previously obscured by the diffraction limit of light. Additionally, PNJs enhance Raman scattering, increasing the detection capabilities of molecular vibrations by concentrating light into a small volume. Moreover, the ability of PNJs to manipulate nanoparticles makes them useful in fields such as nanotechnology and materials science, where precise control over particle positioning and assembly is required[18].

Heifetz highlights these PNJs are characterized by several distinctive properties: their beamwidth can be subwavelength, reaching down to about $\lambda/3$ for microspheres, and they are a non-resonant phenomenon, appearing across a broad range of diameters as long as the refractive index contrast relative to the background medium is less than about 2:1. Additionally, PNJs can exhibit intensities that far exceed the illuminating wave. Importantly, the introduction of a nanoparticle within a PNJ can drastically

perturb the far-field backscattered power from the microstructure. This perturbation is significantly greater than what would be expected from Rayleigh scattering, enhancing sensitivity to nanoscale objects. These properties equip PNJs for advanced applications in nanopatterning, nanolithography, and enhanced microscopy, potentially transforming nano-photonics and optical data storage fields[17].

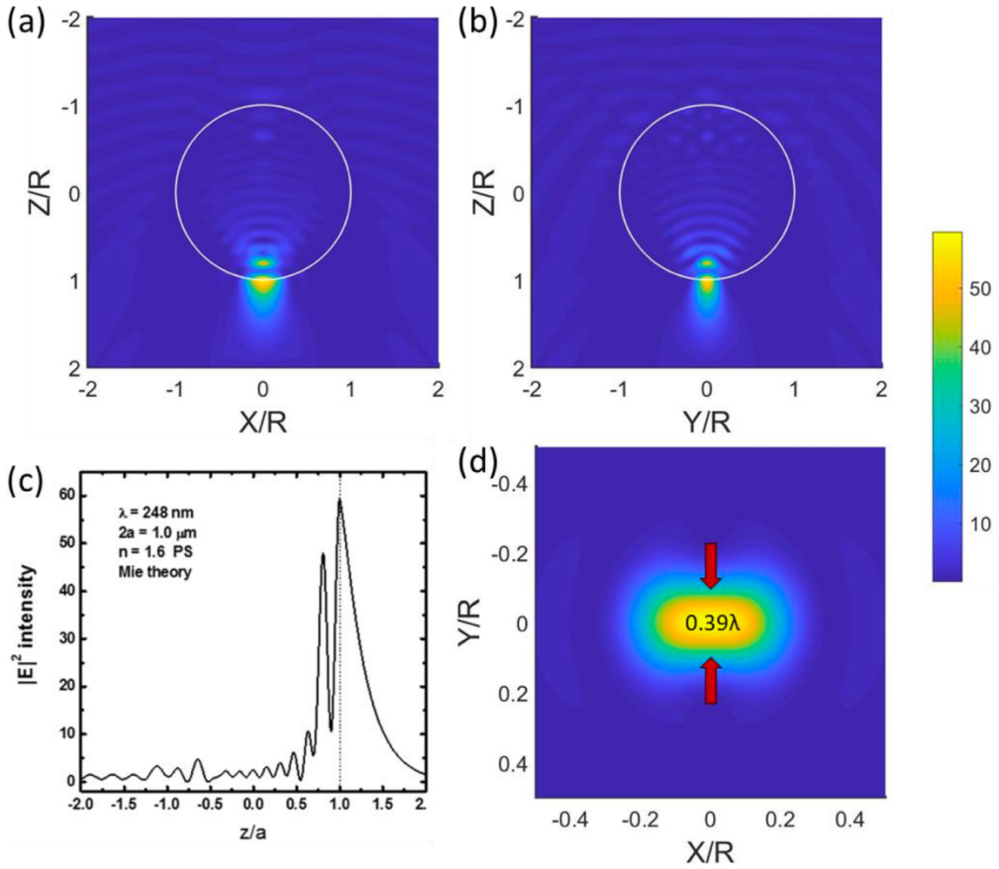

Figure 2.2-5 PNJ generated by 1μm polystyrene (n=1.6) microsphere illuminated by a laser at λ=248nm. Electric field intensity distribution, $|E|^2$, at (a) XZ-plane (parallel to polarization) and (b) YZ-plane (perpendicular to polarization). (c) Intensity along Z-axis (propagation direction). (c) Lateral field distribution (XY-plane) of focal spot under the microsphere (z=a)[74].

In the given example depicted in figure 2.2-5, a PNJ is formed by a polystyrene

microsphere, 1.0 μm in diameter, with a refractive index of 1.6, when it is illuminated by a laser beam with a wavelength of 248 nm. The electric field intensity significantly increases beneath the microsphere, amplifying by 59.6 times at the microsphere's radius (z=a), and subsequently decreases to 1.57 times at z=2a. The PNJ manifests an elliptical profile in the lateral (XY-plane) dimension with a waist of only 0.39λ in the direction perpendicular to the incident polarization. This waist is substantially narrower than the traditional diffraction limits of 0.61λ (Rayleigh criterion) and 0.5λ (Sparrow criterion). This reduction in waist size illustrates the PNJ's capability to considerably diminish the full width at half maximum (FWHM), highlighting its utility in enhancing optical resolution in various applications.

2.3 Superlens-assisted laser manufacturing

2.3.1 Microsphere metamaterial superlens

Microsphere metamaterial superlens is an innovative type of lens that leverages the unique properties of microspheres, typically made of dielectric materials, to overcome the diffraction limit of conventional optics[23,75]. Microsphere superlenses can focus light to a spot size smaller than the wavelength of light, a capability that conventional lenses cannot achieve due to the diffraction limit. This feature is crucial for applications requiring high-resolution imaging and precise manipulation of light at the nanoscale[76]. These lenses utilize the near-field optical phenomena that occur when light interacts with microspheres at distances smaller than the wavelength of the light. The microspheres enhance the evanescent waves and convert them into propagating waves that can be focused[77]. The microspheres are often made from transparent dielectric materials such as silica[78], polystyrene[79] TiO_2 and $BaTiO_3$[80]. Their high refractive index and spherical symmetry enable unique optical behaviours, including the aforementioned focusing and near-field enhancement.

There are two main applications for microsphere superlenses: super-resolution imaging and micro/nano manufacturing[23]. By surpassing the diffraction limit, these superlenses are utilized in microscopy to observe features at the nanometer scale, which were previously inaccessible with traditional optical instruments[81]. Microsphere superlenses can focus laser beams to a spot size smaller than the wavelength of light, enabling the fabrication of features at scales much finer than those achievable with conventional photolithography. This capability to focus light beyond the diffraction limit is essential for the precise patterning of materials needed in advanced semiconductor manufacturing[16,82].

While offering unprecedented precision, the applications of microsphere superlenses in photolithography and nanofabrication face challenges such as alignment accuracy, integration into existing manufacturing processes, and scalability for industrial production. Future research might focus on automating the alignment of microspheres over large areas and improving the durability and repeatability of the lenses for commercial-scale applications.

2.3.2 Microsphere monolayer preparation

In order to successfully implement microsphere array laser manufacturing in a large area on flat substrates like glass slides, a deep understanding of the specific techniques involved in fabricating hexagonal close-packed microsphere monolayer arrays is essential. This requires exploring the precise deposition methods that ensure uniform microsphere alignment and adhesion on substrate surfaces, which are critical for achieving accurate and efficient laser marking outcomes. Recent advancements have focused on enhancing the precision and scalability of monolayer formations. Key methods such as Langmuir-Blodgett techniques and self-assembly deposition have been optimized to improve monolayer uniformity and functional integration.

In 1917, building on the foundational work of A. Pockels[83], I. Langmuir and K. Blodgett showcased that monolayers formed at a water-air interface could be

successfully transferred to solid substrates using a device now known as the Langmuir-Blodgett trough, depicted in figure 2.3-1. The Langmuir-Blodgett method is a key technique for depositing monolayer films onto various substrates, extensively used in creating electronic components such as semiconductors[84], biosensors[85], and more recently, in the development of algal bio photovoltaic fuel cells[86]. This method involves dispensing a colloidal nanoparticle solution onto a liquid surface in the trough. These nanoparticles then spread out to form a self-assembled monolayer. A barrier subsequently moves in, compressing the monolayer at a rate dependent on the nanoparticle properties, pressing it against a vertically positioned substrate. The substrate is then carefully raised, allowing the monolayer to adhere vertically, thus forming the desired coating on the substrate surface.

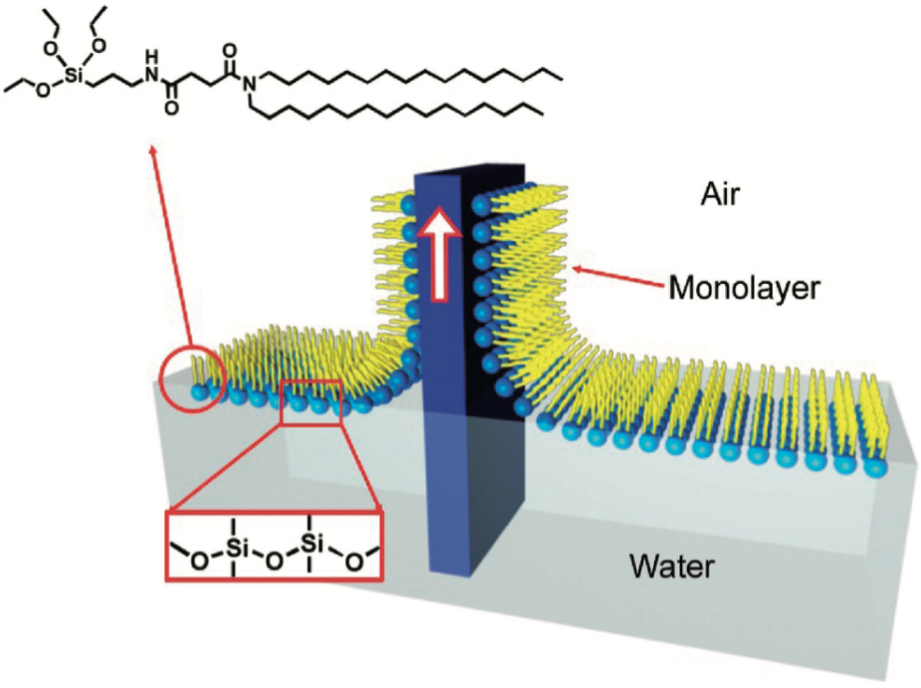

Figure 2.3-1 Illustration of the Langmuir-Blodgett method at air-water interface[87].

Lotito introduced a method for depositing microsphere monolayers on flat glass substrates using self-assembly[88]. Initially, as illustrated in the figure 2.3-2, a colloidal suspension is applied to a parent substrate through techniques such as dip-coating or

manual spreading. The particles are then transferred to an air/water interface by submerging the parent substrate, allowing them to self-assemble and float at the interface. The subsequent step involves horizontally aligning the floating monolayer with a target substrate to facilitate the transfer of the assembled layer. As the water is released from the apparatus, the monolayer, formed at the water/air interface, is lowered onto the substrate beneath. This method employs a straightforward setup, eliminating the need for complex equipment, effectively reducing nucleation centers, and decreasing polycrystallinity. The setup also promotes the formation of a monolayer at the three-phase contact line, leading to a more ordered assembly.

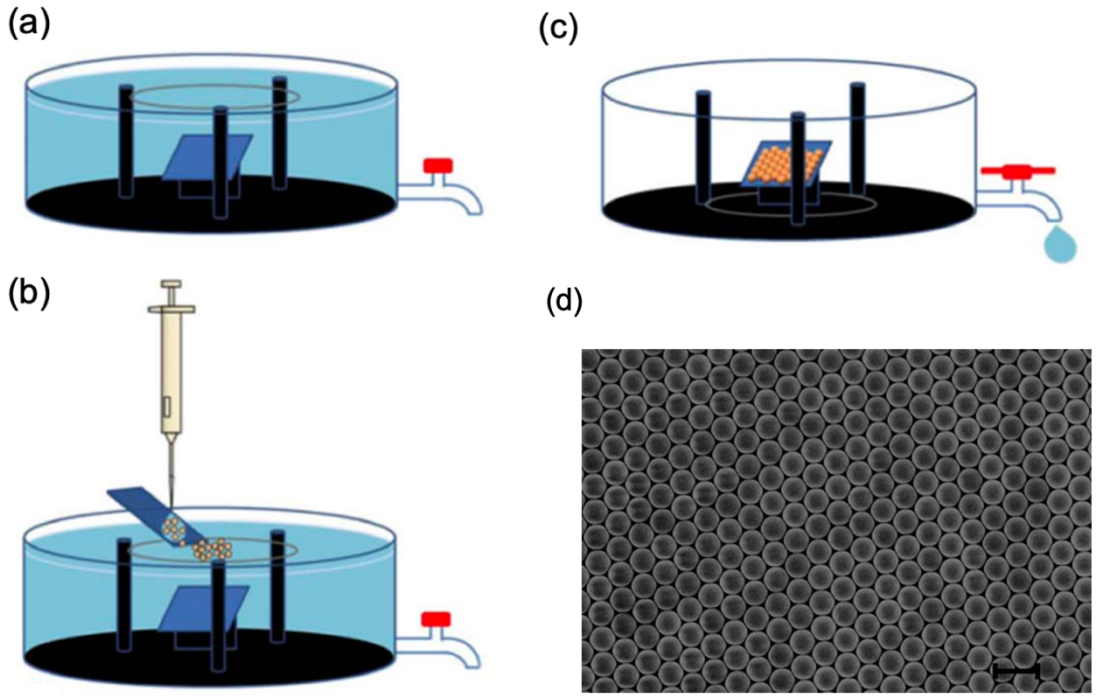

Figure 2.3-2 (a-c) Illustration of the preparation process for microsphere monolayer deposition on a glass substrate. (d) SEM micrographs of monolayers of particles. Scale bars: 2 µm[88].

Future directions in microsphere monolayer research are likely to concentrate on integrating these layers with other nanoscale materials and technologies to create more complex, multi-functional structures. There is also an increasing push towards

environmentally friendly materials and processes, driven by sustainability goals.

2.3.3 Nanohole array generation

Research into the capabilities of microsphere superlenses has evolved significantly since the early 2000s. The initial discovery that a microsphere could generate a sub-wavelength focus opened new avenues for precision in nanoscale engineering[14]. The researchers utilized spherical silica particles, each 0.5 μm in diameter, strategically placed on a silicon (100) substrate. These were then exposed to a 248-nm KrF excimer laser with a carefully controlled pulse fluence of 340 mJ/cm². This setup aimed to explore the microsphere's potential to enhance localized laser effects at a submicron scale. These tools provided detailed views of the substrate's surface where circular hillocks, about 100 nm in size, had formed at the exact locations of the silica particles shown in figure 2.3-3. The presence of these hillocks served as a clear confirmation of the microspheres' role in focusing the laser energy to a fine point, effectively interacting with the laser to manipulate the surface structure at a scale previously considered challenging to achieve.

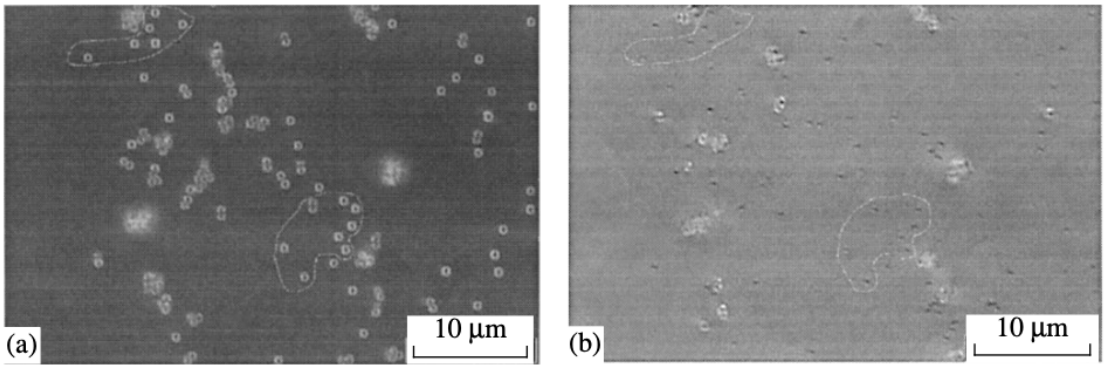

Figure 2.3-3 Observation of localized hillocks on a surface via optical microscope following particle-enhanced laser irradiation: (a) pre-irradiation and (b) post-irradiation views[14].

Since its discovery in 2004, this phenomenon has been termed the 'photonic nanojet' (PNJ). This effect involves the concentration of light into a tiny, high-intensity spot that can travel beyond the diffraction limit of light[15]. PNJ technology has been extensively applied in laser cleaning, where it enables the removal of minute particles from delicate surfaces without damage. In laser direct nano-writing, PNJs are used to fabricate microscopic structures with high resolution, enhancing the development of electronic and photonic devices. Additionally, PNJs play a crucial role in signal enhancement, particularly in optical systems, by boosting the intensity and clarity of signals in sensors and communication devices. The versatility and efficiency of photonic nanojets have made them a cornerstone in the field of nano-optics, pushing the boundaries of what's possible with light manipulation.

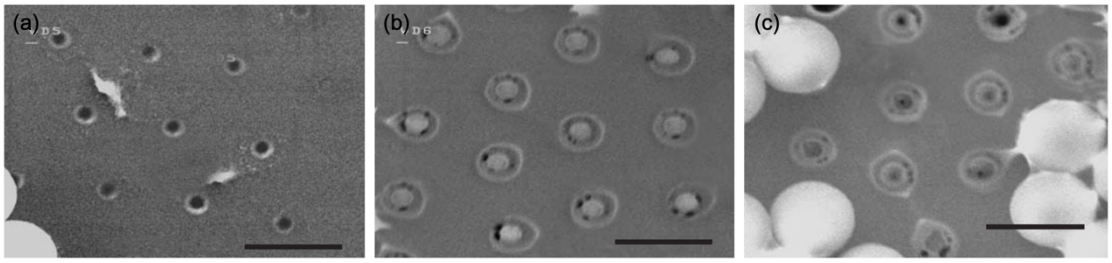

Figure 2.3-4 SEM images of nanodent structures formed on GST film after one laser pulse irradiation at increasing laser fluences. Scale bar is 1.0 μm[89].

A study utilized a 100-nm-thick GST film on a 0.6-mm polycarbonate substrate, with monodisperse polystyrene particles of 1.0 μm diameter serving as a mask for laser irradiation[89]. The paper contrasts these theoretical calculations, based on both Mie theory without a substrate and exact solutions with a substrate, showing enhanced and more focused optical near-field effects when the substrate is present. Experimentally, at lower fluences (up to 7.2 mJ/cm²), the resultant nanostructures were predominantly bowl-shaped with an average diameter increase linearly correlating with the fluence. However, beyond this fluence, the structure sizes

reached a saturation point, shifting to sombrero-shaped and then to halo-shaped as the fluence increased further (Fig. 2.3-4). This transition is attributed to the material and temperature dynamics at the surface, where higher fluences induce complex convective fluxes affecting the nanodent formations.

The development of microsphere monolayer deposition techniques, along with the enhancement of microsphere superlens array marking, is committed to advancing high-precision micro/nano manufacturing technologies. In 2008, Wang discusses the innovative technique of laser micro/nano fabrication using a particle lens array (PLA) irradiated with a femtosecond laser for processing glass[90]. This method highlights the ability to fabricate high-precision, crack-free micro/nano-structures on or inside glass, efficiently creating three-dimensional structures across multiple layers. It emphasizes the medium-tuned optical field enhancement around the PLA and notes significant differences in focusing properties between air and liquid media, with liquid extending the focal length and depth, which proves advantageous for creating higher-aspect-ratio structures.

In recent years, Romano has explored the generation of nanohole arrays via laser direct writing by depositing silica microspheres in a hexagonal close-packed monolayer on stainless steel plates using the Langmuir-Blodgett technique[91]. As shown in figure 2.3-5, a near-infrared ultrashort pulsed laser with circular polarization is steered across the substrate using a 3D scan lens. The interaction of the laser with the microspheres utilizes the photonic nanojet (PN) effect to focus the laser energy beyond the optical diffraction limit, allowing for the creation of subwavelength features such as nanoholes. Laser parameters such as energy, focal offset, and the number of pulses are carefully controlled to achieve the desired ablation while maintaining the integrity of the microspheres and substrate. Post-processing involves cleaning the sample in an ultrasonic ethanol bath to remove any residual spheres and debris. This technique provides a precise, non-contact, maskless method for fabricating detailed nano-features by harnessing the resolution-enhancing capabilities of the photonic nanojet phenomenon.

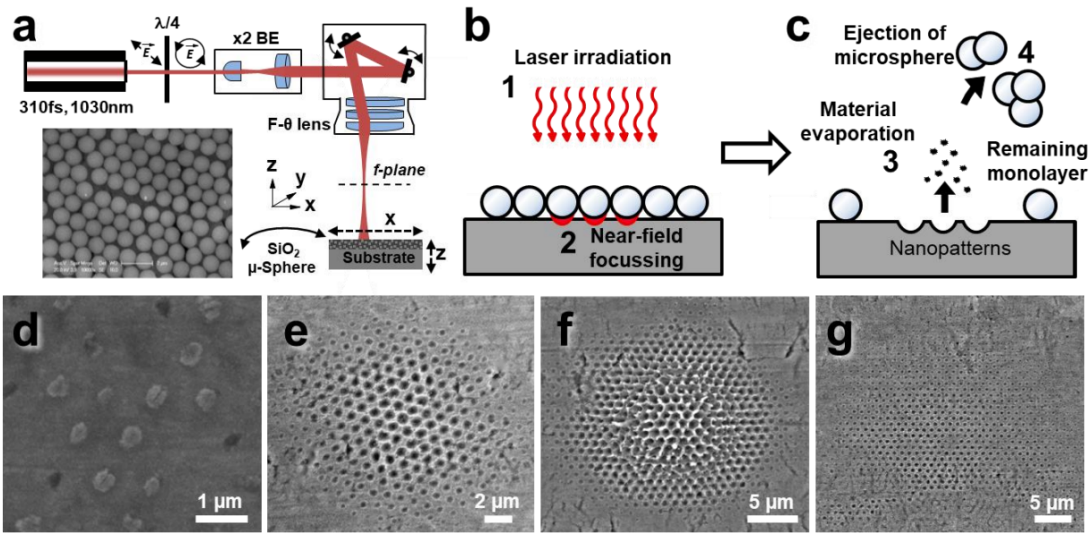

Figure 2.3-5 (a) Experimental setup for direct laser ablation-based nanopatterning by irradiating 1μm-diameter microspheres with a femtosecond laser beam. (b-c) The schematic steps of the nanohole generation process, where microspheres are partially removed from the ablation area. (d-g) Array of nanoholes created by a single irradiation[91].

Additionally, a paper presents a novel method for improving the fabrication of nanohole arrays on silicon substrates, crucial for enhancing the efficiency of thin-film silicon solar cells[92]. Utilizing a picosecond laser, assisted by polystyrene microspheres, the study highlights that applying a thin gold coating significantly refines the morphology and boosts the ablation rate of these nanoholes. This coating minimizes the presence of sputtered nanoparticles and smooths the nanoholes' cross-sectional profiles compared to those on uncoated substrates. It enhances the laser energy absorption, facilitating more efficient nanohole creation. As figure 2.3-7, the process achieves well-ordered arrays with larger, deeper nanoholes at laser fluences between 1.19 and 1.39 J/cm^2, effectively optimizing light absorption capabilities for improved photovoltaic device performance.

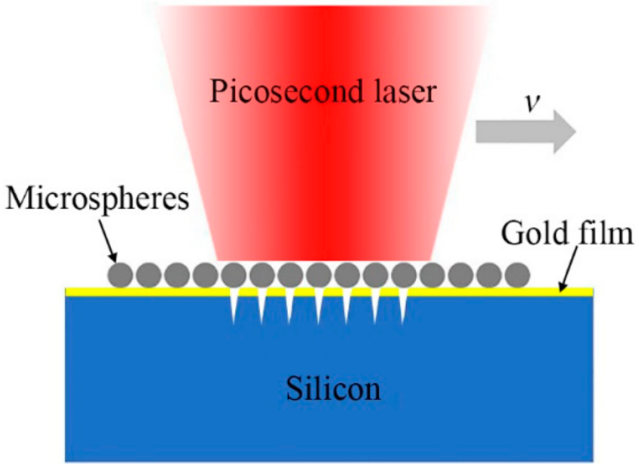

Figure 2.3-6 Schematic diagram of microsphere-assisted picosecond laser processing nanohole arrays on silicon substrate[92].

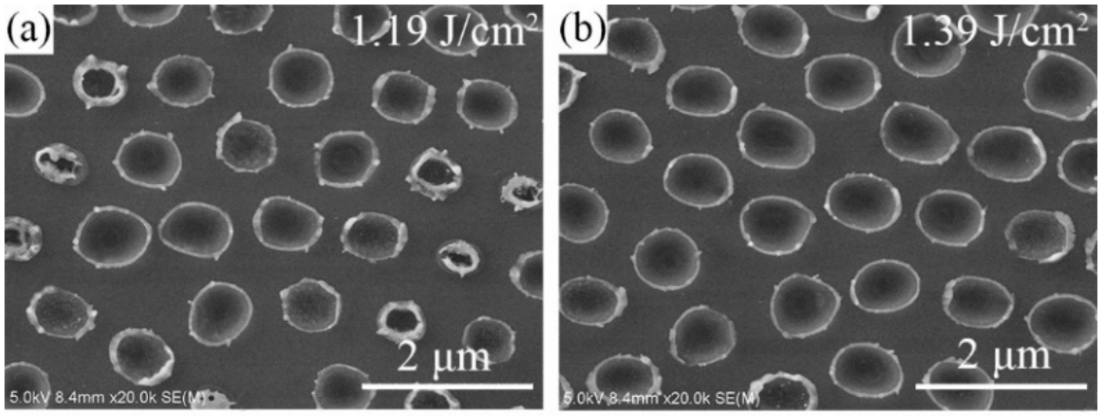

Figure 2.3-7 SEM images of nanohole arrays on a gold-coated silicon substrate using laser fluences of (a) 1.19 J/cm^2 and (b) 1.39 J/cm^2, respectively[92].

2.3.4 Single particle patterning of complex patterns

Research conducted by McLeod introduces a groundbreaking technique in the realm of nanopatterning, leveraging optically trapped microsphere superlens to achieve subwavelength direct-write capabilities. This method transcends the limitations imposed by the diffraction threshold typical of conventional-lens-based laser writing

systems, facilitating the creation of ultra-fine features significantly tinier than the wavelength of the utilized laser[90].

The core of the technique involves employing a Bessel beam to secure and manoeuvre microspheres in close proximity to a substrate surface. These microspheres function as miniature lenses that intensify and concentrate the laser energy onto precise locations on the substrate, thus enabling material modifications at scales notably smaller than the beam's original width. As illustrated in figure 2.3-8, the experiments successfully demonstrated the ability to generate features as diminutive as 100 nm using polystyrene spheres. This capability was tested on various substrates, including polyimide films and polycarbonate, showcasing the adaptability of the method. The study concludes by asserting that superlens-assisted laser manufacturing marks a major progression in nanofabrication technology. It offers a versatile and scalable approach for crafting features at subwavelength scales, heralding a new era of possibilities in nanoscale engineering.

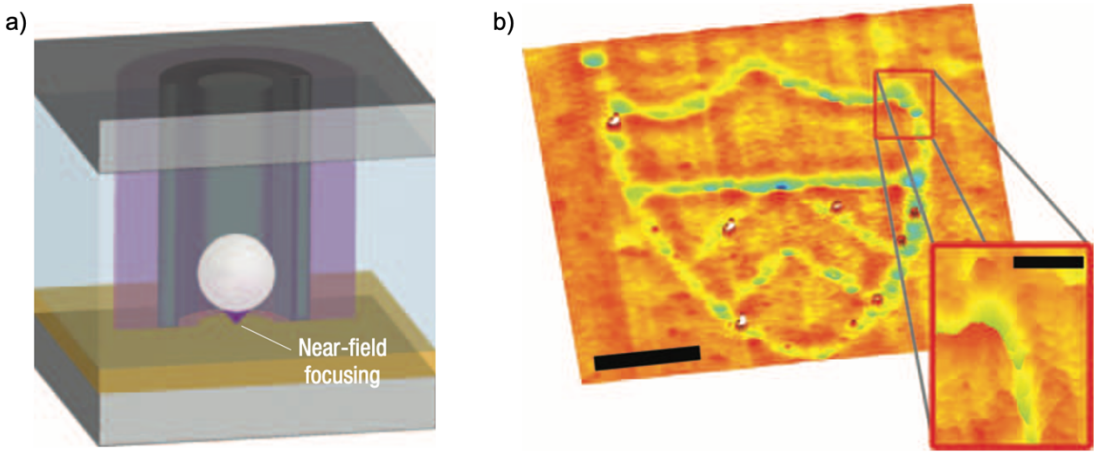

Figure 2.3-8 (a) A microsphere in white is optically trapped near the polyimide surface in orange in the trapping laser beam in purple. (b) Nanopatterned of 5 mm wide shield on polyimide film . Main scale bar, 2 mm; Inset scale bar, 1 mm[90].

Another research reported by Shakhov explores advanced techniques in laser

manufacturing[93], particularly the nanostructuring of glass using femtosecond laser pulses and optically trapped microspheres, as shown in figure 2.3-9. The technique employs femtosecond laser pulses guided through optically trapped silica microsphere superlens, which concentrate the laser's energy onto the glass surface. This configuration harnesses the near-field effects produced by the microspheres, enabling highly precise fabrication. The process successfully generates features smaller than 100 nm in diameter, remarkably below the wavelength of the light used, illustrating the method's superior resolution capabilities.

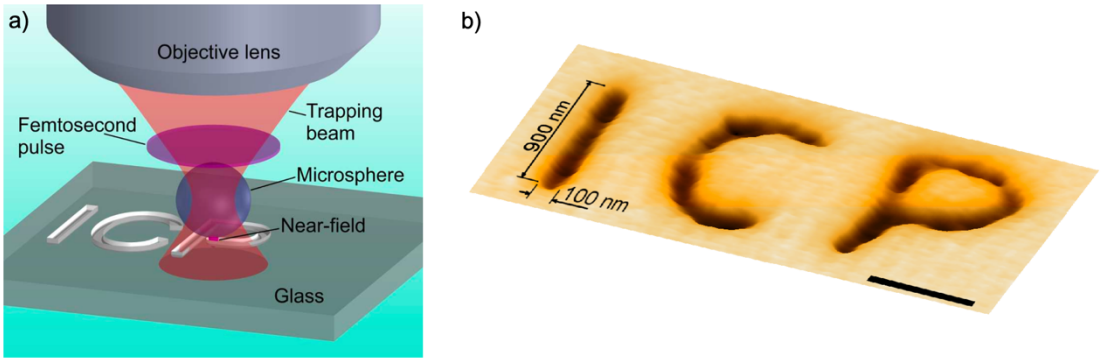

Figure 2.3-9 (a) Schematic of superlens-assisted nanostructuring: Amplified femtosecond pulses are directed through a silica microsphere superlens, focusing tightly in the near-field zone on the sample surface to facilitate laser manufacturing. (b) A two-dimensional image of the abbreviation "ICP" etched onto a borosilicate glass surface, where the average depth of the grooves is 20 nm. Scale bar, 500 nm[93].

2.3.5 Angular patterning with 80 nm resolution

Guo and colleagues introduce a pioneering approach in the field of nanofabrication, detailed in their publication on the near-field laser parallel nanofabrication of arbitrary-shaped patterns[22]. This innovative method leverages the near-field focusing capabilities of a self-assembled particle array positioned on the substrate, which interacts dynamically with an angularly incident laser beam. The process not

only eliminates the need for traditional projection masks but also achieves remarkably high resolution, with spot sizes as small as 80 nm. Additionally, this technique enables the simultaneous creation of over 6 million uniform nanopatterns within a compact area of 5x5 mm², requiring only a few laser pulses to accomplish what would traditionally take much longer.

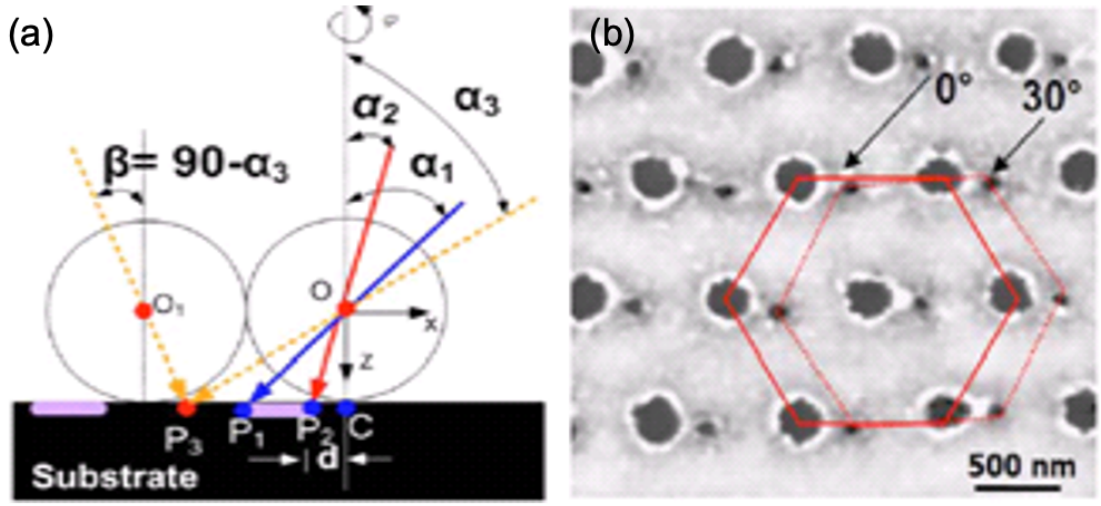

Figure 2.3-10 Schematic diagram of (a) The experimental setup for direct laser writing of a nanoline array on a substrate surface. (b) SEM images of two hexagonal nanodent arrays created by a single KrF laser pulse at incident angles of 0° with a fluence of 6.5 mJ/cm², and 30° with a fluence of 1.0 mJ/cm², respectively[22].

The core of this technology involves a KrF excimer laser with parameters: a wavelength of 248 nm, a pulse duration of 15 ns, and a repetition rate of 1 Hz. These characteristics make the laser particularly suited for precise, controlled nanoscale fabrication. The SEM images (Fig. 2.3-10) show hexagonal nanodent arrays created using a single laser pulse at varying incident angles and fluences, 0° with 6.5 mJ/cm² and 30° with 1.0 mJ/cm², demonstrating the technique's ability to control nanoscale features. Notably, the nanodents formed at 30° are significantly smaller, approximately 80 nm in diameter, compared to those at 0°, which are around 300 nm. This surpasses the

diffraction-limited resolution of 124 nm, attributed to the dominance of evanescent wave modes. By methodically scanning the laser beam across the substrate at various angles, the particle array acts as a series of microscopic lenses. These lenses focus and intensify the laser spots at the surface, enhancing the precision of the nanopatterning process. This capability to direct and manipulate laser light with such accuracy opens up new possibilities for designing and developing advanced nanoelectronic and nanophotonic devices, which require intricate patterns etched at the nanometer scale.

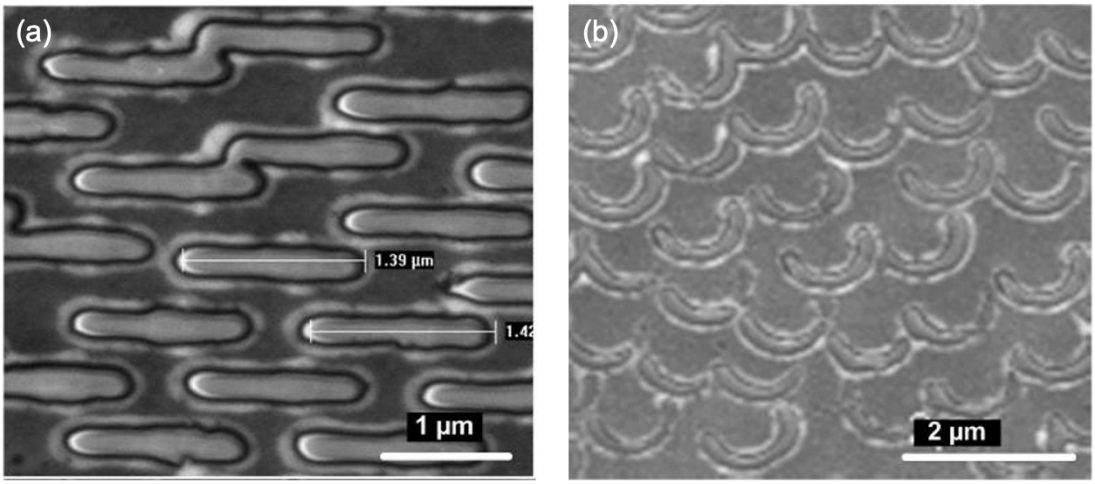

Figure 2.3-11 SEM images show an ordered array of line structures fabricated using the angular scanning technique: (a) The average line length is 1400 nm, and the width is 360 nm. (b) The scanning path follows an angular trajectory, resulting in an array of c-shaped nanostructures[22].

2.3.6 Laser patterning on curved surfaces by superlens arrays

The technology of laser direct writing using microsphere superlens arrays for generating nanoholes on flat substrates has been well-established[27,97,98]. However, it is a challenge to extend this technique to curved surfaces. A paper introduces a novel technique for near-field optical micro/nanopatterning on curved surfaces using transported micro-particle lens arrays (PLA)[94]. The method involves

creating a hexagonal closed-packed monolayer of SiO_2 microspheres on a flat glass surface, which is then transferred to a curved substrate for patterning. This approach utilizes a 532 nm wavelength Nd laser and achieves patterning through near-field enhancement around the particles.

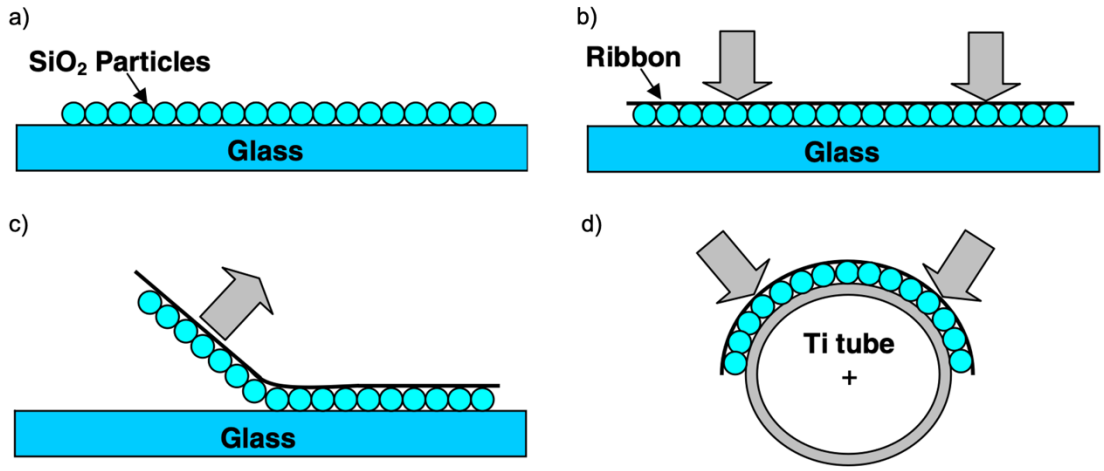

Figure 2.3-12 Process of transferring particles includes the following steps: (a) A monolayer of particles is created on a glass surface. (b) An adhesive ribbon is positioned over the monolayer and pressed down to adhere. (c) The ribbon, now bearing the monolayer, is peeled away from the glass surface. (d) The ribbon is then carefully wrapped around the titanium tube[94].

The process of transferring a particle monolayer onto a curved surface as detailed in the paper involves an innovative use of a flexible, optically transparent adhesive ribbon. As shown in figure 2.3-12, initially, a monolayer of silica spheres is formed through self-assembly on a flat, clean, hydrophilic glass slide. This assembly process utilizes a diluted solution of silica particles, which, as it dries, forms a hexagonal close-packed array due to capillary forces. Once the monolayer is formed, the next step involves the transfer of this array to a titanium tube curved surface. To achieve this transfer, the adhesive ribbon, chosen for its flexibility and transparency to the specific laser wavelength used (532 nm), is carefully applied onto the glass slide bearing the

particle monolayer. By gently pressing and subsequently peeling off the ribbon, the particles adhere to the ribbon due to a thin layer of polyolefin resin acting as an adhesive. This monolayer-coated ribbon is then accurately wrapped around the cylindrical surface of the titanium tube. This method ensures that the particle monolayer is effectively transferred onto the curved surface, ready for the subsequent laser patterning step.

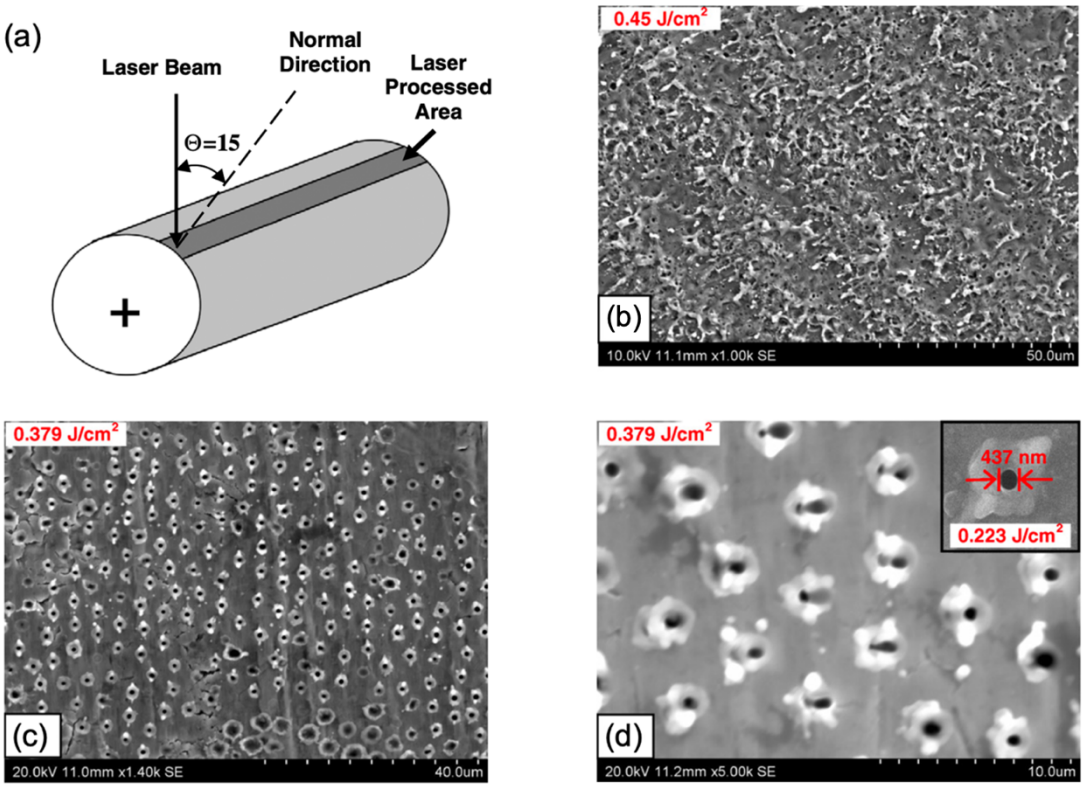

Figure 2.3-13 (a) Diagram of the scanned area on the curved tube surface. (b) Debris observed on the Ti surface at a laser fluence of 0.45 J/cm². (c-d) SEM images of patterns created on the Ti surface at 0.379 J/cm². The inset displays the pattern formed at a fluence of 0.223 J/cm²[22].

The laser was directed through the ribbon to the surface of the Ti tube. Given the curvature and material properties of the tube, adjustments were made to the laser's incident angle and fluence to optimize patterning. The tube was rotated to expose

different areas to the laser, ensuring even patterning across its surface. The technique facilitated the patterning of a large area with good quality. It was observed that reducing the laser fluence below 0.379 J/cm² prevented damage to the ribbon while still achieving sufficient intensity enhancement by the particles to effectively texture the surface, as shown in figure 2.3-13. The finest features produced had diameters of around 437 nm, achieved at a laser fluence of 0.223 J/cm², demonstrating the method's capability to generate sub-micrometer scale features with high precision.

Based on the technology of superlens-assisted laser patterning on curved surfaces, this thesis successfully makes significant improvements in the application of superlens-assisted laser manufacturing technology by adapting the method to work on the cylindrical surfaces of functional devices such as optical fibers. This work opens up new possibilities for enhancing fiber optics technology, potentially improving light manipulation and transmission characteristics through precision nanoscale modifications.

2.3.7 Microsphere monolayer deposition techniques on optical fiber

Numerous studies have described the technique for depositing microsphere monolayers on the surface of optical fibers. Korposh reports a method of microsphere coating on optical fibers that involves a detailed layer-by-layer deposition process using poly(allylamine hydrochloride) (PAH) or poly(diallyl dimethylammonium chloride) (PDDA) and silica nanoparticles (SiO_2 NPs). Initially, as shown in figure 2.3-14, the optical fiber, equipped with a LPG, is secured in a holder and rinsed in deionized water. It is then immersed in a 1 wt% ethanolic potassium hydroxide (KOH) solution for 20 minutes to negatively charge the fiber's surface. Subsequently, the fiber is alternately dipped into solutions of positively charged PAH and negatively charged SiO_2 nanoparticles for 20 minutes each, forming a mesoporous multilayer film. After each deposition step, the fiber is rinsed with distilled water and dried using nitrogen gas[95].

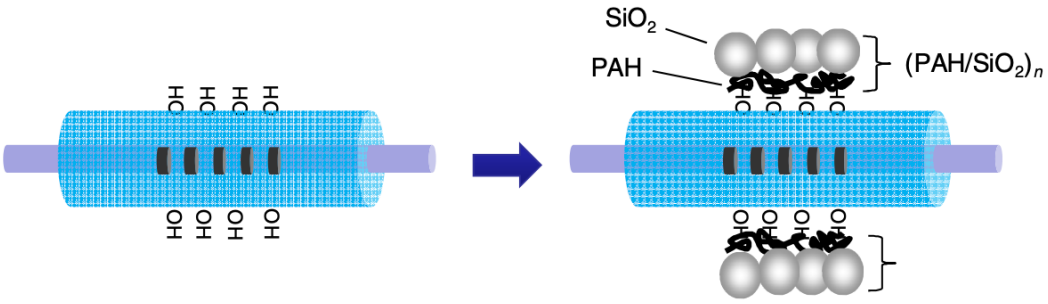

Figure 2.3-14 Schematic illustration of the alternating deposition of SiO_2 microspheres and PAH on the LPG[95].

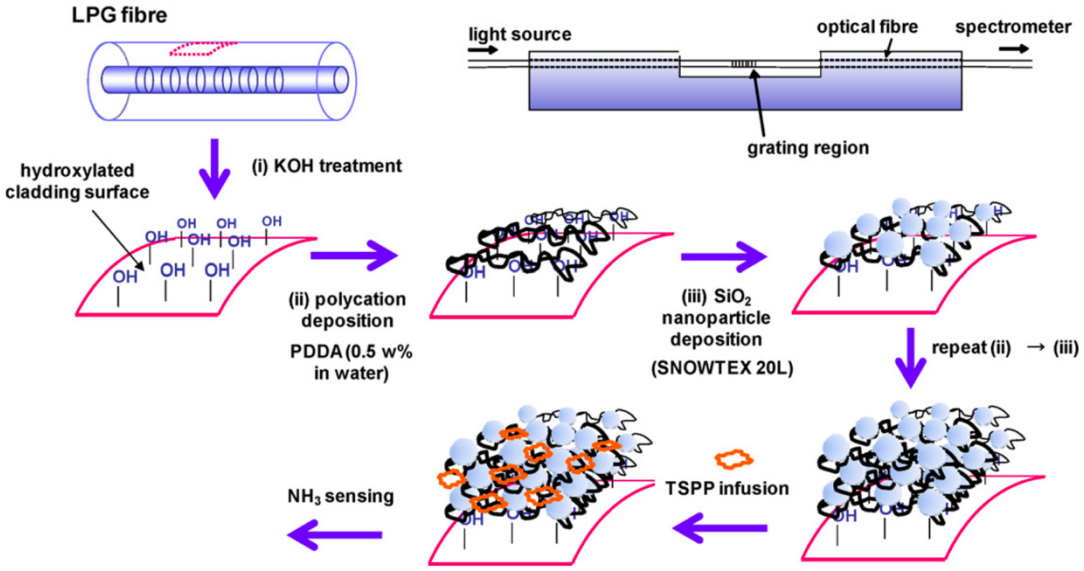

Figure 2.3-15 Schematic illustration of the electrostatic self-assembly deposition process and the deposition cell containing a fixed LPG[96].

In another described method illustrated in the figure 2.3-15, the optical fiber's surface is treated to terminate with OH groups, and then subjected to a similar layer-by-layer deposition process. This process is repeated until the desired thickness is achieved. The fiber is then immersed in a solution containing a functional compound (such as TSPP or PAA) for two hours to infuse the compound into the porous coating. The fiber is subsequently rinsed and dried, preparing it for sensor operation, which relies on

electrostatic interactions within the coated layer to detect environmental changes, such as the presence of ammonia in water[96]. These coating processes enhance the optical fiber's sensitivity to changes in the refractive index of surrounding media, making it highly effective for sensing applications. The controlled thickness and refractive index of the deposited film allow for high sensitivity and rapid response, which are crucial for accurate real-time measurements in various environments.

2.3.8 Mie theory

In geometric optics, light is treated as a collection of rays that travel in straight lines. According to Snell's law, light bends when it passes through different media and reflects at interfaces[97]. For this project, Mie theory which was proposed by Gustav Mie in 1908 serves as the simulation theoretical method to enhance the understanding of how incident light interacts within a microsphere lens[98].

Mie theory is a powerful mathematical framework used to describe the scattering of electromagnetic waves by particles. It is particularly useful for simulating the interaction of light with particles that are about the same size as the wavelength of the light, which includes many situations in optical engineering. In the context of particle lens simulation, Mie theory helps predict how light waves will be scattered or absorbed by particles such as aerosols, droplets, or other spherical bodies. The theory provides a way to calculate the scattering, absorption, and extinction cross sections of the particles based on their size, composition, and the wavelength of the light. Essential aspects of Mie theory in particle lens simulation include the size parameter, which is the ratio of a particle's circumference to the wavelength of light and greatly influences the scattering pattern. The refractive index also plays a pivotal role, as it dictates how light is absorbed and refracted by the particle[99,100].

When light interacts with a small particle, it triggers oscillations in the electrical charges of the electrons and protons through the optical electric field. Consequently, part of the incident light is absorbed, and the remainder is scattered. Both the electric

and magnetic fields, whether inside or outside the sphere, adhere to the vector Helmholtz equation[98]:

$$\nabla^2 E + k^2 E = 0 \tag{2.3-1}$$

$$\nabla^2 H + k^2 H = 0 \tag{2.3-2}$$

where ∇ is the Laplacian and $k = \frac{\omega}{c}\sqrt{\varepsilon}$ is the wave vector.

For non-magnetic particles, four primary input parameters are considered: the incident light wavelength (λ), the refractive index of the medium (n_m), the particle radius (a), and the particle refractive index (n_p). These parameters can be simplified to two independent size parameters, designated as (q_p, q_m), defined as follows[74]:

$$q_0 = \frac{2\pi\alpha}{\lambda} \tag{2.3-3}$$

$$q_p = q_0 n_p = \frac{2\pi\alpha n_p}{\lambda}$$
$$q_m = q_0 n_m = \frac{2\pi\alpha n_m}{\lambda} \tag{2.3-4}$$

where q_0 is the fundamental size parameter.

The incident plane wave is expressed as a combination of spherical waves, and by applying boundary conditions, the coefficients for this expansion are determined. The

electric and magnetic fields of both the scattered and internal waves can be expressed in the spherical coordinate system {r, θ, ϕ} as follows[74]:

$$E_r^{(s)} = \frac{\cos\varphi}{(k_m r)^2}\sum_{\ell=1}^{\infty} i^{\ell+1}(2\ell+1)a_\ell \zeta_\ell(k_m r)P_\ell^{(1)}(\cos\theta)$$

(2.3-5)

$$E_\theta^{(s)} = -\frac{\cos\varphi}{k_m r}\sum_{\ell=1}^{\infty} i^{\ell+1}\frac{2\ell+1}{\ell(\ell+1)}\left[a_\ell \zeta_\ell'(k_m r)P_\ell^{(1)'}(\cos\theta)\sin\theta - ib_\ell \zeta_\ell(k_m r)\frac{P_\ell^{(1)}(\cos\theta)}{\sin\theta}\right]$$

(2.3-6)

$$E_\varphi^{(s)} = -\frac{\sin\varphi}{k_m r}\sum_{\ell=1}^{\infty} i^{\ell+1}\frac{2\ell+1}{\ell(\ell+1)}\left[a_\ell \zeta_\ell'(k_m r)\frac{P_\ell^{(1)'}(\cos\theta)}{\sin\theta} - ib_\ell \zeta_\ell(k_m r)P_\ell^{(1)}(\cos\theta)\sin\theta\right]$$

(2.3-7)

$$H_r^{(s)} = \sqrt{\varepsilon_m}\frac{\sin\varphi}{k_m r}\sum_{\ell=1}^{\infty} i^{\ell+1}(2\ell+1)b_\ell \zeta_\ell(k_m r)P_\ell^{(1)}(\cos\theta)$$

(2.3-8)

$$H_\theta^{(s)} = i\sqrt{\varepsilon_m}\frac{\sin\varphi}{k_0 r}\sum_{\ell=1}^{\infty} i^{\ell+1}\frac{2\ell+1}{\ell(\ell+1)}\left[a_\ell \zeta_\ell(k_m r)\frac{P_\ell^{(1)}(\cos\theta)}{\sin\theta} + ib_\ell \zeta_\ell'(k_m r)P_\ell^{(1)'}(\cos\theta)\sin\theta\right]$$

(2.3-9)

$$H_{\varphi}^{(s)} = -i\sqrt{\varepsilon_m}\frac{\cos\varphi}{k_0 r}\sum_{\ell=1}^{\infty} i^{\ell+1}\frac{2\ell+1}{\ell(\ell+1)}\left[a_\ell \zeta_\ell'(k_m r)P_\ell^{(1)'}(\cos\theta)\sin\theta + ib_\ell\zeta_\ell(k_m r)\frac{P_\ell^{(1)}(\cos\theta)}{\sin\theta}\right]$$

(2.3-10)

$$E_r^{(\alpha)} = \frac{\cos\varphi}{(k_p r)^2}\sum_{\ell=1}^{\infty} i^{\ell+1}(2\ell+1)c_\ell\psi_\ell(k_p r)P_\ell^{(1)}(\cos\theta)$$

(2.3-11)

$$E_\theta^{(\alpha)} = -\frac{\cos\varphi}{k_p r}\sum_{\ell=1}^{\infty} i^{\ell+1}\frac{2\ell+1}{\ell(\ell+1)}\left[c_\ell\psi_\ell'(k_p r)P_\ell^{(1)'}(\cos\theta)\sin\theta - id_\ell\psi_\ell(k_p r)\frac{P_\ell^{(1)}(\cos\theta)}{\sin\theta}\right]$$

(2.3-12)

$$E_\varphi^{(\alpha)} = -\frac{\sin\varphi}{k_p r}\sum_{\ell=1}^{\infty} i^{\ell+1}\frac{2\ell+1}{\ell(\ell+1)}\left[c_\ell\psi_\ell'(k_p r)\frac{P_\ell^{(1)'}(\cos\theta)}{\sin\theta} - id_\ell\psi_\ell(k_p r)P_\ell^{(1)}(\cos\theta)\sin\theta\right]$$

(2.3-13)

$$H_r^{(\alpha)} = \sqrt{\varepsilon_m}\frac{\sin\varphi}{k_m r}\sum_{\ell=1}^{\infty} i^{\ell+1}(2\ell+1)d_\ell\psi_\ell(k_p r)P_\ell^{(1)}(\cos\theta)$$

(2.3-14)

$$H_\theta^{(\alpha)} = i\sqrt{\varepsilon_m}\frac{\sin\varphi}{k_0 r}\sum_{\ell=1}^{\infty} i^{\ell+1}\frac{2\ell+1}{\ell(\ell+1)}\left[c_\ell\psi_\ell(k_p r)\frac{P_\ell^{(1)}(\cos\theta)}{\sin\theta} + id_\ell\psi_\ell'(k_p r)P_\ell^{(1)'}(\cos\theta)\sin\theta\right]$$

(2.3-15)

$$H_{\varphi}^{(\alpha)} = -i\sqrt{\varepsilon_m}\frac{\cos\varphi}{k_0 r}\sum_{\ell=1}^{\infty} i^{\ell+1}\frac{2\ell+1}{\ell(\ell+1)}\left[c_\ell \psi_\ell'(k_p r)P_\ell^{(1)'}(\cos\theta)\sin\theta + id_\ell\psi_\ell(k_m r)\frac{P_\ell^{(1)}(\cos\theta)}{\sin\theta}\right]$$

(2.3-16)

These equations detail the components of electric and magnetic fields scattered by a spherical particle according to Mie theory. In these equations, P_ℓ represent the associated Legendre functions, and ζ & ψ are the spherical Bessel functions. The wave numbers in the medium and in vacuum are denoted by k_m and k_0, respectively. The coefficients a_ℓ and b_ℓ are associated with the scattering waves, while c_ℓ and d_ℓ pertain to the internal waves which can define as[74]:

$$a_\ell = \frac{q_p\psi_\ell^{'}(q_m)\psi_\ell(q_p) - q_m\psi_\ell(q_m)\psi_\ell^{'}(q_p)}{q_p\zeta_\ell^{'}(q_m)\psi_\ell(q_p) - q_m\psi_\ell^{'}(q_m)\zeta_\ell(q_p)}$$

$$b_\ell = \frac{q_p\psi_\ell^{'}(q_p)\psi_\ell(q_m) - q_m\psi_\ell(q_p)\psi_\ell^{'}(q_m)}{q_p\psi_\ell^{'}(q_p)\zeta_\ell(q_m) - q_m\psi_\ell(q_p)\zeta_\ell^{'}(q_m)}$$

$$c_\ell = \frac{q_p\zeta_\ell(q_m)\psi_\ell^{'}(q_m) - q_p\zeta_\ell^{'}(q_m)\psi_\ell(q_m)}{q_p\zeta_\ell^{'}(q_m)\psi_\ell(q_p) - q_m\psi_\ell^{'}(q_p)\zeta_\ell(q_m)}$$

$$d_\ell = \frac{q_p\zeta_\ell^{'}(q_m)\psi_\ell(q_m) - q_p\zeta_\ell(q_m)\psi_\ell^{'}(q_m)}{q_p\psi_\ell^{'}(q_p)\zeta_\ell(q_m) - q_m\psi_\ell(q_p)\zeta_\ell^{'}(q_m)}$$

(2.3-17)

2.4 Optical fiber waveguides & coupling theory

Light propagation within a waveguide is characterized by guided electromagnetic waves called waveguide modes. In optical fibers, multiple modes can propagate concurrently and interact through coupling at the core-cladding boundary, where the electric and magnetic field components interplay with specific propagation constants for each mode. Introducing a periodic disturbance along the fiber enables the transfer

of power between these modes, a phenomenon known as mode coupling. The coupled-mode theory, particularly as described by Erdogan's models of short- and long-period gratings, provides a framework to analyze these energy transfers induced by fiber gratings[101,102].

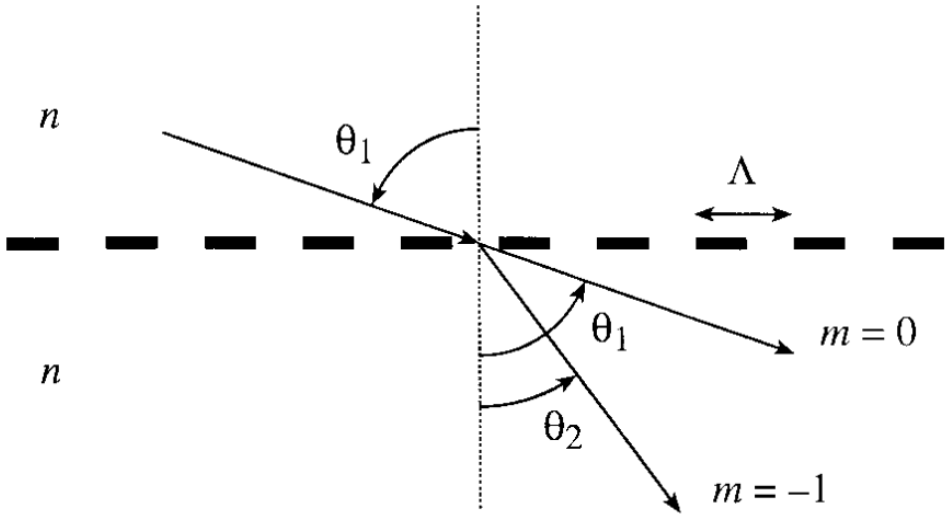

Figure 2.4-1 Schematic of light wave diffraction by a grating[101].

Based on figure 2.4-1, a fiber grating functions as an optical diffraction grating, meaning its impact on a light wave arriving at an angle can be explained using the well-known grating equation[101]:

$$n\sin(\theta_2) = n\sin(\theta_1) + m\frac{\lambda}{\Lambda} \tag{2.4-1}$$

where θ_1 is the angle of the incident light wave, θ_2 is the angle of the diffracted wave, the integer m determines the diffraction order, λ denotes the wavelength, and Λ represents the period of the grating.

2.4.1 Fiber Bragg gratings

For short-period gratings, a Fiber Bragg grating (FBG) is a specialized type of Bragg reflector implemented within optical fibers, functioning akin to segmented reflection filters. This design primarily interacts with wavelengths closely matching its counter-propagating (backward) mode[103].

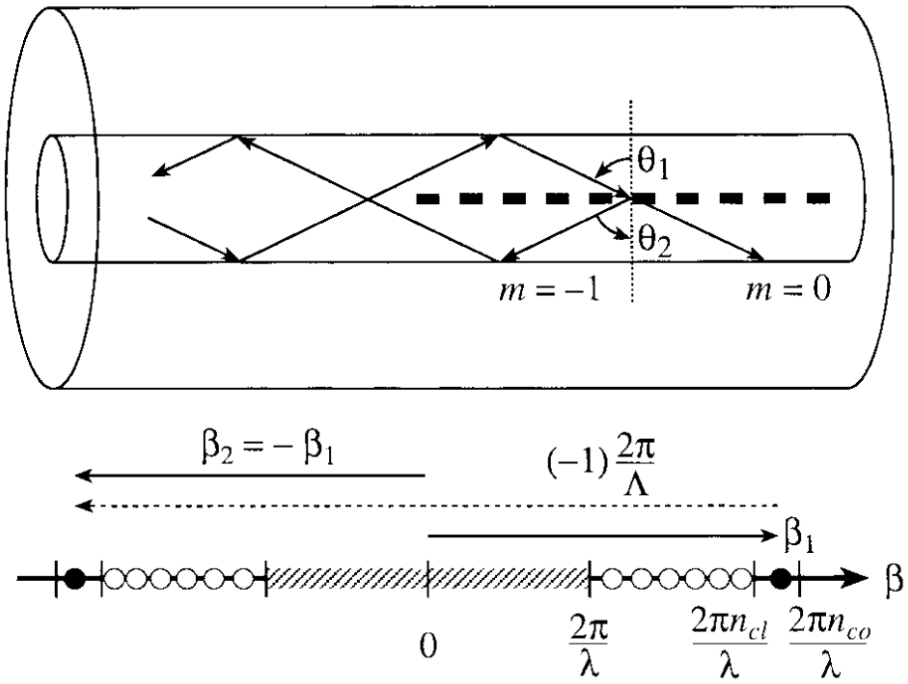

Figure 2.4-2 Schematic of FBG core mode reflection[101].

Figure 2.4-2 illustrates the reflection by a Bragg grating where a mode incident at an angle θ_1 reflects into the same mode traveling in the opposite direction at an angle $\theta_2 = -\theta_1$. β represents the z-component of the wave propagation and constant k is the parameter in describing fiber modes, can be expressed as[101]:

$$\beta = \frac{2\pi}{\lambda} n_{eff}, \text{ where } n_{eff} = n_{co} \sin\theta \tag{2.4-2}$$

where n_{eff} and n_{co} represent effective refractive index and refractive index of core, respectively. The mode remains guided as long as β meets the condition $n_{clad}k < \beta < n_{co}k$, where n_{clad} is the refractive index of cladding and $k = \frac{2\pi}{\lambda}$.

The Coupled Mode Theory method revolves around first defining and solving the modes of the unperturbed or uncoupled structures. Subsequently, a linear combination of these modes is employed as a trial solution for Maxwell's equations in more complex perturbed or coupled structures. The complex amplitudes are described by coupled-mode equations[101]:

$$\frac{dR(z)}{dz} = i\hat{\sigma}R(z) + i\kappa S(z)$$
$$\frac{dS(z)}{dz} = -i\hat{\sigma}S(z) - i\kappa^{*}R(z) \tag{2.4-3}$$

where the amplitudes R and S are defined as:

$$R(z) \equiv A(z)e^{i\delta z - \frac{\phi}{2}}$$
$$S(z) \equiv B(z)e^{-i\delta z + \frac{\phi}{2}} \tag{2.4-4}$$

In the equation 2.5-3, κ is the cross-coupling coefficient and $\hat{\sigma}$ is a general self-coupling coefficient defined as:

$$\hat{\sigma} \equiv \delta + \sigma - \frac{1}{2}\frac{d\phi}{dz} \tag{2.4-5}$$

where δ is the wave detuning parameter which is independent of z for all gratings is

defined as:

$$\delta \equiv \beta - \frac{\pi}{\Lambda} = \beta - \beta_B = 2\pi n_{eff}\left(\frac{1}{\lambda} - \frac{1}{\lambda_B}\right)$$

(2.4-6)

where $\lambda_B = 2n_{eff}\Lambda$ is the Bragg wavelength for scattering by an infinitesimally weak grating ($\delta n_{eff} \to 0$) with a period Λ.

For a single-mode Bragg reflection grating, the following straightforward relations are derived:

$$\sigma = \frac{2\pi}{\lambda}\overline{\delta n_{eff}}$$

$$\kappa = \kappa^* = \frac{\pi}{\lambda} v \overline{\delta n_{eff}}$$

(2.4-7)

As only uniform gratings along z-component are considered in this thesis, $\overline{\delta n_{eff}}$ is a constant, thus κ, σ and $\hat{\sigma}$ are all constant.

As a result, the transmission spectrum is written as a 2 × 2 matrix with elements[104]:

$$T = \begin{bmatrix} cosh(\gamma L) - i\frac{\delta}{\gamma}sinh(\gamma L) & -i\frac{\kappa}{\gamma}sinh(\gamma L) \\ i\frac{\kappa}{\gamma}sinh(\gamma L) & cosh(\gamma L) + i\frac{\delta}{\gamma}sinh(\gamma L) \end{bmatrix}$$

(2.4-8)

where γ is defined as $\sqrt{\kappa^2 - \delta^2}$ and the grating length L. Also, for a grating with uniform index modulation and a specific period, the reflectivity is given by:

$$R = \frac{\kappa^2 \, sinh^2(\gamma L)}{\delta^2 \, sinh^2(\gamma L) + \kappa^2 \, cosh^2(\gamma L)}$$

(2.4-9)

Two controllable factors can influence the intensity of the reflection power, the grating length L and the operational wavelength λ. The expression for the maximum reflectivity R_{max}, can be defined as:

$$R_{max} = tanh^2(\kappa L)$$

(2.4-10)

Grating Length (mm)	Reflectivity obtained (%)
05	59.86
07	79.04
10	93.28
15	99.09
16	99.39
18	99.73
20	99.90
22	99.95
25	**99.98**
28	99.99
30	99.99
35	99.99
40	99.99

Table 2.4-1 Reflectivity of different grating lengths from 5 mm to 40 mm[104].

Based on the theory described above, reflection spectra for different grating lengths were examined by Ikhlef, as shown in table 2.4-1[104]. This examination confirmed that the spectral characteristics of uniform gratings are similar to those of a sinc function. The reflection spectra for grating lengths of 5 mm, 7 mm, 10 mm, 15 mm, and 25 mm are illustrated in figure 2.4-3. Specifically, the maximum reflectivities measured at these lengths were 59.86%, 79.04%, 93.28%, and 99.09%, respectively.

At a length of 25 mm, the reflectivity peaked at 99.98%, accompanied by an increase in the intensity of side lobes. Subsequent increases in grating length did not further improve the maximum reflectivity, which stabilized at 99.99%.

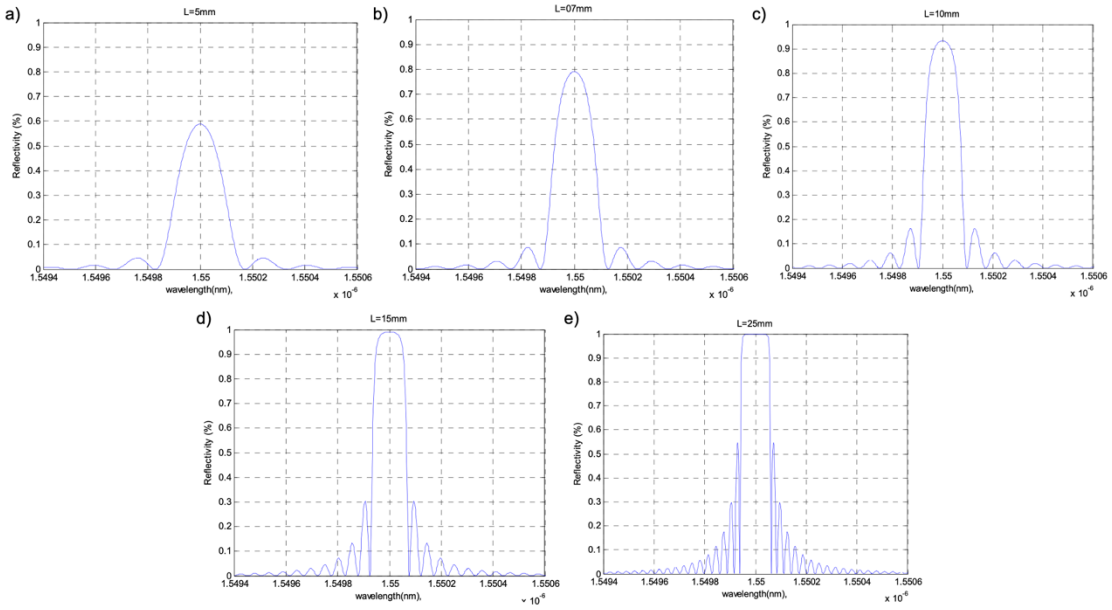

Figure 2.4-3 Reflectivity spectrum at (a) L = 5 mm, (b) L = 7 mm, (c) L = 10 mm, (d) L = 15 mm, (e) L = 25 mm[104].

2.4.2 Long period gratings

Long-period gratings (LPG) are a distinct category of Bragg reflector integrated into optical fibers, operating as pass-through wavelength filters rather than reflectors. Unlike FBG, which reflect specific wavelengths back along the fiber, LPGs couple light from a guided mode into forward-propagating cladding modes. This coupling occurs at wavelengths that satisfy the phase-matching condition, allowing the LPG to influence longer wavelength ranges than FBGs and selectively filter out specific bands of wavelengths while transmitting others. This interaction makes LPGs highly effective for spectral shaping and gain equalization in optical fiber systems[105,106].

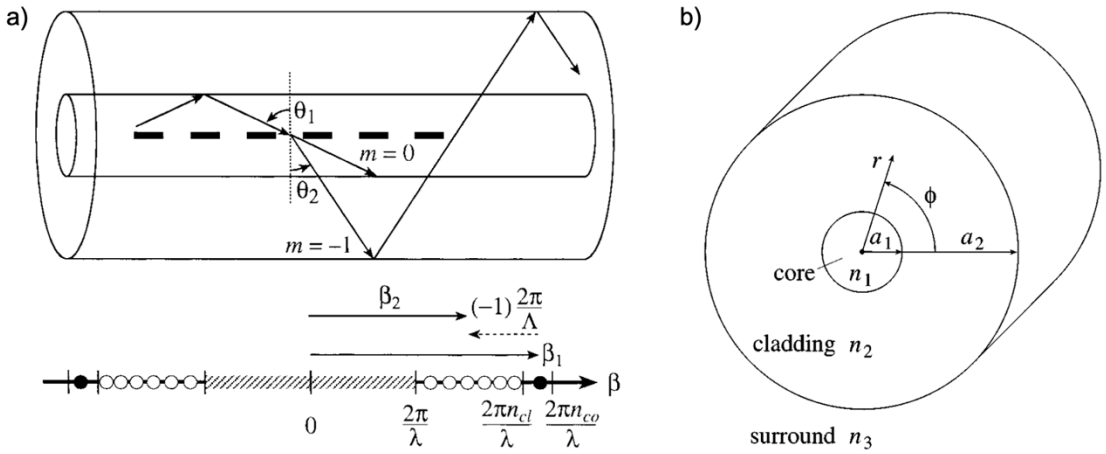

Figure 2.4-4 (a) Schematic of LPG cladding mode coupling transmission[101]. (b) Diagram of a cross-sectional view of the fiber geometry, illustrating the coordinate system and the refractive indices of various components: The core (n_1), the cladding (n_2), and the surround (n_3). The radii of the core (a_1) and the cladding (a_2)[102].

Figure 2.4-4 depicts the diffraction of a mode with an initial bounce angle θ_1, transitioning into a forward-propagating mode at a bounce angle θ_2, via a transmission grating. The initial mode operates within the core, while the subsequent mode propagates within the cladding. In this scenario, with β being positive, the resonant wavelength for the transmission grating is determined as follows[101]:

$$\lambda_R = \left(n_{1,m}^{eff} - n_{2,m}^{eff}\right)\Lambda \tag{2.4-11}$$

where n_1^{eff} and n_2^{eff} denote the effective refractive index of core and cladding, respectively.

The linearly polarized (LP) approximation is adequately equipped to characterize a mode guided by the fiber core. This approximation is employed to determine the mode propagation constant. However, the field is described in terms of radial and

azimuthal vector components, as the ultimate goal is to calculate overlap integrals with the exact fields of the cladding modes. Specifically, the dispersion relation used to derive the effective index for the LP01 mode is as follows[102]:

$$V\sqrt{1-b}\frac{J_1\left(V\sqrt{1-b}\right)}{J_0\left(V\sqrt{1-b}\right)} = V\sqrt{b}\frac{K_1\left(V\sqrt{b}\right)}{K_0\left(V\sqrt{b}\right)}$$

(2.4-12)

where J represents a Bessel function of the first kind and K denotes a modified Bessel function of the second kind, $V = (2\pi/\lambda)a_1\sqrt{n_1^2 - n_2^2}$ is the V number of the fiber at wavelength λ, $b = (n_{eff,co}^2 - n_2^2)/(n_1^2 - n_2^2)$ is the normalized effective index.

For the field expressions characterizing the core mode, the exact radial and azimuthal vector components within the core region of the fiber can be approximated. The dispersion relation for a cladding mode, defined by the condition $n_3 < n_2^{eff} < n_2$, is provided as follows[102]:

$$\zeta_0 = \zeta_0'$$

(2.4-13)

where:

$$\zeta_0 = \frac{1}{\sigma_2}\frac{u_2\left(JK + \frac{\sigma_1\sigma_2 u_{21}u_{32}}{n_2^2 a_1 a_2}\right)p_l(a_2) - Kq_l(a_2) + Jr_l(a_2) - \frac{1}{u_2}s_l(a_2)}{-u_2\left(\frac{u_{32}}{n_2^2 a_2}J - \frac{u_{21}}{n_1^2 a_1}K\right)p_l(a_2) + \frac{u_{32}}{n_1^2 a_2}q_l(a_2) + \frac{u_{21}}{n_1^2 a_1}r_l(a_2)}$$

(2.4-14)

$$\zeta_0' = \sigma_1 \frac{u_2\left(\frac{u_{32}}{a_2}J - \frac{n_3^2 u_{21}}{n_2^2 a_1}K\right)p_l(a_2) + \frac{u_{32}}{a_2}q_l(a_2) + \frac{u_{21}}{a_1}r_l(a_2)}{u_2\left(\frac{n_3^2}{n_2^2}JK + \frac{\sigma_1\sigma_2 u_{21}u_{32}}{n_1^2 a_1 a_2}\right)p_l(a_2) - \frac{n_3^2}{n_1^2}Kq_l(a_2) + Jr_l(a_2) - \frac{n_2^2}{n_1^2 u_2}s_l(a_2)}$$

(2.4-15)

where the definitions used in equations (2.5-13) and (2.5-14) are given by:

$$\sigma_1 \equiv il{n_2^{eff}}/{Z_0}$$

$$\sigma_2 \equiv il{n_2^{eff}}Z_0$$

(2.4-16)

$$u_{21} = \frac{1}{u_2^2} - \frac{1}{u_1^2}$$

$$u_{32} = \frac{1}{w_3^2} - \frac{1}{u_2^2}$$

(2.4-17)

where

$$u_j^2 \equiv (2\pi/\lambda)^2\left(n_j^2 - n_{eff,clad}^2\right) \quad [\, j \in (1,2)\,]$$

$$w_3^2 \equiv (2\pi/\lambda)^2\left(n_{eff,clad}^2 - n_3^2\right)$$

(2.4-18)

$$J \equiv \frac{J_l'(u_1 a_1)}{u_1 J_l(u_1 a_1)}$$

$$K \equiv \frac{K_l'(w_3 a_2)}{w_3 K_l(w_3 a_2)}$$

(2.4-19)

$$p_l(r) \equiv J_l(u_2 r)N_l(u_2 a_1) - J_l(u_2 a_1)N_l(u_2 r)$$

$$q_l(r) \equiv J_l(u_2 r)N_l'(u_2 a_1) - J_l'(u_2 a_1)N_l(u_2 r)$$

$$r_l(r) \equiv J_l'(u_2 r)N_l(u_2 a_1) - J_l(u_2 a_1)N_l'(u_2 r)$$

$$s_l(r) \equiv J_l'(u_2 r)N_l'(u_2 a_1) - J_l'(u_2 a_1)N_l'(u_2 r)$$

(2.4-20)

In the above equations, $Z_0 = 377\ \Omega$ is the free space electromagnetic impedance, l is a given azimuthal number, N represents a Bessel function of the second kind, and the prime notation signifies differentiation with respect to the entire argument. The coupling coefficient varying z dependence for forward-propagating core-core mode κ_{co-co} and core-cladding mode κ_{co-cl} coupling in optical fibers can be written as[102]:

$$\kappa_{co-co}(z) = \sigma(z)\frac{2\pi}{\lambda}\frac{n_1^2 b}{n_2\sqrt{1+2b\Delta}}\left[1 + \frac{J_0^2\left(V\sqrt{1-b}\right)}{J_1^2\left(V\sqrt{1-b}\right)}\right]$$

(2.4-21)

$$\kappa_{co-cl}(z) = \sigma(z)\frac{2\pi}{\lambda}\left(\frac{\pi b}{Z_0 n_2\sqrt{1+2b\Delta}}\right)^{\frac{1}{2}} \times \frac{n_1^2 u_1}{u_1^2 - V^2\,(1-b)/a_1^2}$$
$$\times\left(1 + \frac{\sigma_2\zeta_0}{n_1^2}\right)E_{cl}\left[u_1 J_1(u_1 a_1) \times \frac{J_0\left(V\sqrt{1-b}\right)}{J_1\left(V\sqrt{1-b}\right)} - \frac{V\sqrt{1-b}}{a_1}J_0(u_1 a_1)\right]$$

(2.4-22)

where $\sigma(z)$ denotes the slowly varying envelope of the grating, $\Delta = (n_1 - n_2)/n_1$ denotes the index modulation and E_{cl} denotes the normalization constant of the electric field for the cladding modes based on a particular normalization choice.

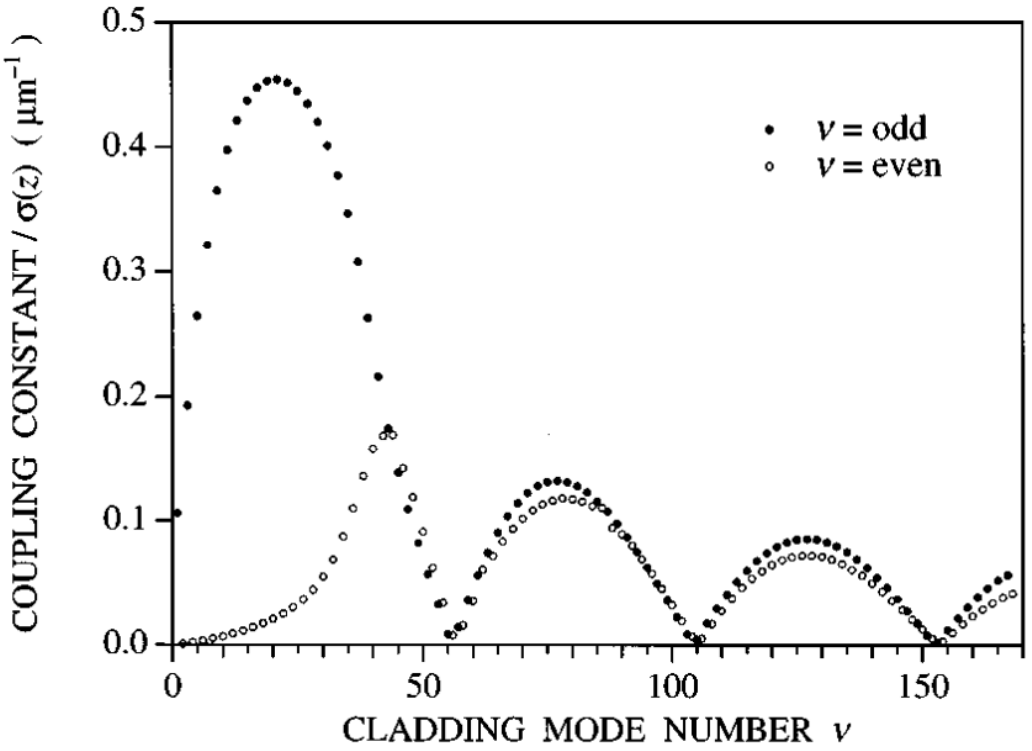

Figure 2.4-5 Core-cladding mode coupling coefficient κ_{co-cl} for the 168 $l = 1$ cladding modes in a LPG[102].

In evaluating the coupling strength variations between the LP_{01} core mode and all cladding modes at a 1550 nm wavelength, the coupling constants were determined using the fiber geometry depicted in figure 2.4-5. A total of 168 modes were identified below cutoff at this wavelength. The analysis revealed that coupling between the core mode and the lowest-order even cladding modes is markedly weaker compared to the lowest-order odd cladding modes. However, starting from cladding modes of order 40 onwards, both even and odd modes demonstrate similar levels of coupling strength. This trend of gradual oscillations in coupling strength relative to the cladding mode number reflects a similar oscillation pattern observed with wavelength in the coupling from the core mode to the continuum of radiation modes within the fiber[102].

Similar to the case with FBG, $\hat{\sigma}$ is defined as a general self-coupling coefficient,

expressed as follows[101]:

$$\hat{\sigma} \equiv \delta + \frac{1}{2}\kappa_{co-co}$$

(2.4-23)

where δ is the detuning parameter defined as:

$$\delta \equiv \frac{1}{2}(\beta_1 - \beta_2) - \frac{\pi}{\Lambda}$$

(2.4-24)

where $\beta_1 = (2\pi/\lambda)n_1^{eff}$ and $\beta_2 = (2\pi/\lambda)n_2^{eff}$ for core mode and cladding mode, respectively. Thus, the transmission spectrum can be obtained as:

$$T = cos^2\left(\sqrt{\kappa_{co-cl}^2 + \hat{\sigma}^2}L\right) + \frac{\hat{\sigma}^2}{\hat{\sigma}^2 + \kappa_{co-cl}^2} sin^2\left(\sqrt{\kappa_{co-cl}^2 + \hat{\sigma}^2}L\right)$$

(2.4-25)

Subsequently, the maximum transmission T_{max} of cladding modes LPG with a grating length of L is specified as:

$$T_{max} = sin^2(\kappa_{co-cl}L)$$

(2.4-26)

According to the transmission equation for LPG mode coupling, figure 2.4-6 shows a MATLAB simulation example[107], the fiber parameters were set as follows: Core radius $a_1 = 4.15\,\mu m$, core refractive index $n_1 = 1.4681$, cladding radius $a_2 = 62.5\,\mu m$, cladding refractive index $n_2 = 1.4628$, surrounding refractive index $n_3 =$

1.0. The transmittance T at each wavelength was obtained as shown in figure 2.5-5. The positions of the four loss peaks were $1340.7\ nm$, $1.369.3\ nm$, $1428.1\ nm$ and $1533.7\ nm$ and the corresponding peak loss values were $-1.0\ dB$, $-3.9\ dB$, $-10.1\ dB$ and $-30.0\ dB$.

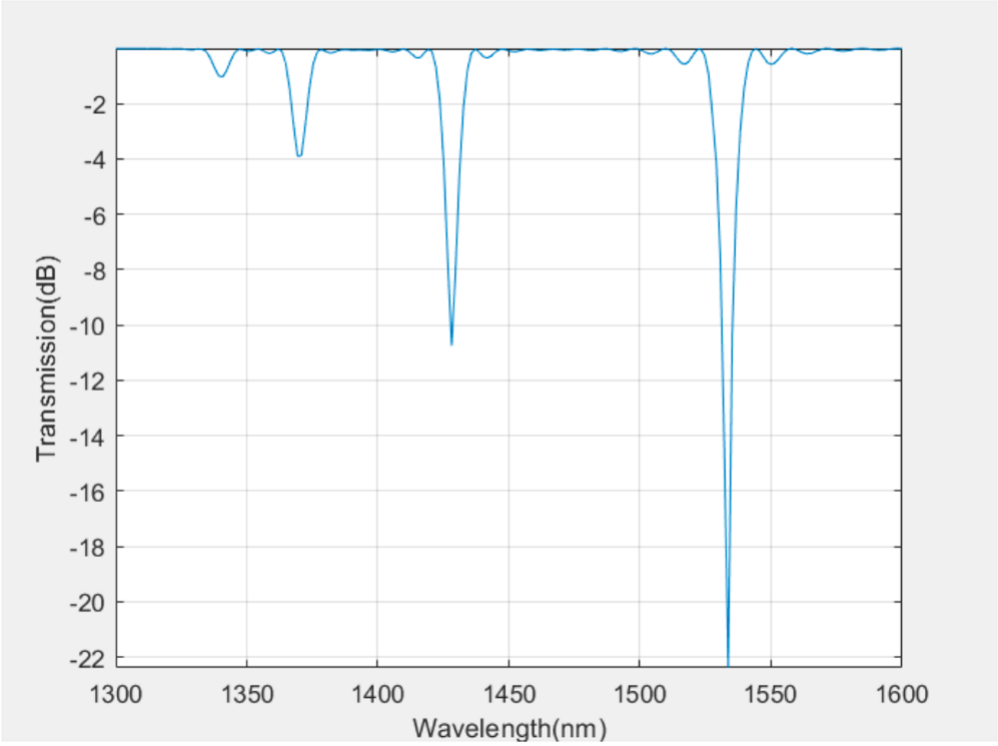

Figure 2.4-6 Transmission spectrum simulation of LPG[107].

2.4.3 Sensitization principle of optical fiber grating sensor

FBG can be used as a type of optical sensor to measure strain, temperature, and other physical parameters. They are based on the principle of Bragg reflection, where light within a certain wavelength is reflected back from a periodic perturbation in the fiber's refractive index[108]. FBG sensors first emerged in the early 1990s when researchers started to leverage the unique properties of optical fibers for sensing purposes. The ability to embed gratings within fibers allowed for the direct measurement of physical changes through shifts in the Bragg wavelength. This technology has become popular

due to its high sensitivity, small size, electromagnetic immunity, and the ability to multiplex multiple sensors along a single fiber[109,110].

For strain sensing, the wavelength shift, denoted as $\Delta\lambda_{BS}$, resulting from an applied longitudinal strain $\Delta\varepsilon$, is given by[111]:

$$\Delta\lambda_{BS} = \lambda_B(1 - \rho_\alpha)\Delta\varepsilon \tag{2.4-27}$$

where ρ_α is the photoelastic coefficient of the fiber. For temperature sensing, the wavelength shift, represented as $\Delta\lambda_{BT}$, due to temperature change ΔT, is given by:

$$\Delta\lambda_{BT} = \lambda_B(1 - \zeta)\Delta T \tag{2.4-28}$$

where ζ is the fiber thermo-optic coefficient.

LPG can be used as a type of optical fiber sensor that modulates the transmission properties of light in a fiber due to changes in external conditions. Unlike FBG sensors that reflect light, LPG sensors couple light from a guided mode to cladding modes, causing attenuation bands at specific wavelengths. This makes LPG sensors particularly useful for measuring changes in refractive index, temperature and strain[112,113]. LPG sensors emerged in the optical sensing field in the mid-1990s. The development of LPG sensors was driven by their potential for higher sensitivity to environmental changes compared to other optical sensors[114].

Table 2.4-2 provides a summary of the sensitivities to wavelength-strain and wavelength-temperature for FBGs with varying wavelengths. For silica fibers, the sensitivities to wavelength-strain for FBGs at 800 nm and 1.55 μm have been recorded at approximately $0.64\ pm/\mu\varepsilon$ and 1.2 $pm/\mu\varepsilon$, respectively. Additionally, the sensitivities to wavelength-temperature for the same FBGs at 800 nm and 1.55 μm are

approximately $6.8\ pm/°C$ and $13\ pm/°C$, respectively[111].

Wavelength (μm)	Strain sensitivity (pm $\mu\varepsilon^{-1}$)	Temperature sensitivity (pm $°C^{-1}$)
0.83	~0.64	~6.8
1.3	~1	~10
1.55	~1.2	~13

Table 2.4-2 Strain & temperature sensitivities of FBG sensors across various λ_B[111].

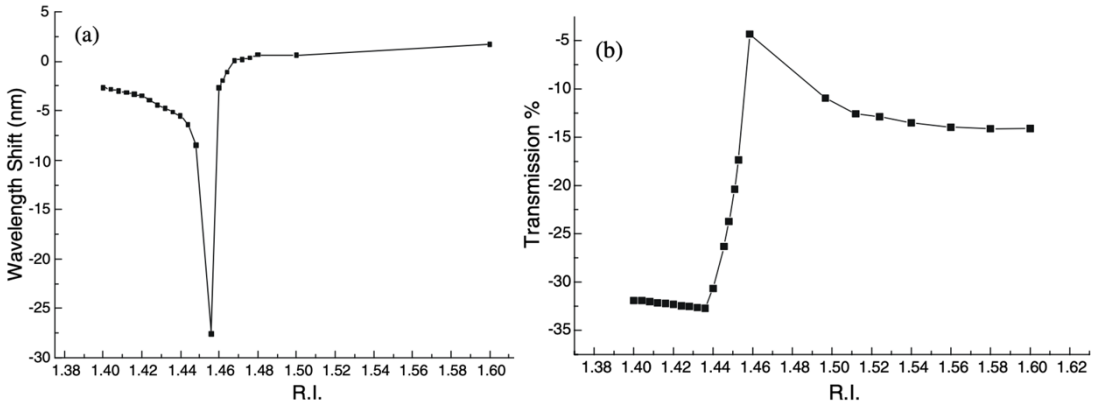

Figure 2.4-7 The relationship between the refractive index (RI) of the material surrounding and (a) the wavelength shift, (b) the minimum transmission based on a 400 μm period LPG[115].

The refractive index sensitivity of LPG is linked to how the effective refractive index of the cladding modes reacts to the surrounding medium. Specifically, the central wavelengths of LPG attenuation bands shift in response to changes in the surrounding refractive index, provided it is lower than the cladding's index. This sensitivity is most pronounced in higher-order modes when the refractive index nears that of the cladding, leading to the disappearance of discrete modes and the occurrence of broadband radiation-mode losses. Conversely, if the surrounding refractive index exceeds that of the cladding, the attenuation bands become less sensitive and their

extinction diminishes, altering the transmission spectrum[116]. This behavior is exemplified in figure 2.4-7.

2.5 Chapter summary

In summary, significant progress has been made in microsphere-assisted nanopatterning and monolayer deposition on flat and curved surfaces, but their application to optical fiber grating surfaces remains limited. Adapting these techniques to the cylindrical geometry of optical fibers presents challenges, such as ensuring uniform particle alignment and precise patterning. Moreover, integrating nanopatterned structures with fiber optic devices for enhanced sensing and light manipulation needs further development. Similarly, while super-resolution nanoimaging and nanopatterning systems exist independently, a combined system capable of simultaneous operation has yet to be achieved. Technologies like microsphere superlenses and photonic nanojets excel in either imaging or patterning but lack integration into dual-function platforms. This gap limits advancements in real-time nanoscale monitoring and fabrication for applications such as anti-counterfeiting, semiconductor manufacturing, and nanophotonics.

Chapter 3.
Research Methodology: Theoretical Simulation & Equipment

3.1 Introduction

Chapter 3 outlines the research methodologies used in exploring advanced optical phenomena and equipment setups. This chapter connects theoretical models with practical implementation by detailing both simulation techniques and the experimental apparatus employed. It provides in-depth insights into the simulation tools and computational models used to understand complex optical interactions, including xMie software, CST Microwave Studio, and MATLAB, which is important for predicting and analyzing behaviors prior to conducting physical experiments. Additionally, the equipment section describes the various instruments used throughout the research. These include various laser systems, optical spectrum analyzers, and characterization equipment, which are instrumental in analyzing the experimental results discussed in subsequent chapters. This chapter sets the stage for the following chapters, where the outcomes of these methodologies are analyzed and discussed, linking back to the theoretical models presented in Chapter 2.

3.2 Optical simulation

This section introduces the simulation tools and conditions detailed in Chapter 4. It covers the use of several advanced simulation platforms: xMie software, CST Microwave Studio, and MATLAB. Each tool is applied to explore distinct optical phenomena and components. Specifically, xMie software is employed to analyze the focusing characteristics of a single homogeneous dielectric microspherical particle. Meanwhile, CST Microwave Studio is utilized to study the transmission properties of

graphene across various layer thicknesses. Additionally, MATLAB is leveraged to simulate the optical behavior of FZP and to evaluate the performance of fiber grating sensors. These simulations are crucial for understanding complex interactions in photonics and contribute significantly to the theoretical models discussed in the previous chapter.

3.2.1 xMie software

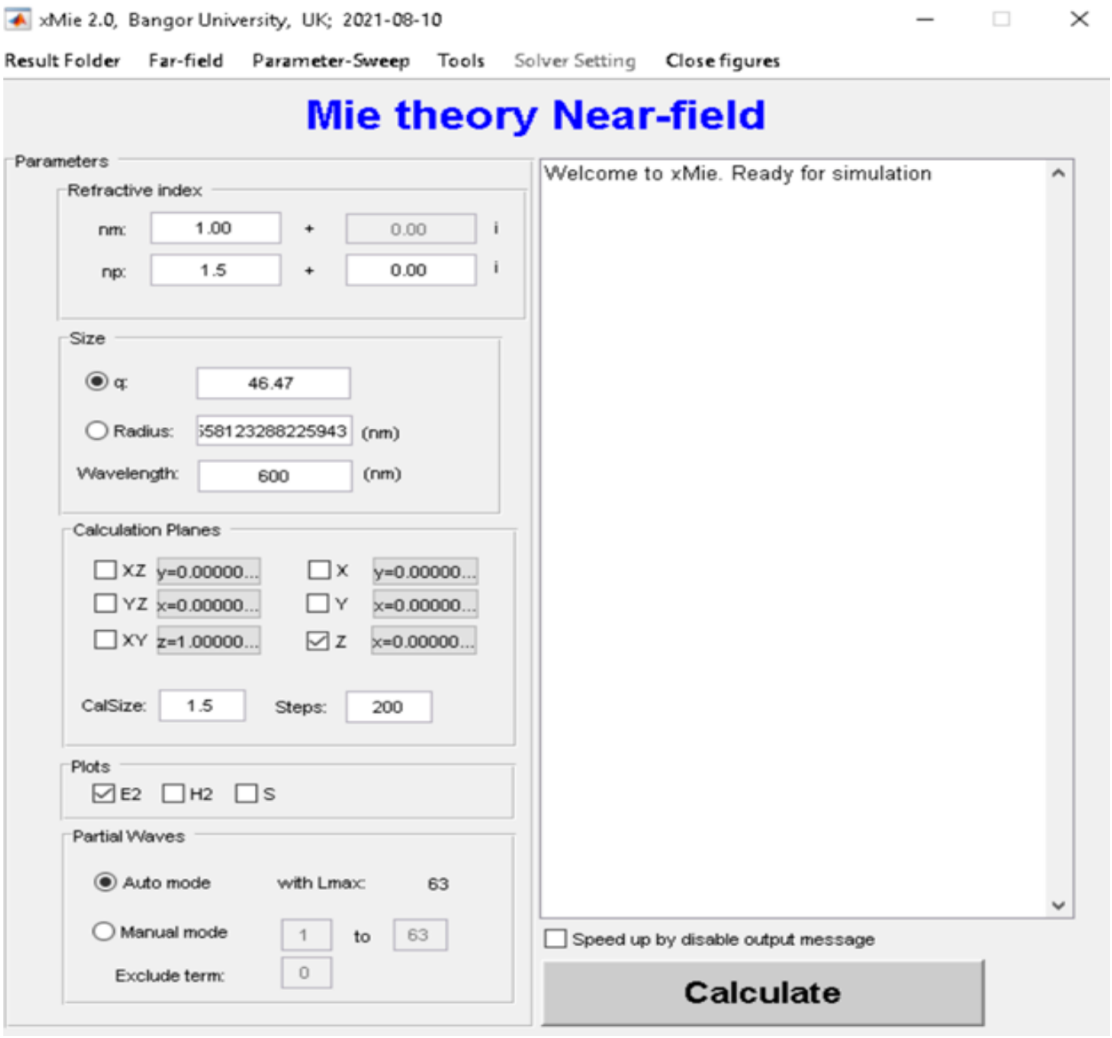

Figure 3.2-1 The user interface of xMie software.

xMie, a simulation software developed by Dr. Zengbo Wang, is built on Mie theory to simulate the field distribution both inside and outside a single microsphere, as depicted in figure 3.2-1. This software employs the analytical method to calculate the Mie solutions of Maxwell's equations for a microsphere embedded in a homogeneous medium and illuminated by a uniform light source. xMie is notable for its ability to efficiently handle calculations related to scattering on a single particle and near-field effects, providing fast and accurate results. It utilizes MATLAB for its graphical user interface, allowing users to define parameters for the particle and incident light to accurately plot and generate detailed visualizations of electric field intensity in a 2D format.

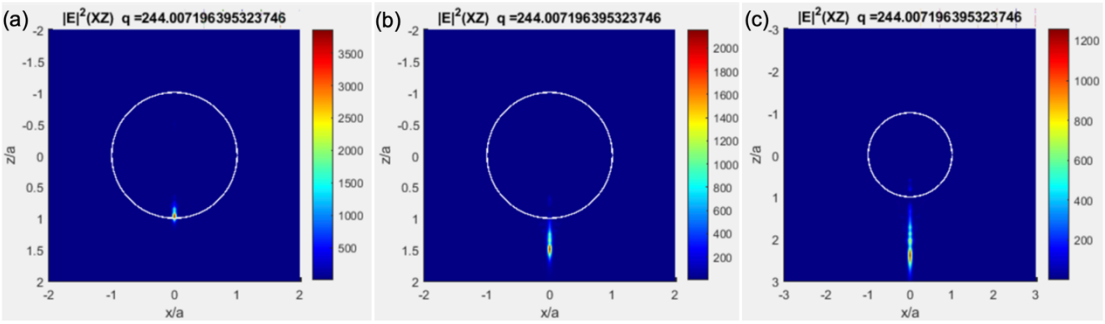

Figure 3.2-2 Electric field intensity $|E|^2$ of 80 µm BTG microsphere irradiated by 1030 nm laser in (a) air, (b) water and (c) UV glue on the XZ plane.

In this project, the xMie simulation software was employed to study the effects of a dielectric particle's environment on the width and length of the PNJ. The simulations were conducted using a Barium Titanate Glass (BTG) microsphere with a diameter of 80 µm, set in three different media: air, water, and UV glue. The key input parameters for these simulations included: n_m (the refractive index of the medium), n_p (the refractive index of the microsphere), R (the radius of the microsphere) and λ (the wavelength of the incident laser light). Specifically, n_p was fixed at 1.9, while n_m varied among 1.0 (air), 1.33 (water), and 1.56 (UV glue). Additionally, q (the size parameter) determines the near-field profile of the Mie scattering, as outlined in

equation 2.3-3. The simulation results, including the focus size and the electric field intensity $|E|^2$, are illustrated in figures 3.2-2, demonstrating the influence of these media on the PNJ characteristics.

3.2.2 CST Microwave Studio

CST MWS employs a range of electromagnetic simulation solvers based on numerical methods such as the Finite Difference Time Domain Method (FDTM) and the Finite Integration Technique (FIT). The FIT, a core technique in CST, offers a universal spatial discretization scheme that is capable of handling electromagnetic problems across a spectrum—from static field calculations to dynamic, high-frequency applications in both time and frequency domains. Unlike many numerical methods that discretize Maxwell's equations in differential form, FIT does so in an integral form, enhancing the accuracy and applicability of simulations[117].

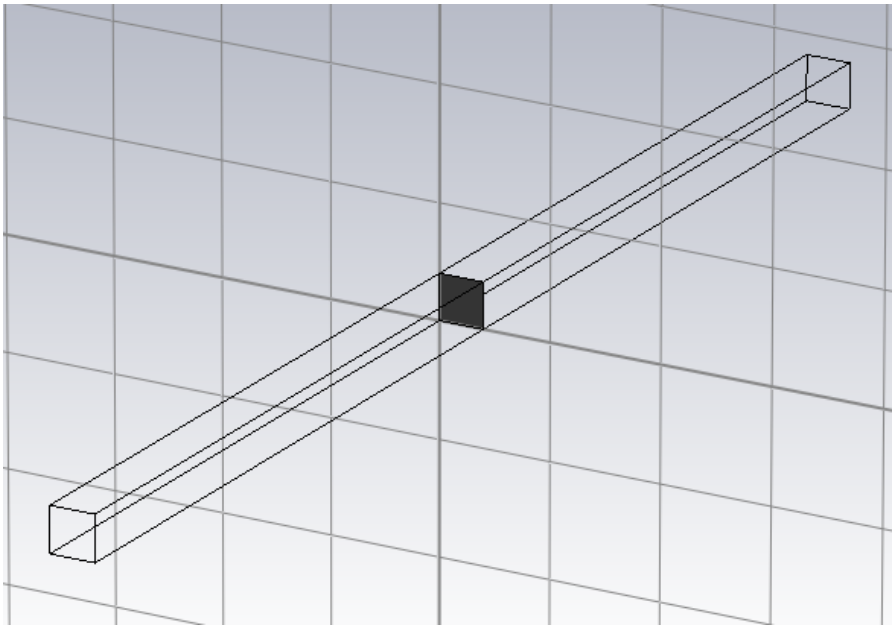

Figure 3.2-3 CST with monolayer graphene model.

In this project, CST Microwave Studio (CST MWS) was utilized to investigate various

electromagnetic phenomena, including the transmission characteristics of graphene with differing layer counts. CST interface with visual representations of the model is depicted in figure 3.2-3.

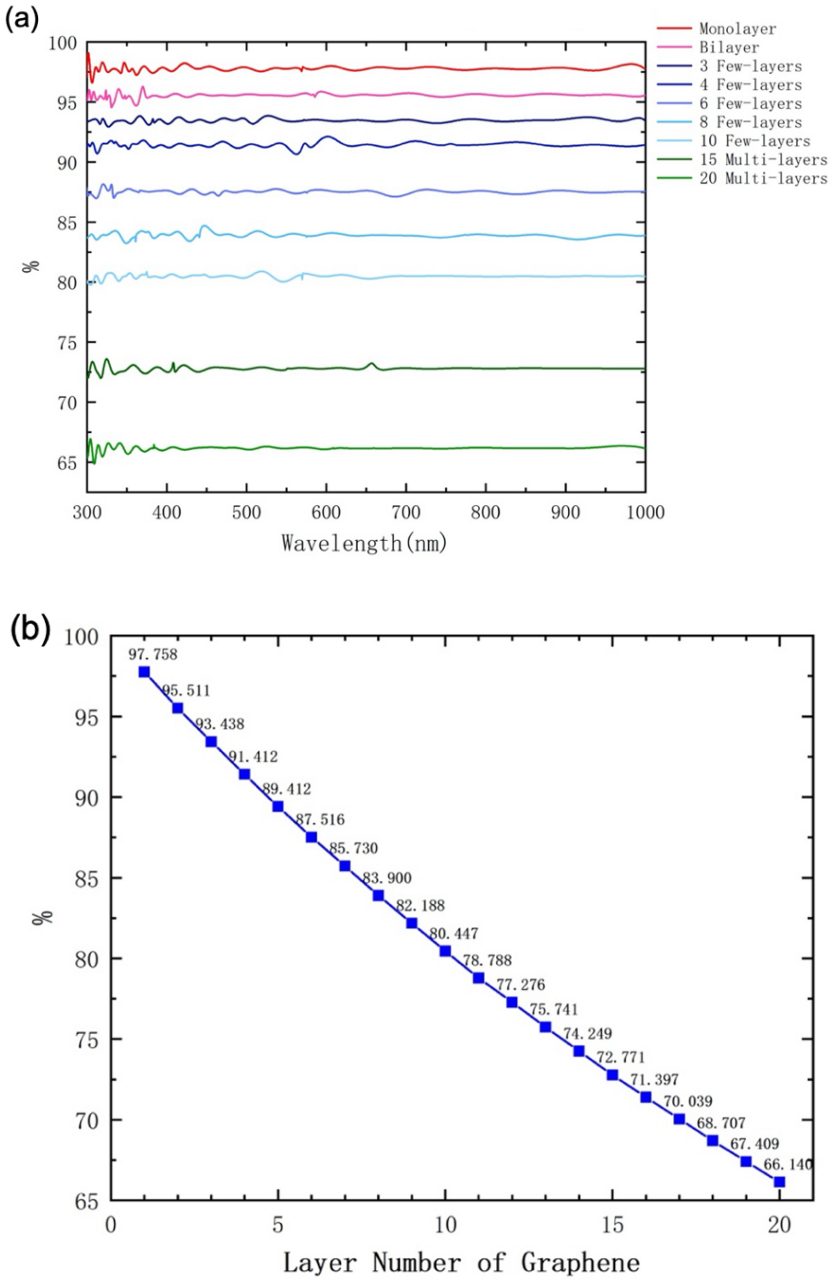

Figure 3.2-4 (a) CST simulated transmittance of multi-layer graphene, (b) average transmittance of (a), ranging from monolayer layer up to 20 layers.

Figure 3.2-4a displays CST simulation results depicting the transmission characteristics of graphene for varying layer counts, from a monolayer up to 20 layers. On the x-axis, the number of graphene layers is shown, while the y-axis reflects the percentage of light transmittance. The graph clearly demonstrates a downward trend in transmittance as the number of layers increases, with each line on the graph representing the transmittance values measured at different layer counts. Meanwhile, figure 3.2-4b presents a scatter line plot that charts the average CST simulation results of transmittance for multi-layer graphene, starting from a high of 97.758% for a monolayer to a lower 66.140% for 20 layers. The y-axis again tracks transmittance percentages, underscoring the decrease in light transmission with an increase in layers. Each data point connects with a smooth line, illustrating the general trend across the range of layer counts.

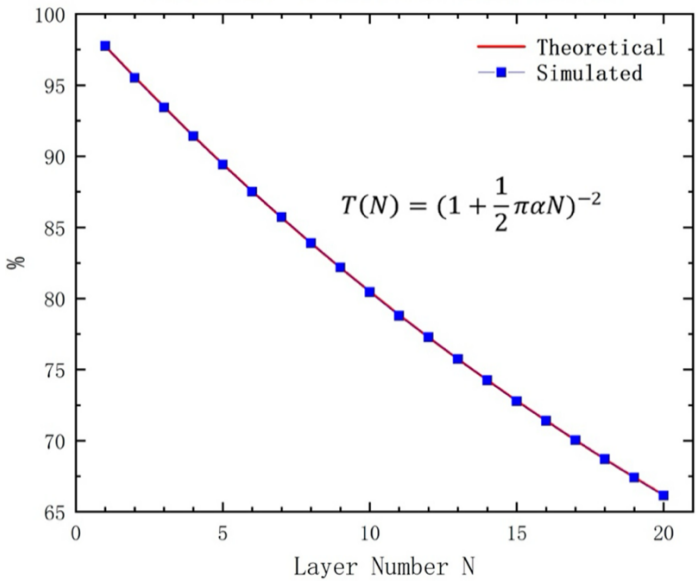

Figure 3.2-5 CST simulated (blue) and theoretical (red) transmittance results of multi-layer graphene.

The figure above illustrates the transmittance of multi-layer graphene, comparing results from both CST simulations (in blue) and theoretical calculations (in red) which is given by[118]:

$$T(N) = \left(1 + \frac{1}{2}\pi\alpha N\right)^{-2}$$

(3.2-1)

where the fine structure constant $\alpha \approx 1/137$. The transmittance percentage decreases progressively as the number of layers increases, reflecting a predictable reduction in light transmission through additional graphene layers. Notably, the CST simulated results closely align with the theoretical predictions across all layer counts, underscoring the accuracy of the simulation in capturing the optical behavior of graphene. This alignment is visually emphasized by the overlapping lines, which validate the theoretical model used to predict the transmittance properties of multi-layer graphene.

3.2.3 MATLAB 2D FZP simulation

MATLAB, a powerful computing environment, is utilized for coding and plotting to generate models of a 2D FZP featuring varying numbers of zones. This modeling approach is specifically tailored to facilitate the fabrication of the FZP on a thin film substrate using laser direct writing techniques. The design of the model is crucial for the fabrication process, delineating areas of transmission (to be laser-marked) in black and blocked (non-marked) areas in white. This binary color scheme aids in the accurate translation of digital models into physical structures by clearly defining which regions should absorb laser energy. The precise control offered by MATLAB allows for the adjustment of parameters such as zone width and total number of zones, which are essential for optimizing the focusing properties of the FZP. Furthermore, this approach supports iterative testing and refinement of the design to ensure high fidelity between the modeled and fabricated products.

In addition, radius r_n for each zone n and diameter of primary focal point D_f are given by[119]:

$$r_n = \sqrt{n\lambda F + \left(\frac{n\lambda}{2}\right)^2} \quad n = 1,2, \dots, N$$

(3.2-2)

$$D_f = \frac{\lambda F}{\sqrt{n\lambda F + \left(\frac{n\lambda}{2}\right)^2}}$$

(3.2-3)

where the FZPs are designed with focal length $F = 1\,mm$ and incidence wavelength $\lambda = 640\,nm$.

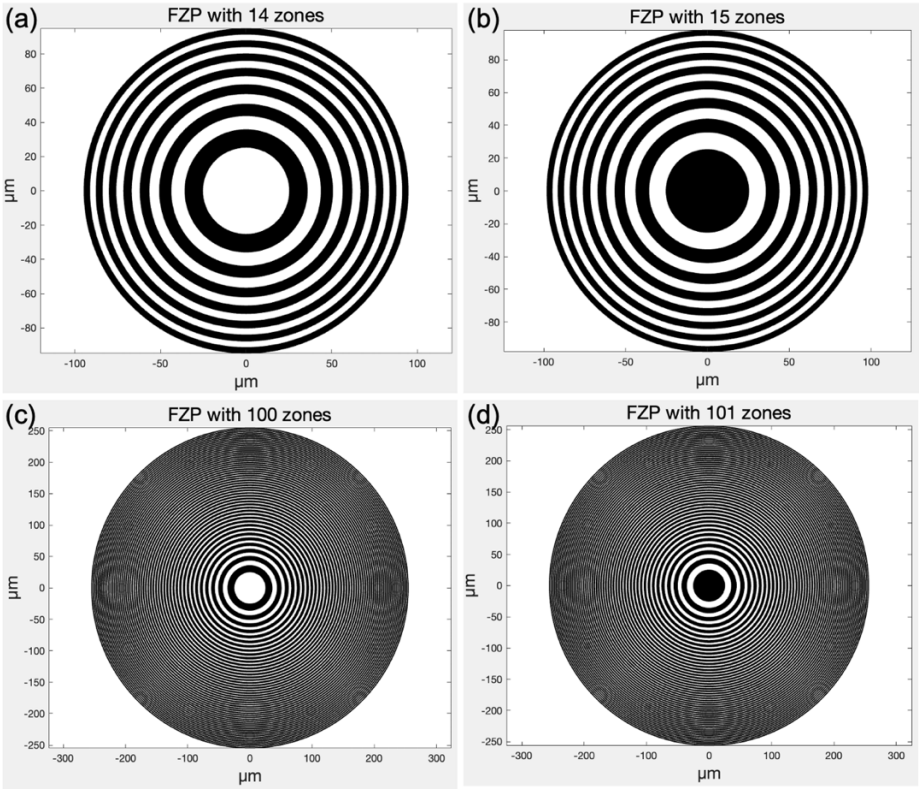

Figure 3.2-6 (a) Even mode FZP with 14 zones, (b) Odd mode FZP with 15 zones, (c) Even mode FZP with 100 zones, (d) Odd mode FZP with 101 zones.

Figure 3.2-6 illustrates various models of FZPs designed using MATLAB, based on specific coding parameters. These models display both even and odd-numbered zones, showcasing different patterns that influence the optical properties of the FZPs. In panels (a) and (b), the FZPs with 14 and 15 zones are depicted, with total diameters of 94.76 µm and 98.10 µm respectively. The width of the outermost zone in these models is 3.45 µm for the 14-zone FZP and 3.33 µm for the 15-zone FZP. This dimension is critical as it determines the minimum resolution required for the laser direct writing process used in fabrication; only resolutions finer than these widths can accurately render the FZP's intricate patterns onto a physical substrate. Panels (c) and (d) show FZPs with significantly more zones—100 and 101 respectively—highlighting a trend where an increase in the number of zones leads to a larger overall size of the FZP. This increase in zones and size also demands a decrease in the width of the outermost zone, which are 1.30 µm for the 100-zone FZP and 1.29 µm for the 101-zone FZP. These smaller widths indicate a requirement for higher precision in the laser direct writing process to achieve the necessary detail in the fabrication.

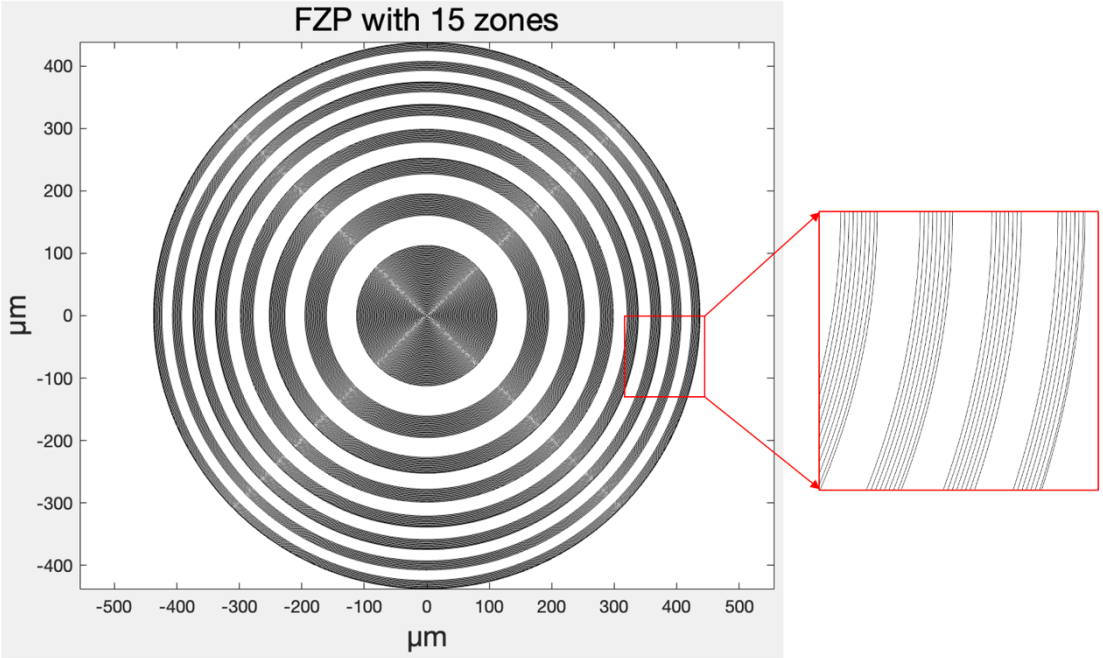

Figure 3.2-7 Laser line-marking calibrated FZP mode with 15 zones.

Figure 3.2-7 presents an enhanced design of a FZP with 15 zones, specifically tailored for fabrication using laser direct writing technology. In this refined model, each zone is composed of finely detailed lines that match precisely with the resolution capabilities of the laser system. This arrangement is crucial as it ensures that each microscopic line is accurately produced by the laser, adhering to the precise width required to maintain the FZP's optical performance. The figure prominently features a zoomed-in section highlighting the precise detail within the outermost zones. The adaptation of the zone structure to match the laser's resolution settings is a key innovation that significantly enhances the fidelity of the fabricated FZP. By aligning the digital design so closely with the physical capabilities of the laser system, this approach minimizes errors and maximizes the efficiency of the energy focusing properties of the FZP.

Such advancements are instrumental for applications requiring high precision in optical manipulation, such as in microscopy, imaging systems, and photonic devices. The implications of these design variations on the FZP's focusing abilities and overall performance will be further explored and detailed in chapter 4 of the study. This subsequent analysis will include discussions on the physical fabrication of these FZPs and the testing of their focal properties to assess their practical applications in optical systems.

3.2.4 MATLAB fiber grating sensor simulation

Additionally, two MATLAB programs have been developed to simulate the transmission spectra of FBG and LPG. These programs serve a critical role in providing theoretical foundations for experimental setups in two distinct but related sensing applications. The first program focuses on the transmission characteristics of FBGs. The second program is dedicated to simulating the transmission spectrum of LPGs, which are used extensively in sensing the refractive index of surrounding environments. This capability is particularly valuable in applications where changes

in refractive index can indicate the presence of specific chemicals or variations in the concentration of a substance. By accurately predicting how LPGs interact with different refractive indices, the program supports the experimental design, helping to ensure that the LPG-based sensors are both sensitive and specific to the intended environmental conditions.

3.2.4.1 FBG simulation

MATLAB code (see in Appendix B) for modeling the reflection spectra of FBG includes critical configurable parameters essential for simulating FBG behavior, such as the grating period (Λ), the grating length (L), and the effective refractive index (n_{eff}). These parameters are fundamental in determining the optical properties of the FBG, particularly in how it interacts with light at specific wavelengths. The code utilizes these parameters to calculate the center Bragg wavelength using the equation 2.4-6, $\lambda_B = 2n_{eff}\Lambda$, which defines the wavelength at which peak reflection occurs in the FBG, based on its physical and optical properties.

The figure below presents the simulated reflection spectra of FBGs at a fixed Bragg wavelength of 1550 nm, highlighting the impact of grating length on reflectivity. As shown, a grating length of 5 mm achieves a reflectivity of about 60%, which increases to 80% for 7 mm, and exceeds 99% for lengths of 15 mm or more. This increase in reflectivity with longer grating lengths also leads to more intense side lobes, indicating more complex interference patterns that could affect spectral purity in practical applications. Their increased intensity can be attributed to the more complex interference patterns formed as the grating length extends, which can affect the spectral purity and may have implications for certain applications where a clean spectral response is required.

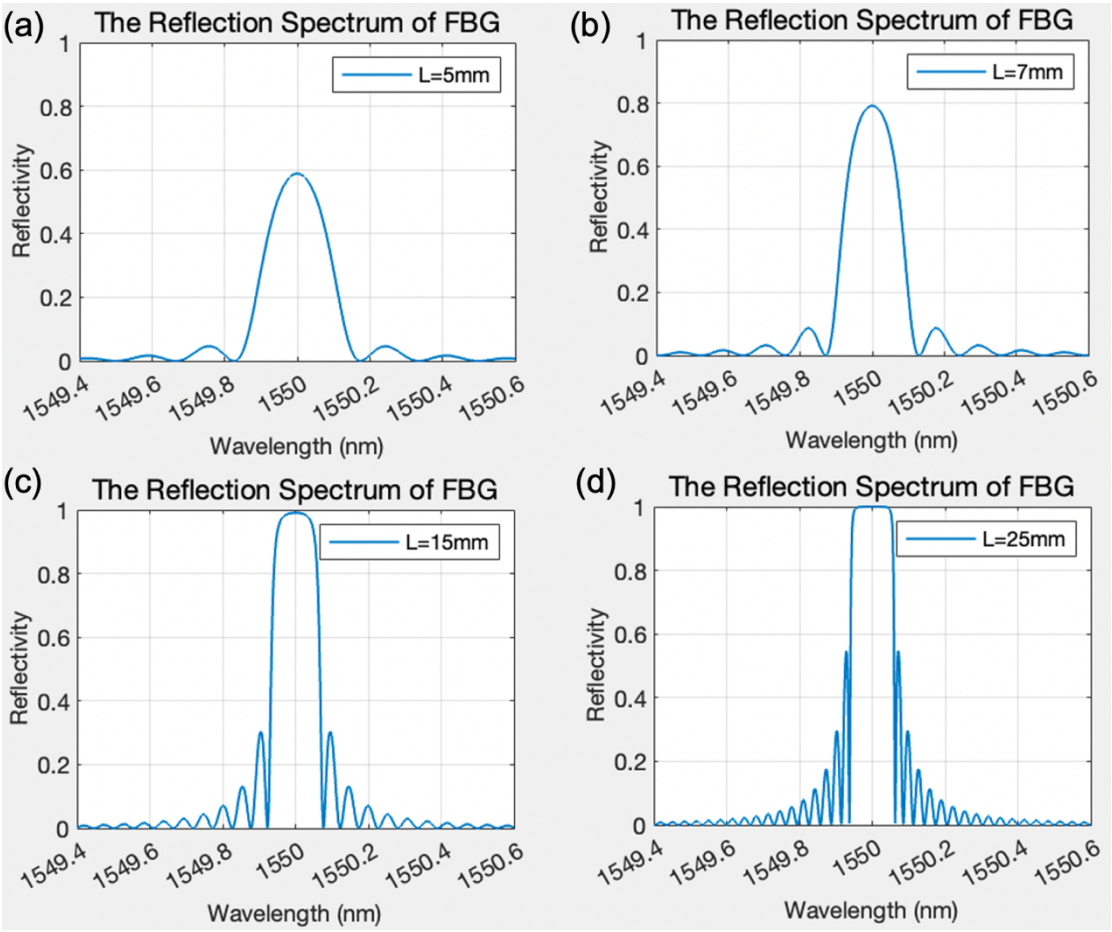

Figure 3.2-8 MATLAB simulation results of FBG reflectivity spectrum at grating length (a) L = 5 mm, (b) L = 7 mm, (c) L = 15 mm, (d) L = 25 mm.

By enabling adjustments to the grating period, length, and refractive index, the MATLAB code provides a versatile tool for simulating and optimizing FBG designs. The ability to predict and manipulate the Bragg wavelength through simulation not only enhances the development process but also significantly reduces the experimental trial and error, leading to faster innovation and deployment of FBG-based sensing technologies.

3.2.4.2 LPG simulation

MATLAB programme (see in Appendix C) simulates the transmission spectrum of

LPGs. The code snippet highlights key configurable parameters critical for the simulation, such as the refractive indices of the fiber core (n_1), cladding (n_2), and surrounding medium (n_3), as well as the radii of the fiber core (a_1) and cladding (a_2). Additionally, the grating period (Λ) and the grating length (L) are also specified, allowing for detailed adjustments to model how these factors influence the LPG's transmission characteristics under different environmental conditions. This detailed configurability facilitates precise simulations, aiding in the understanding and prediction of the transmission spectrum of LPGs across various surrounding environments.

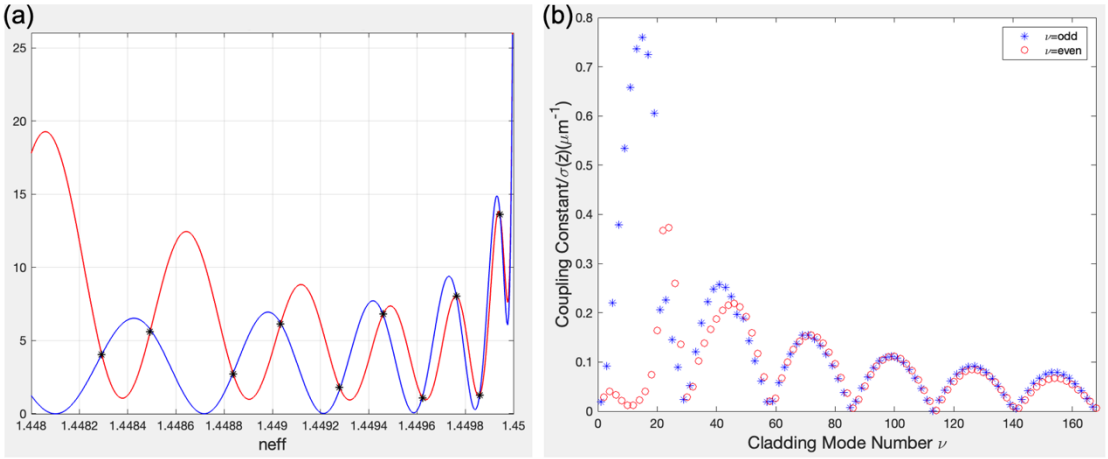

Figure 3.2-9 MATLAB simulation tests of (a) Order of effective refractive index of cladding n_2^{eff}, (b) Coupling constant $\sigma(z)$ via different cladding mode number v.

The MATLAB simulation provides detailed visual representations of the calculated results for the effective refractive index n_2^{eff} and the coupling constants $\sigma(z)$ in a study of cladding modes within optical fibers as shown in figure 3.2-12. Panel (a) depicts the effective refractive index n_2^{eff} for different orders, calculated using the specified equation 2.4-13 $\zeta_0 = \zeta_0'$. It illustrates the variation in n_2^{eff} with smooth and periodic peaks, indicating how each mode interacts differently within the fiber

structure. Panel (b) of the figure displays the coupling constant $\sigma(z)$ as a function of the cladding mode number v, with data points representing both odd and even modes. The coupling constant, which measures the efficiency of power transfer between the fiber core and the cladding modes, shows distinct peaks for specific modes, highlighting variations in coupling efficiency across the spectrum. This graph corroborates the results found in reference paper[102], using the same parameters.

The transmission spectrum of LPG simulation by the MATLAB program is shown in figure 3.2-10. The spectrum features distinct loss peaks indicative of the LPG's response at various wavelengths. Notably, the spectrum shows five pronounced loss peaks at wavelengths of 1270.7 nm, 1292.3 nm, 1347.5 nm, 1437.1 nm, and 1620.7 nm. The corresponding peak loss values are -0.4 dB, -1.7 dB, -3.5 dB, -7.0 dB, and -10 dB, respectively. These peaks represent critical points where the LPG effectively couples the core mode to cladding modes, resulting in significant transmission losses at these specific wavelengths.

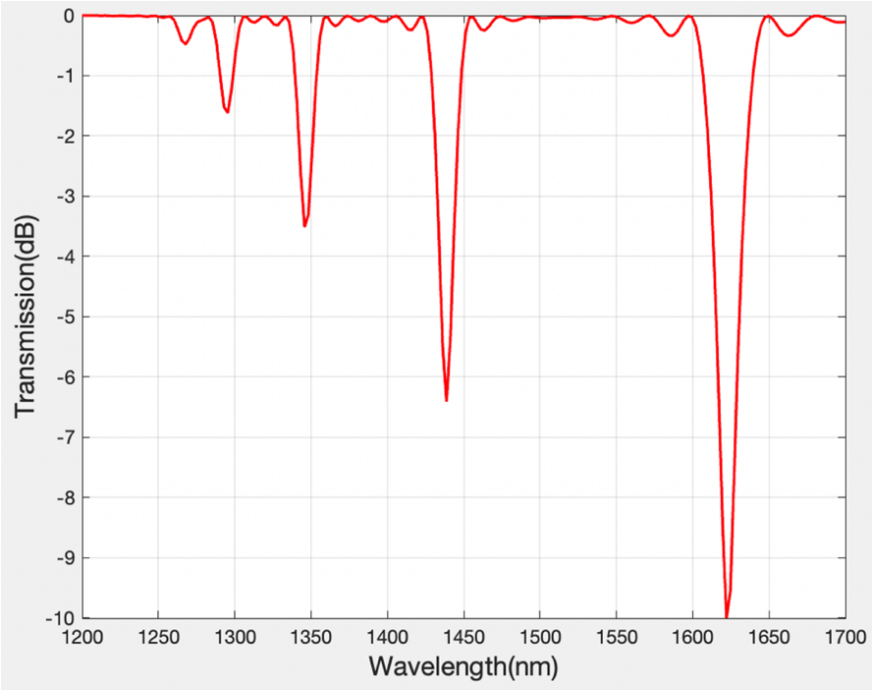

Figure 3.2-10 MATLAB simulation result of LPG transmission spectrum.

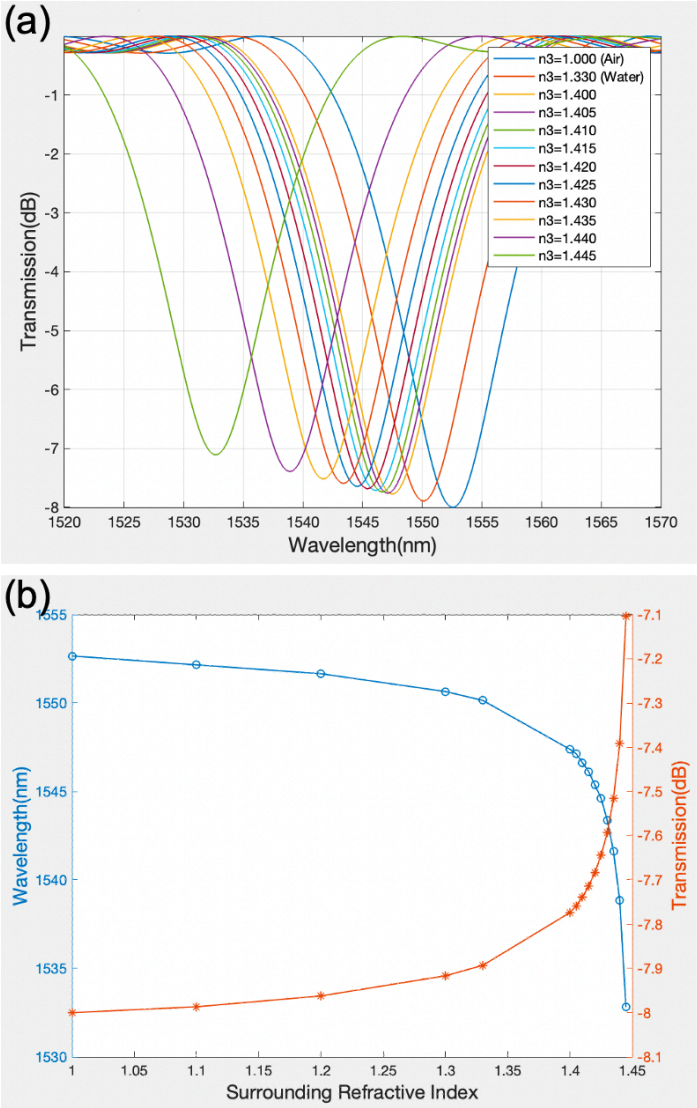

Figure 3.2-11 MATLAB simulation results of LPG (a) Wavelength peak shifts under various refractive index of surrounding medium from air (1.000), water (1.330) to 1.445, (b) Wavelength peak shift and minimum transmission value of an attenuation band against the RI of surrounding medium.

The MATLAB simulations depicted in the figures illustrate how the transmission characteristics of an LPG are influenced by the refractive index of the surrounding medium. In figure 3.2-11a, shifts in the wavelength peaks of the transmission spectrum are observed across a range of surrounding refractive indices from air (n=1.000) to 1.445. Each curve corresponds to a different refractive index, showing a clear trend where the resonant wavelength peak shifts towards longer wavelengths

as the surrounding refractive index increases. Figure 3.2-11b presents a detailed plot of both the resonant wavelength and the minimum transmission (depth of the attenuation band) against the surrounding refractive index. The blue line traces the wavelength shift, which steadily moves to longer wavelengths with increasing refractive index, while the orange line represents the transmission depth, which also deepens significantly as the refractive index increases. This dual response feature of the LPG, depicted by both the shift in wavelength and changes in transmission intensity with variations in refractive index, is particularly useful for designing sensitive optical sensors capable of detecting minute changes in the environment. This data is essential for applications in optical filtering and sensing, where precise control over wavelength selectivity is required. The detailed simulation helps in predicting and optimizing the LPG's performance for targeted applications in telecommunications or sensor technology, providing a valuable tool for designing devices that operate with high precision across varied optical spectra. These sensors are applicable in fields ranging from biomedical to environmental monitoring.

3.3 Experiment laser systems

This section describes the various types of laser system equipment utilized throughout the experiments conducted during the entire PhD project process. Each system is differentiated by its specific capabilities and applications, playing a crucial role in the comprehensive exploration and analysis of the phenomena under study. The descriptions cover the specifications and the experimental relevance of each type of laser system employed in the research.

3.3.1 UV nanosecond pulsed laser system

The GKNQL-355-10-20 Ultraviolet Laser setup depicted in figure 3.3-1 is a Diode-Pumped Solid-State (DPSS) laser. DPSS lasers are known for their stability, high

efficiency, and ability to produce a tightly focused beam at ultraviolet wavelengths. It is engineered to perform nano-scale hole marking experiments on substrates, including flat glass slides and the curved surfaces of optical fibers. The laser operates at a wavelength of 355 nm and is configured to pulse duration of 100 ns & repetition rate of 50 kHz to achieve optimal results during experimentation. The system's optics are designed with a focal length of 290 mm, producing a beam size of approximately 50 µm, ideal for micro-scale applications. This system is equipped with a manual Z-stage, which allows for precise adjustment of the substrate's position with a fine resolution of 0.5 µm.

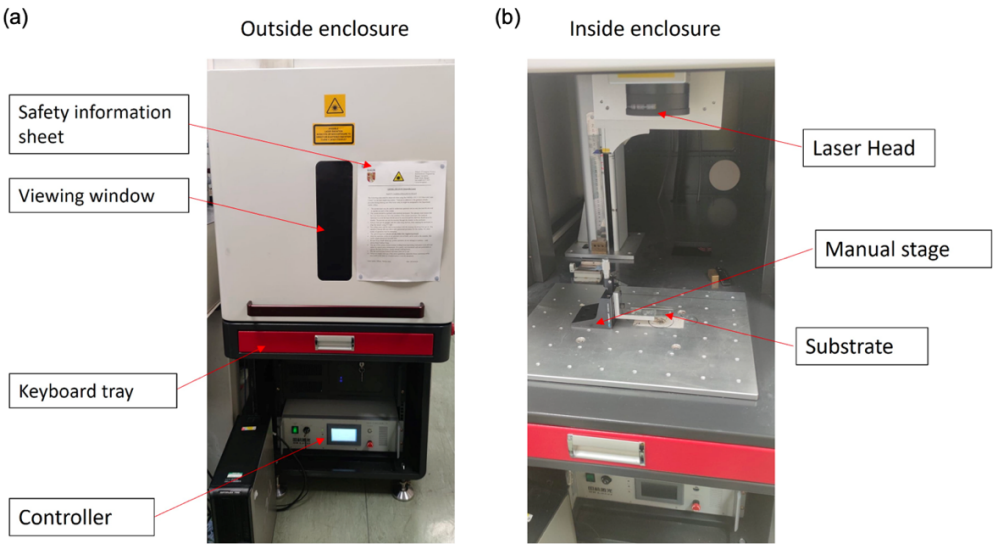

Figure 3.3-1 UV nanosecond laser system photograph with annotated information (a) Outside and (b) Inside the enclosure.

The figure below plots a graphical representation of the output power as a function of Q-pulse duration, demonstrating a clear relationship between pulse duration and laser power. Prior to conducting experiments, the power output was systematically measured, showing a decrease from approximately 9 watts at the shortest pulse duration of 1.0 µs down to lower than 1 watt at 20.0 µs. This data is crucial for calibrating the laser parameters to ensure accuracy and consistency in the

experimental results.

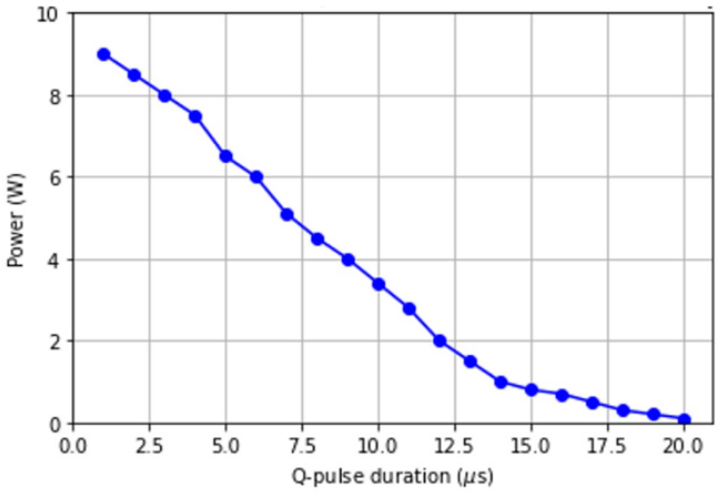

Figure 3.3-2 Plot of average power output versus Q-pulse duration at a 50 kHz repetition rate.

3.3.2 Picosecond SuperNANO imaging & patterning laser system

The Thorlabs picosecond microchip lasers are Q-switched devices operating at wavelengths of 1030 nm with pulse durations around 500 ps. This laser uses a microchip design with a fiber-coupled pump laser to produce picosecond pulses, where the Q-switching is achieved through gain switching[120]. The key specifications of the picosecond laser system is given in the table 3.3-1.

Centre Wavelength	**1030 nm ± 1 nm**
Average Output Power	**350 - 450 mW**
Repetition Rate	**8 - 10 kHz**
Pulse Energy (Typical)	**35 - 50 µJ**
Output Peak Power	**>65 kW**

Pulse Duration	500 ps ± 100 ps
Ellipticity	>0.94

Table 3.3-1 Key specifications of QSL103A Q-Switched Picosecond Microchip Laser System.

The figure below provides a detailed view of this system, which includes the laser head, the controller, and the connecting cable. This setup highlights the integral components of the system that work synergistically to deliver precise and controlled laser pulses at the picosecond scale.

Figure 3.3-3 QSL103A Q-Switched Picosecond Microchip Laser System with laser head, controller and cable.

A unique super-resolution instrument, SuperNANO, is designed with dual functions: super-resolution imaging and fabrication. This innovative tool enables simultaneous label-free super-resolution imaging and direct laser nanofabrication for the first time. The detailed designing information will be introduced in chapter 6.

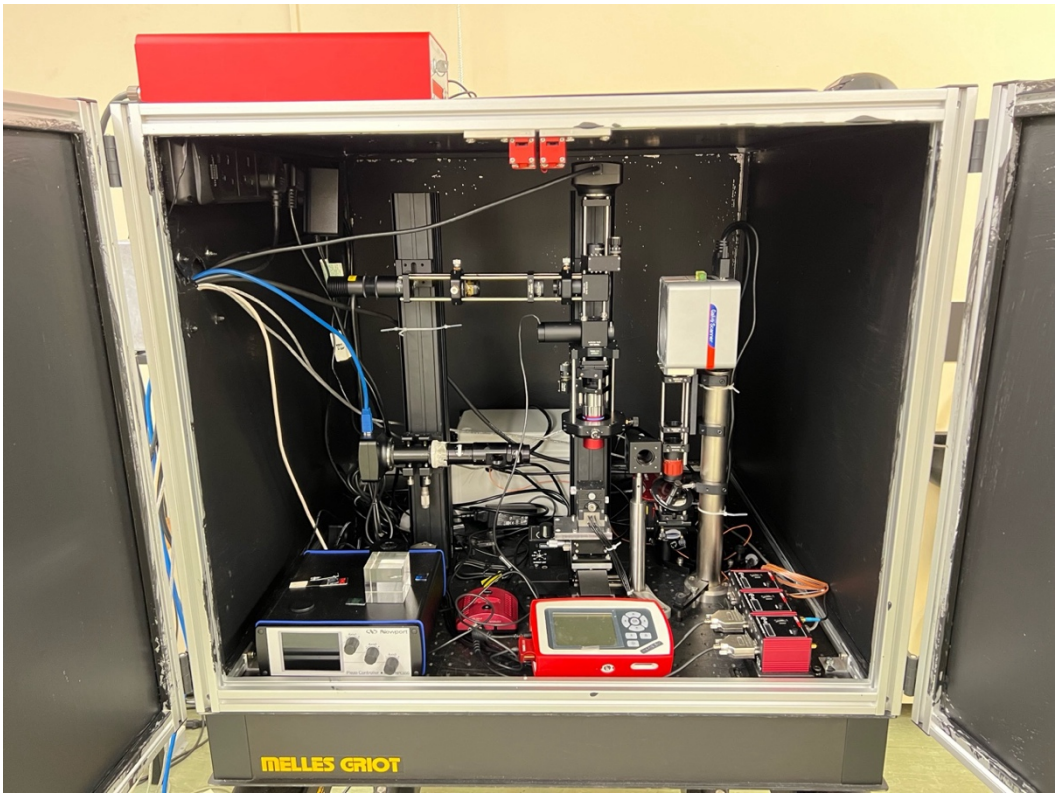

Figure 3.3-4 Overview photograph SuperNANO imaging & patterning laser system.

3.3.3 Supercontinuum white light laser system & Optical Spectrum Analyzer

The SUPERK COMPACT Supercontinuum white light laser system, designed by NKT Photonics and depicted in the figure 3.3-5, provides a high-performance solution for various applications including spectroscopy and general laboratory use. It produces light using a nonlinear optical process called supercontinuum generation. This process occurs when intense laser pulses interact with an optical fiber, triggering nonlinear effects that transform the initial narrowband laser light into a continuous spectrum. As a result, the system emits white light spanning a broad wavelength range from 450 nm to 2400 nm[121]. This system is used as a light source for fiber grating experiments, making it a valuable tool in both research and practical applications.

Figure 3.3-5 SuperK COMPACT Supercontinuum white light laser system with SuperK splitter and fiber delivery.

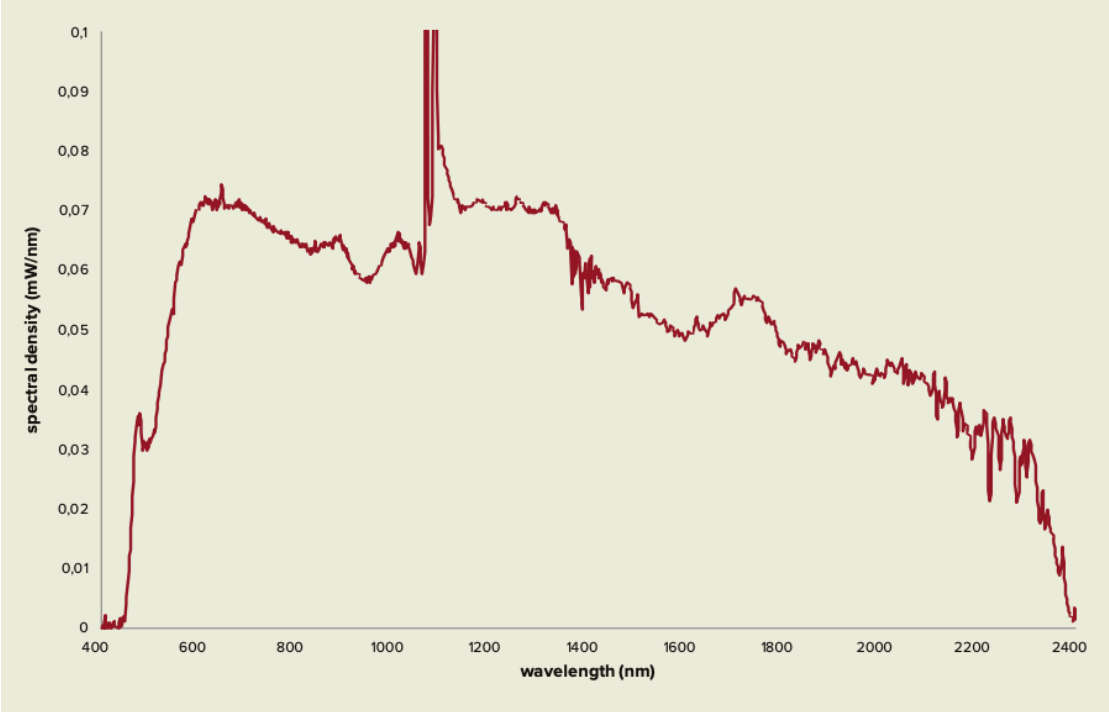

Figure 3.3-6 SuperK COMPACT Supercontinuum white light laser output spectrum.

The system's ability to deliver diffraction-limited light across a wide spectral range from 450 nm to 2400 nm makes it ideal for capturing detailed spectral information given in figure 3.3-6, which is crucial in fiber optic research and development. Its high brightness, significantly more intense than traditional light sources like incandescent lamps, provides the necessary illumination to explore the intricate properties of fiber gratings. Moreover, the system's variable repetition rate and excellent power stability ensure consistent performance, critical for experiments that require precise control over light intensity and wavelength.

The Anritsu MS9740B Optical Spectrum Analyzer, as referenced in figure 3.3-7, is a sophisticated benchtop device crucial for the analysis of transmission and reflection spectra in FBG and LPG experiments. This model is particularly valued for its broad wavelength range of 600 nm to 1750 nm and its high-resolution capabilities, which enable detailed spectral analysis crucial in fiber optic research. Key features of the MS9740B include a dynamic range from 42 to 70 dB and a fast measurement processing time, capable of completing sweeps in less than 0.35 seconds for a 30 nm wavelength span. The analyzer's high sensitivity (down to -90 dBm) and the ability to perform accurate side mode suppression ratio (SMSR) measurements of 45 dB or more make it ideal for evaluating complex optical components and systems.

Figure 3.3-7 Photograph of Anritsu MS9740B Optical Spectrum Analyzer.

3.4 Characterization equipment

In this project, a comprehensive suite of characterization equipment has been employed to carefully analyze the surfaces of various samples. It includes both optical and confocal microscopes, which are essential for detailed visual inspection and for capturing high-resolution images at different depths. Raman spectroscopy is another pivotal tool, providing insights into molecular structures through its ability to identify vibrational, rotational, and other low-frequency modes in a system. Additionally, Atomic Force Microscopy (AFM) and Scanning Electron Microscopy (SEM) have been utilized to obtain nanoscale images and properties of surfaces, which is important for understanding topographical details that are not discernible by other microscopic techniques. These diverse technologies together ensure a holistic approach to material characterization in our project, allowing for a thorough exploration of both structural and chemical properties.

3.4.1 Optical microscope

Figure 3.4-1 Olympus DSX1000 Digital Microscope.

The DSX1000 Digital Microscope from Olympus, when used with the DSX10-XLOB40X objective lens, is designed for detailed characterization across various applications. Key specifications include a high-resolution telecentric optical system, motorized zoom, and automatic calibration. The microscope achieves up to 9637X magnification on a 27-inch monitor with precise XY accuracy guaranteed after calibration. It features a color CMOS camera with a resolution range up to 5760 × 3600 pixels, LED illumination, and versatile observation methods including brightfield, darkfield, and polarization.

3.4.2 Confocal microscope

Figure 3.4-2 Olympus LEXT™ OLS5100 3D Laser Scanning Confocal Microscope.

The Olympus LEXT™ OLS5100 3D Laser Scanning Confocal Microscope is a sophisticated device tailored for precise material analysis and failure analysis. It features high-resolution magnification ranging from 5x to 100x and employs a reflection-type confocal laser scanning system. Specifications of the optical lenses is given in table 3.4-1. This microscope is equipped with a photomultiplier and a CMOS color camera, offering a dynamic range of 16 bits and a display resolution down to 0.5 nm for height measurements. It guarantees measurement accuracy tailored to a

constant environment and includes a motorized XY stage that varies in size based on the model, supporting comprehensive sample analysis.

Magnification	Numerical Aperture	Focal Distance (mm)
5x	0.15	20.00
10x	0.30	10.40
20x	0.60	1.00
50x	0.95	0.35
100x	0.95	0.35

Table 3.4-1 Specifications of optical lenses for Olympus LEXT™ OLS5100 3D Laser Scanning Confocal Microscope.

3.4.3 AFM – Atomic Force Microscopy

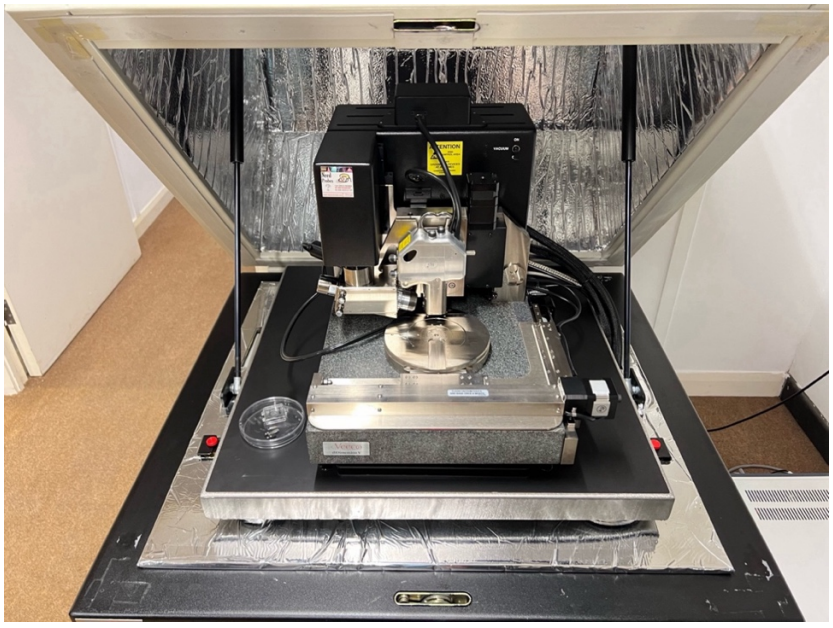

Figure 3.4-3 Photograph of Veeco Dimension 3100 AFM.

The Veeco Dimension 3100 AFM offers various scanning modes including contact, tapping, phase imaging, Electrostatic Force Microscopy (EFM), Magnetic Force Microscopy (MFM), and Conductive AFM (CAFM). The microscope features sub-nanometer resolution achieved through 16-bit digital-to-analog conversion, and it supports a motorized X-Y stage with a 100 mm by 120 mm inspectable area and 2 µm linear positioning resolution. It can accommodate samples up to 200 mm in diameter and 12 mm thick, with an optical field of view ranging from 150 to 675 microns. The Dimension 3100 operates with less than 0.5 Å RMS noise in the vertical dimension using a vibration isolation system, ensuring high precision. Additionally, it has a peak power consumption of 1800 W, compatible with various voltage standards (100, 120, or 220-240 V) and frequencies (50 or 60 Hz).

3.4.4 SEM – Scanning Electron Microscopy

Figure 3.4-4 Hitachi Tabletop Microscopes TM4000Plus II.

The Hitachi TM4000Plus offers photographic magnifications ranging from 10x to 100,000x and monitor display magnifications up to 250,000x. The microscope supports multiple accelerating voltages (5 kV, 10 kV, 15 kV, and 20 kV) for versatile

imaging. It features a dedicated low vacuum secondary electron (SE) detector and a high-sensitivity 4-segment backscatter electron (BSE) detector, enabling detailed imaging of both conductive and non-conductive samples. The TM4000Plus II supports various vacuum modes, including conductor, standard, and charge reduction. It can handle samples up to 80 mm in diameter and 50 mm in thickness, with an X-Y stage travel of 40 mm by 35 mm. Enhanced features include the Multi Zigzag function for stitching high-magnification images, an optional STEM holder for transmission imaging, and advanced software for easy report creation and elemental analysis.

3.5 Coating equipment

3.5.1 Spin Coater

Figure 3.5-1 Photograph of Schwan EZ4 Spin Coater.

The Schwan EZ4 Spin Coater from Lebo Science stands out as an advanced tool engineered for precise thin film applications. This coater is adept at controlling film thickness and uniformity with an adjustable spin speed that can be varied from 500 to 8000 RPM. Users can fine-tune the spin duration as well, with the ability to program times anywhere from 1 to 999 seconds in one-second increments. Designed to accommodate substrates as large as 150mm in diameter, the device incorporates a vacuum chuck that ensures substrates remain securely fixed during the spin-coating process. Enhancing usability, the Schwan EZ4 features a digital display that provides real-time feedback on spin parameters, making it easier for users to monitor and adjust settings as needed. The user-friendly control panel simplifies operation, allowing for straightforward adjustments and customization of the spin-coating parameters. Its compact footprint is ideal for use in space-constrained laboratory settings, maximizing workspace efficiency without compromising performance. The device is integral to the USO fabrication experiment, where it applies UV glue onto plano-convex lens.

3.5.2 Dip Coater

Figure 3.5-2 Photograph of Ossila Dip Coater.

The Ossila Dip Coater is designed for the deposition of thin wet films through a controlled process of dipping and withdrawing substrates from a solution. This precision instrument is particularly suited for research and development environments, enabling uniform film coatings on a variety of substrates. Key features of the Ossila Dip Coater include a high-precision motor that allows for finely controlled immersion and withdrawal speeds, from 0.01 mm/s to 50 mm/s, to achieve different film thicknesses and properties. The system supports a maximum travel distance of 100 mm and can handle substrates up to 100 mm in length. The coater is equipped with integrated software that enhances its functionality by allowing manual or automatic operations and supports up to 20 savable programmable routines for easy repeatability without resetting parameters each time. Safety features include a crash detection switch that stops the motor if it encounters an obstruction, ensuring the protection of both the substrates and the equipment. The dip coater also features adjustable clamp pressure to accommodate both delicate and robust substrates and has a wide base that can accommodate beakers up to 2 liters. The device is used in deposition experiment of microsphere monolayers on optical fibers, facilitating the coating of microspheres.

Chapter 4.
Conventional Direct Laser Manufacturing & Superlens-enabled Marking

4.1 Introduction

This chapter explores the frontier of laser manufacturing technologies, tracing the journey from conventional applications like laser-induced graphene and micromanufacturing of FZPs to advanced anti-counterfeiting measures using superlens-enabled marking. These technologies exemplify the progression and innovation within the field of laser applications, pushing the boundaries of precision, efficiency, and security in manufacturing.

First, the realm of UV laser-induced nitrogen and sulfur-doped graphene is introduced. This method leverages the specificity of laser energy to create graphene directly on substrates without the need for traditional metal catalysts. This section will detail the process parameters and material interactions that enable the formation of high-quality graphene layers.

Next, the microfabrication of FZPs is discussed, which is critical in the miniaturization of optical devices for lab-on-chip applications. The intricacies of using laser direct writing to achieve micron-scale precision in creating these zone plates underscore the potential of laser technology in enhancing the capabilities of compact electronic and photonic devices. The challenges and innovations of the process, particularly in addressing issues of material removal and maintaining design fidelity, are examined.

Finally, this chapter showcases a two-level security approach that significantly enhances the difficulty of replicating marked items by incorporating superlens systems into the laser marking process. The use of DotCode technology, integrated with nanoscale features, introduces a robust barrier to counterfeit activities,

ensuring the authenticity and traceability of products in various industries.

Throughout the chapter, a series of case studies and experimental setups illustrate the practical applications of these technologies, as well as their implications for future developments in materials science, manufacturing, and product security. Each section not only demonstrates technical expertise and innovative approaches but also aligns with broader trends in sustainability and cost-efficiency.

4.2 UV laser-induced N & S-Doped graphene manufacturing technology

Laser direct writing can treat materials with minimal thermal damage to substrates, offering precise control over laser energy, beam-material interaction time, and heat penetration depths[122]. Traditionally, laser irradiation has been considered a thermal reaction source for chemical vapor deposition (CVD), commonly used for large-area graphene growth. The number of graphene layers produced could be controlled by adjusting the pulsed or continuous wave laser and the laser scanning speeds. These processes typically required metallic precursors such as Cu and Ni. Research from Rice University demonstrated that continuous 10.6 μm wavelength CO_2 laser infrared irradiation could thermally convert polyimide (PI) and polyetherimide (PEI) solid sheets into graphene without using Cu or Ni[43]. In this section, a laser direct writing technique to form graphene patterns on polybenzimidazole (PBI) thin film and glass substrates using a low-cost nanosecond UV laser system is reported. This method avoids thermal damage to the substrates and does not require a metallic precursor. The UV laser beam induces photochemical reactions that break specific molecular bonds to form graphene on the substrate without causing substrate damage[6]. Unlike in Ref. [6], which uses a picosecond UV laser, in this work, we employ a lower-cost nanosecond UV laser.

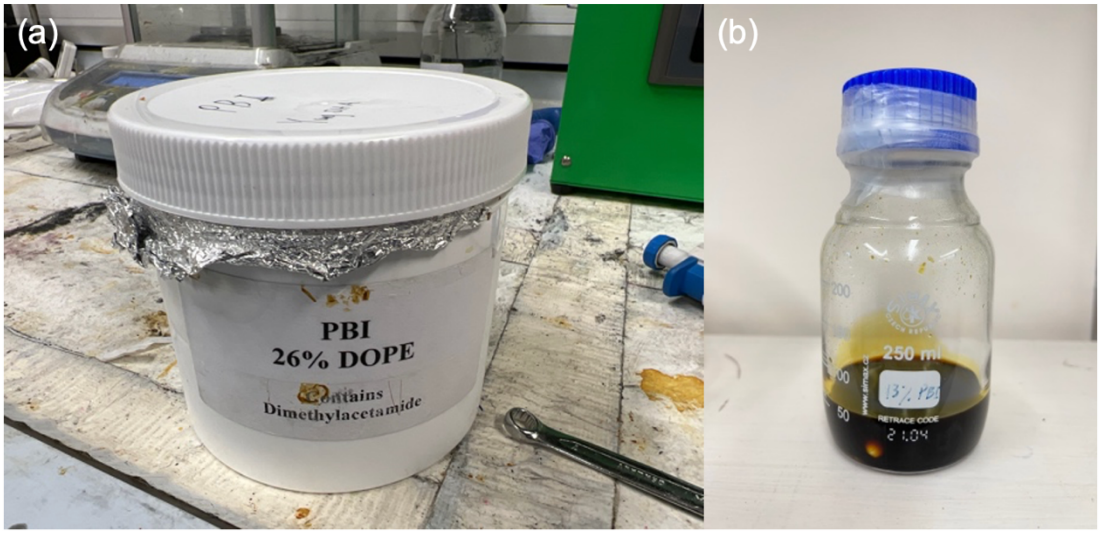

Figure 4.2-1 Photograph of (a) 26% polybenzimidazole(PBI), (b) 13% PBI solution.

As methodology, start by dissolving 26% polybenzimidazole (PBI) (Fig. 4.2-1a) in dimethylacetamide (DMAC) to produce a 13% PBI solution (Fig. 4.2-1b). This mixture should be stirred continuously for 1 hour at a temperature of 30°C until the PBI is completely dissolved as figure 2a. Once the solution is prepared, set the micropipette coater (Fig. 4.2-2) to apply a uniform coating with a thickness of 15 µm on each side.

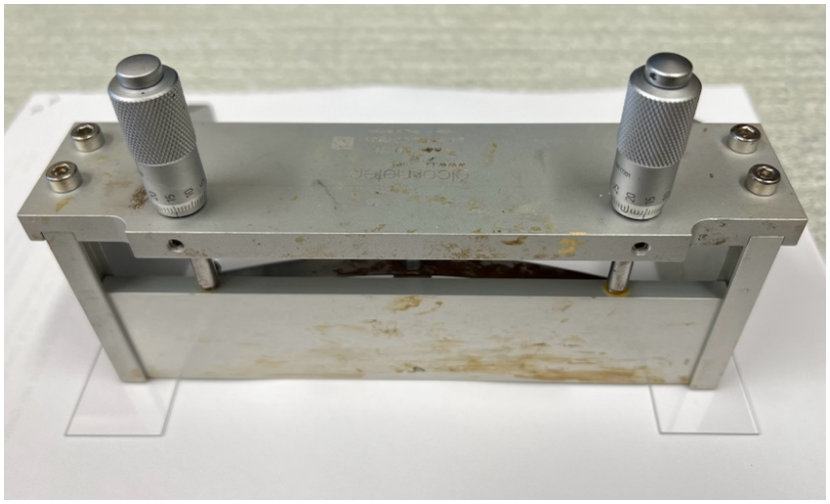

Figure 4.2-2 Photograph of micropipette coater set as 15 µm on each side.

Next, as shown in figure 4.2-3, use the micropipette with a specified diameter to selectively deposit 0.02 mL droplets of the PBI ink onto a glass sheet that is 1 mm thick. This deposition should be carried out carefully to ensure even coverage. After the PBI ink has been applied, dry the coated glass sheet at 80°C until the coating is fully set.

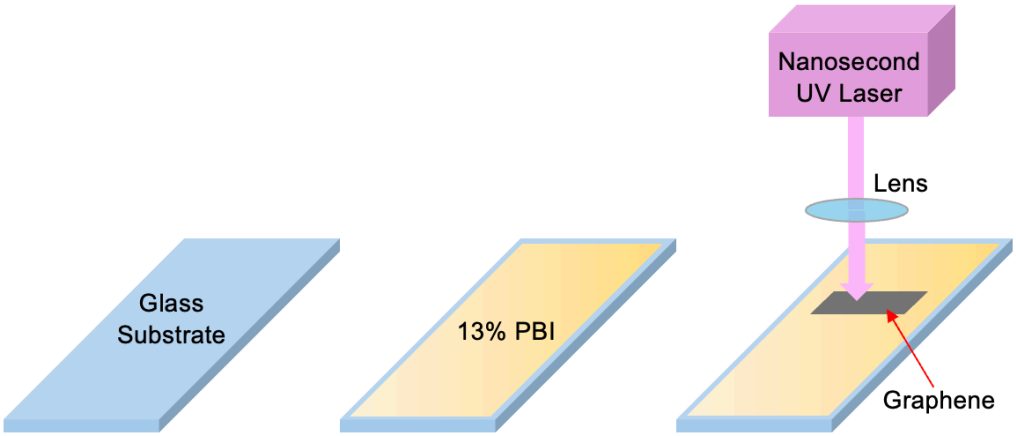

Figure 4.2-3 Schematic of the graphene production process induced by nanosecond UV laser direct writing.

Following the drying process, employ a nanosecond UV laser with a wavelength of 355 nm, a pulse duration of 100 ns, and a frequency of 50 kHz to treat the PBI-coated glass sheet. The laser should be scanned across the surface at a speed of 20 mm/s. The goal is to induce the formation of flaky silver-black graphene on the PBI sheets. This transformation occurs under a specific laser power and is influenced by the thermal effects and Q factor, which should be maintained between 16.0 and 17.0. The processing area for the laser should be 10 mm wide, with a hatch pattern created by lines spaced 0.01 mm apart. This precise control of the laser parameters and scanning process ensures the successful conversion of the PBI coating into graphene, characterized by its unique flaky silver-black appearance.

Figure 4.2-4a displays a sample of UV laser direct writing on PBI film, with the Q factor

ranging from 16.0 to 17.0 in increments of 0.2. A Q factor around 16.4 yields the best performance, with an induced graphene sample exhibiting a resistance of approximately 50Ω over a distance of 2 mm. The laser fluence was gradually increased from 9 to 11 mJ/cm² in response to changes in the Q factor on the PBI-coated substrate. A 10 × 2.5 mm rectangular hatch pattern with a hatch spacing of 0.01 mm was applied at a scanning speed of 20 mm/s. This hatch design, shown in the inset of figure 4.2-4a, was used consistently for all laser-written patterns in the experiment. Figure 4.2-4b shows the 2D Raman spectrum mapping of the UV laser-induced graphene from the PBI thin film. The degree of carbon crystallization is illustrated by the ratio I(D)/I(G) of the D peak (1350 cm^{-1}) to the G peak (1590 cm^{-1}) in the Raman spectrum. A higher D peak indicates a higher defect ratio. The presence of the 2D peak (2700 cm^{-1}) confirms the formation of graphene.

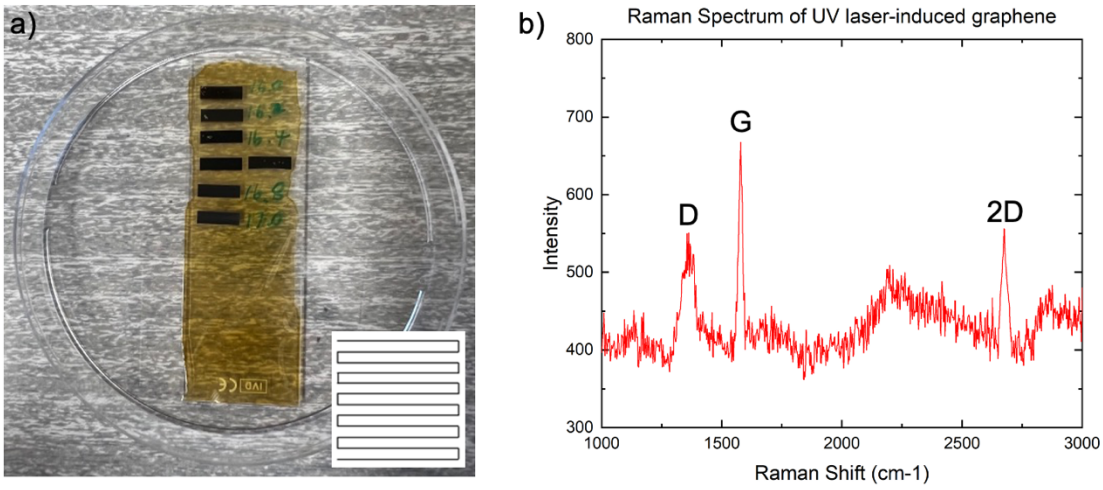

Figure 4.2-4 (a) UV laser-induced graphene sample on the PBI sheet under different Q factor. The same rectangular laser hatch pattern (inset) was applied across all test conditions. (b) 2D Raman spectrum of sample under Q = 16.4.

4.3 2D Fresnel lens fabrication by laser direct writing

Lab-on-chip devices are becoming increasingly important in the field of modern

electronics and photonics, particularly in the fabrication of micro-devices. These traditional micro-devices frequently encounter problems related to their complex manufacturing processes and the high costs involved. To address these challenges, the use of thin film FZP lenses presents a promising solution. These lenses are characterized by their micron-scale focal lengths, making them highly compatible with the compact scale and integrated nature of lab-on-chip technologies. The process of microfabricating FZP lenses involves laser direct writing on thin films. While this technique is technically feasible, it often results in the removal of excess material, which can lead to significant discrepancies between the device's theoretical design and its actual physical representation[8]. Although utilizing high-resolution laser systems, such as femtosecond lasers, can improve the accuracy of these fabrications, the cost associated with these systems is prohibitively high for many applications.

In response to these challenges, this section describes a novel method that offers a low-cost, straightforward, and rapid alternative for the design and fabrication of micro-compensated FZP lenses. This method leverages widely available laser systems and incorporates a custom-designed software program specifically tailored to compensate for the common problem of excess material removal during the laser writing process on thin films. The proposed approach not only reduces the financial burden but also simplifies the manufacturing process, making advanced microfabrication techniques more accessible and practical for a wider range of applications in the electronics and photonics industries.

4.3.1 Design of micro compensate FZP on thin film

The schematic illustration provided in figure 4.3-1 outlines the process for designing and fabricating compensated FZPs using laser direct writing on a thin film. In this setup, design parameters are programmed into a system that controls a Galvo scanner which, in turn, directs an infrared laser to etch the thin film substrate. The

specific characteristics of the laser include a wavelength of 1064 nm, a pulse duration of 100 nanoseconds, and a repetition rate of 20 kHz. This configuration allows the laser to achieve a linewidth stability ranging from 1 to 3 microns during rapid etching processes.

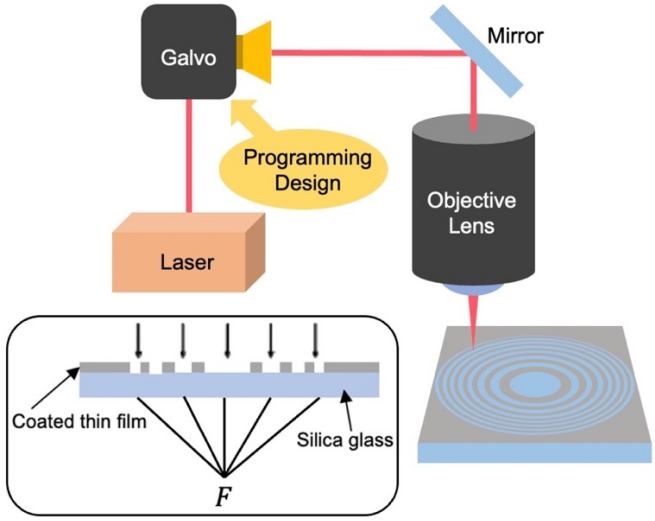

Figure 4.3-1 Schematic for the process of microfabricating FZPs through laser direct writing on thin films with designed compensate program.

The design specifications for the micro compensate FZPs include a focal length (F) of 1 mm and an incidence wavelength (λ) of 640 nm. These FZPs are tailored with two different types of zone numbers to enhance their performance: 14 zones for the even type and 15 zones for the odd type. The radii of the FZP zones are calculated based on equation 3.2-2. This equation is crucial as it directly influences the precision and efficiency of the FZP lenses by determining the optimal zone radii needed to focus light accurately at the specified focal length and wavelength.

Figure 4.3-2b illustrates the method for designing FZP with adjusted widths to compensate for material removal during fabrication. Taking the second transmission

zone of the even-type FZP as highlighted in figure 4.3-2a, the ideal zone width is designed to be 10.5 µm. During the laser etching process on thin films, each edge of a zone typically undergoes excess material removal of approximately 1.5 µm due to the nature of the laser-material interaction. This results in an actual etched width of 13.5 µm for a designed zone width of 10.5 µm. To compensate for this, all zone widths were reduced by 3 µm in the design, so that after fabrication, the actual dimensions align with the target specification. This approach was applied uniformly, and verification confirmed that zones 2, 4, 6, 8, 12, and 14 matched the intended dimensions post-compensation. Through this approach, even low-cost laser systems can achieve high precision in producing micro-scale FZPs on thin films. The strategy effectively mitigates the issues of over-etching, thus preserving the optical integrity and functional accuracy of the FZPs within lab-on-chip devices.

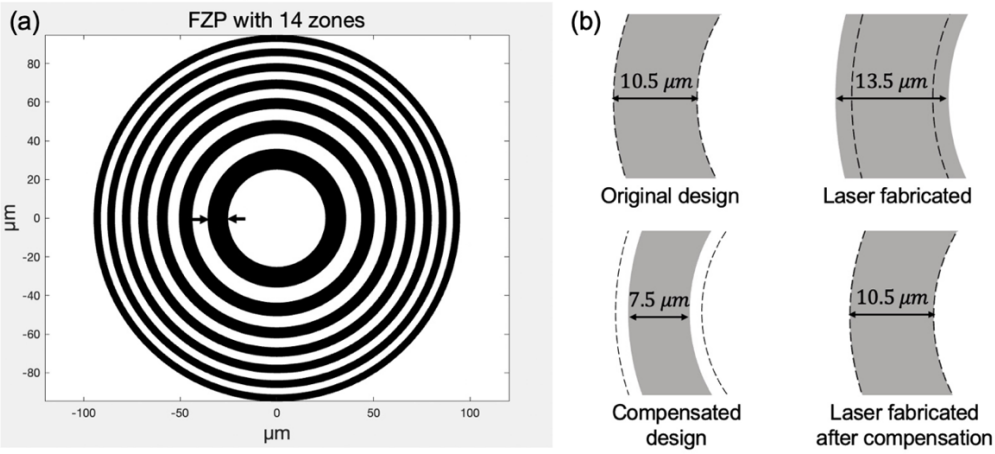

Figure 4.3-2 (a) A FZP with 14 zones. (b) The compensation strategy used in the design and fabrication of the FZP to address material removal during the laser etching process. The diagrams compare the original design, laser-fabricated results without compensation, the compensated design, and the laser fabricated results with compensation.

4.3.2 FZP fabrication and focusing performance

Figure 4.3-3 presents the results of quality tests performed on FZPs fabricated on aluminum-coated microscope slides (100 nm aluminum on AL.1000.ALSI, Platypus Technologies, USA[123]). The test focused on verifying the accuracy of the radii in the initial transmission zones for both even and odd FZP types. It display microscope measurements of the first zone radius in both FZP types. These measurements closely match the theoretical expected value of 50.600 µm, with the actual measured values being 50.608 µm and 50.612 µm, respectively, indicating a minimal deviation from the expected dimensions. This high level of accuracy demonstrates the effectiveness of the laser etching process used in the fabrication of these micro-optical devices. The linewidth of the laser etching plays a crucial role in defining the size and accuracy of the FZP, with the precision maintained as long as the etching linewidth remains narrower than the width of the outermost zone. This ensures that the focusing capabilities of the FZPs are optimized for applications requiring precise optical manipulation.

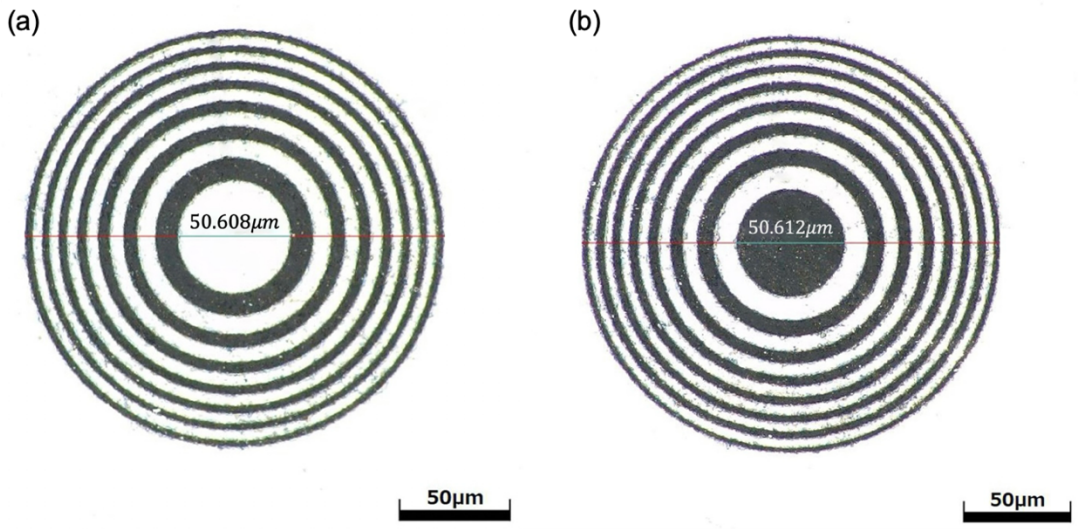

Figure 4.3-3 Even (a) & odd (b) FZPs fabricated on aluminum thin films, showing the precision in the first zone radius measurements of 50.608 & 50.612 µm, respectively.

The focusing tests were conducted at the lens surface (zero focal distance) using a

CCD camera and a 640 nm wavelength laser source. Results are shown in figures 4.3-4a and 4.3-4d, demonstrating the beam concentration and symmetry at the focal region. In these tests, the light was successfully transmitted through the red zones while being blocked by the black zones. The precision in controlling and eliminating excess material removal allowed for an impressive zone width accuracy of 99.3%. The experiments demonstrated that, although lower energy levels and slower etching speeds can significantly enhance the accuracy of zone width, they also extend the processing time. However, the areas compensated for excess material removal exhibited the same transmission efficiency as those directly etched, maintaining the accuracy of the focal length and balancing manufacturing costs with improved efficiency.

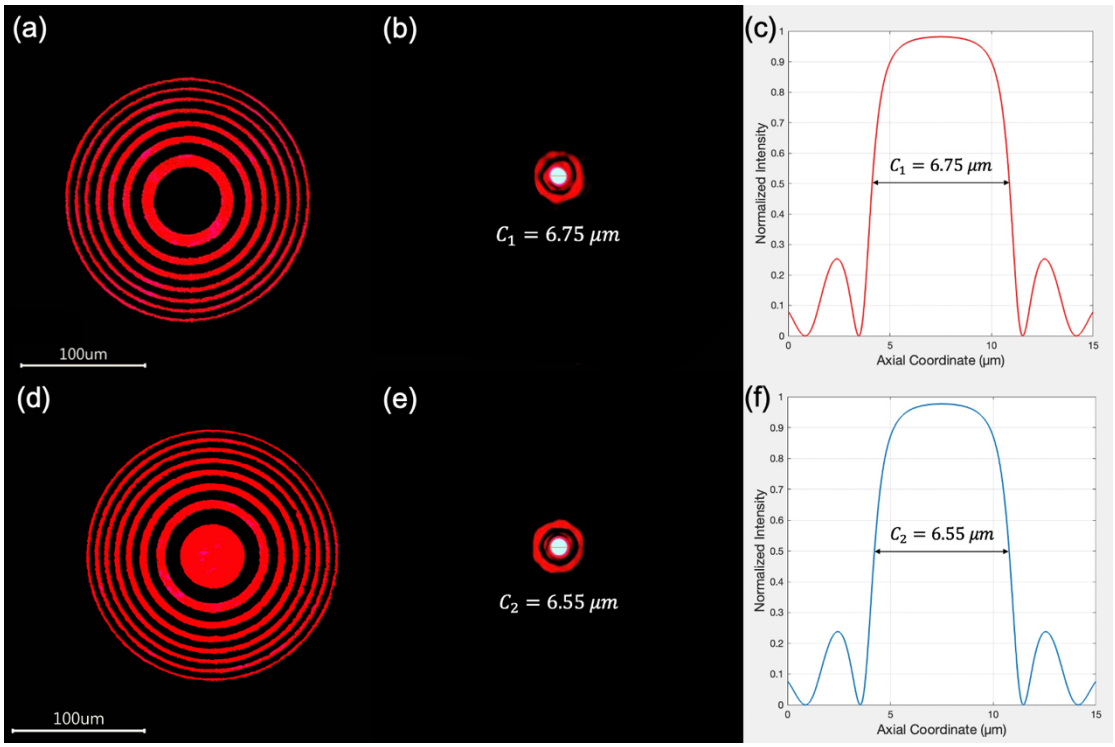

Figure 4.3-4 Even type focusing test at (a) surface, (b) focal length (beam profile). (c) FWHM of focus at focal length. Odd type focusing test at (d) surface, (e) focal length (beam profile). (f) FWHM of focus at focal length.

When the focal distance was increased to the designed focal length (F = 1000 μm), figure 4.3-4b & 4.3-4e captured the optimal focusing effects of these two lenses. Notably, the odd-type lens displayed more uniform performance at the central focus compared to the even-type. The measurement results of the Full Width at Half Maximum (FWHM) from figure 4.3-4c & 4.3-4f reveal that the odd-type lens has a slightly larger FWHM value of 6.75 μm compared to the even-type's 6.55 μm, a difference of less than 3%. This discrepancy diminishes as the number of zones increases, affirming that a higher number of zones leads to improved focusing effects in FZP designs. Moreover, FZP designs without compensation, under the same testing conditions, resulted in significant errors, underscoring the effectiveness and feasibility of the compensation method used in these tests.

The images in figure 4.3-5 illustrate the results of uniformity tests conducted at various focal distances ranging from 100 to 1200 μm, utilizing a CCD camera and a laser with a 640 nm incidence wavelength. These tests demonstrate the focusing capabilities of the FZP under different focal distance conditions. Among these, only the image in figure 4.3-5c, taken at a focal distance of 500 μm, shows a discernible focused spot, which corresponds to the secondary focal point of the FZP. In contrast, the primary focus, which is clearly depicted in figures 4.3-4b & 4.3-4e at a focal distance of 1000 μm, displays a more prominent and well-defined focus. The absence of a focusing effect at other tested distances reinforces the precision required in setting the focal length to achieve optimal imaging results. This distinction highlights the specific focal properties of the FZP, where effective focusing is achieved only at certain predefined distances.

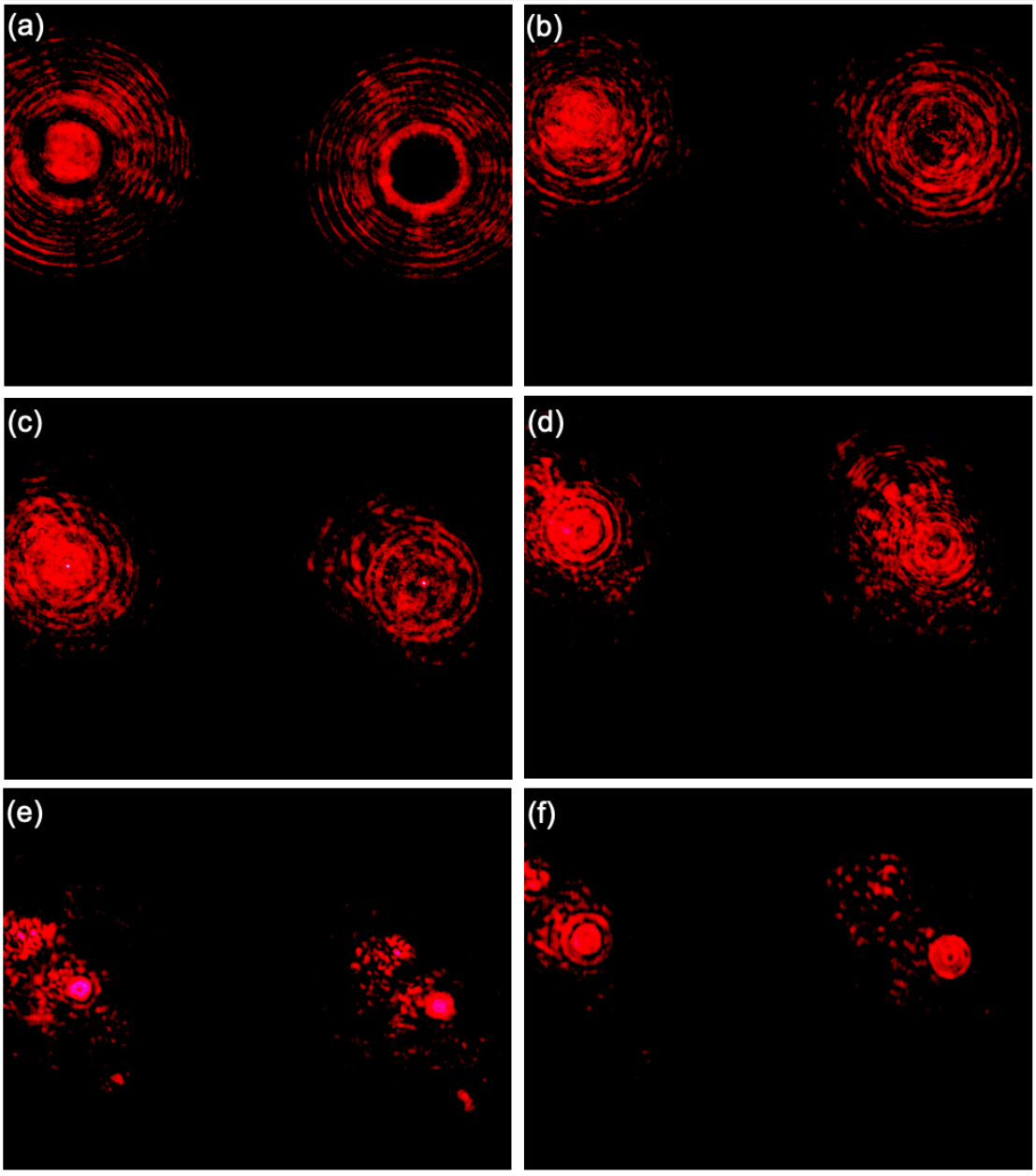

Figure 4.3-5 Focusing test at (a) 100 µm, (b) 300 µm, (c) 500 µm, (d) 700 µm, (e) 900 µm, (f) 1200 µm.

A comprehensive analysis of the focusing performance for an even-type micro-compensated FZP at a focal distance of 1000 µm is shown in figure 4.3-6. The horizontal and vertical focusing intensity distributions are characterized by a prominent peak at the center, surrounded by smaller peaks, graphically demonstrating how light is concentrated across the pixel numbers. The 3D

visualization of the focusing intensity distribution provides a spatial view of how the light converges at the focal point, showing intensity variations both horizontally and vertically. The focusing point contour map outlines the intensity contours around the focal point, with denser contours near the center indicating higher intensity that spreads outward with decreasing intensity. These panels effectively illustrate the precision of the FZP's focusing capability, highlighting its effectiveness in manipulating light at the specified focal distance.

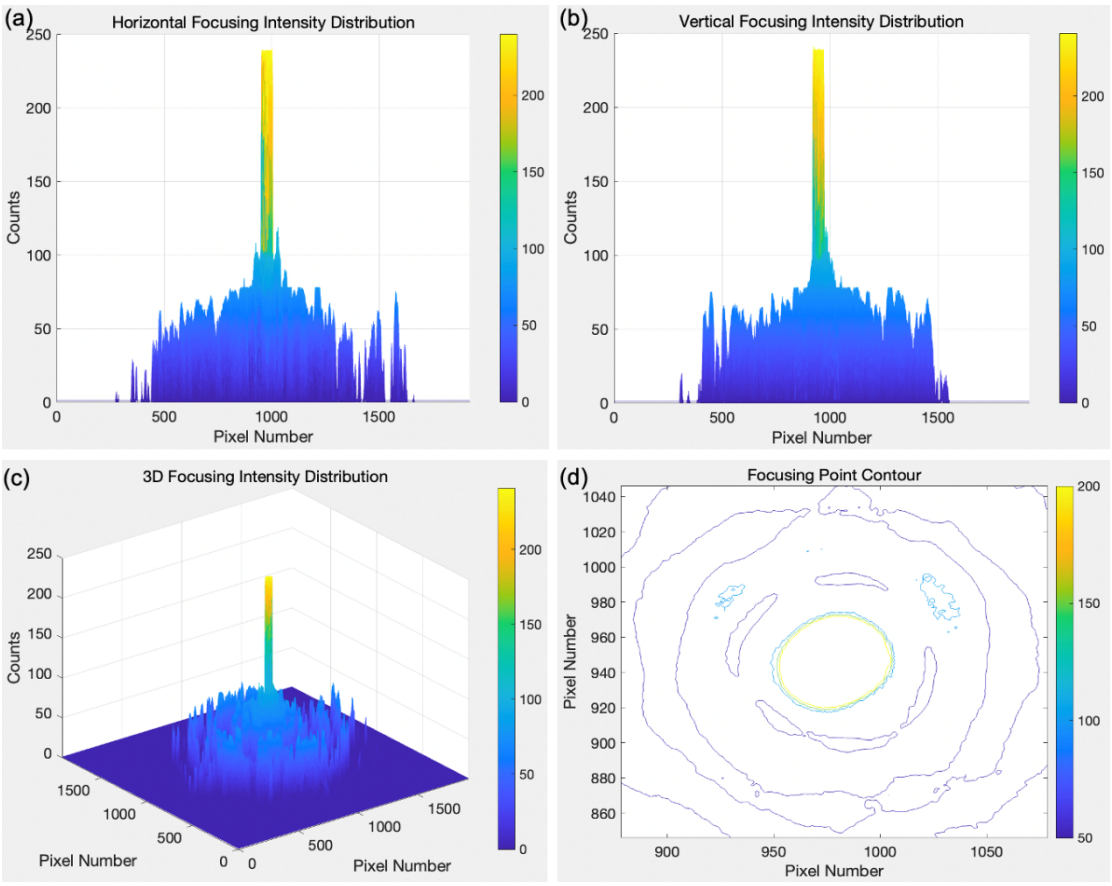

Figure 4.3-6 Focusing performance analysis for even type micro compensate FZP at focal distance D = F = 1000 μm by (a) Horizontal distribution, (b) Vertical distribution, (c) 3D distribution, (d) Focusing point contour.

4.4 Superlens-enabled laser direct marking

Laser marking is widely used as an effective tool in anti-counterfeiting applications[124]. Compared to ink-based marking, laser-marked patterns are difficult to rub off, making them an ideal solution for traceability and anti-counterfeiting purposes. Laser marking creates a permanent and indelible mark[125]. However, with the rapid growth of laser technology, particularly fiber laser technology, the prices of conventional-lens-based laser marking systems have considerably dropped in recent years, leading to an increase in counterfeiting activities. Consequently, new innovations are needed to enhance the security level of markings and prevent counterfeiters with laser marking systems from copying or reproducing marks. To address this, a novel two-level security marking approach has been proposed: firstly, encoding the text to be marked into a DotCode; secondly, adding nanoscale features to the dots with the assistance of a superlens. These nanoscale features enhance the security of the marking, providing an effective anti-counterfeiting solution to protect authentic products.

4.4.1 Microsphere monolayer substrate preparation

The deposition process of spherical particles is carefully designed, leveraging the natural properties of water, especially its high surface tension, which ranks among the highest for liquids, similar to mercury. The process begins by submerging the substrate in water. Spherical particles are then introduced into suspension above the water, allowing them to deposit and self-assemble at the water/air interface within a confined area. This is facilitated by the unique characteristics of water which supports the particles and enables their organization into a precise monolayer.

As shown in the series of illustrations (Fig. 4.4-1a to 4.4-1d), the initial step involves dispersing 1 μm silica microspheres in methanol, which are then deposited onto the water surface (Fig. 4.4-1a). The microspheres spread across the water's surface,

aligning according to the spread direction (Fig. 4.4-1b). This alignment is crucial as it ensures uniform arrangement of the particles. Following this, the substrate is gently tilted (Fig. 4.4-1c), initiating the gradual drainage of water. This action delicately transfers the microspheres from the water/air interface down onto the substrate, maintaining the integrity of the monolayer formation. Finally, the positioned particles on the substrate are subjected to UV laser marking (Fig. 4.4-1d).

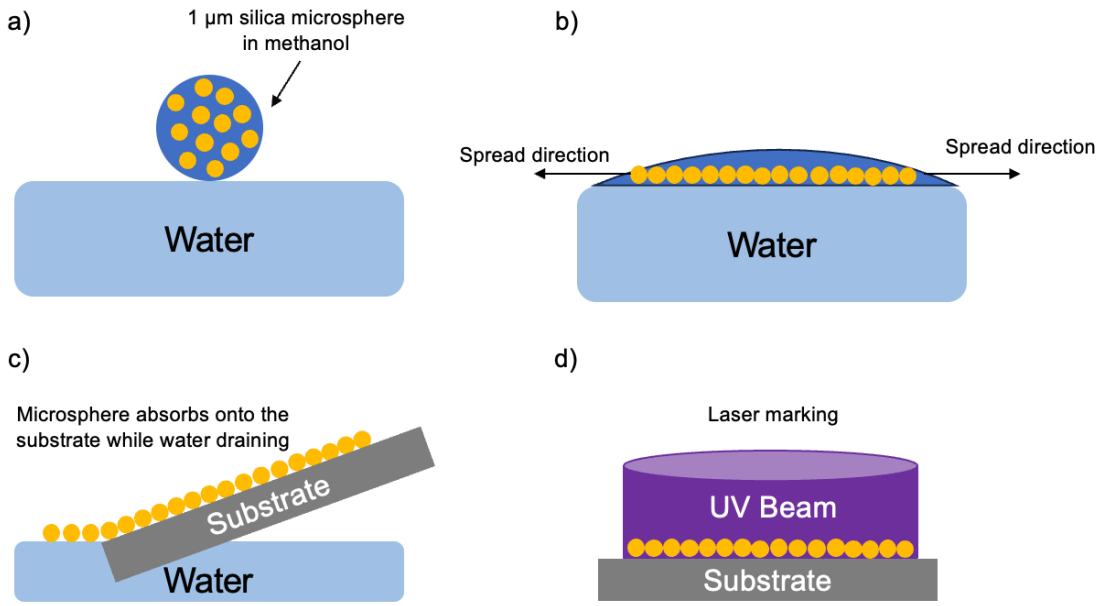

Figure 4.4-1 (a) – (d) Illustration of the preparation of silica monolayer.

The image provided exemplifies the successful application of the experimental setup described in figure 4.4-2, illustrating a large-area monolayer of microsphere arrays deposited on a glass substrate. This monolayer showcases a densely packed arrangement of microspheres, each approximately 1 µm in diameter, highlighting the effectiveness of the technique in achieving high-resolution, uniform surface coverage. The laser selectively interacts with the microspheres, engraving detailed, durable markings without disrupting the underlying substrate or the configuration of the microspheres. This method not only ensures high precision in particle deposition but

also contributes significantly to applications requiring precise patterns such as in advanced manufacturing and microfabrication technologies.

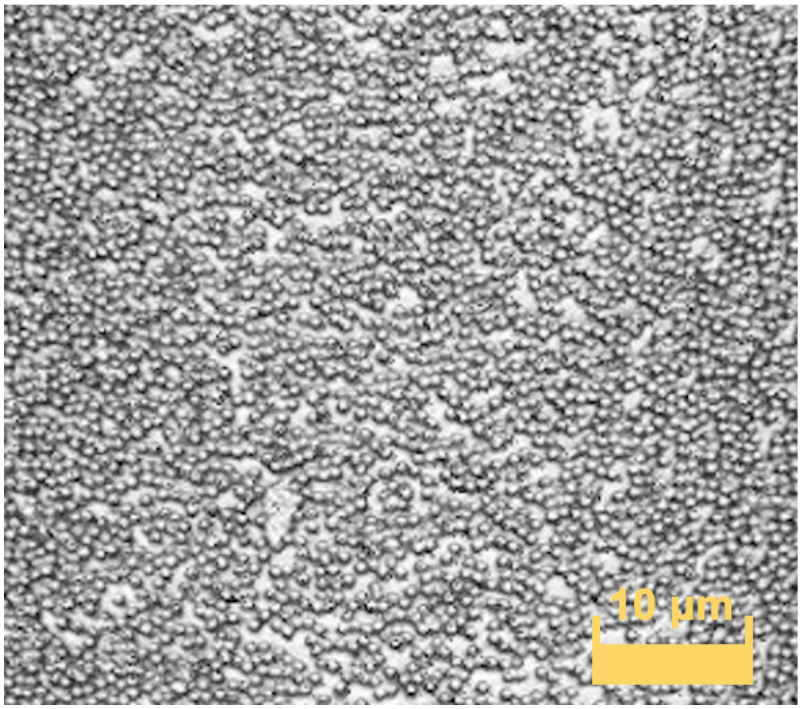

Figure 4.4-2 Confocal micro-image of prepared silica monolayer.

4.4.2 Superlens-assisted DotCode marking

Figure 4.4-3 delineates the progressive evolution of marking technology from basic laser text marking to more advanced micro and nano DotCode systems, facilitated by superlens technology. Initially, the process begins with standard text marking, such as the word "Bangor," using conventional-lens-based laser techniques that provide the first level of security. This is then transformed into a more secure Micro DotCode format, which consists of a series of black dots arranged to form a specific pattern. These dots are larger and visible to the naked eye. The security level is further enhanced as the Micro DotCode transitions into a Nano Two-level DotCode, where each dot comprises multiple smaller dots arranged in a distinctive pattern.

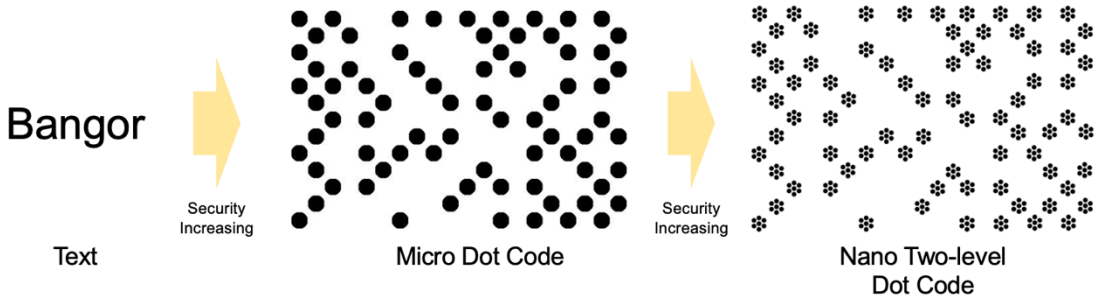

Figure 4.4-3 Conventional-lens-based laser text to micro DotCode and to nano DotCode marking by superlens.

This advanced technique not only raises the security bar against counterfeiting but also meets the demand for low-cost solutions in security marking technologies. By employing a superlens-assisted marking technique, it is possible to intricately and efficiently mark materials at a microscopic level, thereby providing a robust anti-counterfeiting measure that integrates seamlessly into existing production processes. This approach is particularly advantageous for industries requiring high levels of authenticity and traceability, offering a scalable and effective solution to safeguard products against illicit replication.

The detailed experimental setup designed to create a large-area monolayer of microsphere arrays on a glass substrate using advanced laser marking technology is shown in figure 4.4-4. The core component of this setup is a 355 nm UV laser, which operates at a repetition rate of 50 kHz, enabling precise and efficient marking. This UV laser beam is directed through a series of optical components to enhance its accuracy and focus. The laser beam first encounters a galvo-scanner, which is instrumental in dynamically steering the laser beam across the target surface. The galvo-scanner's ability to rapidly adjust the beam's position allows for quick and precise patterning over large areas, essential for creating uniform microsphere monolayers. After the galvo-scanner, the laser beam is further refined as it passes through a F-theta field lens with field size 110 mm * 110 mm. This lens focuses the UV laser light precisely onto the microsphere monolayer that is evenly distributed on

the glass substrate beneath.

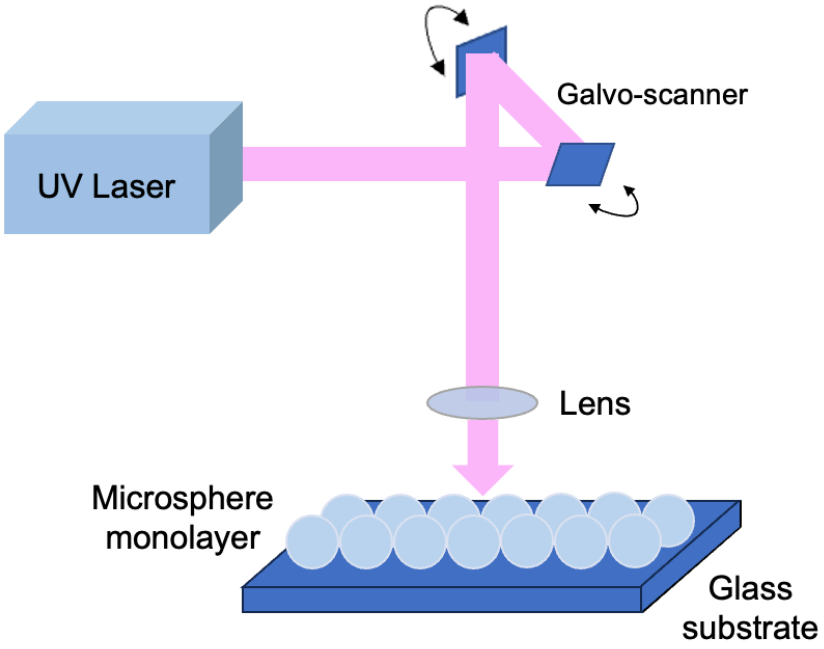

Figure 4.4-4 Schematic of the experimental setup with UV nanosecond laser source to process a large-area monolayer of microsphere arrays on a glass surface sample.

This setup is crucial for the deposition process as it ensures that the UV laser can interact accurately with the microsphere monolayer, engraving or altering the microspheres at a microscopic level to achieve desired patterns or features. The configuration of the UV laser, coupled with the galvo-scanner and focusing lens, forms an integral part of a superlens-assisted marking technique that not only meets the demand for low-cost solutions but also offers high precision and scalability in microsphere array production.

The images shown in figure 4.4-5 illustrate the results of a precision laser marking process applied to a sample, where "Bangor University" was encoded using a DotCode pattern. This marking was achieved using a particle superlens, with the laser energy set to 1.796 W as measured by the power meter (see Figure 3.3.2). Given that

the repetition rate and spot size of the UV laser system are 50 kHz and 50 µm, respectively, the fluence was calculated to be 1.83 J/cm². In figure 4.4-5a, the image depicts the overall pattern of the DotCode, characterized by a high contrast between the areas processed by the laser (appearing in black) and the unprocessed areas (in gray), demonstrating a sharp and clear delineation of the encoded data. The scale marked on the image indicates that the field of view spans 5 micrometers, providing a macroscopic perspective of the patterning. Zooming into a detailed section of this pattern, figure 4.4-5b provides an atomic force microscopy (AFM) image with a significantly enhanced resolution. Here, individual laser-processed spots are shown to contain clusters of nanoholes, each approximately 180 nm in size. These nanoholes were formed by the focused effect of the particle superlens, which likely facilitated the precision and miniaturization of the features within the DotCode. The scale here shows a more focused view at 500 nanometers, highlighting the microscopic level of detail achieved in the laser marking process.

Figures 4.4-5c and 4.4-5d from the study present the variations in the dimensions of nanoholes created by varying laser fluences, ranging from 1.42 to 1.83 J/cm². These graphs summarize the measured changes in both the width and depth of the nanoholes as influenced by different energy levels. In figure 4.4-5c, the graph illustrates the changes in the width of the nanoholes, measured at Full Width at Half Maximum (FWHM). The data points show a relatively steady width at lower fluences, but as the fluence approaches 1.8 J/cm², there is a noticeable increase in width, climbing sharply from around 160 nm to nearly 180 nm. The error bars associated with each data point suggest a variability in the measurements, estimated between 10 to 20 nm, which might be attributed to factors such as laser stability or material inconsistencies. The depth of the nanoholes under the same conditions is shown in figure 4.4-5d. This graph depicts a more consistent upward trend as the laser fluence increases. Starting from approximately 140 nm at the lowest fluence, the depth steadily increases, reaching about 180 nm at the highest fluence. The error bars here also indicate a variation in the depth measurements, which, although consistent

across the fluence range, show a similar variability as observed in the width measurements.

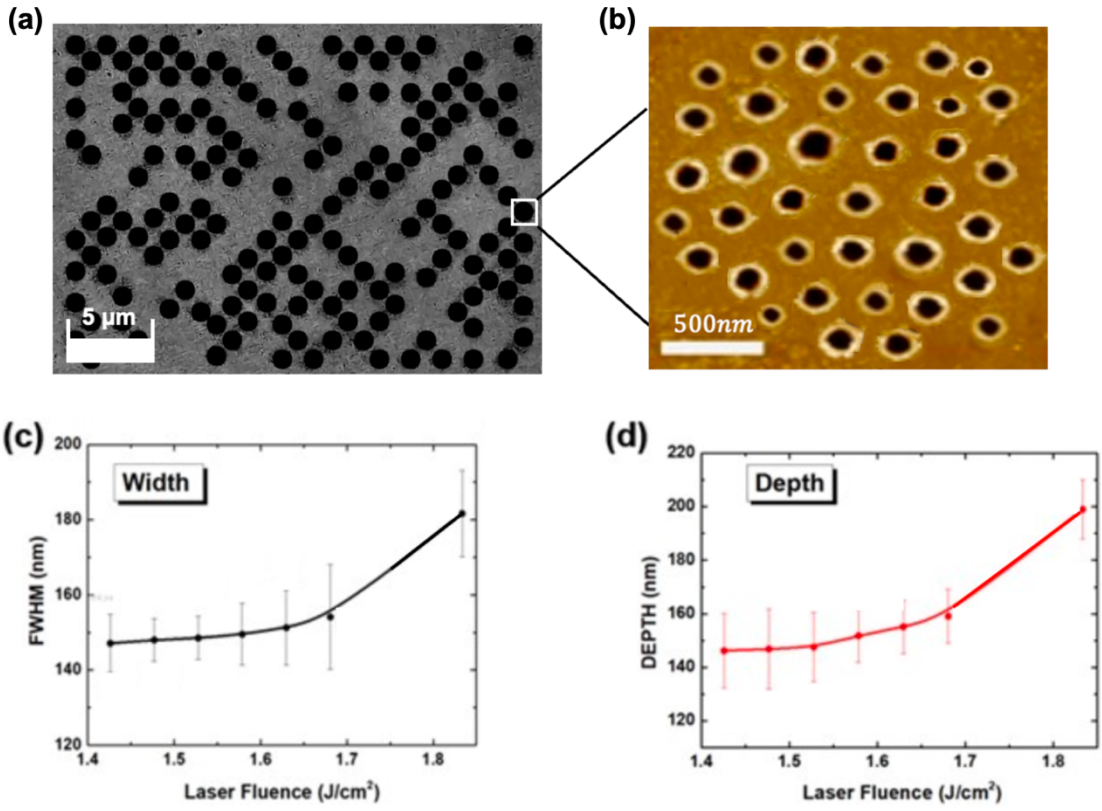

Figure 4.4-5 DotCode 'Bangor University' superlens nano marking by UV laser. (a) Microscope, (b) AFM image marking at 1.83 J/cm^2 laser fluence. (c) Width of nanoholes at FWHM. (d) Depth of the nanoholes.

These observations collectively highlight a direct relationship between the laser fluence and the dimensional properties of the nanoholes. The increase in both width and depth with higher fluences can be attributed to the greater energy input from the laser, which likely causes more extensive material ablation or melting, thereby enlarging the holes. This data is crucial for optimizing laser processing parameters in applications requiring precise control over micro and nano-scale features.

4.5 Chapter summary

This chapter explores advanced laser direct writing techniques, showcasing strides in material science and optical engineering. A low-cost, nanosecond UV laser method is introduced for creating graphene patterns on PBI thin films and glass substrates, avoiding thermal damage and the need for metallic precursors, and producing graphene as confirmed by Raman spectroscopy. This scalable, cost-effective approach enhances graphene production. Additionally, a straightforward and rapid method for designing and fabricating high-accuracy micro FZPs on thin films compensates for excess material removal, ensuring the precise replication of design parameters and achieving excellent focusing effects with both even and odd types of FZP lenses. The correlation between theoretical expectations and measured focal lengths and focus widths highlights this method's potential for cost-effective optical component microfabrication. Finally, a novel laser-based anti-counterfeiting technology utilizing a particle superlens creates subwavelength nanoscale holes, enhancing security beyond traditional laser marking methods. Using 1 μm silica microspheres and a 355 nm UV laser, this technique adds a robust layer of protection to the DotCode scheme.

These innovations highlight the versatility and precision of conventional-lens-based laser manufacturing technologies, addressing emerging needs in microfabrication and security while adhering to broader trends in cost-efficiency and scalability. Additionally, they establish a foundation for further research on superlens-assisted laser manufacturing in subsequent chapters.

Chapter 5.
Superlens-based Laser Nanostructuring of Optical Fiber Grating Sensor

5.1 Introduction

Over the past few decades, we have witnessed significant growth and prominence of optical fiber grating sensors in various fields, including pharmacy, life sciences, security, food industry, and environmental monitoring. The development of optical fiber sensing technology is driven by its recognized advantages, such as its compact size, lightweight nature, immunity to electromagnetic interference, exceptional sensitivity, real-time monitoring capabilities, and the ability to multiplex[126–129], etc. Optical fiber grating sensors, as an important category of optical fiber sensors including FBG and LPG sensors, are based on the fundamental principle of leveraging evanescent fields created by the propagation of light within fiber-based devices and their interaction with the surrounding environment and media[130]. In the aspect of applications, FBGs are normally used for temperature and strain sensing, and LPGs work for refractive index sensing and monitoring of chemical processes most of the time[131]. The LPG gratings consist of periodic changes in the RI of fiber core, causing coupling between the core mode and co-propagating cladding modes and the resonance bands in the transmission spectrum. Each resonance band corresponds to a different cladding mode and offers varying sensitivity to environmental changes[132]. The RI sensitivity of LPGs is determined by the effective RI of the cladding modes. This effectiveness, in turn, depends on the contrast between the RIs of the cladding and the surrounding medium. Typically, the highest sensitivity of LPGs is achieved when the RI of the surrounding medium closely matches that of the cladding[133].

Various technologies have been employed to enhance the RI sensitivity of LPG sensors. These include the deposition of uniform thin-film coatings, such as PVA (Poly(vinyl

alcohol))[134], PDMS (Polydimethylsiloxane)[135], polyimide[136], graphene[137], graphene oxide[138], and Zn/ZnO[139], as well as nanoparticle coatings[140–142], and nanoparticle-embedded composite coatings[143,144]. Among the various methods for applying coatings to LPGs, the Layer-by-Layer technique is notable due to its outstanding capability to precisely control both the thickness and composition of nanoparticles in the resulting thin films. This versatile method enables the monitoring of a wide range of substances, including ethanol[145], ammonia[96], and low molecular analytes[146].

In this chapter, we propose a novel approach to enhance the RI sensitivity of LPG sensors. This involves employing the technology of direct laser nanostructuring of the surfaces of LPGs, assisted by microsphere superlenses that are coated onto the LPG surfaces. This results in the formation of nanohole-structured LPGs (NS-LPGs). The use of microsphere lenses as optical superlenses for nanoscale sub-wavelength patterning, imaging, and sensing has been an active research area since 2000 where we carried out the pioneering work[147]. The patterning resolutions of 80-400 nm and imaging resolutions of 45-100 nm were reported in the literature[89,148,149], but no reports exist on microsphere-assisted nanostructuring of the fiber surface of LPG sensors to create NS-LPG sensors. In our experiments, we used a dip coating technique to apply a monolayer of silica microspheres across the entire surface of the optical fiber[150]. Subsequently, a pulsed UV laser system was used to ablate nanoholes on the surface of the fiber. The microsphere monolayer act as a focusing lens array, enabling the creation of numerous nanoholes. The RI sensing performance of the fabricated NS-LPGs were tested in both sucrose and glycerin solutions, and their efficiencies were compared with those obtained by standard LPG sensors. Our results indicated that the NS-LPG sensor can deliver higher sensitivity than the conventional LPG sensor. Also, we investigated the influences of nanohole density on sensing performance, finding that higher nanohole density can further improve sensitivity of NS-LPG.

5.2 Experiments of fiber grating sensing

This section delves into the capabilities of optical fiber grating sensing by conducting a series of current existing sensing experiments. The focus is primarily on two types of gratings: FBG for temperature measurements and LPG for monitoring variations in the surrounding RI. These experiments are methodically designed to evaluate the viability and effectiveness of optical fiber gratings for advanced sensing applications across various environmental conditions. The experimental outcomes provide invaluable data for the development and enhancement of superlens-based laser nanostructuring technologies. These technologies are being integrated into precision sensing frameworks with the aim to significantly improve the sensitivity and specificity of the gratings. This enhancement is expected to facilitate finer detection capabilities and more accurate measurements, thereby expanding the utility of optical fiber sensors in highly specialized fields such as biomedical applications, environmental monitoring, and industrial process control.

5.2.1 FBG temperature sensing

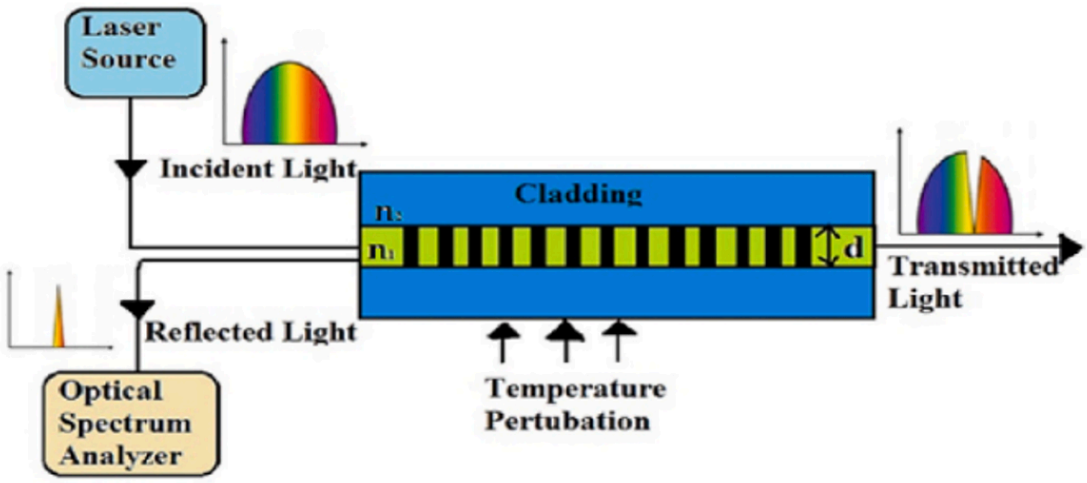

Figure 5.2-1 Schematic of FBG temperature sensing setup[151].

The experimental setup described herein incorporates several components, as outlined in Chapter 3, and is further detailed in figure 5.2-1. Central to the setup is the SUPERK COMPACT Supercontinuum white light laser system, which provides a broad spectrum of light necessary for high-resolution measurements. Additionally, the Anritsu MS9740B Optical Spectrum Analyzer is employed to carefully analyze the optical spectra obtained during the experiments. Key elements of the sensor apparatus include the TP-01 FBG sensor from FBGS, which features a Bragg wavelength of 1560 nm and is designed to measure temperatures ranging from -20 to 110 ℃. This sensor is critical for capturing precise temperature fluctuations within the experimental framework. Complementing the FBG sensor is a 1550 nm optical circulator from Thorlabs, which is used for routing the reflected spectrum back to the detection equipment.

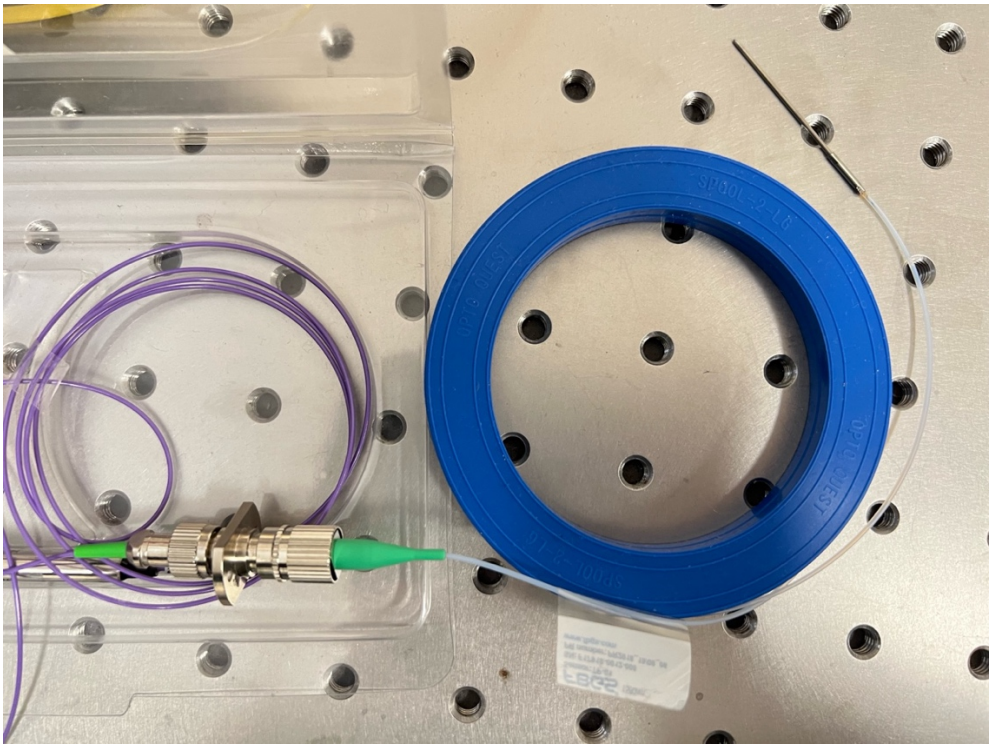

Figure 5.2-2 FBG sensor with temperature probe connected with circulator.

As illustrated in figure 5.2-2, features the FBG sensor equipped with a temperature

probe, which is connected to an optical circulator. For the purpose of this experiment, a beaker filled with water at varying temperatures ranging from 30 to 100 °C is utilized to test the sensor's responsiveness. When the FBG probe is immersed in the water, the key observation is the behavior of the reflection spectrum: specifically, the peak of the reflection spectrum shifts in response to changes in temperature. This shift is characterized by a red shift in the peak as the temperature of the water increases. This phenomenon is important for understanding how the FBG sensor responds to temperature changes, offering insights into the dynamics of optical behavior under varying thermal conditions.

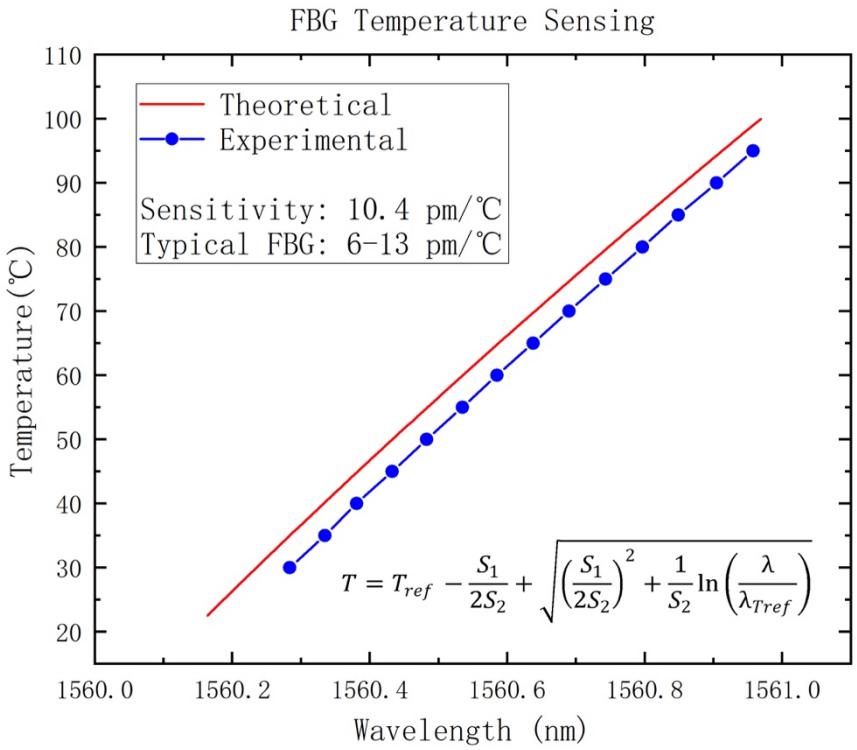

Figure 5.2-3 Relationship between FBG Bragg wavelength shift and temperature.

Figure 5.2-3 presents a comparison between theoretical and experimental results for FBG temperature sensing. The theoretical curve, provided by the supplier FBGS, is

aligned closely with the experimental data, which demonstrates a linear relationship with sensitivity of 10.4 pm/°C. This sensitivity falls within the typical range for Fiber Bragg Gratings, which is usually between 6 to 13 pm/°C. The graph plots temperature against wavelength shift, showing a linear relationship as expected. As the temperature increases, there is a clear red shift in the Bragg wavelength, confirming the theoretical predictions. The close match between the theoretical and experimental results not only validates the experimental setup but also underscores the reliability of the FBG sensor used in this study for accurate temperature measurements.

5.2.2 LPG surrounding liquid refractive index sensing

In another fundamental experiment, LPG sensors are utilized to measure the RI of various surrounding mediums. Different concentrations of sugar solutions were used in the experiment. Unlike the setup for FBG sensors, the LPG experiments do not require an optical circulator, as the focus is solely on analyzing the transmittance spectrum. The LPGs used in the experiment has a central wavelength of 1555/1550 nm, a grating period of 550 μm, and a grating length of 20 mm. The experimental arrangement, depicted in figure 5.2-4, involves immersing the LPG grating area completely in the sugar solutions to ensure adequate exposure to the test medium.

As outlined in Chapter 3, varying sugar concentrations result in different refractive indices of the solutions, which in turn influence the behavior of the transmitted light through the LPG sensor. Specifically, as the sugar concentration in the solution increases, the refractive index also increases. This change causes a blue shift in the peak of the LPG transmission spectrum. This shift is indicative of the relationship between the concentration of the solution and its optical properties, providing a clear, measurable response in the LPG sensor output.

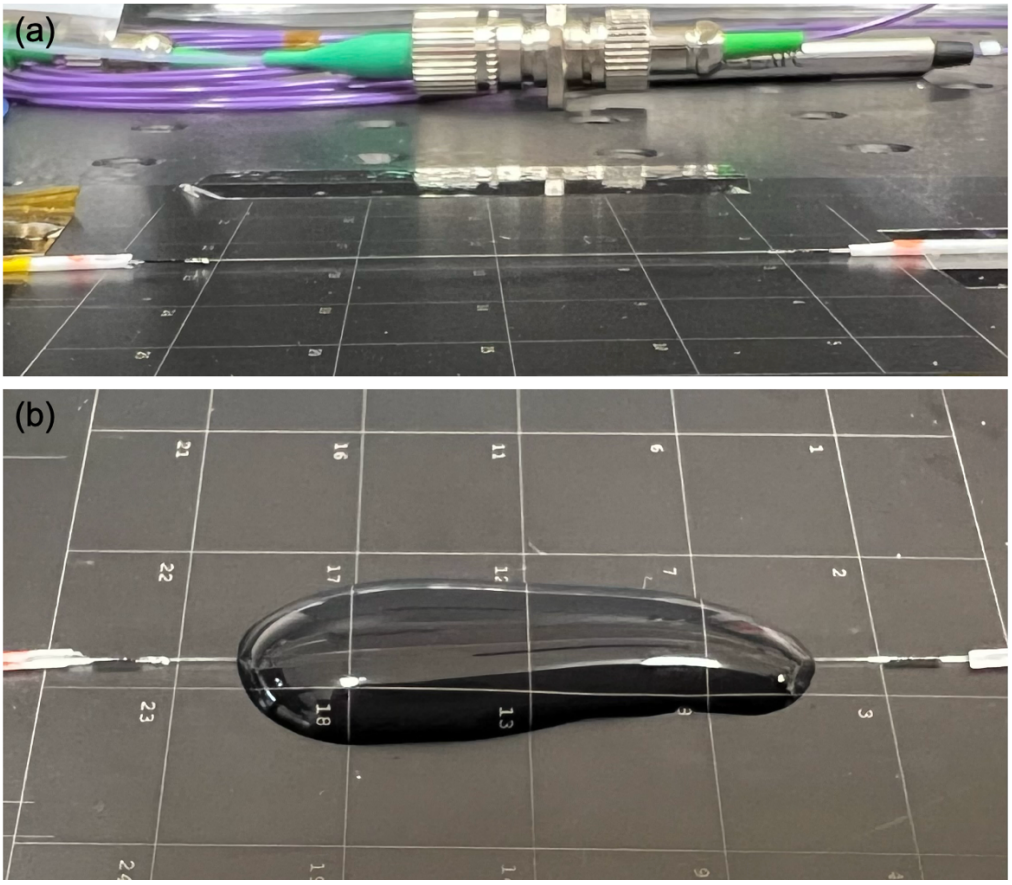

Figure 5.2-4 (a) LPG grating area. (b) LPG grating area with sugar solution immersing.

In contrast to the linear relationship observed in FBG temperature sensing, the sensitivity of Long Period Grating (LPG) sensors to changes in the refractive index (RI) of the surrounding medium exhibits more complex behavior. The sensitivity of LPGs increases as the refractive index of the surrounding medium approaches that of the cladding material. This heightened sensitivity results from the enhanced interaction between the core and cladding modes at closer refractive indices.

However, there is a limitation to consider: if the RI of the ambient medium surpasses that of the cladding, the typical sensing behavior of the LPG is disrupted, and the previously observed relationships no longer apply. This phenomenon highlights that within the RI range of approximately 1.4 to 1.45, LPG sensors exhibit exceptionally

high sensitivity, making them particularly useful for precise measurements within this specific range.

The detailed experimental outcomes demonstrating these dynamics will be discussed in the subsequent section. These results will also serve as a baseline for evaluating the effectiveness of superlens-assisted laser nanostructuring techniques applied to LPGs, aiming to enhance their performance and expand their applicability in more complex sensing scenarios.

5.3 Superlens-assisted laser nanostructuring of LPGs for enhanced RI sensing

5.3.1 Materials

Chemicals: Chemical reagents were sourced from established suppliers: Potassium hydroxide (KOH, 56.11 g/mol), poly(diallyl dimethylammonium chloride) (PDDA, 200k-350k molecular weight, 20 wt% in water), high-purity sucrose (≥ 99.5%), and glycerol (≥ 99.5%) were all obtained from Sigma-Aldrich (UK). Deionized (DI) water used in the experiments was from Thermo Fisher Scientific Inc. (UK). Different concentration solutions were prepared with DI water, and reagents were used as received, without further purification.

Microspheres: Colloidal silica microspheres with a diameter of 1 micrometer, a concentration of 50 mg/ml, and a coefficient of variation (CV) less than 3% were procured from ALPHA Nanotech Inc. (United Kingdom).

LPGs: Long Period Fiber Gratings with a cladding diameter of 125 µm, core diameter of 8.2 µm, grating length of 20 mm, and grating period of 550 µm were sourced from oeMarket (Australia). These were fabricated from single-mode fiber (SMF-28).

5.3.2 Deposition of microsphere monolayer

The dip coating method was used to deposit a silica microsphere monolayer onto the LPG surface, using the Type G Ossila Dip Coater from Ossila, UK. The solutions included 5 wt% ethanolic KOH (ethanol/water = 3:2 v/v), 10 wt% PDDA in DI water, and 10 wt% silica microspheres in DI water. The LPG was attached to a dip coater holder, and then rinsed and cleaned with DI water and ethanol, respectively. It was immersed in the 5 wt% KOH solution for 20 minutes to produce a negatively charged surface. This was followed by submersion in a 10 wt% PDDA solution for an additional 20 minutes, succeeded by the 10 wt% silica microspheres solution. After these steps, the LPG was air-dried at 50℃ for an hour using a hotplate (Fisher Scientific Heater) to facilitate the deposition of the silica microsphere monolayer[88,95,152] (Fig. 5.3-1a). The dip and withdrawal speeds were consistently set at 50 mm/min and 2 mm/min, respectively. The microsphere-coated LPG sample was characterized using an advanced optical microscope (Olympus DSX1000) and a laser confocal microscope (3D Measuring Laser Confocal Microscope OLS5000).

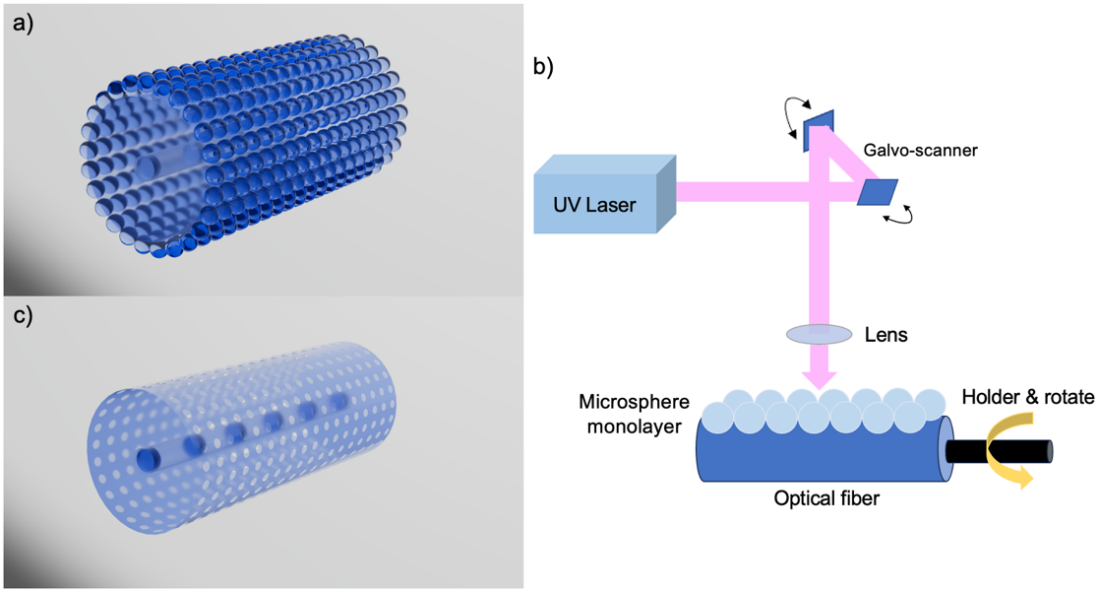

Figure 5.3-1 Schematic of the experimental processes. (a) Microsphere coating on LPG, (b) Laser processing, (c) Nanoholes fabricated on LPG.

5.3.3 Nanohole generation

As previously mentioned, microspheres can function as superlenses, focusing light to sub-wavelength spot sizes[94,150,153]. In our experiments (Fig. 5.3-1), a pulsed UV nanosecond laser beam (Guoke Laser, GKD-C40C20B, power: 10-Watt, wavelength: 355 nm, pulse duration: 100 ns, repetition rate: 50 kHz, spot size: 50 µm) was directed onto the microsphere-coated LPG sample and precisely scanned across it using a Galvo scanner at a speed of 100 mm/s (Fig. 5.3-1b). Following the laser treatment, nanoholes appeared beneath each microsphere, and most microspheres were removed due to the laser ablation process and the thermal expansion it caused. Therefore, it is necessary to rinse off any remaining particles after the initial pass and then recoat the particles across the entire fiber surface before conducting a second pass of laser exposure. It is noted that the fiber sample is represented by a cylinder in the diagram. To ensure processing the entire surface of the LPG, the LPG sample needed to be rotated after each pass, facilitated by a specially designed rotational holder. It is important to mention that the laser power was carefully controlled at approximately 0.53 J/cm^2 to prevent damage to the LPG grating within the fiber areas not covered by microspheres. This assurance stems from laser exposure tests conducted on standard LPG samples before applying microsphere coatings, where consistent sensing performance was observed before and after laser exposure, indicating no damage to the grating. In the experiments, two sets of nanohole densities were compared: sample LPG1 involved a single pass of microsphere deposition and laser processing, while sample LPG2 experienced double passes of microsphere deposition and laser processing for a larger nanohole density. Although this process can be repeated to further increase nanohole density, our study focuses on single-pass and double-pass processing only. For simplifying comparison, the unprocessed original LPG sample was referred to as LPG0, as shown in table 5.3-1. The nanostructured LPG samples were characterized using various imaging techniques, including dark field microscopy, scanning electron microscopy (SEM, Hitachi TM4000Plus) and atomic force microscopy (AFM, Veeco Dimension 3100/V).

Sample	Description	Hole Density, *D* (hole area/total surface area)
LPG0 (S1, S2)	Original, non-processed LPG. S1: LPG0 for single-pass S2: LPG0 for double-pass	0%
LPG1	Single-pass processed LPG	5%
LPG2	Double-pass processed LPG	7.9%

Table 5.3-1 List of samples.

5.3.4 Refractive index sensing

The RI of solutions varies with concentration, with distinct RIs for each solute[154]. LPG sensors detect RI shifts, especially within the range of the RIs of water between 1.33 to 1.46 which is slightly smaller than that of cladding. LPG sensitivity can increase as the ambient RI approaches the RI of the cladding[116]. The laser-processed NS-LPGs are used to test the RIs of the solutions of varying concentrations of sucrose (0-70 wt%) and glycerin (0-90 wt%) in this study.

Our experimental setup illustrated in figure 5.3-2, utilized a broadband light source (BBS, NKT Photonics SuperK COMPACT) connected to an optical spectrum analyzer (OSA, Anritsu MS9740B) via NKT Photonics SuperK Fiber Delivery. After each immersion, the LPG was cleaned and dried to ensure consistent readings and prevent contamination.

The response of the LPG is influenced by the RI of the surrounding material. These changes can tune the spectral output of LPG, as the wavelengths of light attenuation depend on the effective RI of the cladding mode[133]. The LPG transfers of light from the core to specific cladding modes. Within the cladding, light diminishes due to

scattering, leading to observable loss bands in the core output[114].

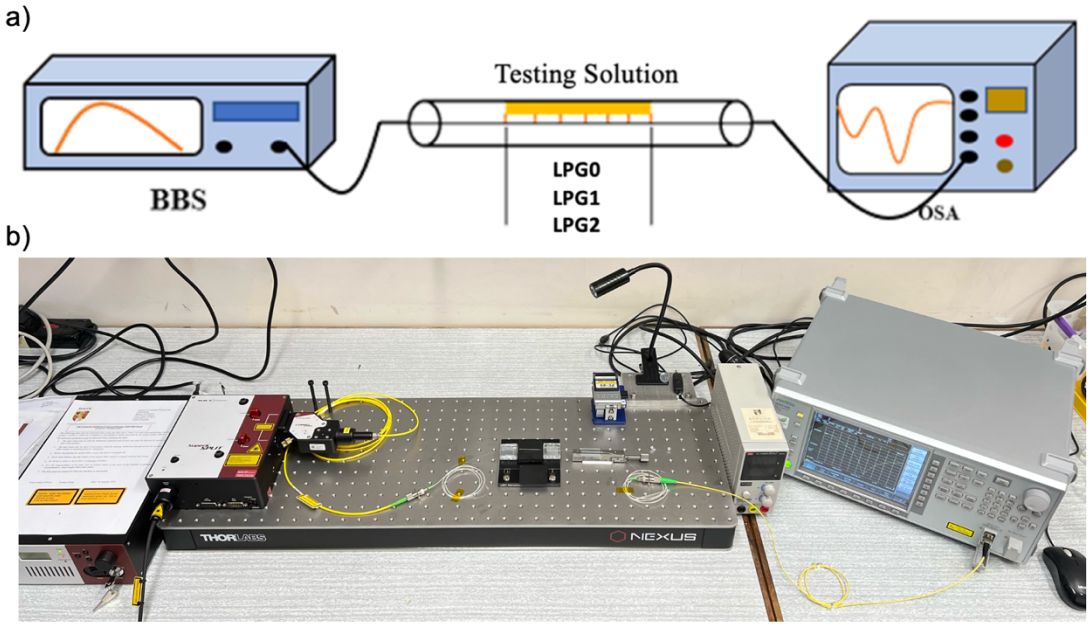

Figure 5.3-2 Experimental setup for sensing testing. (a) Schematic representation, (b) Photograph of the setup.

5.3.5 Morphology of microsphere-coated LPG

Figure 5.3-3 presents a detailed analysis of the surface morphology of LPGs coated with a monolayer of silica microspheres. Dark field optical images in figure 5.3-3a emphasize the efficient alignment and uniform distribution of microspheres across the fiber surface. The coating process achieved extensive coverage with approximately 95% of the surface area of the fiber. In figure 5.3-3b, the 3D confocal image illustrates the arrangement of microspheres on the curved surface of the LPG. Notably, the monolayer of the microspheres exhibits consistency of the uniform coverage across the entire curved surface of the LPG, rather than any irregular distribution. Figure 5.3-3c provides a close view of the monolayer-coated LPG, revealing the silica particles with the diameter of 1000 nm. This detailed view clearly demonstrates the silica

microparticles arranged in a hexagonal honeycomb pattern, despite defects that could exist within them.

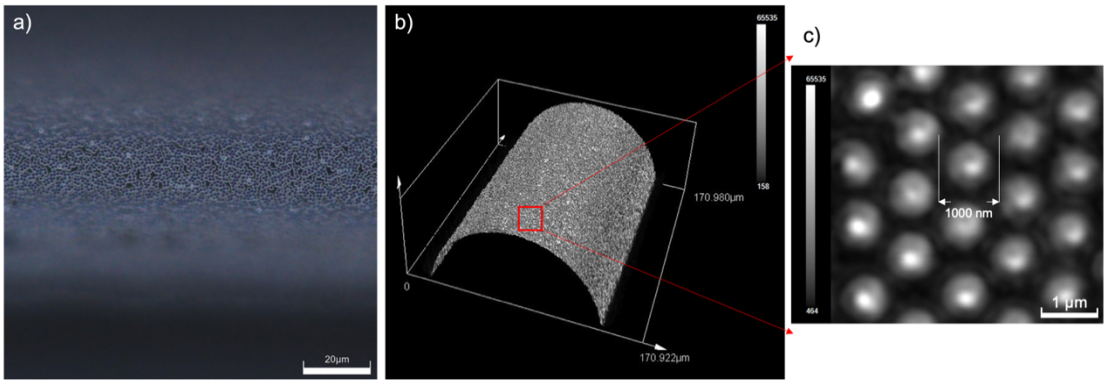

Figure 5.3-3 Microscopic images of the microsphere-coated LPG surface. (a) Dark field optical image, (b) 3D confocal image of the curved surface coated with microspheres, and (c) Magnified view of the microsphere array from (b).

5.3.6 Morphology of nanostructured LPG

Figure 5.3-4 illustrates the surface morphologies of LPG1 and LPG2 samples, following superlens-assisted laser nanostructuring for single-pass and double-pass, respectively. Nanoholes are clearly visible in dark-field optical microscopy (Fig. 5.3-4a). The zoomed SEM (Fig. 5.3-4b) and AFM images (Fig. 5.3-4c-d) reveal that these nanoholes are in the circular shape, with the diameters ranging from 300 to 500 nm and the depths ranging from 60 to 120 nm. Compared to figure 5.3-3, the patterns depicted in figure 5.3-4 demonstrate a notable increase in size variation and the presence of more defects. This disparity primarily stems from the laser processing procedure rather than the quality of the microsphere array. Firstly, the use of a non-flat top Gaussian beam results in particles within the spot being exposed to varying energy levels. Secondly, fluctuations in the temporal output of the laser energy during experimentation can greatly influence the generation of nanoholes. Moreover, the curved surface of the

fiber impacts how laser energy is transmitted from the microsphere to the substrate at different surface points, consequently affecting nanohole quality. To mitigate these issues, employing a uniform laser beam, such as a flat-top beam by adding a beam homogenizer in the beam path is recommended to enhance nanohole quality and minimize defects in subsequent iterations of the process[155].

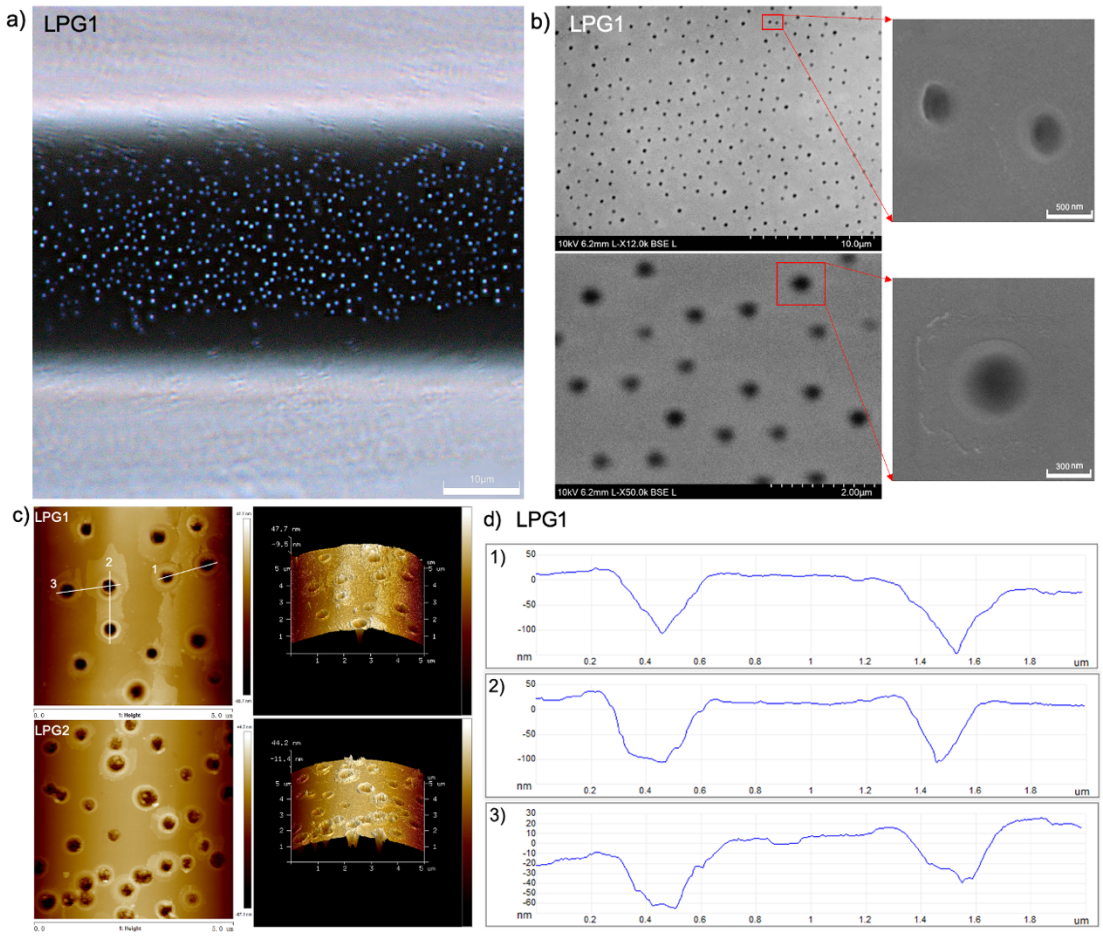

Figure 5.3-4 Surface morphologies of processed LPG1 and LPG2 samples. (a) Dark-field optical image of LPG1 sample. (b) SEM image LPG1 sample, (c) AFM images of LPG1 and LPG2 samples, (d) depth profile of the LPG1 sample in c.

Comparing the samples in LPG1 and LPG2, it is observed that the double-pass processing results in higher nanohole densities. The calculated nanohole densities,

defined as a ratio of the area with the generated nanoholes to the total surface area of the fiber, are approximately 5% for the LPG1 sample and 7.9% for the LPG2 sample. As noted earlier, after the initial laser processing pass, most microspheres on the fiber surface are ejected. Therefore, rinsing and reapplying them across the entire fiber surface before subsequent laser exposure rounds are crucial. This may lead to varied particle positions, causing uneven distribution and overlapping of resulting nanoholes (see LPG2 in Fig. 5.3-4c), but effectively increases nanohole density. Further density enhancement through repeated processing falls outside this study's scope but deserves future exploration.

5.3.7 RI sensitivity measurement

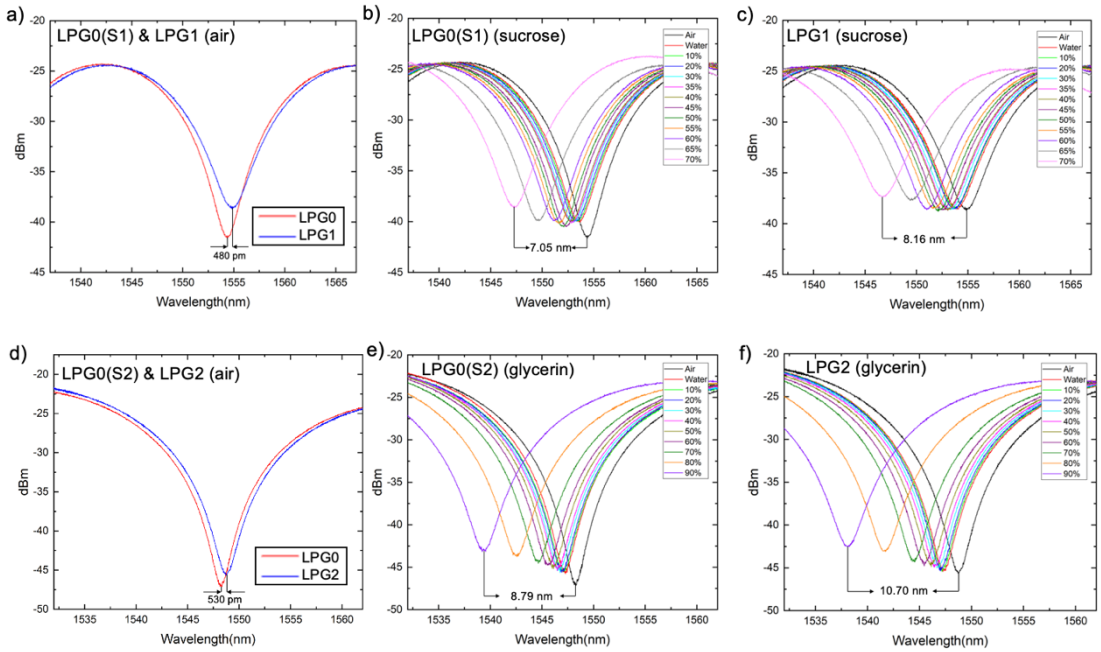

Figure 5.3-5 Transmission spectrum of (a) LPG1 in air, before and after nanostructuring, (b-c) LPG1 sensing of sucrose solution at various concentrations before and after nanostructuring, (d) LPG2 in air, before and after nanostructuring, (e-f) LPG2 sensing of glycerin solution at various concentrations before and after nanostructuring.

In a series of experiments, LPG1 with a 5% nanohole density was exposed to sucrose aqueous solutions with the concentration ranging from 0% to 70% (DI water). Figure 5.3-5a shows a significant red shift of 480 pm in the ambient air after nanohole structuring. The overall peak shift increased from 7.05 nm (unprocessed) to 8.16 nm (structured with nanoholes), representing a 15.7% total shift increase (Fig. 5.3-5b-c). For LPG2, featuring double-pass nanostructuring with a 7.9% nanohole density, the experiments involved the glycerin aqueous solutions with the concentration ranging from 0% to 90%. Figure 5.3-5d demonstrates a red shift of 530 pm in the ambient air following nanohole structuring. The total peak shift increased from 8.79 nm (unprocessed) to 10.70 nm, indicating a 21.7% total shift increase (Fig. 5.3-5e-f).

The red shifts of the peaks are attributed to the laser-generated nanoholes on the fiber, which lead to an increased surface contact area with enhanced light coupling between the cladding and the sensing medium. This will be considered in our model below, which differs from the classical model that uses a reduced cladding diameter[101,156].

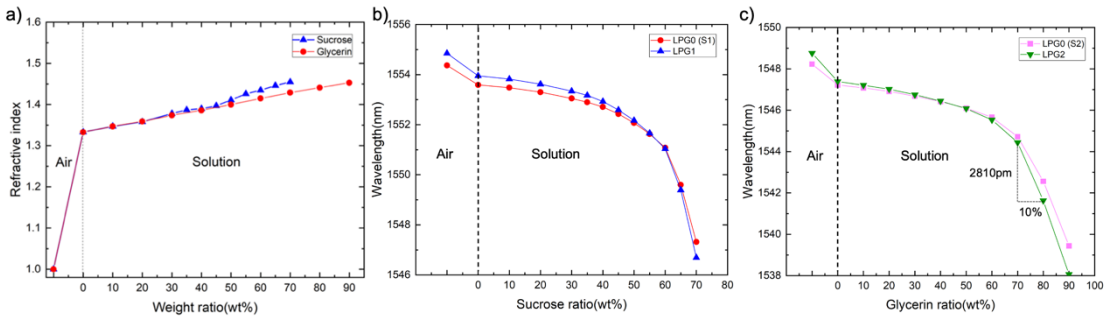

Figure 5.3-6 (a) Relationships between solution weight ratio and refractive index, (b) shifted peak locations of LPG0 (S1) & LPG1 at varying solution concentrations, (c) shifted peak locations of LPG0 (S2) & LPG2 at varying solution concentrations.

The relationship between the solution weight ratio and RI for both sucrose and glycerin aqueous solutions is shown in figure 5.3-6a, displaying linear characteristics in line with the results in[154]. Figure 5.3-6b & 5.3-6c presents the shifted peak locations of two

LPGs, indicating their response to different solution concentrations before and after nanohole structuring. The slopes of these curves represent RI sensitivity, a critical sensing parameter that improves as the surrounding RI approaches the cladding material's RI[116]. The RI sensitivity is defined by the slope which is calculated by delta wavelength / delta weight ratio, giving a non-linear relationship. As an example, the sensitivity of LPG2 under glycerin concentration between 70% and 80% is 281 pm/% shown in figure 5.3-6c. The results of both LPG1 and LPG2 samples clearly demonstrate an improvement in slope, reflecting enhanced sensitivity after nanostructuring. The results also demonstrate that nanostructured LPG1 and LPG2 samples exhibit higher sensitivity compared to their original counterparts, as depicted in figure 5.3-7a and figure 5.3-7b, respectively. LPG1 shows the most significant sensitivity enhancement at 26.32% within the 35-40% sucrose weight ratio range (Fig. 5.3-7a), indicating an optimal concentration for maximum interaction between the cladding and the sensing medium. Also, figure 5.3-7b illustrates that LPG2's peak sensitivity increase is at 30.09% in the presence of a 70-80% glycerin weight ratio, suggesting a similar optimal concentration threshold for heightened response.

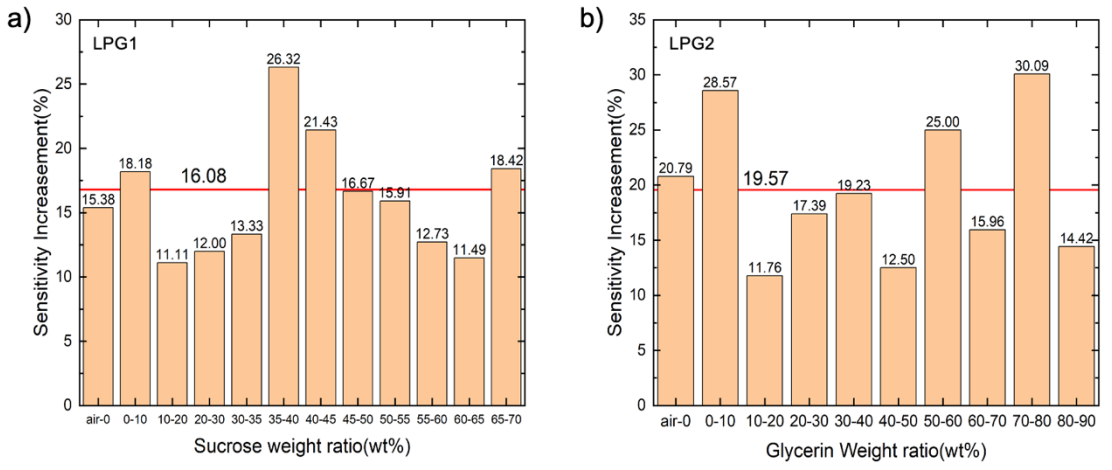

Figure 5.3-7 Sensitivity increase of (a) LPG1 for sucrose solution concentration interval, (b) LPG2 for glycerin solution concentration interval.

These experiments highlight the improved performance of nanostructured LPGs compared to the original unprocessed LPGs, with greater enhancements observed in structures with higher nanohole density. The increased total peak shifts indicate the improved performance of nanostructured LPGs and their potential for various optical and sensing applications. Ongoing efforts are focused on refining methods to achieve even higher nanohole density samples, thereby further advancing the sensitivity of nanostructured LPGs in applications based on the RI measurements. Moreover, the nanostructured surface may offer a novel avenue for interacting with sensing samples. For instance, virus particles or drug nanoparticles could potentially be entrapped within nanoholes, enabling detection.

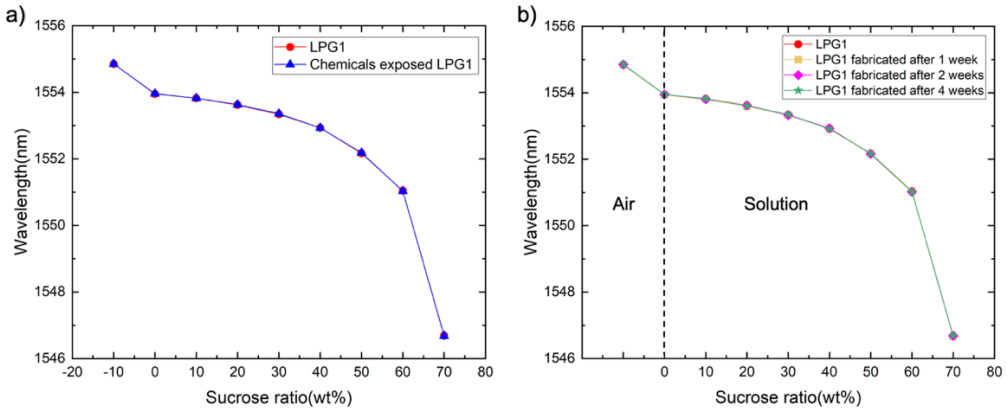

Figure 5.3-8 LPG1 sucrose solution sensing performance. (a) Comparison of wavelength responses of LPG1 before and after exposure to chemicals at varying sucrose concentrations. (b) Repeatability of LPG1 wavelength responses measured after fabrication time intervals of 1, 2, and 4 weeks.

We conducted durability tests on nanostructured LPG1 sensors in diverse environmental conditions, including exposure to chemicals such as acetone, methanol, and xylene. As shown in figure 5.3-8a, the nanohole-structured LPG1 maintained consistent sensing performance, with no significant degradation in wavelength response after chemical exposure. In contrast, surface-coated LPGs, such as those

using polymethyl methacrylate (PMMA), were prone to damage during these tests, with the coatings being removed, degraded, or losing sensing functionality. Figure 5.3-8b further highlights the robustness of the nanostructured LPG1, demonstrating repeatable and stable sensing performance over time, even after prolonged intervals. These results emphasize the superior durability and reusability of nanostructured LPG1 compared to coated counterparts.

The fabrication process consists of two main steps: microsphere dip-coating and laser processing. In the first step, microspheres are deposited onto the surface of optical fibers via a dip-coating method. Experimental results demonstrate that the coating quality is both repeatable and consistent, provided that key environmental parameters—such as coating solution concentration, ambient temperature, and dipping-coating speed—are carefully maintained. Under these controlled conditions, uniform microsphere layers were consistently achieved across multiple coating batches.

The dip-coating process typically requires approximately 20 minutes per batch, with a dipping speed of 50 mm/min. Crucially, this step supports parallel processing, enabling multiple fibers to be coated simultaneously within the same solution bath. In the second step, laser nanostructuring is applied to the coated fibers. This stage is also readily scalable, as multiple fibers can be processed in parallel using a uniform flat-top beam configuration. Together, these two steps form a fabrication workflow that is highly amenable to high-throughput production and scalable deployment of nanostructured optical fiber sensors.

5.3.8 Modelling and simulation

To advance the understanding of the sensitivity characteristics of nanostructured LPGs, we have refined an existing MATLAB computational model based on the coupled mode theory relevant to optical fiber waveguides[101,156]. This enhanced model, named

the ‘K2-model’, accurately computes the transmission spectra for LPGs, facilitating a comprehensive investigation into the correlation between spectral peak shifts within optical fiber waveguides and the dynamic RI changes in the surrounding medium. The model expresses the LPG transmission as follows:

$$T = cos^2\left(\sqrt{K_2^2 + K_1^2}\cdot L\right) + (K_1^2/(K_1^2 + K_2^2))\cdot sin^2\left(\sqrt{K_2^2 + K_1^2}\cdot L\right)$$

(5.3-1)

In this expression, $K_1 = \delta + \frac{1}{2}\kappa_1$, with δ as the self-detuning coefficient as outlined in reference[107], and $K_2 = \alpha\,\kappa_2$, where α is the newly introduced parameter for this work termed the 'κ_2 enhancement factor'. κ_1 and κ_2 are the light coupling coefficients of core and cladding, respectively (see Fig. 5.3-9a). The term L denotes the grating length. The ‘κ_2 enhancement factor', α, is the principal modification to the existing model in[101]. This factor is a measure of the nanohole density (D) and the light scattering efficiency (S) by the nanoholes at the cladding/medium interface, and is given by the relationship:

$$\alpha = 1 + S\cdot D$$

(5.3-2)

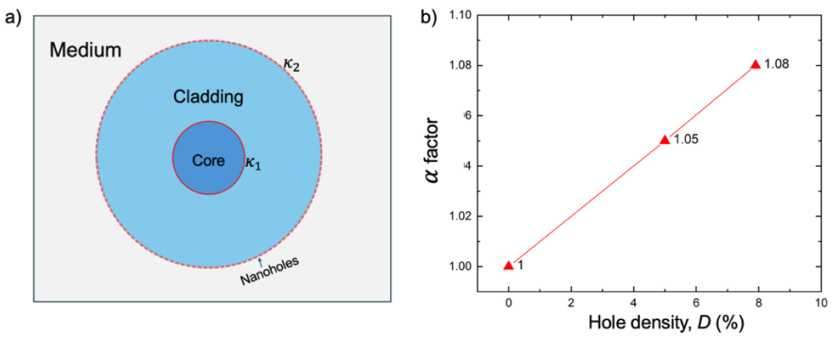

Figure 5.3-9 (a) Schematic of modelling geometry (not to scale) and (b) α, the enhancement factor of K_2, as a function of hole density.

The integration of α is vital as it captures the primary effect we observed in nanostructured LPGs. For our analysis, S is estimated at 1.01, with D at 5% for LPG1 and 7.9% for LPG2. The simulation replicates the parameters of the experimental LPGs, with a cladding diameter of 125 µm, core diameter of 8.2 µm, grating length of 20 mm, and a grating period of 550 µm. Particular attention is given to the peak with the highest sensitivity to RI changes, which is emphasized by the nanostructured surface.

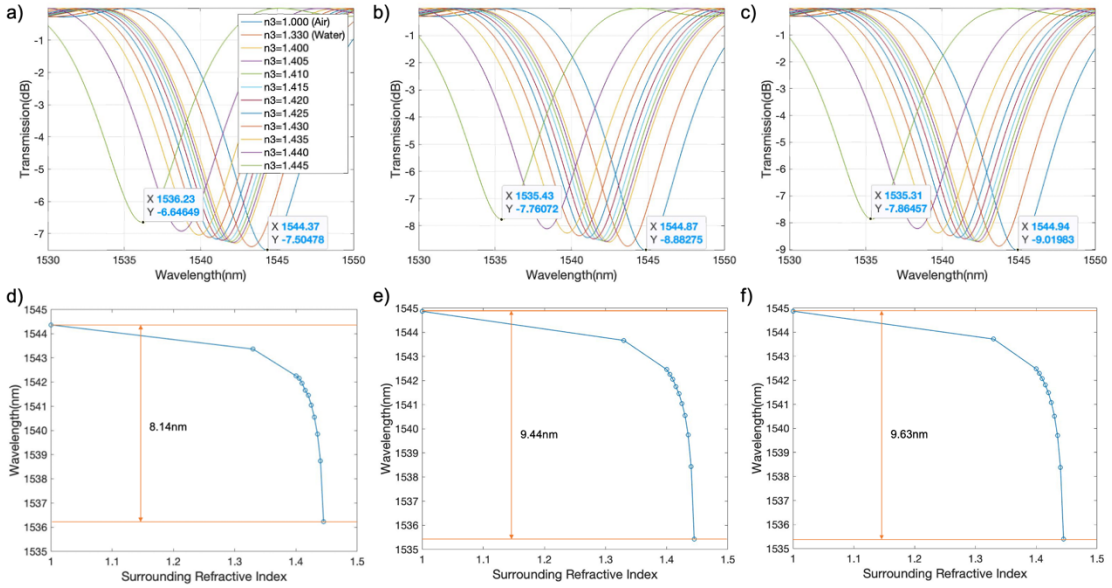

Figure 5.3-10 Simulated transmission curves and corresponding peak wavelength as function of RI ranging from 1.0 to 1.445 for (a,d) LPG0 (original), (b,e) LPG1 (5% hole density) and (c,f) LPG2 (7.9% hole density) samples, respectively.

Figures 5.3-10a & 5.3-10d depict the simulated peak shifts for the original, unprocessed LPG0 sample. The total peak shift spans 8.14 nm as the RI varies from 1.0 to 1.445, serving as the baseline for subsequent comparisons with processed samples. During the single-pass nanostructuring model of the LPG1 sample, nanoholes were generated at a density of 5%, leading to a 500 pm redshift of the transmission peaks

in air compared to the LPG0 sample under the same conditions. Over the refractive index range from 1.0 to 1.445, the cumulative shift amounted to 9.44 nm for the LPG1 sample, indicating a 15.97% increase compared to the unprocessed LPG0 sample, as illustrated in figures 5.3-10b and 5.3-10e. Aligned with experimental results, a 480 pm red-shift and a 16.08% enhancement in shift was observed. Similarly, for the LPG2 sample subjected to double-pass nanostructuring model, nanoholes were generated at a density of 7.9%, resulting in a 570 pm redshift of the peak wavelength in an air environment. The total shift reached 9.63 nm, reflecting an 18.30% increase compared to the unprocessed LPG over the entire refractive index range, which is also in line with experimental results showing a 530 pm redshift and a 19.57% increase in shift.

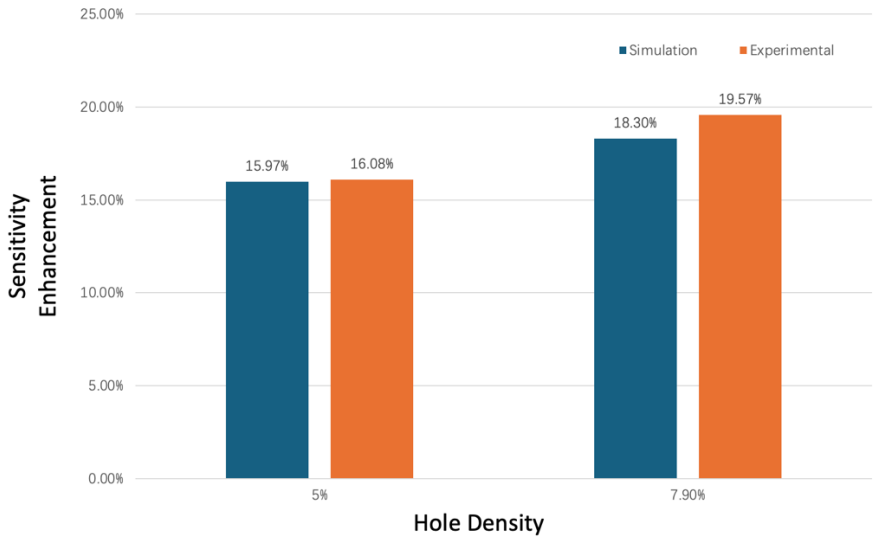

Figure 5.3-11 Comparison of sensitivity enhancement between simulation and experimental results for LPGs with different hole densities.

In conclusion, our proposed 'K2-model' effectively elucidates the improved sensing performance and fundamental physics of nanostructured holes on LPG sensors. The incorporation of nanoholes increases the surface area, thereby improving the coupling between the cladding layer and the sensing medium. This results in the observed

sensitivity enhancement, as shown in figure 5.3-11, where simulation predicts sensitivity improvements ranging from 15.97% to 18.30%, closely aligning with experimental results of 16.08% to 19.57%. This strong agreement between theoretical and experimental data highlights the effectiveness and accuracy of the K2-model in describing the performance of nanostructured LPG sensors.

5.4 Chapter summary

In summary, an innovative approach to enhance the sensitivity of LPGs for refractive index sensing was presented. This enhancement is achieved by creating NS-LPGs using a novel microsphere-assisted superlens laser nanostructuring technology. Our experiments compared the NS-LPGs with different nanohole densities in sucrose and glycerin solutions. The results demonstrated a remarkable increase in sensitivity, with NS-LPGs showing enhancements of 16.08% and 19.57% in sucrose and glycerin solutions, respectively, compared to traditional LPGs. Higher nanohole density resulted in greater sensitivity improvements. Crucially, these nanohole structures provide exceptional durability by eliminating the problem of coating layer damage, effectively resolving common issues encountered with conventional surface-coated LPGs. Our research represents a significant advancement in LPG sensor technology, emphasizing the potential of surface nanostructuring to enhance refractive index sensing capabilities. This innovation holds promise for a wide range of practical applications.

Chapter 6.
Integrated Super-resolution Nanofabrication & Nanoimaging System

6.1 Introduction

Laser technology has become indispensable in micro/nanopatterning due to its widespread usage. This versatile tool facilitates the precise creation of intricate structures through non-contact and maskless laser direct-writing techniques. However, a significant challenge in laser processing persists because of optical diffraction limit, particularly when aiming the production of extremely small features[62]. The minimum size of features achievable with surface patterning technologies, such as photolithography and direct laser writing, as well as the resolution of optical imaging systems, is inherently constrained by this limit. To overcome the diffraction limit, super-resolution techniques such as structured illumination microscopy, metamaterial superlenses, and microsphere superlenses have been developed[15,149,157–159]. Among these, the microsphere superlens technique is fundamental to this study. This technique is closely associated with the so-called 'photonic nanojet' effect, which helps focus light beams beyond the diffraction limit by leveraging the complex interplay of light interactions—such as reflection, refraction, and interference—occurring at the surface of micro- or nanoscale dielectric structures. This enables finer resolution in both imaging and fabrication processes[16,160,161]. A comprehensive review of the microsphere superlens technique, including its fundamentals and applications, can be found in the publication[149]. Key advancements in photonic nanojets mainly pursue two research directions: first, focusing laser beams onto the sample surface to achieve nanopatterning with sub-100 nm feature sizes, and secondly, manipulating light reflected from the sample surface, forming the foundation of super-resolution optical imaging to observe subwavelength objects and structures with

resolution as fine as 45 nm[162,163]. Previous publications have demonstrated 80 nm resolution in laser nanopatterning[22] and 45–50 nm resolution in nanoimaging[148,162], alongside other notable developments[75].

The dual functional nature of the proposed system roots from the distinct particle lens setup and super-resolution mechanism it employs. In nanopatterning experiments, it is well established that the patterning resolution is proportional to the particle size. Previous researchers have demonstrated the realization of patterning resolutions ranging from 1 μm to sub-micron levels, including sub-100 nm, using relatively small SiO_2 particle lenses[164,165]. This mechanism differs from that employed in nanoimaging. In super-resolution imaging, the microsphere superlens operates in a virtual imaging mode. It collects and transforms near-field evanescent waves, which carry high-spatial-frequency information of the object, into propagating waves that reach the far-field by forming a magnified virtual image. Here, the efficiency of evanescent-to-propagating conversion (ETPC) determines the final imaging resolution, rather than the spot size on the sample surface as in nanopatterning[18,166]. This mechanism enables the use of larger microspheres as superlenses for super-resolution imaging. At present, $BaTiO_3$ (BTG) microspheres with sizes ranging between 20 and 60 μm are widely used as dielectric superlenses[149].

Integrating both nanopatterning and nanoimaging capabilities within a single system requires design of the SuperNANO objective to accommodate both working modes: focusing mode and virtual imaging mode, normally based on microsphere material, size, refractive index contrast, integration with external components, and optimization[167–170]. Additionally, the system possesses the capability to position the microsphere superlens precisely at desired locations and scan over an area, which is crucial for practical applications since a single microsphere has a limited field of view (FOV). Consequently, scanning is utilized to expand the FOV of the system for a dynamic imaging[171,172]. Various scanning schemes were used in this field, including integration with an atomic force microscope (AFM) system, encapsulation of the microsphere in a solid film, optical trapping, etc. The most recent scanning design

involves bonding the microsphere superlens directly with an objective lens to create a unibody design[173,174]. In 2020, two approaches to unibody design and their applications in nanopatterning[11] and super-resolution imaging[175] were respectively published. The Plano-Convex-Microsphere (PCM) design stands out as a key innovation. It refers a compound-lens design realized by positioning a high-index microsphere onto a Plano-Convex lens and then integrating them into a conventional objective lens. However, these microsphere-based imaging and patterning systems were not integrated with each other, making real-time simultaneous nanoimaging and nanopatterning impossible. This significantly limits its applications in advanced anti-counterfeiting marking and other potential uses, such as real-time nanoscale laser processing at desired locations with nanoscale positional accuracy, biomedical applications, high-resolution diagnostic tools, and semiconductor manufacturing[14,176–178].

This chapter presents a novel super-resolution instrument, SuperNANO, which integrates dual functions for super-resolution imaging and fabrication. It enables simultaneous label-free super-resolution imaging and direct laser nanofabrication for the first time. The versatility of the instrument is demonstrated by its capability to create anti-counterfeiting security markings on an aluminum film sample. Through real-time direct laser writing, 'invisible' nano-security features, with arbitrary shapes, are generated at precise locations on the sample. Applications are shown in two-level anti-counterfeiting marking for security features, as well as nanoscissors for precise directional cutting of silver nanowires with a width of 80 nm, utilizing the synchronized nanoimaging system. The gap distance between the sample and lens is monitored by an auxiliary side-view microscope system, which proves critical for achieving reliable distance control in instrumentation.

6.2 SuperNANO system design

6.2.1 SuperNANO system setup

Figure 6.2-1 shows the schematic of the SuperNANO system. A Thorlabs QSL103A Picosecond Microchip Laser (wavelength of 1030 nm, with a pulse duration ranging from 550 ps ± 100 ps, repetition rate of 100 kHz) is the core of the system. This laser undergoes precise control as it passes through a series of essential components. Initially, it encounters a precision shutter and a beam expander, both carefully managed to ensure optimal beam quality and intensity. Subsequently, the laser enters the G3 Base galvo-scanner from BEIJING JCZ TECHNOLOGY CO. (Beijing, China), a dynamic component capable of achieving scanning speeds of up to 5000 mm/s. This swift scanning capability facilitates precise nanopatterning on the target substrate. The setup of the SuperNANO system is partitioned into distinct left and right sections, each dedicated to specific tasks. On the left, the focus is on super-resolution fabrication, while the right segment caters to super-resolution imaging.

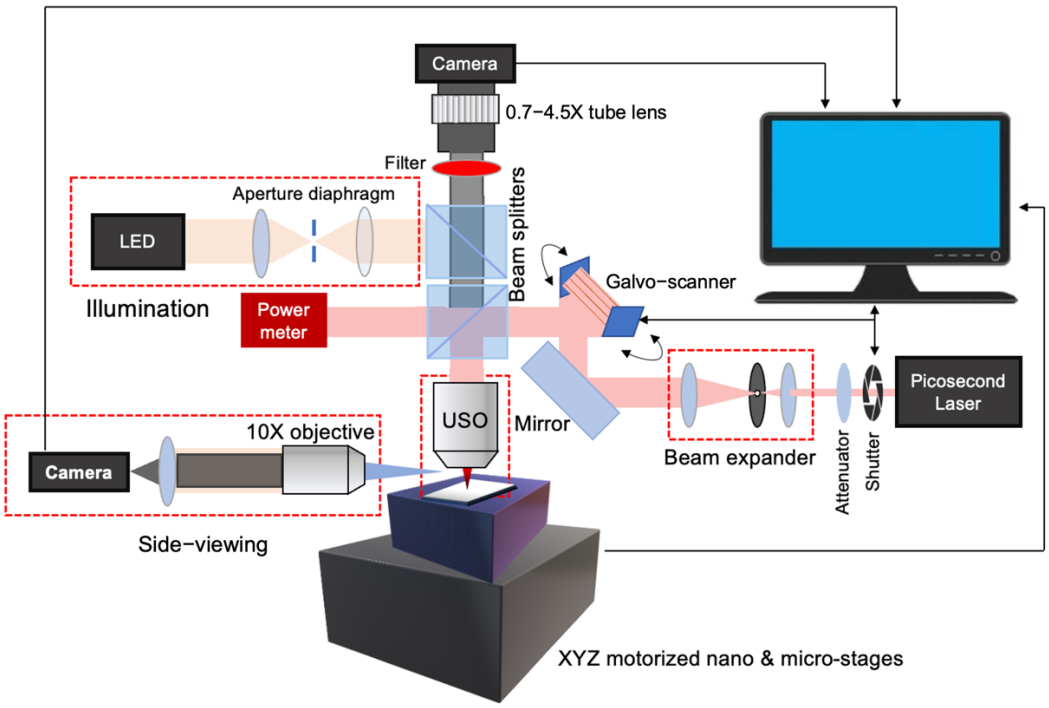

Figure 6.2-1 Schematic of SuperNANO system setup.

These sections were combined in the middle, seamlessly sharing a common optical pathway and a pivotal component known as the unibody superlens objective (USO). This integration ensures efficient utilization of resources and facilitates seamless transitions between fabrication and imaging processes. A 50:50 beam splitter plays a role in dividing the laser beam, allocating portions for both power metering and USO operations. This division facilitates nanoimaging capabilities by directing a portion of the laser beam towards reflection and subsequent capture by a CCD camera. To further enhance precision, the system incorporates XYZ motorized nano-stage and micro-stage mechanisms, orchestrating the alignment between the USO and the substrate. Meanwhile, the illuminations are carefully configured, featuring an LED illumination and an aperture diaphragm to ensure optimal lighting conditions for nanoscale manipulation. Furthermore, the system boasts sophisticated monitoring and control functionalities, exemplified by the inclusion of a side-viewing microscope seamlessly integrated with the stage system. This combination enables real-time monitoring and precise adjustment of gap distances, further enhancing the system's capabilities in achieving unparalleled levels of precision and control in nanoscale manipulation.

6.2.2 Fabrication of Unibody Superlens Objective

Figure 6.2-2a shows the manufacturing process of the USO lens (Fig. 6.2-2b), which is based on integrating a conventional objective (with a numerical aperture of 0.65) with an 80 μm $BaTiO_3$ (BTG) microsphere lens in a single design, as first introduced in our previous work[179]. The two components of USO are mechanically bonded together through a transparent encapsulation layer, typically composed of ultraviolet glue (UV light: wavelength 395 nm, power 3W, set time 2 hours). The fabrication process commences with the attachment of a microsphere onto a UV glue-coated objective (Fig. 6.2-2a1), facilitated by the precise manipulation of the Z-axis of the nano-stage to position the microsphere in touch and detach from the substrate surface (see Fig. 6.2-2a2,a3). Subsequently, the microsphere is secured in place through UV light curing,

facilitated by the side-viewing component of the system. Challenges were encountered in accurately positioning the microsphere at the center of the USO lens during fabrication, often requiring multiple attempts to achieve the desired outcome, which affected reproducibility. To address this issue, an XY translating lens mount has been incorporated into the system (see Fig. 6.2-2b). This enhancement allows for precise adjustments if the microsphere shifts, substantially increasing error tolerance during the fabrication process. Additionally, it is crucial to ensure that the thickness of the UV glue layer is less than the size of the microsphere to prevent it from becoming completely immersed. This controlled immersion not only maintains the correct focus position but is also essential for achieving optimal super-resolution performance by enabling the system to fully harness the enhancement capabilities of the microsphere lens, as demonstrated in our previous work[11].

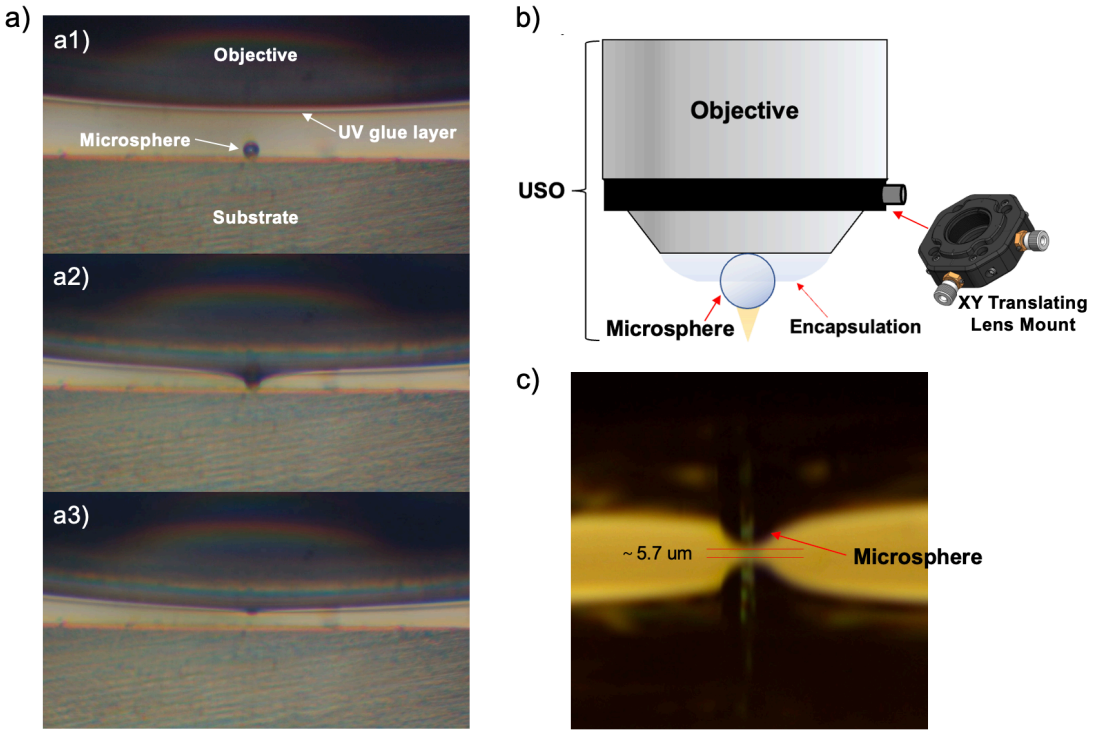

Figure 6.2-2 (a) Production process of USO objective made by microsphere and Plano-Convex lens: (a1) objective with UV glue approaching substrate, (a2) touching the substrate, (a3) detaching from the substrate. (b) Unibody Superlens Objective

integrated with a lens mount for precise microsphere centering. (c) Focusing distance measurement by the side-view microscope system. The substrate acts like a mirror in the image.

In our work, the BTG microsphere used has a refractive index of 1.95, and the UV glue (NOA 60) has a refractive index of 1.52 at visible wavelengths. For super-resolution applications, a microsphere size of several to several tens of micrometers is recommended in the literature. Here, a large-end size of 80 μm to ensure a working distance of about 5–6 μm for patterning applications was chosen. Smaller BTG microspheres would result in a smaller working distance, making fast and reliable nanopatterning more challenging[180–182]. Furthermore, the encapsulation status of the microsphere—whether fully or partially encapsulated within the bonding layer—provides additional control over the superlens performance. Partial encapsulation, for instance, may allow for nuanced adjustments to the microsphere's position and orientation, potentially fine-tuning the focal point and enhancing the overall resolution. In short, the final focusing resolution is mainly controlled by the microsphere size, material, and encapsulation status (e.g., partial or full encapsulation).

Figure 6.2-2c depicts the measurement of the working distance of the USO objective focusing as cap-tured by the side-view microscope system. By adjusting the Z-axis of the nano-stage, the focal length of the fabricated USO is determined to be 5.7 ± 0.03 μm. Here, the micro-sphere lens has a mirrored image generated by the underlying reflective substrate. This side-view imaging system not only enables accurate focal length measurements but also effectively monitors the position of the superlens, playing a crucial role in safeguarding both the lens and the sample. The USO objective is employed in both nano-imaging and laser nanofabrication processes, including nano-marking and nano-cutting as described below, to achieve enhanced resolution.

Figure 6.2-3 Photograph of fabricated USO.

Figure 6.2-3 depicts the actual USO, where multiple particle lenses are visible on the lens. Despite the presence of these additional lenses, they do not compromise the system's functionality or affect the precision of the central lens, which is effectively the only relevant component for the patterning process. The central particle lens is the key component, as it is the only one that can be precisely focused. This focus capability makes it essential for accurate patterning tasks.

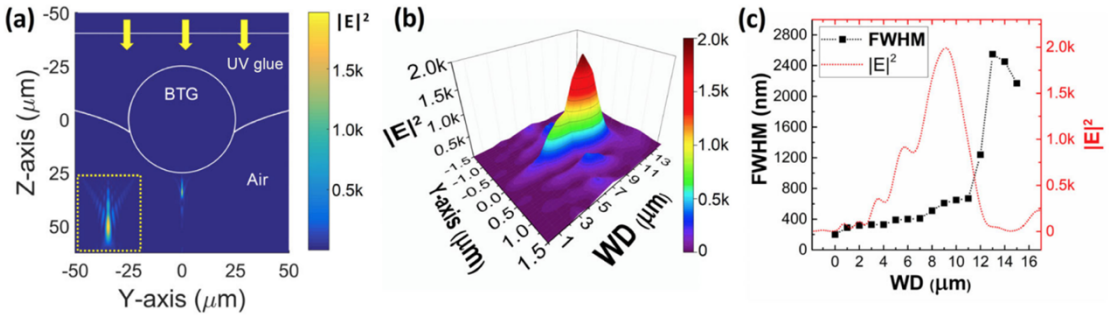

Figure 6.2-4 Theoretical modelling of USO lens focusing properties. (a) Side view of focusing with inset showing a magnified view of the focus area. (b) Field enhancement factor vs. working distance. (c) FWHM vs. working distance.

Figure 6.2-4 illustrates the calculated focusing field profile, field enhancement, and FWHM (Full width at half-maximum) spot size as functions of working distance. It shows that the focusing field elongates and diverges with increasing distance. The calculated FWHM spot size starts at 200 nm at the boundary of the microsphere and gradually increases to 670 nm as the distance reaches 11 µm, eventually reaching the microscale due to light divergence. Super-resolution of better than 400 nm is achieved for distances within 6 µm from the bottom of the USO lens, which aligns with the experimental finding of a 5.7 µm working distance and a patterning feature size of about 320 nm, as observed in this work.

6.3 Multi-level laser security marking

Counterfeiting is a global issue and has considerable negative impacts on our society, both economically and socially. Laser marking has been used as an effective tool in anti-counterfeiting applications. Compared to ink-based marking, laser-marked patterns are difficult to rub off, making them an ideal solution for traceability and anti-counterfeiting purposes. Laser marking creates a permanent and indelible mark in various forms, including text, image, and 2D codes (QR code, Data Matrix Code, and DotCode)[125,175,176]. However, with the rapid growth of laser technology, especially fiber laser technology, the prices of conventional-lens-based laser marking systems have considerably dropped in recent years, which has led to an increase in counterfeiting activities. Therefore, new innovations are needed to enhance the security level of markings, preventing counterfeiters with laser marking systems from copying or reproducing our fabrications. Here, our solution is multi-level security marking: the sample will be first marked with microscale markings, then a second level of nanoscale marking will be added by using the developed SuperNANO system. More levels of security can be realized by encoding nanoscale information in different strategies. Compared to other nanofabrication techniques such as photolithography, our technique does not involve complex processes such as spin coating, exposure, and

lift off but a single step of direct laser writing. When coupled with ultrafast laser sources, the technique can be performed on almost any material surface or inside body of transparent materials[183,184].

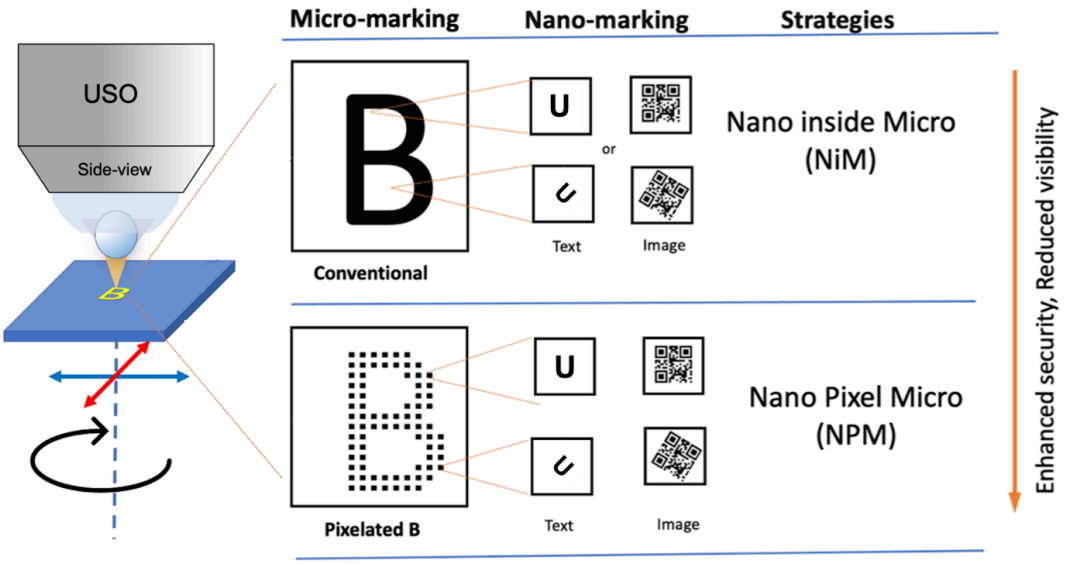

Figure 6.3-1 Strategies of multi-level laser security marking. NiM (Nano inside Micro): On top of conventional-lens-based laser marking, adding designed nanopattern inside. NPM (Nano Pixel Micro): Pixelized micro-marking, replacing each pixel with designed nanopattern. The arrows are micro- & nano-stage moving directions.

Figure 6.3-1 shows two proposed multi-level security marking strategies. The first is the Nano inside Micro (NiM) strategy, where nanoscale markings (the letter 'S') were added to a microscale marking (the letter 'B'). The second strategy is Nano Pixel Micro (NPM), where the conventional-lens-based laser marking design was first pixelized (see the pixelized 'B' in Fig. 6.3-1). Each pixel is then replaced with a nano-design (the letter 'U'), either text or an image. Each pixel is laser nano-marked, and the overall fabricated image forms a micro marking image. Compared to the NiM strategy, the pixelized mark has reduced visibility but improved security.

6.3.1 NiM strategy marking

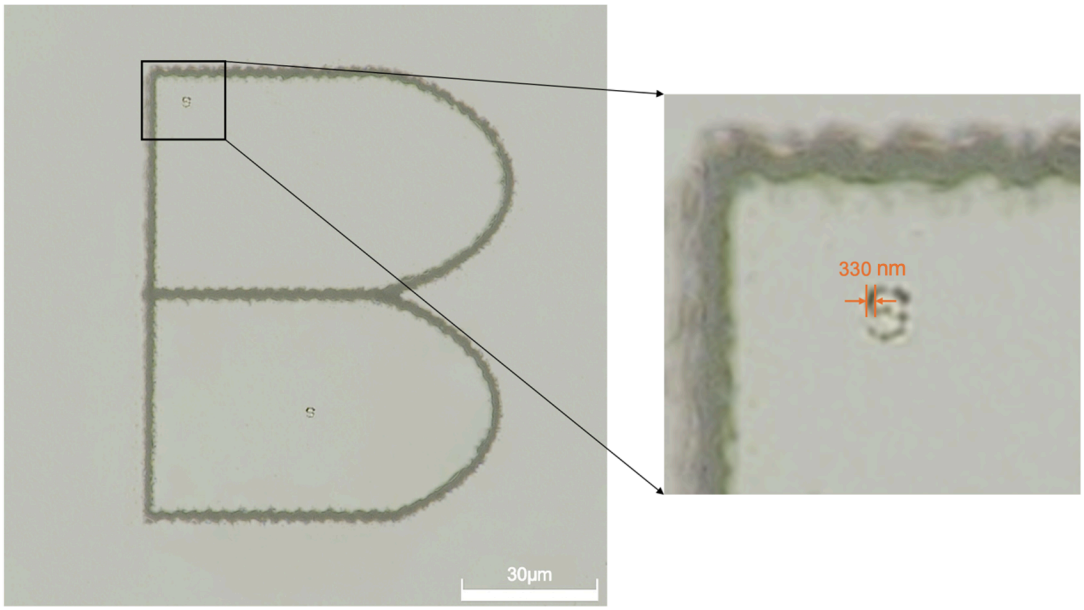

Figure 6.3-2 Microscope image of laser marked microscale ‘B’ letter with inside nanoscale ‘S’ letter.

Figure 6.3-2 showcases the advanced capabilities of the SuperNANO system in achieving nanoscale-resolution marking within microscale structures. The image features a large ‘B’ letter, microscopically engraved on the surface of the ALG (100 nm Aluminum thin film coated on a 1mm-thick Soda glass slides) sample. Zooming into the image, a smaller ‘S’ letter can be observed within the structure of the ‘B’. In the magnified view, the dimensions of the nanoscale marking become evident, with the ‘S’ letter measuring approximately 330 nm in line width. This ‘S’ letter is etched with nanoscale precision, demonstrating the remarkable accuracy and control of the SuperNANO system in creating intricate patterns on a nanolevel. Here, the ‘S’ letter with nanoscale line width was marked using the USO lens described above, while the micro-sized ‘B’ letter was marked using conventional-lens-based laser marking technology without the USO lens.

6.3.2 NPM strategy marking

The ability of nanoscale-resolution marking by the SuperNANO system is demonstrated through the creation of a microscale 'U' letter marked on the aluminum sample surface, with nanoscale marking resolution, as shown in figure 6.3-3. Each ‘U’ exhibits dimensions of 1.32 µm in length and 1.98 µm in width, with a marking resolution of 320 nm represented by the line width. Dark field illumination in figure 6.3-3b emphasizes surface irregularities and variations in reflectivity by illuminating the sample from oblique angles, thereby enhancing the visibility of markings and making them stand out against the background. These irregularities are mainly caused by the small mechanical vibrations and laser energy fluctuations associated with the system. Moreover, the marking process is seamlessly integrated with the imaging system, providing real-time observation and monitoring of the fabrication process.

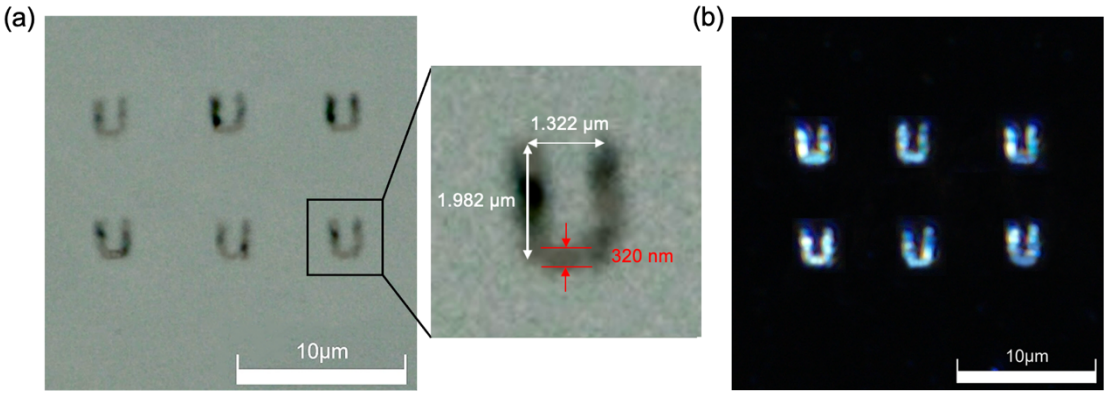

Figure 6.3-3 Microscope image of laser marked ‘U’ letters under (a) bright-field and (b) dark-field imaging modes.

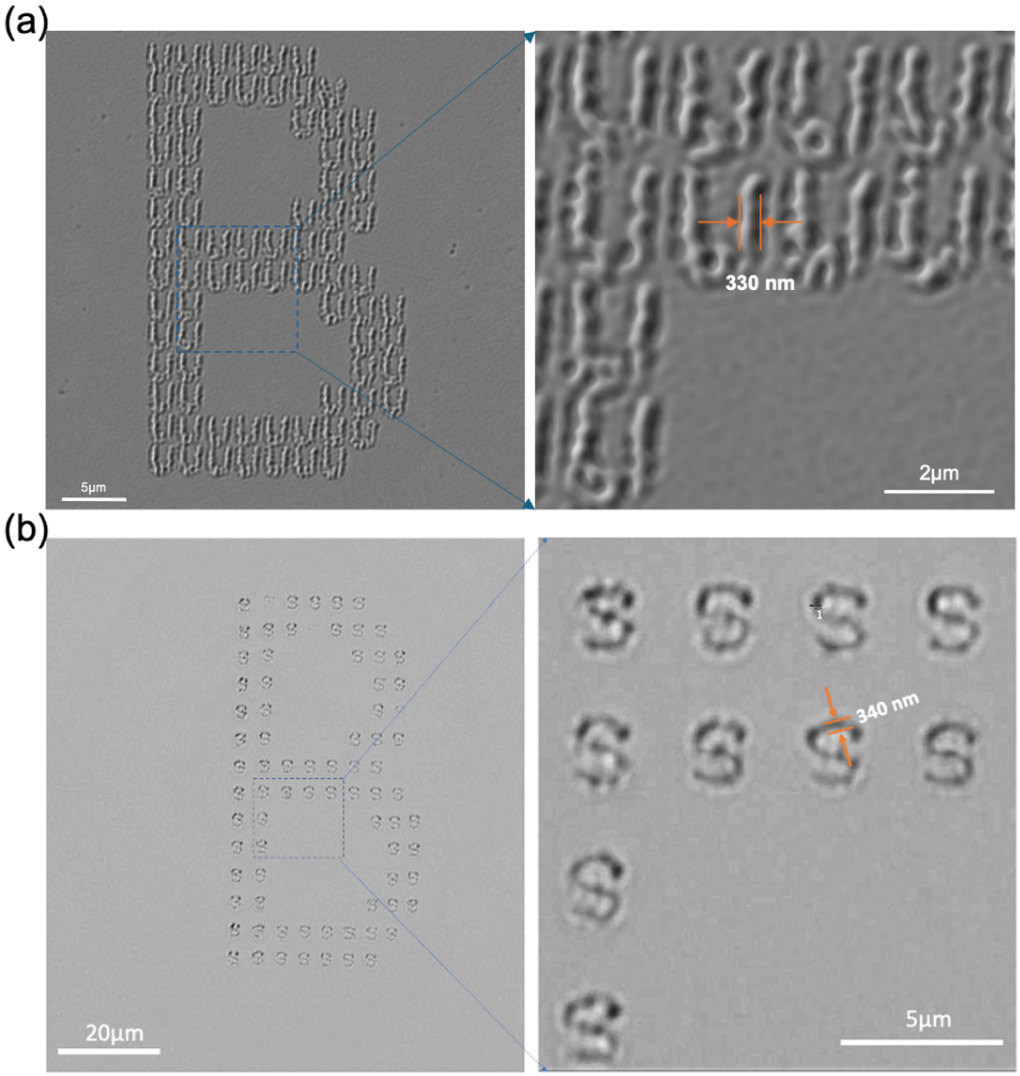

Figure 6.3-4 Microscope image of (a) pixelated 'B' with each pixel is marked with a nano-letter 'U', (b) pixe-lated letter 'B' with each pixel is marked with a nano-letter 'S'.

Figure 6.3-4 presents two examples of NPM strategy marking on the surface of an ALG sample. The output power of the picosecond laser system (refer to Chapter 3.3.2) was set to low power of 18 mW using the attenuator, with a scanning speed of 200 mm/s. As results, in the first one, figure 6.3-4a, the pixelated micro-sized letter 'B' is formed by nano-sized elements of 'U' with a line width of 330 nm, where BU represents Bangor University. The pixelated nanoelement offers versatility, allowing for the substitution of any desired letter form. As demonstrated in the second example in figure 6.3-4b, the original pixel unit 'U' is replaced with 'S', forming BS representing

Bangor Superlens, while maintaining a consistent line width of approximately 340 nm. Notably, the spacing between each letter, referred to as the pixel unit, is adjustable, affording precise control over the resolution of the entire pixelated letter 'B'. The spacing was set to 2 µm and 3 µm in figure 6.3-4a and figure 6.3-4b, respectively. In the system, the nano-letters 'U' or 'S' are generated by a Galvoscanning beam, while the position of each letter is controlled by a micro-stage. This setup enables not only the creation of intricate pixelated structures but also offers flexibility in adjusting resolution and letter forms, making it highly adaptable to diverse nano-marking applications. This configuration enables the rapid completion of the entire patterning process within seconds while ensuring uniformity. The ability to produce an extensive array of nano-letters underscores the system's robust repeatability, which are critical for applications demanding high accuracy and consistent outcomes. Optimizing processing parameters, such as laser power, scanning speed, and focal conditions, further enhances repeatability, ensuring that each pattern is reliably reproduced with minimal variation. This high level of control not only reduces processing time but also improves overall efficiency, making the system well-suited for advanced nanofabrication and research applications that require both speed and precision. The repeatability of nanoscale letter marking was found to be reasonably good. Repeated patterns exhibited consistent overall quality, with only minor variations observed in fine structural details. This level of repeatability is sufficient for anti-counterfeiting applications. Further improvements in uniformity could be achieved through the use of a flat-top (top-hat) laser beam to ensure more consistent energy distribution across the marked area. However, the current fabrication process is influenced by environmental vibrations and laser energy fluctuations, which affect the uniformity of the nanostructures. Enhancing the system with advanced antivibration mechanisms and a more stable laser source would improve uniformity, though this would increase the overall system cost.

In the experiments mentioned above, the SuperNANO system demonstrated a 330 nm line width on an aluminum sample. Due to challenges in achieving uniformity and

resolution at smaller scales on the ALG substrate, the focus was subsequently shifted to nanowire cutting. Silver nanowires, with a lower melting point (~400–500 °C) compared to ~600 °C for ALG, were selected to better demonstrate the resolution capabilities of the system. This choice allowed finer ablation control by carefully adjusting laser fluence such that only the central peak region of the Gaussian beam exceeded the material's ablation threshold, enabling narrower cuts. In these cutting experiments, the system achieved resolutions as fine as 50 nm, with the results visualized directly through the cutting gap sizes. These finer features, including cuts ranging from 50 nm to 280 nm—both below the demonstrated 330 nm line width—were also successfully nanoimaged using the USO lens, showcasing the SuperNANO system's ability to operate beyond the diffraction limit and achieve super-resolution imaging and fabrication.

6.4 Nanowire cutting

As explained above, to explore the resolution limit in manufacturing performed nano-cutting experiments by the SuperNANO system on a silver nanowire (AgNW), which has many potential applications such as transparent conductive films, photovoltaics, and wearable electronics[185–187]. The AgNW was purchased from ACS MATERIAL.

As illustrated in figure 6.4-1, the SuperNANO imaging system provides a comprehensive view of both the original and cut states of silver nanowires, showing the nanowire width around 80 nm and cutting width of approximately 440 nm. The laser fluence used is about 800 mJ/cm^2. Notably, the outline of the USO superlens is prominently visible as the circular edge shown in figure 6.4-1, delineating the area available for imaging and laser marking. Within this white region, measuring approximately a circle with a diameter of 10 microns, lies the focal point where precise imaging and laser marking operations can be executed. This dual-functionality system seamlessly integrates imaging and marking capabilities, thereby facilitating the accurate localization of target nanowires and enabling uniform cutting at desired

positions.

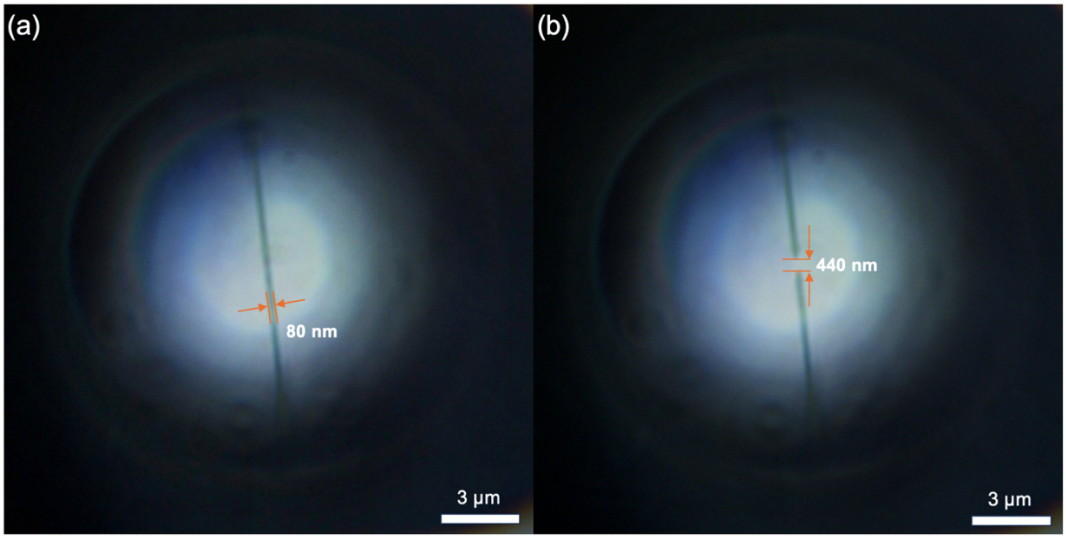

Figure 6.4-1 Example of silver nanowire cutting by SuperNANO system, (a) before and (b) after cutting.

The nanowire cutting mechanism is based on localized laser-induced ablation by evaporation, where material removal is initiated by the high-intensity peak region of the focused Gaussian beam. By carefully tuning the fluence so that only the central region exceeds the ablation threshold, material removal is confined there, enabling sub-diffraction-limited cutting[188]. Figure 6.4-2 illustrates cut sizes of 50 nm and 280 nm achieved at fluences of 573 mJ/cm² and 685 mJ/cm², respectively, confirming fluence-dependent resolution control.

To minimize thermal effects, a scanning speed of 2000 mm/s was employed—significantly higher than that used in nano-patterning. As a result, each nanowire cut could be completed in less than 0.5 seconds. Repeated trials under the same conditions produced consistent cutting widths and profiles, demonstrating good repeatability of the process. The fluence range and scanning parameters were optimized to balance ablation efficiency and resolution.

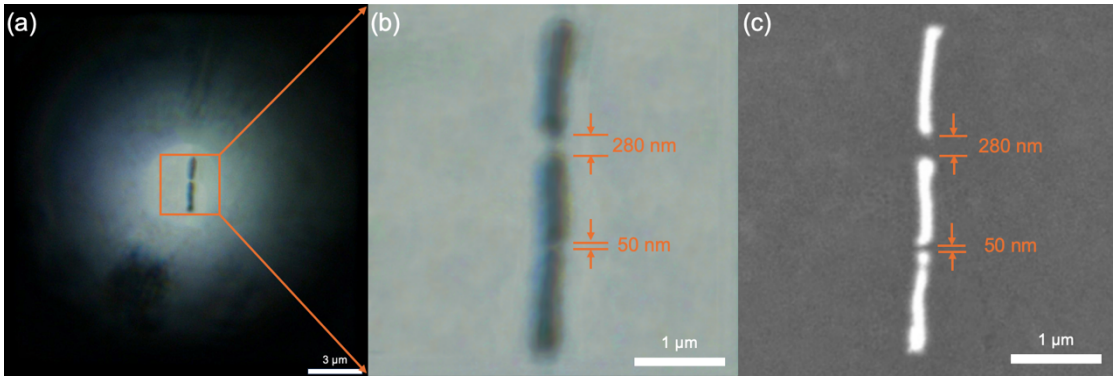

Figure 6.4-2 Silver nanowire cutting samples under (a) SuperNANO imaging system, (b) zoomed view of SuperNANO image in (a,c) SEM.

To investigate the influence of laser fluence on nanowire cutting dimensions, silver nanowire samples were irradiated with varying fluence levels ranging from 573 mJ/cm² to 800 mJ/cm². The cutting widths were measured using scanning electron microscopy (SEM), and a clear trend was observed: higher laser fluence resulted in wider cuts. As shown in figure 6.4-3, this includes representative cut sizes of 140 nm (Fig. 6.4-3a) and 390 nm (Fig. 6.4-3b), corresponding to intermediate and upper fluence levels within this range. The plot in figure 6.4-3c illustrates the positive correlation between laser fluence and cutting size, confirming that laser fluence can be precisely tuned to control the nanowire cutting dimension. These results strengthen the experimental basis for fluence-dependent nanostructuring and clarify the methodology used in generating the data. Of particular significance is the achievement of the smallest cutting width approaching less than 50 nm, underscoring a significant milestone in the capabilities of our system. This breakthrough opens up avenues for precise nanoscale manipulation with unprecedented accuracy.

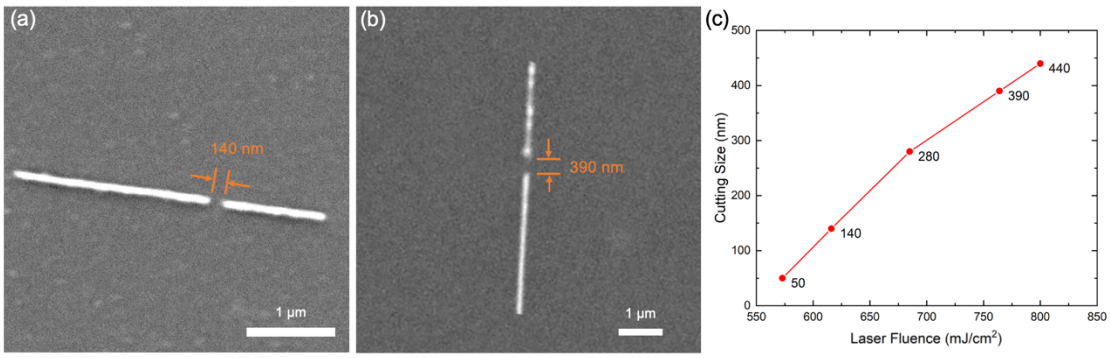

Figure 6.4-3 SEM of silver nanowire cutting samples at laser fluence of (a) 616 mJ/cm^2 and (b) 764 mJ/cm^2, (c) Relationship between laser fluence & nanowire cutting size.

To further improve the stability and resolution of the cutting process, future work will explore the use of a shorter-wavelength femtosecond laser. Additionally, gaps below 50 nm remain distinguishable only under SEM, emphasizing the importance of enhanced imaging resolution. As part of ongoing system upgrades, the use of a higher-performance TiO_2 superlens is being considered to further improve cutting precision. This strategic upgrade holds promise for further enhancing the resolution and capabilities of the SuperNANO imaging system, thereby unlocking new possibilities in nanofabrication and nanoengineering.

Another compelling application within our research scope is the automation of nanowire ruler cutting. This process involves the utilization of a programmable micro-stage to carefully position and cut the nanowires at specified intervals, yielding ruler-shaped nanostructures. As showcased in the results depicted in figure 6.4-3, obtained through both microscope and SEM measurements, this automated approach offers a systematic and controlled means of fabricating nanowire-based rulers with precision and consistency. Central to the success of nanowire ruler cutting is the management of the cutting width during the cutting process. By carefully adjusting the laser energy levels, the cutting width is maintained within the range of 850-900 nm. While opting for higher energy levels may result in larger cutting widths, it is crucial for ensuring the stability and reliability of the entire automated cutting procedure.

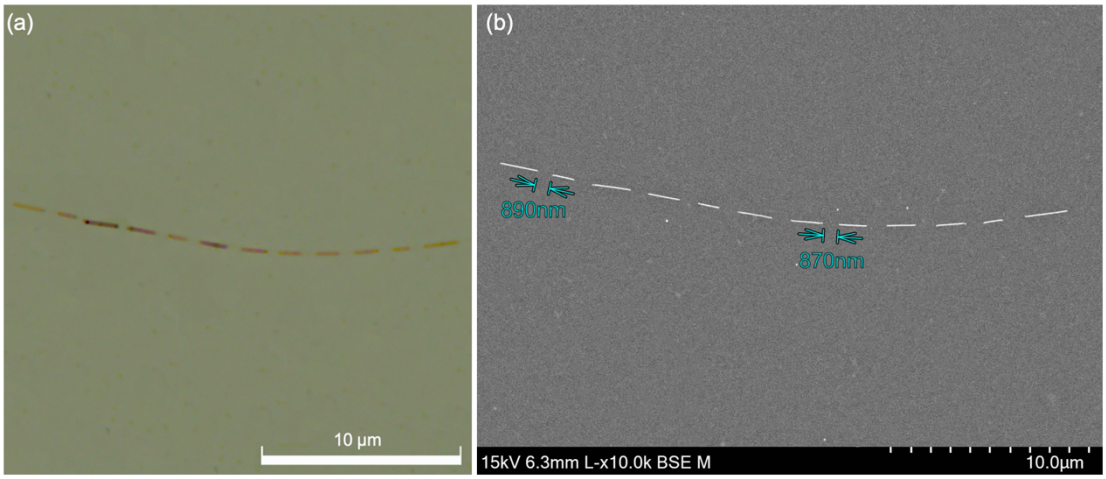

Figure 6.4-4 Silver nanowire ruler cutting sample under (a) Microscope & (b) SEM.

Moving forward, our research endeavors will be dedicated to further enhancing the stability and precision of the automated cutting process. One promising avenue involves the transition to a shorter wavelength femtosecond laser, which is anticipated to offer superior stability and control over the cutting process. By harnessing the advanced capabilities of such laser technology, the aim is to achieve even smaller cutting sizes in nanowire ruler cutting. In the literature, there are also reports on micro lens array (MLA)-assisted laser nanopatterning. These demonstrations are, however, based on nonlinear effects in fs laser ablation and the special materials being used. No super-resolution is associated with MLA focusing and they are not suitable for super-resolution imaging applications. Other reports on microsphere-based laser patterning techniques assisted by laser trapping or AFM positioning were also considered[90]. They are slow and complex, so they will not meet general needs for fast and reliable nano-patterning; it is also difficult to achieve dual functions, as demonstrated in our instrument. Our technique is unique in integrating real-time nanoimaging and nano-fabrication capabilities using the Unibody Superlens Objective (USO) with a microsphere superlens. This system offers significant advantages in terms of speed and cost-effectiveness, achieving similar or better resolution compared to AFM-based or

laser trapping systems while enabling rapid operation. These combined features distinguish our approach from others currently available in the literature, making it a more efficient and versatile solution for high-resolution nanopatterning and -imaging.

In the quest for achieving finer features beyond the 50–300 nm threshold, the adoption of either a higher performance superlens or a femtosecond laser with a shorter wavelength is being explored. One promising approach focuses on the design and fabrication of a novel TiO_2 composite superlens, leveraging the stacking of TiO_2 nanoparticles to replace the currently used BTG superlens. TiO_2 is an ideal candidate for this advancement due to its exceptional optical properties, including a high refractive index (n=2.5), excellent light scattering, and superior resolution-enhancing capabilities[80]. Our recent investigations have revealed that the TiO_2 superlens consistently outperforms the BTG microsphere superlens across various metrics, including focusing spot size, imaging contrast, clarity, field of view, and imaging resolution[80]. However, the TiO_2 composite superlens may exhibit a shorter working lifespan compared to the BTG lens due to its composite nature.

6.5 Chapter summary

In summary, the development of the SuperNANO instrument represents a significant advancement in nanotechnology. The demonstrated capabilities of the SuperNANO instrument extend beyond mere imaging and fabrication, encompassing applications such as two-level anti-counterfeiting marking and precise directional cutting of silver nanowires. The instrument utilizes innovative superlens technology and precise system design to achieve outstanding resolutions of 320 nm and 50 nm in nano-security marking and nanowire cutting, respectively. The incorporation of a nanoimaging system plays a pivotal role, enabling real-time positioning, visualization, and monitoring throughout the entire marking and fabrication process. The synergistic

integration of super-resolution imaging and fabrication functionalities opens up a plethora of opportunities in various fields, including nanotrapping, -sensing, -welding, -drilling, and -signal enhancement, and -detection. Its unique combination of imaging and fabrication functions paves the way for groundbreaking advancements in a wide array of disciplines, driving innovation and pushing the boundaries of what is achievable in nanoscience and nanotechnology.

Chapter 7.
Conclusion and Future Work

7.1 Conclusion

This thesis has made substantial contributions to the field of laser manufacturing by advancing both conventional and superlens-assisted techniques. The research developed a low-cost nanosecond UV laser-induced method for producing high-quality, nitrogen and sulfur-doped graphene on PBI and glass substrates. This approach successfully achieved graphene with a resistance of approximately 50 Ω over a 2 mm span, as verified by Raman spectroscopy, offering an efficient and economical pathway for fabricating functional graphene materials.

In the area of micro-fabrication, the thesis presented a precise approach for fabricating micro-compensated Fresnel Zone Plates (FZP) on thin films. This method successfully addressed challenges in material removal, achieving a first zone radius accuracy of 50.608 µm for even types and 50.612 µm for odd types, with a zone width accuracy as high as 99.3%. These precision levels are critical for lab-on-chip applications, where accurate focusing is essential.

The research also explored superlens-assisted laser marking for advanced anti-counterfeiting applications. By encoding information into DotCode formats and enhancing them with nanoscale features, the study achieved high-resolution markings with individual nanoholes approximately 180 nm in size, offering a robust method for complicating counterfeiting efforts.

In enhancing refractive index sensing, the thesis developed a method for improving the sensitivity of Long Period Optical Fiber Gratings (LPGs) through superlens-assisted laser nanostructuring. The research demonstrated sensitivity increases of 16.08% and 19.57% in LPGs with nanohole densities of 5% and 7.9%, respectively,

compared to conventional LPGs. These sensors also showed exceptional durability and consistent performance in diverse environmental conditions, including exposure to temperatures ranging from -20°C to 150°C.

The development and application of the SuperNANO system, with its dual functionality in super-resolution imaging and nano-fabrication, marked another significant achievement. The system achieved resolutions ranging from 50 to 320 nm, demonstrating its exceptional accuracy in applications such as anti-counterfeiting and the precise cutting of nanowires down to widths as small as 50 nm.

In conclusion, this thesis not only addresses existing challenges in laser manufacturing but also introduces innovative techniques that enhance the precision and scalability of fabrication processes. These advancements, quantified by significant improvements in material properties, sensor sensitivity, and resolution capabilities, offer promising avenues for future research and hold the potential for significant impact in industrial and scientific applications, particularly in the areas of sensor technology and secure manufacturing.

7.2 Future work

7.2.1 Development of other real-time functionalities of SuperNANO system

Beside current nanoimaging and nanomanufacturing functions, other functions such as nanoscale real-time trapping and Raman spectroscopy would be highly desirable and is suggested for future development.

Real-time trapping and analysis of nanoplastic particles: This initiative involves the integration of a novel real-time trapping mechanism that employs state-of-the-art super-resolution imaging technology. The primary goal is to achieve precise

identification of the chemical compositions of individual nanoplastic particles, which are often challenging to isolate and analyze due to their microscopic size and similarity to natural biotic materials.

The new trapping mechanism is designed to capture nanoplastics efficiently in various environmental samples, including water and soil, where these particles are predominantly found. The integration with super-resolution imaging allows for the detailed visualization of these tiny particles at a molecular level, thus enabling a more accurate analysis of their chemical structures. This enhancement will also facilitate the development of targeted strategies for the mitigation and removal of nanoplastics from the environment. By understanding the specific chemical makeup of these particles, more effective filtration and degradation technologies can be developed, tailored to the unique properties of different types of nanoplastic pollution. Ultimately, this capability in real-time trapping and super-resolution analysis not only advances the scientific understanding of nanoplastic pollution but also contributes to more effective environmental protection and sustainability efforts.

Real-time nano Raman spectroscopy: The integration of real-time nano-Raman spectroscopy into existing nanoimaging and nanomanufacturing systems. This integration aims to enhance the capabilities of these systems by providing detailed, real-time material characterization at the nanoscale. The proposed development involves the careful design and engineering of a compact Raman spectrometer that can be integrated seamlessly without compromising the high-resolution capabilities of current technologies.

To achieve this, it is essential to modify existing nanoimaging systems to accommodate the new Raman spectroscopy module. This step will ensure that the integration not only enhances the imaging capabilities but also maintains the system's existing functionalities. Calibration and validation of the system are necessary to ensure the accuracy and reproducibility of the Raman signals at such small scales. This process will involve conducting a series of calibration procedures followed by testing the system with known materials and nanostructures. Once calibrated, the system will

undergo rigorous application testing and refinement in real-world scenarios to gauge its effectiveness and reliability.

7.2.2 Machine learning assisted SuperNANO system

To increase throughput and efficiency in imaging processes, the transition from a single microsphere to a 3x3 microsphere array is proposed, which could potentially increase imaging speed by at least nine times (see Fig. 7.2-1). Further improvements may include expanding the array size, contingent on successful optimization of the manufacturing and imaging protocols.

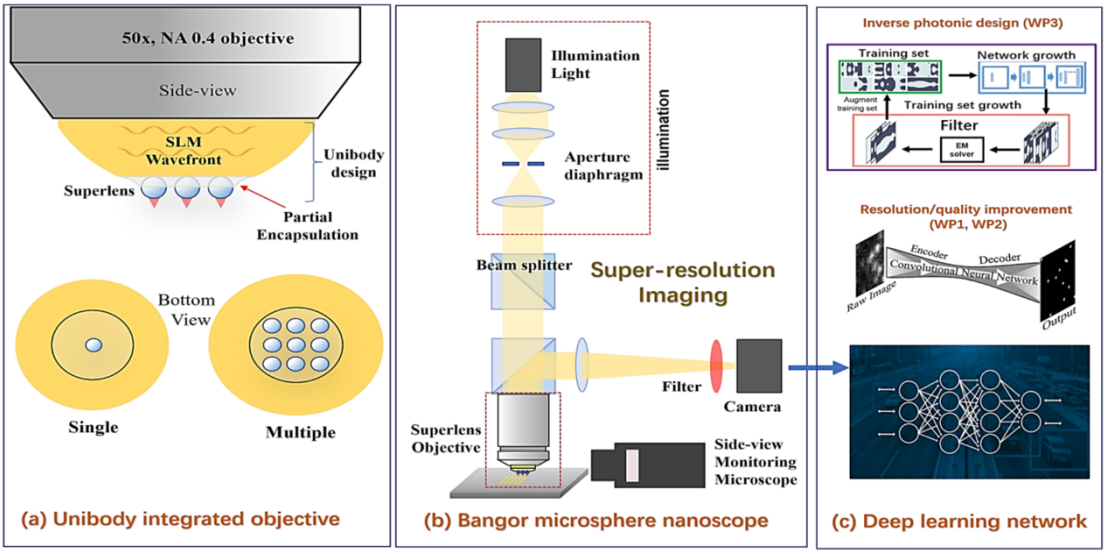

Figure 7.2-1 (a) Unibody integrated objective, (b) Bangor microsphere nanoscope, (c) Deep learning network.

Parallel efforts will address the challenge of enhancing low-contrast images obtained through the microsphere lens array, where previous rule-based image processing methods have failed. A machine learning model will be developed and trained to elevate the quality of these images to levels comparable with those acquired through

SEM. This training will utilize a combination of lower-quality microsphere nanoscope (MSN) images and higher-quality SEM images, employing techniques such as image data augmentation to enrich the training dataset. Upon successful offline testing, this model will be deployed for real-time enhancement in the online nanoscope system.

Additionally, the application of deep learning in the inverse design of photonic structures is planned, leveraging extensive nanoscopy image data collected from both the microsphere nanoscope and SEM. This initiative aims to enable the rapid and precise development of photonic structures, enhancing the ability to innovate within the field of photonics. These strategic enhancements and innovations are poised to advance nanoplastic research and photonic technology development, merging advanced imaging and computational methods for groundbreaking applications.

7.2.3 Modelling and simulation of nanostructured fiber grating sensor

The initial simulations of nanostructured LPG conducted in MATLAB provided only preliminary, approximate estimates. To achieve a more detailed and accurate analysis, it is planned to utilize COMSOL Multiphysics for advanced modeling and simulation. This future work will focus on two main configurations: a FBG with a nanostructured core, and an LPG with nanostructured cladding. Utilizing COMSOL's full-wave simulation capabilities will allow for a comprehensive study of the optical properties and performance enhancements possible with nanostructuring. This approach aims to provide deeper insights into the interaction between light and the nano-engineered structures within the fiber optics, potentially leading to innovative applications in sensing technology.

References:

[1] Y.C. Shin, B. Wu, S. Lei, G.J. Cheng, Y. Lawrence Yao, Overview of Laser Applications in Manufacturing and Materials Processing in Recent Years, Journal of Manufacturing Science and Engineering 142 (2020). https://doi.org/10.1115/1.4048397.

[2] R. Bogue, Lasers in manufacturing: a review of technologies and applications, Assembly Automation 35 (2015) 161–165. https://doi.org/10.1108/AA-07-2014-066.

[3] K. Sugioka, Progress in ultrafast laser processing and future prospects, Nanophotonics 6 (2017) 393–413. https://doi.org/10.1515/nanoph-2016-0004.

[4] M. Duocastella, C. Florian, P. Serra, A. Diaspro, Sub-wavelength Laser Nanopatterning using Droplet Lenses, Sci Rep 5 (2015) 16199. https://doi.org/10.1038/srep16199.

[5] S.N. Khonina, A.V. Ustinov, E.A. Pelevina, Analysis of wave aberration influence on reducing focal spot size in a high-aperture focusing system, J. Opt. 13 (2011) 095702. https://doi.org/10.1088/2040-8978/13/9/095702.

[6] Y. Huang, L. Zeng, C. Liu, D. Zeng, Z. Liu, X. Liu, X. Zhong, W. Guo, L. Li, Laser Direct Writing of Heteroatom (N and S)-Doped Graphene from a Polybenzimidazole Ink Donor on Polyethylene Terephthalate Polymer and Glass Substrates, Small 14 (2018) 1803143. https://doi.org/10.1002/smll.201803143.

[7] A. Turnali, O. Tokel, I. Pavlov, F.Ö. Ilday, Direct Laser Writing of Volume Fresnel Zone Plates in Silicon, in: 2015 European Conference on Lasers and Electro-Optics - European Quantum Electronics Conference (2015), Paper CM_4_5, Optica Publishing Group, 2015: p. CM_4_5. https://opg.optica.org/abstract.cfm?uri=CLEO_Europe-2015-CM_4_5 (accessed July 11, 2024).

[8] V.R.M. Rodrigues, J. Thomas, C. Santhosh, H. Ramachandran, D. Mathur, Microfabrication of Fresnel zone plates by laser induced solid ablation, J. Opt. 18 (2016) 075403. https://doi.org/10.1088/2040-8978/18/7/075403.

[9] A. Hu, R. Li, S. Bai, Y. Yu, W. Zhou, D. Bridges, Y. Deng, L. Zhang, Introduction to Laser Micro-to-Nano Manufacturing, in: A. Hu (Ed.), Laser Micro-Nano-Manufacturing and 3D Microprinting, Springer International Publishing, Cham, 2020: pp. 1–74. https://doi.org/10.1007/978-3-030-59313-1_1.

[10] D.J. Nieves, M.A.B. Baker, Pushing the super-resolution limit: recent improvements in microscopy below the diffraction limit, Biochemical Society Transactions 49 (2021) 431–439. https://doi.org/10.1042/BST20200746.

[11] B. Yan, L. Yue, J.N. Monks, X. Yang, D. Xiong, C. Jiang, Z. Wang, Superlensing plano-convex-microsphere (PCM) lens for direct laser nano-marking and beyond, Opt. Lett., OL 45 (2020) 1168–1171. https://doi.org/10.1364/OL.380574.

[12] M. Kamal Hossain, Nanoscale Imaging of Interstitial-Dependent Optical Confinement through Near-Field Scanning Optical Microscopy, The Chemical Record 22 (2022) e202200108. https://doi.org/10.1002/tcr.202200108.

[13] G. Yuan, K.S. Rogers, E.T.F. Rogers, N.I. Zheludev, Far-Field Superoscillatory Metamaterial Superlens, Phys. Rev. Applied 11 (2019) 064016. https://doi.org/10.1103/PhysRevApplied.11.064016.

[14] Y.F. Lu, L. Zhang, W.D. Song, Y.W. Zheng, B.S. Luk'yanchuk, Laser writing of a subwavelength structure on silicon (100) surfaces with particle-enhanced optical irradiation, Jetp Lett. 72 (2000) 457–459. https://doi.org/10.1134/1.1339899.

[15] Z. Chen, A. Taflove, V. Backman, Photonic nanojet enhancement of backscattering of light by nanoparticles: a potential novel visible-light ultramicroscopy technique, Opt. Express, OE 12 (2004) 1214–1220. https://doi.org/10.1364/OPEX.12.001214.

[16] Y. Wen, H. Yu, W. Zhao, F. Wang, X. Wang, L. Liu, W.J. Li, Photonic Nanojet Sub-Diffraction Nano-Fabrication With in situ Super-Resolution Imaging, IEEE Transactions on Nanotechnology 18 (2019) 226–233. https://doi.org/10.1109/TNANO.2019.2896220.

[17] A. Heifetz, S.-C. Kong, A.V. Sahakian, A. Taflove, V. Backman, Photonic Nanojets, Journal of Computational and Theoretical Nanoscience 6 (2009) 1979–1992. https://doi.org/10.1166/jctn.2009.1254.

[18] A. Darafsheh, Photonic nanojets and their applications, J. Phys. Photonics 3 (2021) 022001. https://doi.org/10.1088/2515-7647/abdb05.

[19] A. Darafsheh, N.I. Limberopoulos, J.S. Derov, D.E. Walker Jr., V.N. Astratov, Advantages of microsphere-assisted super-resolution imaging technique over solid immersion lens and confocal microscopies, Applied Physics Letters 104 (2014) 061117. https://doi.org/10.1063/1.4864760.

[20] X. Sedao, T.J.-Y. Derrien, G.R.B.E. Romer, B. Pathiraj, A.J. Huis in 't Veld, Large area laser surface micro/nanopatterning by contact microsphere lens arrays, Appl. Phys. A 111 (2013) 701–709. https://doi.org/10.1007/s00339-013-7651-1.

[21] A. Urrutia, J. Goicoechea, F.J. Arregui, Optical Fiber Sensors Based on Nanoparticle-Embedded Coatings, Journal of Sensors 2015 (2015) 805053. https://doi.org/10.1155/2015/805053.

[22] W. Guo, Z.B. Wang, L. Li, D.J. Whitehead, B.S. Luk'yanchuk, Z. Liu, Near-field laser parallel nanofabrication of arbitrary-shaped patterns, Applied Physics Letters 90 (2007) 243101. https://doi.org/10.1063/1.2748035.

[23] L. Chen, Y. Zhou, Y. Li, M. Hong, Microsphere enhanced optical imaging and patterning: From physics to applications, Applied Physics Reviews 6 (2019) 021304. https://doi.org/10.1063/1.5082215.

[24] R.J. Jackman, J.L. Wilbur, G.M. Whitesides, Fabrication of Submicrometer Features on Curved Substrates by Microcontact Printing, Science 269 (1995) 664–666. https://doi.org/10.1126/science.7624795.

[25] Q. Wang, M. Tahir, J. Zang, X. Zhao, Dynamic Electrostatic Lithography: Multiscale On-Demand Patterning on Large-Area Curved Surfaces, Advanced Materials 24 (2012) 1947–1951. https://doi.org/10.1002/adma.201200272.

[26] W. Jiang, J. Wang, Y. Yang, Y. Bu, A Review of Microsphere Super-Resolution Imaging Techniques, Sensors 24 (2024) 2511. https://doi.org/10.3390/s24082511.

[27] T.H. Maiman, 1960. Stimulated optical radiation in ruby, in: 1960. Stimulated Optical Radiation in Ruby, University of Chicago Press, 2010: pp. 113–114. https://doi.org/10.7208/9780226284163-019.

[28] G. Gamow, Zur Quantentheorie der Atomzertrümmerung, Z. Physik 52 (1929) 510–515. https://doi.org/10.1007/BF01339451.

[29] R.M. Herd, Mrcp(uk), J.S. Dover, K.A. Arndt, BASIC LASER PRINCIPLES, Dermatologic Clinics 15 (1997) 355–372. https://doi.org/10.1016/S0733-8635(05)70446-0.

[30] J.D. Majumdar, I. Manna, Introduction to LaserAssisted Fabrication of Materials, in: J.D. Majumdar, I. Manna (Eds.), Laser-Assisted Fabrication of Materials, Springer, Berlin, Heidelberg, 2013: pp. 1–67. https://doi.org/10.1007/978-3-642-28359-8_1.

[31] T.S. Alster, A.B. Lewis, Dermatologic Laser Surgery: A Review, Dermatologic Surgery 22 (1996) 797. https://doi.org/10.1111/j.1524-4725.1996.tb00731.x.

[32] S. Fa¨hler, H.-U. Krebs, Calculations and experiments of material removal and kinetic energy during pulsed laser ablation of metals, Applied Surface Science 96–98 (1996) 61–65. https://doi.org/10.1016/0169-4332(95)00466-1.

[33] R. Bogue, Fifty years of the laser: its role in material processing, Assembly Automation 30 (2010) 317–322. https://doi.org/10.1108/01445151011075771.

[34] J.R. Deepak, A. R.p, S. Saran Sundar, Applications of lasers in industries and laser welding: A review, Materials Today: Proceedings (2023). https://doi.org/10.1016/j.matpr.2023.02.102.

[35] J. Shao, X. Liang, Y. Lin, Q. Shen, J. Ren, J. Han, Excimer laser marking − A precise patterning technique for material surfaces, Optics & Laser Technology 176 (2024) 110974. https://doi.org/10.1016/j.optlastec.2024.110974.

[36] K.A. Hubeatir, M.M. AL-Kafaji, H.J. Omran, A Review: Effect of Different Laser Types on Material Engraving Process, 6 (2018).

[37] S. Wang, Z. Zhou, B. Li, C. Wang, Q. Liu, Progresses on new generation laser direct writing technique, Materials Today Nano 16 (2021) 100142. https://doi.org/10.1016/j.mtnano.2021.100142.

[38] M. A. Montealegre, G. Castro, P. Rey, J.L. Arias, P. Vázquez, M. González, SURFACE TREATMENTS BY LASER TECHNOLOGY, CM 1 (2010) 19–30. https://doi.org/10.5767/anurs.cmat.100101.en.019M.

[39] P. Lin, Z. Zhang, S. Kong, H. Zhou, X. Tong, L. Ren, Mechanical properties of composite coating on cast iron by laser, Surface Engineering 34 (2018) 289–295. https://doi.org/10.1080/02670844.2016.1201367.

[40] N. Faisal, D. Zindani, K. Kumar, S. Bhowmik, Laser Micromachining of Engineering Materials—A Review, in: K. Kumar, D. Zindani, N. Kumari, J.P. Davim (Eds.), Micro and Nano Machining of Engineering Materials: Recent Developments, Springer International Publishing, Cham, 2019: pp. 121–136. https://doi.org/10.1007/978-3-319-99900-5_6.

[41] K.M.T. Ahmmed, C. Grambow, A.-M. Kietzig, Fabrication of Micro/Nano Structures on Metals by Femtosecond Laser Micromachining, Micromachines 5 (2014) 1219–1253. https://doi.org/10.3390/mi5041219.

[42] R. Ye, D.K. James, J.M. Tour, Laser-Induced Graphene: From Discovery to Translation, Advanced Materials 31 (2019) 1803621. https://doi.org/10.1002/adma.201803621.

[43] J. Lin, Z. Peng, Y. Liu, F. Ruiz-Zepeda, R. Ye, E.L.G. Samuel, M.J. Yacaman, B.I. Yakobson, J.M. Tour, Laser-induced porous graphene films from commercial polymers, Nat Commun 5 (2014) 5714. https://doi.org/10.1038/ncomms6714.

[44] R. Ye, D.K. James, J.M. Tour, Laser-Induced Graphene, Acc. Chem. Res. 51 (2018) 1609–1620. https://doi.org/10.1021/acs.accounts.8b00084.

[45] Y. Chyan, R. Ye, Y. Li, S.P. Singh, C.J. Arnusch, J.M. Tour, Laser-Induced Graphene by Multiple Lasing: Toward Electronics on Cloth, Paper, and Food, ACS Nano 12 (2018) 2176–2183. https://doi.org/10.1021/acsnano.7b08539.

[46] R. Ye, Y. Chyan, J. Zhang, Y. Li, X. Han, C. Kittrell, J.M. Tour, Laser-Induced Graphene Formation on Wood, Advanced Materials 29 (2017) 1702211. https://doi.org/10.1002/adma.201702211.

[47] Q. Zhang, F. Zhang, X. Liu, Z. Yue, X. Chen, Z. Wan, Doping of Laser-Induced Graphene and Its Applications, Advanced Materials Technologies 8 (2023) 2300244. https://doi.org/10.1002/admt.202300244.

[48] H.D. Hristov, Fresnal Zones in Wireless Links, Zone Plate Lenses and Antennas, 1st ed., Artech House, Inc., USA, 2000.

[49] Y. Shi, X.Q. Zhu, L. Liang, Y. Yang, Tunable focusing properties using optofluidic Fresnel zone plates, Lab Chip 16 (2016) 4554–4559. https://doi.org/10.1039/C6LC01115B.

[50] U.T. Sanli, K. Keskinbora, C. Grevent, A. Szeghalmi, M. Knez, G. Schiitz, Multilayer Fresnel Zone Plates for X-ray Microscopy, Microscopy and Microanalysis 21 (2015)

1987–1988. https://doi.org/10.1017/S1431927615010715.

[51] F.D. Hallada, A.L. Franz, M.R. Hawks, Fresnel zone plate light field spectral imaging, OE 56 (2017) 081811. https://doi.org/10.1117/1.OE.56.8.081811.

[52] Y. Jia, S. Wang, F. Chen, School of Physics, State Key Laboratory of Crystal Materials, Shandong University, Jinan 250100, China., Femtosecond laser direct writing of flexibly configured waveguide geometries in optical crystals: fabrication and application, Opto-Electronic Advances 3 (2020) 190042–190042. https://doi.org/10.29026/oea.2020.190042.

[53] H. Wang, C. j. r. Sheppard, K. Ravi, S. t. Ho, G. Vienne, Fighting against diffraction: apodization and near field diffraction structures, Laser & Photonics Reviews 6 (2012) 354–392. https://doi.org/10.1002/lpor.201100009.

[54] S. Tolansky, An introduction to interferometry, in: 1973. https://www.semanticscholar.org/paper/An-introduction-to-interferometry-Tolansky/e70de1a5bee40d9c39a04ef64f869b6f16e5dc80 (accessed July 4, 2024).

[55] J.L. Harris, Diffraction and Resolving Power*, J. Opt. Soc. Am. 54 (1964) 931. https://doi.org/10.1364/JOSA.54.000931.

[56] W. Demtröder, Interference, Diffraction and Scattering, in: W. Demtröder (Ed.), Electrodynamics and Optics, Springer International Publishing, Cham, 2019: pp. 285–330. https://doi.org/10.1007/978-3-030-02291-4_10.

[57] C.J. Daly, T.W. Nuteson, N.A.H.K. Rao, The spatially averaged electric field in the near field and far field of a circular aperture, IEEE Transactions on Antennas and Propagation 51 (2003) 700–711. https://doi.org/10.1109/TAP.2003.811072.

[58] J.E. Harvey, R.V. Shack, Aberrations of diffracted wave fields, Appl. Opt. 17 (1978) 3003. https://doi.org/10.1364/AO.17.003003.

[59] G.D. Gillen, S. Guha, Modeling and propagation of near-field diffraction patterns: A more complete approach, American Journal of Physics 72 (2004) 1195–1201. https://doi.org/10.1119/1.1767102.

[60] A. García-Sánchez, Á.S. Sanz, Analysis of the gradual transition from the near to the far field in single-slit diffraction, Phys. Scr. 97 (2022) 055507. https://doi.org/10.1088/1402-4896/ac6460.

[61] G. Urcid, A. Padilla, Far-field diffraction patterns of circular sectors and related apertures, Appl. Opt., AO 44 (2005) 7677–7696. https://doi.org/10.1364/AO.44.007677.

[62] E. Abbe, Beiträge zur Theorie des Mikroskops und der mikroskopischen Wahrnehmung, Archiv f. mikrosk. Anatomie 9 (1873) 413–468. https://doi.org/10.1007/BF02956173.

[63] L.I. Schiff, Lattice-Space Quantization of a Nonlinear Field Theory, Phys. Rev. 92 (1953) 766–779. https://doi.org/10.1103/PhysRev.92.766.

[64] X. Michalet, S. Weiss, Using photon statistics to boost microscopy resolution, Proceedings of the National Academy of Sciences 103 (2006) 4797–4798. https://doi.org/10.1073/pnas.0600808103.

[65] D.V. Labeke, D. Barchiesi, F. Baida, Optical characterization of nanosources used in scanning near-field optical microscopy, J. Opt. Soc. Am. A, JOSAA 12 (1995) 695–703. https://doi.org/10.1364/JOSAA.12.000695.

[66] E.H. Synge, XXXVIII. A suggested method for extending microscopic resolution into the ultra-microscopic region, The London, Edinburgh, and Dublin Philosophical Magazine and Journal of Science (1928). https://doi.org/10.1080/14786440808564615.

[67] E.A. Ash, G. Nicholls, Super-resolution Aperture Scanning Microscope, Nature 237 (1972) 510–512. https://doi.org/10.1038/237510a0.

[68] J. Jersch, K. Dickmann, Nanostructure fabrication using laser field enhancement in the near field of a scanning tunneling microscope tip, Applied Physics Letters 68 (1996) 868–870. https://doi.org/10.1063/1.116527.

[69] E. Betzig, J.K. Trautman, T.D. Harris, J.S. Weiner, R.L. Kostelak, Breaking the Diffraction Barrier: Optical Microscopy on a Nanometric Scale, Science 251 (1991) 1468–1470. https://doi.org/10.1126/science.251.5000.1468.

[70] T. Roy, Control and localisation of light with engineered nano-structures, phd, University of Southampton, 2014. https://eprints.soton.ac.uk/369991/ (accessed July 5, 2024).

[71] A. Bek, R. Vogelgesang, K. Kern, Apertureless scanning near field optical microscope with sub-10nm resolution, Review of Scientific Instruments 77 (2006) 043703. https://doi.org/10.1063/1.2190211.

[72] D.W. Pohl, W. Denk, M. Lanz, Optical stethoscopy: Image recording with resolution λ/20, Applied Physics Letters 44 (1984) 651–653. https://doi.org/10.1063/1.94865.

[73] J. Zhu, L.L. Goddard, All-dielectric concentration of electromagnetic fields at the nanoscale: the role of photonic nanojets, Nanoscale Adv. 1 (2019) 4615–4643. https://doi.org/10.1039/C9NA00430K.

[74] B. Yan, All-dielectric superlens and applications, Bangor University (United Kingdom), 2018. https://search.proquest.com/openview/b4ff83ce2a392c11fa52304799e7ea25/1?pq-origsite=gscholar&cbl=51922&diss=y&casa_token=u-bua-UEl4IAAAAA:YodpbL4SLnJNSZU3efDmJ0yACsKzpBn70POhNV3ViWkmN3zSa21PjXZFPm-nxCU4myoJtN2u (accessed July 5, 2024).

[75] Z. Wang, B. Luk'yanchuk, Super-Resolution Imaging and Microscopy by Dielectric Particle-Lenses, in: V. Astratov (Ed.), Label-Free Super-Resolution Microscopy, Springer International Publishing, Cham, 2019: pp. 371–406.

https://doi.org/10.1007/978-3-030-21722-8_15.

[76] T.X. Hoang, Y. Duan, X. Chen, G. Barbastathis, Focusing and imaging in microsphere-based microscopy, Opt. Express, OE 23 (2015) 12337–12353. https://doi.org/10.1364/OE.23.012337.

[77] R. Boudoukha, S. Perrin, A. Demagh, P. Montgomery, N.-E. Demagh, S. Lecler, Near- to Far-Field Coupling of Evanescent Waves by Glass Microspheres, Photonics 8 (2021) 73. https://doi.org/10.3390/photonics8030073.

[78] I. Kandas, B. Zhang, C. Daengngam, I. Ashry, C.-Y. Jao, B. Peng, S.K. Ozdemir, H.D. Robinson, J.R. Heflin, L. Yang, Y. Xu, High quality factor silica microspheres functionalized with self-assembled nanomaterials, Opt. Express, OE 21 (2013) 20601–20610. https://doi.org/10.1364/OE.21.020601.

[79] M. Kuwata-gonokami, K. Ema, K. Takeda, Lasing and Intermode Correlation of Whispering Gallery Mode in Dye-Doped Polystyrene Microsphere, Molecular Crystals and Liquid Crystals Science and Technology. Section A. Molecular Crystals and Liquid Crystals 216 (1992) 21–25. https://doi.org/10.1080/10587259208028743.

[80] R. Dhama, B. Yan, C. Palego, Z. Wang, Super-Resolution Imaging by Dielectric Superlenses: TiO2 Metamaterial Superlens versus BaTiO3 Superlens, Photonics 8 (2021) 222. https://doi.org/10.3390/photonics8060222.

[81] W. Adams, M. Sadatgol, D.Ö. Güney, Review of near-field optics and superlenses for sub-diffraction-limited nano-imaging, AIP Advances 6 (2016) 100701. https://doi.org/10.1063/1.4964498.

[82] S. Li, C. Du, X. Dong, L. Shi, X. Luo, X. Wei, Y. Zhang, Superlens nano-patterning technology based on the distributed Polystyrene spheres, Opt. Express, OE 16 (2008) 14397–14403. https://doi.org/10.1364/OE.16.014397.

[83] A. Pockels, On the Spreading of Oil upon Water, Nature 50 (1894) 223–224. https://doi.org/10.1038/050223a0.

[84] S. Acharya, A.B. Panda, N. Belman, S. Efrima, Y. Golan, A Semiconductor-Nanowire Assembly of Ultrahigh Junction Density by the Langmuir–Blodgett Technique, Advanced Materials 18 (2006) 210–213. https://doi.org/10.1002/adma.200501234.

[85] Z. Matharu, G. Sumana, S.K. Arya, S.P. Singh, V. Gupta, B.D. Malhotra, Polyaniline Langmuir−Blodgett Film Based Cholesterol Biosensor, Langmuir 23 (2007) 13188–13192. https://doi.org/10.1021/la702123a.

[86] V. Periasamy, M.M. Jaafar, K. Chandrasekaran, S. Talebi, F.L. Ng, S.M. Phang, G.G. Kumar, M. Iwamoto, Langmuir–Blodgett Graphene-Based Films for Algal Biophotovoltaic Fuel Cells, Nanomaterials 12 (2022) 840. https://doi.org/10.3390/nano12050840.

[87] V. Malgras, Q. Ji, Y. Kamachi, T. Mori, F.-K. Shieh, K.C.-W. Wu, K. Ariga, Y.

Yamauchi, Templated Synthesis for Nanoarchitectured Porous Materials, Bulletin of the Chemical Society of Japan 88 (2015) 1171–1200. https://doi.org/10.1246/bcsj.20150143.

[88] V. Lotito, T. Zambelli, Approaches to self-assembly of colloidal monolayers: A guide for nanotechnologists, Advances in Colloid and Interface Science 246 (2017) 217–274. https://doi.org/10.1016/j.cis.2017.04.003.

[89] Z.B. Wang, M.H. Hong, B.S. Luk'yanchuk, S.M. Huang, Q.F. Wang, L.P. Shi, T.C. Chong, Parallel nanostructuring of GeSbTe film with particle mask, Appl. Phys. A 79 (2004) 1603–1606. https://doi.org/10.1007/s00339-004-2860-2.

[90] E. McLeod, C.B. Arnold, Subwavelength direct-write nanopatterning using optically trapped microspheres, Nat Nanotechnol 3 (2008) 413–417. https://doi.org/10.1038/nnano.2008.150.

[91] J.-M. Romano, R. Ahmed, A. Garcia-Giron, P. Penchev, H. Butt, O. Delléa, M. Sikosana, R. Helbig, C. Werner, S. Dimov, Subwavelength Direct Laser Nanopatterning Via Microparticle Arrays for Functionalizing Metallic Surfaces, Journal of Micro and Nano-Manufacturing 7 (2019). https://doi.org/10.1115/1.4042964.

[92] Q. Wen, X. Wei, P. Zhang, J. Lu, F. Jiang, X. Lu, Enhanced Microsphere-Assisted Picosecond Laser Processing for Nanohole Fabrication on Silicon via Thin Gold Coating, Micromachines 12 (2021) 611. https://doi.org/10.3390/mi12060611.

[93] A. Shakhov, A. Astafiev, A. Gulin, V. Nadtochenko, Femtosecond Nanostructuring of Glass with Optically Trapped Microspheres and Chemical Etching, ACS Appl Mater Interfaces 7 (2015) 27467–27472. https://doi.org/10.1021/acsami.5b09454.

[94] A. Khan, Z. Wang, M.A. Sheikh, D.J. Whitehead, L. Li, Parallel near-field optical micro/nanopatterning on curved surfaces by transported micro-particle lens arrays, J. Phys. D: Appl. Phys. 43 (2010) 305302. https://doi.org/10.1088/0022-3727/43/30/305302.

[95] S. Korposh, S.-W. Lee, S.W. James, R.P. Tatam, Refractive index sensitivity of fibre-optic long period gratings coated with SiO2 nanoparticle mesoporous thin films, Meas. Sci. Technol. 22 (2011) 075208. https://doi.org/10.1088/0957-0233/22/7/075208.

[96] S. Korposh, R. Selyanchyn, W. Yasukochi, S.-W. Lee, S.W. James, R.P. Tatam, Optical fibre long period grating with a nanoporous coating formed from silica nanoparticles for ammonia sensing in water, Materials Chemistry and Physics 133 (2012) 784–792. https://doi.org/10.1016/j.matchemphys.2012.01.094.

[97] A. Vasy, Geometric optics and the wave equation on manifolds with corners, in: N. Chernov, Y. Karpeshina, I.W. Knowles, R.T. Lewis, R. Weikard (Eds.), Contemporary Mathematics, American Mathematical Society, Providence, Rhode Island, 2006: pp. 315–333. https://doi.org/10.1090/conm/412/07784.

[98] G. Mie, Beiträge zur Optik trüber Medien, speziell kolloidaler Metallösungen, Annalen Der Physik 330 (1908) 377–445. https://doi.org/10.1002/andp.19083300302.

[99] T. Wriedt, Mie Theory: A Review, in: W. Hergert, T. Wriedt (Eds.), The Mie Theory: Basics and Applications, Springer, Berlin, Heidelberg, 2012: pp. 53–71. https://doi.org/10.1007/978-3-642-28738-1_2.

[100] T. Wriedt, A Review of Elastic Light Scattering Theories, Particle & Particle Systems Characterization 15 (1998) 67–74. https://doi.org/10.1002/(SICI)1521-4117(199804)15:2<67::AID-PPSC67>3.0.CO;2-F.

[101] T. Erdogan, Fiber grating spectra, Journal of Lightwave Technology 15 (1997) 1277–1294. https://doi.org/10.1109/50.618322.

[102] T. Erdogan, Cladding-mode resonances in short- and long-period fiber grating filters, J. Opt. Soc. Am. A, JOSAA 14 (1997) 1760–1773. https://doi.org/10.1364/JOSAA.14.001760.

[103] A. Cusano, D. Paladino, A. Iadicicco, Microstructured Fiber Bragg Gratings, J. Lightwave Technol., JLT 27 (2009) 1663–1697.

[104] A. Ikhlef, R. Hedara, M. Chikh-Bled, Uniform Fiber Bragg Grating modeling and simulation used matrix transfer method, International Journal of Computer Science Issues (IJCSI) 9 (2012) 368–374.

[105] A.M. Vengsarkar, P.J. Lemaire, J.B. Judkins, V. Bhatia, T. Erdogan, J.E. Sipe, Long-period fiber gratings as band-rejection filters, Journal of Lightwave Technology 14 (1996) 58–65. https://doi.org/10.1109/50.476137.

[106] V. Rastogi, K.S. Chiang, Long-period gratings in planar optical waveguides, Appl. Opt., AO 41 (2002) 6351–6355. https://doi.org/10.1364/AO.41.006351.

[107] S. Miao, X. Hu, Transmission spectrum simulation of long period fiber grating, J. Phys.: Conf. Ser. 1549 (2020) 022146. https://doi.org/10.1088/1742-6596/1549/2/022146.

[108] J.K. Sahota, N. Gupta, D. Dhawan, Fiber Bragg grating sensors for monitoring of physical parameters: a comprehensive review, OE 59 (2020) 060901. https://doi.org/10.1117/1.OE.59.6.060901.

[109] W.W. Morey, G. Meltz, W.H. Glenn, Fiber Optic Bragg Grating Sensors, in: Fiber Optic and Laser Sensors VII, SPIE, 1990: pp. 98–107. https://doi.org/10.1117/12.963022.

[110] Y.-J. Rao, In-fibre Bragg grating sensors, Meas. Sci. Technol. 8 (1997) 355. https://doi.org/10.1088/0957-0233/8/4/002.

[111] Y.-J. Rao, Fiber Bragg grating sensors: principles and applications, in: K.T.V. Grattan, B.T. Meggitt (Eds.), Optical Fiber Sensor Technology: Devices and Technology, Springer US, Boston, MA, 1998: pp. 355–379.

https://doi.org/10.1007/978-1-4615-5787-6_11.

[112] . L.S.M., TEMPERATURE AND STRAIN SENSITIVITY OF LONG PERIOD GRATING FIBER SENSOR: REVIEW, IJRET 04 (2015) 776–782. https://doi.org/10.15623/ijret.2015.0402108.

[113] F. Esposito, (INVITED)Chemical sensors based on long period fiber gratings: A review, Results in Optics 5 (2021) 100196. https://doi.org/10.1016/j.rio.2021.100196.

[114] H.J. Patrick, A.D. Kersey, F. Bucholtz, Analysis of the Response of Long Period Fiber Gratings to External Index of Refraction, J. Lightwave Technol., JLT 16 (1998) 1606.

[115] S. Khaliq, S.W. James, R.P. Tatam, Enhanced sensitivity fibre optic long period grating temperature sensor, Meas. Sci. Technol. 13 (2002) 792. https://doi.org/10.1088/0957-0233/13/5/318.

[116] S.W. James, R.P. Tatam, Optical fibre long-period grating sensors: characteristics and application, Meas. Sci. Technol. 14 (2003) R49. https://doi.org/10.1088/0957-0233/14/5/201.

[117] F. Hirtenfelder, Effective Antenna Simulations using CST MICROWAVE STUDIO®, in: 2007 2nd International ITG Conference on Antennas, 2007: pp. 239–239. https://doi.org/10.1109/INICA.2007.4353972.

[118] R.R. Nair, P. Blake, A.N. Grigorenko, K.S. Novoselov, T.J. Booth, T. Stauber, N.M.R. Peres, A.K. Geim, Fine structure constant defines visual transparency of graphene, Science 320 (2008) 1308. https://doi.org/10.1126/science.1156965.

[119] K. Rastani, A. Marrakchi, S.F. Habiby, W.M. Hubbard, H. Gilchrist, R.E. Nahory, Binary phase Fresnel lenses for generation of two-dimensional beam arrays, Appl. Opt., AO 30 (1991) 1347–1354. https://doi.org/10.1364/AO.30.001347.

[120] Picosecond Microchip Lasers, (n.d.). https://www.thorlabs.com (accessed March 23, 2025).

[121] SuperK COMPACT, NKT Photonics (n.d.). https://www.nktphotonics.com/products/supercontinuum-white-light-lasers/superk-compact/ (accessed March 23, 2025).

[122] G.D. Gautam, A.K. Pandey, Pulsed Nd:YAG laser beam drilling: A review, Optics & Laser Technology 100 (2018) 183–215. https://doi.org/10.1016/j.optlastec.2017.09.054.

[123] Aluminum Coated on Microscope Slides (5 Slides), Platypus Technologies (n.d.). https://www.platypustech.com/product/aluminum-coated-on-microscope-slides-5-slides (accessed March 23, 2025).

[124] M. Chandak, P. Naik, D. Shinde, D. Raut, Process Parameter Optimization for Laser 2D Barcode Engraving using Taguchi Design of Experiment Technique,

International Journal of Engineering and Technical Research 9 (2020) 263–267.

[125] X. Li, L. Yang, B. Chang, T. Li, C. Li, D. Zhang, B. Yan, Simulation and process optimization for laser marking of submillimetre rasterizing 2D code on stainless steel, Int. J. Mod. Phys. B 34 (2020) 2050266. https://doi.org/10.1142/S0217979220502665.

[126] B. Lee, Review of the present status of optical fiber sensors, Optical Fiber Technology 9 (2003) 57–79. https://doi.org/10.1016/S1068-5200(02)00527-8.

[127] B. Culshaw, Optical Fiber Sensor Technologies: Opportunities and - Perhaps - Pitfalls, J. Lightwave Technol., JLT 22 (2004) 39.

[128] X. Fan, I.M. White, Optofluidic microsystems for chemical and biological analysis, Nature Photon 5 (2011) 591–597. https://doi.org/10.1038/nphoton.2011.206.

[129] X. Wang, O.S. Wolfbeis, Fiber-Optic Chemical Sensors and Biosensors (2013–2015), Anal. Chem. 88 (2016) 203–227. https://doi.org/10.1021/acs.analchem.5b04298.

[130] X. Shu, L. Zhang, I. Bennion, Sensitivity Characteristics of Long-Period Fiber Gratings, J. Lightwave Technol., JLT 20 (2002) 255.

[131] G. Rego, A Review of Refractometric Sensors Based on Long Period Fibre Gratings, The Scientific World Journal 2013 (2013) 913418. https://doi.org/10.1155/2013/913418.

[132] V. Bhatia, A.M. Vengsarkar, Optical fiber long-period grating sensors, Opt. Lett., OL 21 (1996) 692–694. https://doi.org/10.1364/OL.21.000692.

[133] Q. Shi, B.T. Kuhlmey, Optimization of photonic bandgap fiber long period grating refractive-index sensors, Optics Communications 282 (2009) 4723–4728. https://doi.org/10.1016/j.optcom.2009.09.030.

[134] T. Venugopalan, T. Sun, K.T.V. Grattan, Long period grating-based humidity sensor for potential structural health monitoring, Sensors and Actuators A: Physical 148 (2008) 57–62. https://doi.org/10.1016/j.sna.2008.07.015.

[135] Q. Wang, C. Du, J. Zhang, R. Lv, Y. Zhao, Sensitivity-enhanced temperature sensor based on PDMS-coated long period fiber grating, Optics Communications 377 (2016) 89–93. https://doi.org/10.1016/j.optcom.2016.05.039.

[136] M. Abadie, High Performance Polymers - Polyimides Based: From Chemistry to Applications, BoD – Books on Demand, 2012.

[137] W. Wei, J. Nong, G. Zhang, L. Tang, X. Jiang, N. Chen, S. Luo, G. Lan, Y. Zhu, Graphene-Based Long-Period Fiber Grating Surface Plasmon Resonance Sensor for High-Sensitivity Gas Sensing, Sensors 17 (2017) 2. https://doi.org/10.3390/s17010002.

[138] C. Liu, Q. Cai, B. Xu, W. Zhu, L. Zhang, J. Zhao, X. Chen, Graphene oxide functionalized long period grating for ultrasensitive label-free immunosensing, Biosensors and Bioelectronics 94 (2017) 200–206. https://doi.org/10.1016/j.bios.2017.03.004.

[139] Y. Li, Y. Wang, C. Wen, Temperature and strain sensing properties of the zinc coated FBG, Optik 127 (2016) 6463–6469. https://doi.org/10.1016/j.ijleo.2016.04.054.

[140] A. Abdelghani, J.M. Chovelon, N. Jaffrezic-Renault, M. Lacroix, H. Gagnaire, C. Veillas, B. Berkova, M. Chomat, V. Matejec, Optical fibre sensor coated with porous silica layers for gas and chemical vapour detection, Sensors and Actuators B: Chemical 44 (1997) 495–498. https://doi.org/10.1016/S0925-4005(97)00172-X.

[141] A. Urrutia, J. Goicoechea, A.L. Ricchiuti, D. Barrera, S. Sales, F.J. Arregui, Simultaneous measurement of humidity and temperature based on a partially coated optical fiber long period grating, Sensors and Actuators B: Chemical 227 (2016) 135–141. https://doi.org/10.1016/j.snb.2015.12.031.

[142] Y.C. Tan, W.B. Ji, V. Mamidala, K.K. Chow, S.C. Tjin, Carbon-nanotube-deposited long period fiber grating for continuous refractive index sensor applications, Sensors and Actuators B: Chemical 196 (2014) 260–264. https://doi.org/10.1016/j.snb.2014.01.063.

[143] D. Viegas, J. Goicoechea, J.L. Santos, F.M. Araújo, L.A. Ferreira, F.J. Arregui, I.R. Matias, Sensitivity Improvement of a Humidity Sensor Based on Silica Nanospheres on a Long-Period Fiber Grating, Sensors 9 (2009) 519–527. https://doi.org/10.3390/s90100519.

[144] S. Lepinay, A. Staff, A. Ianoul, J. Albert, Improved detection limits of protein optical fiber biosensors coated with gold nanoparticles, Biosensors and Bioelectronics 52 (2014) 337–344. https://doi.org/10.1016/j.bios.2013.08.058.

[145] M. Konstantaki, A. Klini, D. Anglos, S. Pissadakis, An ethanol vapor detection probe based on a ZnO nanorod coated optical fiber long period grating, Opt. Express, OE 20 (2012) 8472–8484. https://doi.org/10.1364/OE.20.008472.

[146] R.-Z. Yang, W.-F. Dong, X. Meng, X.-L. Zhang, Y.-L. Sun, Y.-W. Hao, J.-C. Guo, W.-Y. Zhang, Y.-S. Yu, J.-F. Song, Z.-M. Qi, H.-B. Sun, Nanoporous TiO2/Polyion Thin-Film-Coated Long-Period Grating Sensors for the Direct Measurement of Low-Molecular-Weight Analytes, Langmuir 28 (2012) 8814–8821. https://doi.org/10.1021/la301445h.

[147] Y.F. Lu, L. Zhang, W.D. Song, Y.W. Zheng, B.S. Luk'yanchuk, Laser writing of a subwavelength structure on silicon (100) surfaces with particle-enhanced optical irradiation, Jetp Lett. 72 (2000) 457–459. https://doi.org/10.1134/1.1339899.

[148] Z. Wang, W. Guo, L. Li, B. Luk'yanchuk, A. Khan, Z. Liu, Z. Chen, M. Hong, Optical virtual imaging at 50 nm lateral resolution with a white-light nanoscope, Nat

Commun 2 (2011) 218. https://doi.org/10.1038/ncomms1211.

[149] V.N. Astratov, Y.B. Sahel, Y.C. Eldar, L. Huang, A. Ozcan, N. Zheludev, J. Zhao, Z. Burns, Z. Liu, E. Narimanov, N. Goswami, G. Popescu, E. Pfitzner, P. Kukura, Y.-T. Hsiao, C.-L. Hsieh, B. Abbey, A. Diaspro, A. LeGratiet, P. Bianchini, N.T. Shaked, B. Simon, N. Verrier, M. Debailleul, O. Haeberlé, S. Wang, M. Liu, Y. Bai, J.-X. Cheng, B.S. Kariman, K. Fujita, M. Sinvani, Z. Zalevsky, X. Li, G.-J. Huang, S.-W. Chu, O. Tzang, D. Hershkovitz, O. Cheshnovsky, M.J. Huttunen, S.G. Stanciu, V.N. Smolyaninova, I.I. Smolyaninov, U. Leonhardt, S. Sahebdivan, Z. Wang, B. Luk'yanchuk, L. Wu, A.V. Maslov, B. Jin, C.R. Simovski, S. Perrin, P. Montgomery, S. Lecler, Roadmap on Label-Free Super-Resolution Imaging, Laser & Photonics Reviews 17 (2023) 2200029. https://doi.org/10.1002/lpor.202200029.

[150] I. Jasim, J. Liu, C. Zhu, M. Roman, J. Huang, E. Kinzel, M. Almasri, Microsphere Photolithography Patterned Nanohole Array on an Optical Fiber, IEEE Access 9 (2021) 32627–32633. https://doi.org/10.1109/ACCESS.2021.3059439.

[151] P.S. Macheso, M. Zekriti, Modelling and analysis of fiber Bragg grating temperature sensor for Internet of things applications (FBG-4-IoT), International Journal of Intelligent Networks 5 (2024) 224–230. https://doi.org/10.1016/j.ijin.2024.05.006.

[152] J. Hrubý, V. T. Santana, D. Kostiuk, M. Bouček, S. Lenz, M. Kern, P. Šiffalovič, J. van Slageren, P. Neugebauer, A graphene-based hybrid material with quantum bits prepared by the double Langmuir–Schaefer method, RSC Advances 9 (2019) 24066–24073. https://doi.org/10.1039/C9RA04537F.

[153] J. Liu, I. Jasim, T. Liu, J. Huang, E. Kinzel, M. Almasri, Off-axis microsphere photolithography patterned nanohole array and other structures on an optical fiber tip for glucose sensing, RSC Advances 11 (2021) 25912–25920. https://doi.org/10.1039/D1RA02652F.

[154] W.M. bin M. Yunus, A. bin A. Rahman, Refractive index of solutions at high concentrations, Appl. Opt., AO 27 (1988) 3341–3343. https://doi.org/10.1364/AO.27.003341.

[155] Fly's Eye Homogenizers, (n.d.). https://www.thorlabs.com (accessed March 23, 2025).

[156] C.Y.H. Tsao, D.N. Payne, W.A. Gambling, Modal characteristics of three-layered optical fiber waveguides: a modified approach, J. Opt. Soc. Am. A, JOSAA 6 (1989) 555–563. https://doi.org/10.1364/JOSAA.6.000555.

[157] Z. Wang, T. Zhao, H. Hao, Y. Cai, K. Feng, X. Yun, Y. Liang, S. Wang, Y. Sun, P.R. Bianco, K. Oh, M. Lei, High-speed image reconstruction for optically sectioned, super-resolution structured illumination microscopy, Adv. Photon. 4 (2022). https://doi.org/10.1117/1.AP.4.2.026003.

[158] Z. Wang, T. Zhao, Y. Cai, J. Zhang, H. Hao, Y. Liang, S. Wang, Y. Sun, T. Chen,

P.R. Bianco, K. Oh, M. Lei, Rapid, artifact-reduced, image reconstruction for super-resolution structured illumination microscopy, Innovation 4 (2023). https://doi.org/10.1016/j.xinn.2023.100425.

[159] S. Lecler, Y. Takakura, P. Meyrueis, Properties of a three-dimensional photonic jet, Opt. Lett., OL 30 (2005) 2641–2643. https://doi.org/10.1364/OL.30.002641.

[160] F. Wang, L. Liu, H. Yu, Y. Wen, P. Yu, Z. Liu, Y. Wang, W.J. Li, Scanning superlens microscopy for non-invasive large field-of-view visible light nanoscale imaging, Nat Commun 7 (2016) 13748. https://doi.org/10.1038/ncomms13748.

[161] L.A. Krivitsky, J.J. Wang, Z. Wang, B. Luk'yanchuk, Locomotion of microspheres for super-resolution imaging, Sci Rep 3 (2013) 3501. https://doi.org/10.1038/srep03501.

[162] F. Wang, L. Liu, P. Yu, Z. Liu, H. Yu, Y. Wang, W.J. Li, Three-Dimensional Super-Resolution Morphology by Near-Field Assisted White-Light Interferometry, Sci Rep 6 (2016) 24703. https://doi.org/10.1038/srep24703.

[163] Y. Yan, L. Li, C. Feng, W. Guo, S. Lee, M. Hong, Microsphere-Coupled Scanning Laser Confocal Nanoscope for Sub-Diffraction-Limited Imaging at 25 nm Lateral Resolution in the Visible Spectrum, ACS Nano 8 (2014) 1809–1816. https://doi.org/10.1021/nn406201q.

[164] L. Chen, Y. Zhou, Y. Li, M. Hong, Microsphere enhanced optical imaging and patterning: From physics to applications, Applied Physics Reviews 6 (2019) 021304. https://doi.org/10.1063/1.5082215.

[165] A. Khan, Z. Wang, M.A. Sheikh, D.J. Whitehead, L. Li, Laser micro/nano patterning of hydrophobic surface by contact particle lens array, Applied Surface Science 258 (2011) 774–779. https://doi.org/10.1016/j.apsusc.2011.08.089.

[166] B.S. Luk'yanchuk, R. Paniagua-Domínguez, I. Minin, O. Minin, Z. Wang, Refractive index less than two: photonic nanojets yesterday, today and tomorrow [Invited], Opt. Mater. Express, OME 7 (2017) 1820–1847. https://doi.org/10.1364/OME.7.001820.

[167] G. Wu, M. Hong, Optical nano-imaging via microsphere compound lenses working in non-contact mode, Opt. Express, OE 29 (2021) 23073–23082. https://doi.org/10.1364/OE.426231.

[168] J. Ling, D. Li, X. Liu, X. Wang, Ultra-long focusing of microsphere lens via wavefront reconstruction in microsphere, in: Tenth International Conference on Information Optics and Photonics, SPIE, 2018: pp. 463–468. https://doi.org/10.1117/12.2505760.

[169] X. Liu, X. Li, L. Li, W. Chen, X. Luo, Influence of sphere-surface distance and exposure dose on resolution of sphere-lens-array lithography, Opt. Express, OE 23 (2015) 30136–30142. https://doi.org/10.1364/OE.23.030136.

[170] M. Guo, Y.-H. Ye, J. Hou, B. Du, Size-dependent optical imaging properties of high-index immersed microsphere lens, Appl. Phys. B 122 (2016) 65. https://doi.org/10.1007/s00340-016-6335-x.

[171] G. Huszka, H. Yang, M.A.M. Gijs, Microsphere-based super-resolution scanning optical microscope, Opt. Express, OE 25 (2017) 15079–15092. https://doi.org/10.1364/OE.25.015079.

[172] B. Yan, Z. Wang, A.L. Parker, Y. Lai, P.J. Thomas, L. Yue, J.N. Monks, Superlensing microscope objective lens, Appl. Opt., AO 56 (2017) 3142–3147. https://doi.org/10.1364/AO.56.003142.

[173] N. Upreti, G. Jin, J. Rich, R. Zhong, J. Mai, C. Zhao, T.J. Huang, Advances in Microsphere-based Super-resolution Imaging, IEEE Reviews in Biomedical Engineering (2024) 1–16. https://doi.org/10.1109/RBME.2024.3355875.

[174] T. Zhang, H. Yu, P. Li, X. Wang, F. Wang, J. Shi, Z. Liu, P. Yu, W. Yang, Y. Wang, L. Liu, Microsphere-Based Super-Resolution Imaging for Visualized Nanomanipulation, ACS Appl. Mater. Interfaces 12 (2020) 48093–48100. https://doi.org/10.1021/acsami.0c12126.

[175] B. Yan, Y. Song, X. Yang, D. Xiong, Z. Wang, Unibody microscope objective tipped with a microsphere: design, fabrication, and application in subwavelength imaging, Appl. Opt., AO 59 (2020) 2641–2648. https://doi.org/10.1364/AO.386504.

[176] K. Ludasi, T. Sovány, O. Laczkovich, B. Hopp, T. Smausz, G. Regdon, Unique laser coding technology to fight falsified medicines, European Journal of Pharmaceutical Sciences 123 (2018) 1–9. https://doi.org/10.1016/j.ejps.2018.07.023.

[177] Y. Chen, W. Kwok, Z. Wang, Enhancing Security with Superlens-Enabled Laser Direct Marking of Anti-counterfeiting DotCode, in: Frontiers in Optics + Laser Science 2023 (FiO, LS), Optica Publishing Group, Tacoma, Washington, 2023: p. JM7A.34. https://doi.org/10.1364/FIO.2023.JM7A.34.

[178] L. Yue, O.V. Minin, Z. Wang, J.N. Monks, A.S. Shalin, I.V. Minin, Photonic hook: a new curved light beam, Opt. Lett., OL 43 (2018) 771–774. https://doi.org/10.1364/OL.43.000771.

[179] Spider Silk: Mother Nature's Bio-Superlens | Nano Letters, (n.d.). https://pubs.acs.org/doi/full/10.1021/acs.nanolett.6b02641?casa_token=_JtQPweuB2MAAAAA%3ATFWkCnHgh03b3ctf5e2mvX8Afa3nVvzzXtDTk4DdAHKBZlp3d0LTNYp2fC1zYZkgdzTJMNP4prKU7Q (accessed April 15, 2024).

[180] J. Wang, J.P. Barton, Actual focal length of a symmetric biconvex microlens and its application in determining the transmitted beam waist position, Appl. Opt., AO 49 (2010) 5828–5836. https://doi.org/10.1364/AO.49.005828.

[181] Focusing property simulation of tapered-cladding single-mode hemispherical fiber micro-lenses | IEEE Conference Publication | IEEE Xplore, (n.d.). https://ieeexplore.ieee.org/abstract/document/5441045 (accessed April 15, 2024).

[182] A. Bonakdar, M. Rezaei, R.L. Brown, V. Fathipour, E. Dexheimer, S.J. Jang, H. Mohseni, Deep-UV microsphere projection lithography, Opt. Lett., OL 40 (2015) 2537–2540. https://doi.org/10.1364/OL.40.002537.

[183] A. Piqué, Chapter 1.1 - Laser-based microadditive manufacturing technologies, in: T. Baldacchini (Ed.), Three-Dimensional Microfabrication Using Two-Photon Polymerization (Second Edition), William Andrew Publishing, 2020: pp. 1–23. https://doi.org/10.1016/B978-0-12-817827-0.00001-1.

[184] Q. Li, D. Grojo, A.-P. Alloncle, B. Chichkov, P. Delaporte, Digital laser micro- and nanoprinting, Nanophotonics 8 (2019) 27–44. https://doi.org/10.1515/nanoph-2018-0103.

[185] Y.-J. Song, J. Chen, J.-Y. Wu, T. Zhang, Applications of Silver Nanowires on Transparent Conducting Film and Electrode of Electrochemical Capacitor, Journal of Nanomaterials 2014 (2014) 193201. https://doi.org/10.1155/2014/193201.

[186] C.-H. Kim, S.-H. Cha, S.C. Kim, M. Song, J. Lee, W.S. Shin, S.-J. Moon, J.H. Bahng, N.A. Kotov, S.-H. Jin, Silver Nanowire Embedded in P3HT:PCBM for High-Efficiency Hybrid Photovoltaic Device Applications, ACS Nano 5 (2011) 3319–3325. https://doi.org/10.1021/nn200469d.

[187] G.-W. Huang, H.-M. Xiao, S.-Y. Fu, Wearable Electronics of Silver-Nanowire/Poly(dimethylsiloxane) Nanocomposite for Smart Clothing, Sci Rep 5 (2015) 13971. https://doi.org/10.1038/srep13971.

[188] A. Gragossian, S.H. Tavassoli, B. Shokri, Laser ablation of aluminum from normal evaporation to phase explosion, Journal of Applied Physics 105 (2009) 103304. https://doi.org/10.1063/1.3131689.

Appendix A:
MATLAB code of FZP simulation

```
% Laser fabricated Fresnel zone plates
% Black-transmitting zone, White-blocking zone
clc,clear;
close all;

f=1; % Focal length(mm)
wavelen=640; % Light Wavelength(nm)
m=101; % Number of zones

for n=1:m
    r(n)=(f*10^3*n*wavelen*10^(-3)+(n^2*(wavelen*10^(-3))^2)/4)^0.5;
    s(n)=pi*(r(n))^2
end

size=1; % Pixel size(μm)
linespa=0; % Line width of laser(μm)
resol=2; % Laser resolution(μm)

S=pi*(r(m))^2;
Df=(wavelen*f)/(f*n*wavelen+((n^2*(wavelen*10^(-3))^2)/4))^0.5;
Res=r(m)-r(m-1);
fix=linespa/2;

if m<2
    error('Error! m at least 2!')
```

```
end

if mod(m,2)==0
    for k=0:(m/2-1)
        R_black=r(m-2*k)-fix;
        R_white=r(m-(2*k+1))+fix;
        if R_white>=R_black
            break;
        end
        theta=0:0.01:2*pi;
        x1=R_white*sin(theta);
        y1=R_white*cos(theta);
        x2=R_black*sin(theta);
        y2=R_black*cos(theta);
        plot(x2,y2,'k')
        fill(x2,y2,'k')
        hold on
        plot(x1,y1,'w')
        fill(x1,y1,'w')
        xlabel('μm','FontSize',18);
        ylabel('μm','FontSize',18);
        title(['FZP with ',num2str(m),' zones'],'FontSize',20);
        axis([-r(m) r(m) -r(m) r(m)]);
        axis equal
    end
    S_odd=s(1:2:end);
    S_even=s(2:2:end);
    S_tran=(sum(S_even)-sum(S_odd))/S;
    if R_white<R_black
        fprintf('Radius of each ring(μm):');
```

```
        disp(r);
        pixel_white=round((r(1:2:end)+fix)*2/size);
        fprintf('Pixel Number White:');
        disp(pixel_white);
        pixel_black=round((r(2:2:end)-fix)*2/size);
        fprintf('Pixel Number Black:');
        disp(pixel_black);
        fprintf('Total radius(μm):');
        disp(r(m));
        fprintf('Transmission area proportion:');
        disp(S_tran);
        fprintf('Width of outermost ring(μm):');
        disp(Res);
        fprintf('Diameter of primary focal point(μm):');
        disp(Df);
    else
        disp('Error! Over-fixed,please reduce m!');
    end
    if Res<resol
        fprintf('Warning! Resolution does not match! ')
    end

else
    R_black_m=r(m)-fix;
    theta=0:0.01:2*pi;
    x0=R_black_m*sin(theta);
    y0=R_black_m*cos(theta);
    plot(x0,y0,'k')
    fill(x0,y0,'k')
    hold on
```

```
axis equal
for k=0:((m-1)/2-1)
    R_black=r(m-1-(2*k+1))-fix;
    R_white=r(m-1-2*k)+fix;
    if R_white>=R_black_m
        break;
    end
    x1=R_black*sin(theta);
    y1=R_black*cos(theta);
    x2=R_white*sin(theta);
    y2=R_white*cos(theta);
    plot(x2,y2,'w')
    fill(x2,y2,'w')
    hold on
    plot(x1,y1,'k')
    fill(x1,y1,'k')
    xlabel('μm','FontSize',18);
    ylabel('μm','FontSize',18);
    title(['FZP with ',num2str(m),' zones'],'FontSize',20);
    axis([-r(m) r(m) -r(m) r(m)]);
    axis equal
end
S_odd=s(1:2:end);
S_even=s(2:2:end);
S_tran=(sum(S_odd)-sum(S_even))/S;
if R_white<R_black_m
    fprintf('Radius of each ring(μm):');
    disp(r);
    pixel_black=round((r(1:2:end)-fix)*2/size);
    fprintf('Pixel Number Black:');
```

```
            disp(pixel_black);
            pixel_white=round((r(2:2:end)+fix)*2/size);
            fprintf('Pixel Number White:');
            disp(pixel_white);
            fprintf('Total radius(μm):');
            disp(r(m));
            fprintf('Transmission area proportion:');
            disp(S_tran);
            fprintf('Width of outermost ring(μm):');
            disp(Res);
            fprintf('Diameter of primary focal point(μm):');
            disp(Df);
        else
            close all;
            disp('Error! Over-fixed, please reduce m!');
        end
        if Res<resol
            fprintf('Warning! Resolution does not match! ')
        end
end
```

```
% Laser line matched fabricated Fresnel zone plates
% Black-transmitting zone, White-blocking zone
clc,clear;
close all;

f=20; % Focal length(mm)
wavelen=640; % Light Wavelength(nm)
m=15; % Number of zones

for n=1:m
    r(n)=(f*10^3*n*wavelen*10^(-3)+(n^2*(wavelen*10^(-3))^2)/4)^0.5;
    s(n)=pi*(r(n))^2
end

size=1; % Pixel size(μm)
linespa=2; % Line width of laser(μm)
resol=2; % Laser resolution(μm)

S=pi*(r(m))^2;
Df=(wavelen*f)/(f*n*wavelen+((n^2*(wavelen*10^(-3))^2)/4))^0.5;
Res=r(m)-r(m-1);
fix=linespa/2;

if m<2
    error('Error! m at least 2!')
end

if mod(m,2)==0
    for k=0:(m/2-1)
```

```
        R_black=r(m-2*k)-fix;
        R_white=r(m-(2*k+1))+fix;
        if R_white>=R_black
            break;
        end
        a=mod((R_black-R_white),linespa);
        b=((R_black-R_white)-a)/linespa;
        theta=0:0.001:2*pi;
        x1=R_white*sin(theta);
        y1=R_white*cos(theta);
        x2=R_black*sin(theta);
        y2=R_black*cos(theta);
        for i=1:b
            xn=(R_white+i*linespa)*sin(theta);
            yn=(R_white+i*linespa)*cos(theta);
            plot(xn,yn,'k','linewidth',0.0001);
            hold on
        end
        plot(x1,y1,'k','linewidth',0.0001);
        hold on
        plot(x2,y2,'k','linewidth',0.0001);
        hold on
        xlabel('μm','FontSize',18);
        ylabel('μm','FontSize',18);
        title(['FZP with ',num2str(m),' zones'],'FontSize',20);
        axis([-r(m) r(m) -r(m) r(m)]);
        axis equal
%           axis off
    end
```

```
        S_odd=s(1:2:end);
        S_even=s(2:2:end);
        S_tran=(sum(S_even)-sum(S_odd))/S;
        if R_white<R_black
            fprintf('Radius of each ring(μm):');
            disp(r);
            pixel_white=round((r(1:2:end)+fix)*2/size);
            fprintf('Pixel Number White:');
            disp(pixel_white);
            pixel_black=round((r(2:2:end)-fix)*2/size);
            fprintf('Pixel Number Black:');
            disp(pixel_black);
            fprintf('Total radius(μm):');
            disp(r(m));
            fprintf('Transmission area proportion:');
            disp(S_tran);
            fprintf('Width of outermost ring(μm):');
            disp(Res);
            fprintf('Diameter of primary focal point(μm):');
            disp(Df);
        else
            disp('Error! Over-fixed,please reduce m!');
        end
        if Res<resol
            fprintf('Warning! Resolution does not match! ')
        end
%         print('111','-dbitmap','-r200');
else
        R_black=r(1)-fix;
```

```
theta=0:0.001:2*pi;
a=mod(R_black,linespa);
b=(R_black-a)/linespa;
plot(R_black*sin(theta),R_black*cos(theta),'k','linewidth',0.0001);
hold on
    for i=1:b
        xn1=(i*linespa)*sin(theta);
        yn1=(i*linespa)*cos(theta);
        plot(xn1,yn1,'k','linewidth',0.0001);
        hold on
    end
for k=1:(m-1)/2
    R_white=r(2*k)+fix;
    R_black=r(2*k+1)-fix;
    c=mod((R_black-R_white),linespa);
    d=((R_black-R_white)-c)/linespa;
    for j=1:d
        xn=(R_white+j*linespa)*sin(theta);
        yn=(R_white+j*linespa)*cos(theta);
        plot(xn,yn,'k','linewidth',0.0001);
        hold on
    end
    if R_white>r(m)
        break;
    end
    x1=R_black*sin(theta);
    y1=R_black*cos(theta);
    x2=R_white*sin(theta);
    y2=R_white*cos(theta);
```

```
        plot(x1,y1,'k','linewidth',0.0001);
        hold on
        plot(x2,y2,'k','linewidth',0.0001);
        xlabel('μm','FontSize',18);
        ylabel('μm','FontSize',18);
        title(['FZP with ',num2str(m),' zones'],'FontSize',20);
        axis([-r(m) r(m) -r(m) r(m)]);
        axis equal
%           axis off
    end
    S_odd=s(1:2:end);
    S_even=s(2:2:end);
    S_tran=(sum(S_odd)-sum(S_even))/S;
    if R_white>r(m)
        close all;
        disp('Error! Over-fixed, please reduce m!');
    else
        fprintf('Radius of each ring(μm):');
        disp(r);
        pixel_black=round((r(1:2:end)-fix)*2/size);
        fprintf('Pixel Number Black:');
        disp(pixel_black);
        pixel_white=round((r(2:2:end)+fix)*2/size);
        fprintf('Pixel Number White:');
        disp(pixel_white);
        fprintf('Total radius(μm):');
        disp(r(m));
        fprintf('Transmission area proportion:');
        disp(S_tran);
```

```
            fprintf('Width of outermost ring(μm):');
            disp(Res);
            fprintf('Diameter of primary focal point(μm):');
            disp(Df);
        end
        if Res<resol
            fprintf('Warning! Resolution does not match! ')
        end
%         print('222','-dbitmap','-r200');
end
```

Appendix B:
MATLAB code of FBG simulation

```
function [T]=Transmit_Matrix(lambda,lambda_Bragg,L,n_eff,delta_neff,num)
% wave detuning parameter
beta=2*pi*n_eff*(1./lambda-1/lambda_Bragg);
% coupling coefficien
kappa=pi*delta_neff./lambda;
gamma=sqrt(kappa.^2-beta.^2);
% transmission matrix
t11(num)=cosh(gamma(num)*L)-i*(beta(num)/gamma(num))*sinh(gamma(num)*L);
t12(num)=-i*(kappa(num)/gamma(num))*sinh(gamma(num)*L);
t21(num)=i*(kappa(num)/gamma(num))*sinh(gamma(num)*L);
t22(num)=cosh(gamma(num)*L)+i*(beta(num)/gamma(num))*sinh(gamma(num)*L);
T=[t11(num) t12(num);t21(num) t22(num)];

% reflectivity R=(abs(-T(2,1)/T(1,1)))^2
% Maximum reflectivity R_max=(tanh(kappa*L))^2
end
```

```
% FBG Reflection simulation
% FBG typical core & cladding RI difference: About 1e-2
% FBG typical index modulation e-5~e-3
clc,clear;
close all;

period=0.515e-6; % Set grating period(m)
L=17e-3; % Set grating length(m)
n_eff=1.50288; % Set effective refractive index
delta_neff=0.00008; % Set index modulation
wl_start=1547;
wl_end=1549;

lambda_Bragg=2*n_eff*period;
lambda=1e-9*linspace(wl_start,wl_end,1000);
for num=1:1000
    T=Transmission_Matrix(lambda,lambda_Bragg,L,n_eff,delta_neff,num);
    r(num)=T(2,1)/T(1,1);
    R(num)=(abs(-r(num)))^2;
end

subplot(2,1,2)
plot(lambda*1e9,R,'linewidth',1);
axis([wl_start wl_end 0 1]);
title('The Reflection Spectrum of FBG','fontsize',12);
xlabel('Wavelength (nm)','fontsize',10);
ylabel('Reflectivity','fontsize',10);
grid on

subplot(2,1,1)
```

```
plot(lambda*1e9,1-R,'r','linewidth',1);
axis([wl_start wl_end 0 1]);
title('The Transmission Spectrum of FBG','fontsize',12);
xlabel('Wavelength (nm)','fontsize',10);
ylabel('Transmittance','fontsize',10);
grid on

format short
fprintf('FBG Parameters:');
fprintf('\n\n');
fprintf('Bragg Wavelength(nm)--');
disp(lambda_Bragg*1e9);
fprintf('Grating Period(μm)--');
disp(period*1e6);
fprintf('Grating Length(mm)--');
disp(L*1e3);
fprintf('Index Modulation--');
disp(delta_neff);
```

Appendix C:
MATLAB code of LPG simulation

```
function f_core=CoreFormula(wl,neff,n1,n2,a1)
% (1)
% Free-space wave number
k0=2*pi/wl;
% Normalized effective index
b=(neff^2-n2^2)/(n1^2-n2^2);
% V number of the fiber at wavelength
v=k0*a1*sqrt(n1^2-n2^2);
% Core coupling mode LP01 dispersion equation
R=v*sqrt(1-b);
B=v*sqrt(b);
f_core=(R*besselj(1,R)/besselj(0,R))-(B*besselk(1,B)/besselk(0,B));
```

```
function neffcore=CoreDichotamy(a,b,wl,n1,n2,a1,err)
% Dichotomy program
fun=@CoreFormula;
format long
f1=feval(fun,wl,a,n1,n2,a1);
f2=feval(fun,wl,b,n1,n2,a1);
if f1.*f2>0
    disp('Note: f1*f2>0')
else
    max=real(1+round((log(a-b)-log(err))/log(2)));
    for k=1:max
        neffcore=(a+b)./2;
        f3=feval(fun,wl,neffcore,n1,n2,a1);
        if f3==0
            a=neffcore;
            b=neffcore;
        elseif f2.*f3>0
            b=neffcore;
            f2=f3;
        else
            a=neffcore;
            f1=f3;
        end
        if abs(b-a)<err,break,end
    end
    neffcore=(a+b)/2;
    err=abs(b-a);
    f3=feval(fun,wl,neffcore,n1,n2,a1);
end
```

```
function f_clad=CladdingFormula(n1,n2,n3,a1,a2,wl,nu,neff)
% Core coupling mode dispersion equation & parameters
% Paper_LPGCladdingNeffPrinciple
% (9)
% Free-space wave number
k0=2*pi/wl;
% (7)
% Ratio of cladding & core radius
alpha=a2/a1;
% (5)
% Layer phase parameters
u1=k0.*a1.*sqrt(n1^2-neff.^2);
u2=k0.*a1.*sqrt(n2^2-neff.^2);
w3=k0.*a2.*sqrt(neff.^2-n3^2);
% (9)
% Other parameters
s21=(n2/n1)^2;
s23=(n2/n3)^2;
v12=k0*a1*sqrt(n1^2-n2^2);
v23=k0*a2*sqrt(n2^2-n3^2);
x1=n1.*u1.^2.*u2.^2./(nu.*v12^2.*neff);
x2=n3.*alpha^2.*u2.^2.*w3.^2./(nu.*v23^2.*neff);
% (7)
% First-order Bessel function
J=(-besselj(nu+1,u1)+nu./u1.*besselj(nu,u1))./(u1.*besselj(nu,u1));
% Third-order Bessel function
K=(-besselk(nu+1,w3)+nu./w3.*besselk(nu,w3))./(w3.*besselk(nu,w3));
% (9)
% Cross products of Bessel function
p=besselj(nu,alpha.*u2).*bessely(nu,u2)-besselj(nu,u2).*bessely(nu,alpha.*u2);
```

```
q=besselj(nu,alpha.*u2).*(-bessely(nu+1,u2)+nu./u2.*bessely(nu,u2))-(-
besselj(nu+1,u2)+nu./u2.*besselj(nu,u2)).*bessely(nu,alpha.*u2);

r=(-
besselj(nu+1,alpha.*u2)+nu./(alpha.*u2).*besselj(nu,alpha.*u2)).*bessely(nu,u2)-
besselj(nu,u2).*(-bessely(nu+1,alpha.*u2)+nu./(alpha.*u2).*bessely(nu,alpha.*u2));

s=(-besselj(nu+1,alpha.*u2)+nu./(alpha.*u2).*besselj(nu,alpha.*u2)).*(-
bessely(nu+1,u2)+nu./u2.*bessely(nu,u2))-(-
besselj(nu+1,u2)+nu./u2.*besselj(nu,u2)).*(-
bessely(nu+1,alpha.*u2)+nu./(alpha.*u2).*bessely(nu,alpha.*u2));


L1=p.^2+2.*x1.*x2.*(n2^2/(n1*n3)).*(2./(pi.*alpha.*u2.^2)).^2;

L2=x1.^2.*x2.^2.*(J.*(r./(alpha.*u2)+K.*p)-(K.*q./u2+s./(alpha.*u2.^2)));

L3=J.*(s23.*r./(alpha.*u2)+K.*p)-s21.*(K.*q./u2+s23.*s./(alpha.*u2.^2));

L_All=L1+L2.*L3;


R1=x1.^2.*(J.*p-s21.*q./u2).*(J.*p-q./u2);

R2=x2.^2.*(K.*p+r./(alpha.*u2)).*(K.*p+s23.*r./(alpha.*u2));

R_All=R1+R2;


f_clad=L_All-R_All;
```

```
function neffcladding=CladdingDichotamy(n1,n2,n3,a1,a2,wl,nu,n2_threshold)
% Dichotomy program
f=@CladdingFormula;
format long
flag=1e-5;
num=0;
err=1e-10;
neff1=n2;
neff3=n2_threshold;
neff2=neff1-flag;
a=neff1;
b=neff2;

while b>neff3
    fa=feval(f,n1,n2,n3,a1,a2,wl,nu,a);
    fb=feval(f,n1,n2,n3,a1,a2,wl,nu,b);
    c=(a+b)./2;
    if fa.*fb<0
        max=1+round(log2(abs(a-b)./err)-1);
        for j=1:max
            c=(a+b)./2;
            fc=feval(f,n1,n2,n3,a1,a2,wl,nu,c);
            if fa.*fc==0
                a=c;
                b=c;
            elseif fa.*fc<0
                b=c;
                c=(a+b)./2;
                fb=fc;
            else
```

```
                    a=c;
                    c=(a+b)./2;
                    fa=fc;
                end
                if abs(a-b)<err,break,end
            end
            num=num+1;
            neff(num)=c;
        end
        a=c;
        b=b-flag;
end

order=size(neff);
m=1;
n=0;
while (m~=n)
        m=order(2);
        for ii=1:m-1
            if abs(neff(ii)-neff(ii+1))<flag
                neff(ii+1)=0;
            end
        end
        neff=neff(find(neff));
        order=size(neff);
        n=order(2);
end
neffcladding=neff;
```

```
function E=ElectricField_Cladding(r)
global a1 a2 n1 n2 n3 wl nu neff_cladding_i zeta_i;
% Free-space wave number
k0=2.*pi./wl;
% (4)
% Electromagnetic impedance in vacuum
z0=377;
% (8)(9)
% Slowly varying envelope of the grating
sigma1=i.*nu.*neff_cladding_i./z0;
sigma2=i.*nu.*neff_cladding_i.*z0;
% (10)(11)(12)(13)
% Layer phase parameters
u1=k0.*sqrt(n1^2-neff_cladding_i.^2);
u2=k0.*sqrt(n2^2-neff_cladding_i.^2);
w3=k0.*sqrt(neff_cladding_i.^2-n3.^2);
u21=(1./u2).^2-(1./u1).^2;
u32=(1./w3).^2+(1./u2).^2;
% (14)
% First-order Bessel function
J=(-besselj(nu+1,u1.*a1)+nu./(u1.*a1).*besselj(nu,u1.*a1))./(u1.*besselj(nu,u1.*a1));
% (A7)(A8)
% Define quantities
F2=J-u21.*sigma2.*zeta_i./(n1.^2.*a1);
G2=J.*zeta_i+u21.*sigma1./a1;
% (16)(17)(18)(19)
% Cross products of Bessel function
y1=besselj(nu,u2.*r).*bessely(nu,u2.*a1)-besselj(nu,u2.*a1).*bessely(nu,u2.*r);
y2=besselj(nu,u2.*r).*(bessely(nu-1,u2.*a1)-nu./(u2.*a1).*bessely(nu,u2.*a1))-
(besselj(nu-1,u2.*a1)-nu./(u2.*a1).*besselj(nu,u2.*a1)).*bessely(nu,u2*r);
```

```
y3=(besselj(nu-1,u2.*r)-nu./(u2.*r).*besselj(nu,u2.*r)).*bessely(nu,u2.*a1)-
besselj(nu,u2.*a1).*(bessely(nu-1,u2.*r)-nu./(u2.*r).*bessely(nu,u2.*r));

y4=(besselj(nu-1,u2*r)-nu./(u2.*r).*besselj(nu,u2.*r)).*(bessely(nu-1,u2.*a1)-
nu./(u2.*a1).*bessely(nu,u2.*a1))-(besselj(nu-1,u2.*a1)-
nu./(u2.*a1).*besselj(nu,u2.*a1)).*(bessely(nu-1,u2.*r)-
nu./(u2.*r).*bessely(nu,u2.*r));

% (A1)(A2)(A4)(A5)(26)

% Electric field

Eclr2=i.*(pi.*a1.*u1.^2.*besselj(1,u1.*a1)./2).*(-F2.*y1./r+y2./(u2.*r)-
sigma2./n2.^2.*(u2.*G2.*y3-n2.^2.*zeta_i.*y4./n1.^2));

Eclphi2=(pi.*a1.*u1.^2.*besselj(1,u1.*a1)/2).*(sigma2./n2.^2.*(G2.*y1./r-
n2.^2.*zeta_i.*y2./(n1.^2.*u2.*r))+u2.*F2.*y3-y4);

Hclr2=(pi.*a1.*u1.^2.*besselj(1,u1.*a1)/2).*(-
i.*G2.*y1./r+i.*n2.^2.*zeta_i.*y2./(n1.^2.*u2.*r)+i.*sigma1.*(u2.*F2.*y3-y4));

Hclphi2=i.*(pi.*a1.*u1.^2.*besselj(1,u1.*a1)./2).*(i.*sigma1.*(F2.*y1./r-y2./(u2.*r))-
i.*u2.*G2.*y3+i.*n2.^2.*zeta_i.*y4./n1.^2);

E=r.*(Eclr2.*conj(Hclphi2)-conj(Hclr2).*Eclphi2);
```

```
% LPG core effective refractive index solving
% LPG ypical core & cladding RI difference: 3e-3~5e-3
% LPG typical change in refractive index e-5~e-3
clc,clear;
close all;

format long
global a1 a2 n1 n2 n3 wl nu neff_cladding_i zeta_i
wl_start=1520;
wl_end=1570;
N=200; % Sampling number
wavelength=linspace(wl_start,wl_end,N).*1e-9;
n1=1.45594; % Core refractive index
n2=1.45; % Cladding refractive index
n3=1.0; % Surrounding refractive index
a1=4.1e-6; % Fiber core radius
a2=60e-6; % Fiber cladding radius
nu=1; % Bessel azimuthal number
period=500e-6; % Grating period
L=20e-3; % Grating length
delta_n1=1e-4; % Index modulation
mode_order=7; % Mode order number
err=1e-10;

% Define cladding neff threshold
wl_sample=wavelength(N);
n2_threshold=n2-0.005;
while(1)

neff_cl_threshold=CladdingDichotamy(n1,n2,n3,a1,a2,wl_sample,nu,n2_threshold);
```

```
        i_mode=size(neff_cl_threshold);
        if i_mode(2)<mode_order
            n2_threshold=n2-0.005;
        else
            break;
        end
end
n2_threshold=neff_cl_threshold(mode_order)-1e-5;

% Determine neff of core and cladding for each mode
for i_wl=1:N
        wl=wavelength(i_wl);
        k0_i(i_wl)=2.*pi./wavelength(i_wl);
        neff_core(1,i_wl)=CoreDichotamy(n2,n1,wl,n1,n2,a1,err);
        neff_cladding=CladdingDichotamy(n1,n2,n3,a1,a2,wl,nu,n2_threshold);
        for i_num=1:mode_order
            neff_cl(i_num,i_wl)=neff_cladding(i_num);
        end
end

% Uniform dimension
for i_num=1:mode_order
        k0(i_num,:)=k0_i;
        neff_co(i_num,:)=neff_core;
end

% (4)
% Electromagnetic impedance in vacuum
z0=377;
```

```
% Index modulation
sigma_z=delta_n1./n1;

deta=(n1-n2)./n1;

% (1)
% V number of the fiber at wavelength
v=k0.*a1.*sqrt(n1.^2-n2.^2);

% Normalized effective index
b=(neff_co.^2-n2.^2)./(n1.^2-n2.^2);

% (8)(9)
% Slowly varying envelope of the grating
sigma1=i.*nu.*neff_cl./z0;
sigma2=i.*nu.*neff_cl.*z0;

% (10)(11)(12)(13)
% Layer phase parameters
u1=k0.*sqrt(n1.^2-neff_cl.^2);
u2=k0.*sqrt(n2.^2-neff_cl.^2);
w3=k0.*sqrt(neff_cl.^2-n3^2);
u21=(1./u2).^2-(1./u1).^2;
u32=(1./w3).^2+(1./u2).^2;

% (14)(15)
% First-order Bessel function
J=(-besselj(nu+1,u1.*a1)+nu./(u1.*a1).*besselj(nu,u1.*a1))./(u1.*besselj(nu,u1.*a1));
% Third-order Bessel function
K=(-
```

```
besselk(nu+1,w3.*a2)+nu./(w3.*a2).*besselk(nu,w3.*a2))./(w3.*besselk(nu,w3.*a2));


% (16)(17)(18)(19)

% Cross products of Bessel function

pl=besselj(nu,u2.*a2).*bessely(nu,u2.*a1)-besselj(nu,u2.*a1).*bessely(nu,u2.*a2);

ql=besselj(nu,u2.*a2).*(-bessely(nu+1,u2.*a1)+nu./(u2.*a1).*bessely(nu,u2.*a1))-(-
besselj(nu+1,u2.*a1)+nu./(u2.*a1).*besselj(nu,u2.*a1)).*bessely(nu,u2.*a2);

rl=(-besselj(nu+1,u2.*a2)+nu./(u2.*a2).*besselj(nu,u2.*a2)).*bessely(nu,u2.*a1)-
besselj(nu,u2.*a1).*(-bessely(nu+1,u2.*a2)+nu./(u2.*a2).*bessely(nu,u2.*a2));

sl=(-besselj(nu+1,u2.*a2)+nu./(u2.*a2).*besselj(nu,u2.*a2)).*(-
bessely(nu+1,u2.*a1)+nu./(u2.*a1).*bessely(nu,u2.*a1))-(-
besselj(nu+1,u2.*a1)+nu./(u2.*a1).*besselj(nu,u2.*a1)).*(-
bessely(nu+1,u2.*a2)+nu./(u2.*a2).*bessely(nu,u2.*a2));


% (6)

% Dispersion relation left

zeta=1./sigma2.*(((u2.*pl.*(J.*K+sigma1.*sigma2.*u21.*u32./(n2^2*a1*a2)))+(-
K.*ql+J.*rl-sl./u2)).//((-u2.*pl.*((u32./(n2^2*a2).*J-
(u21./(n1^2.*a1).*K))))+(u32.*ql./(n1^2*a2)+u21.*rl./(n1^2*a1))));


% (B2)

% P1(=E1v^2*p1)

p11=neff_cl./z0-neff_cl.*z0.*zeta.^2./n1.^2+(1+neff_cl.^2./n1.^2).*imag(zeta);

p12=besselj(2,u1.*a1).^2-besselj(1,u1.*a1).*besselj(3,u1.*a1);

p13=neff_cl./z0-neff_cl.*z0.*zeta.^2./n1.^2-(1+neff_cl.^2./n1.^2).*imag(zeta);

p14=besselj(0,u1.*a1).^2+besselj(1,u1.*a1).^2;

p1=pi.*a1.^2.*u1.^2./4.*(p11.*p12+p13.*p14);


% (B3)

% P2(=E1v^2*p2)

for i_num=1:mode_order

    for i_wl=1:N
```

```
            wl=wavelength(i_wl);
            zeta_i=zeta(i_num,i_wl);
            neff_cladding_i=neff_cl(i_num,i_wl);
            p2(i_num,i_wl)=real(pi.*quadl(@ElectricField_Cladding,a1,a2));
        end
end

% (A7)(A8)(A15)(A16)
% Define quantities
F2=J-u21.*sigma2.*zeta./(n1^2.*a1);
G2=zeta.*J+u21.*sigma1./a1;
F3=-F2.*pl+1./u2.*ql;
G3=-n3.^2./n2.^2.*(G2.*pl-n2.^2./n1.^2.*zeta./u2.*ql);

% (B16)
% P3(=E1v^2*p3)
p31=neff_cl.*z0.*G3.^2./n3.^2-neff_cl./z0.*F3.^2-
(1+neff_cl.^2./n3.^2).*F3.*imag(G3);
p32=besselk(2,w3.*a2).^2-besselk(1,w3.*a2).*besselk(3,w3.*a2);
p33=neff_cl.*z0.*G3.^2./n3.^2-
neff_cl./z0.*F3.^2+(1+neff_cl.^2./n3.^2).*F3.*imag(G3);
p34=besselk(0,w3.*a2).^2-besselk(1,w3.*a2).^2;
p3=pi.^3.*(a1.*a2).^2.*(u1.*u2).^4.*besselj(1,u1.*a1).^2./(16.*w3.^2.*besselk(1,w3
.*a2).^2).*(p31.*p32+p33.*p34);
E1v=1./sqrt(p1+p2+p3);

% (36)
% Coupling coefficient of core and cladding
kappa_cl_co=sigma_z.*k0.*sqrt(pi.*b./(z0.*n2.*sqrt(1+2.*b.*deta))).*n1.^2.*u1./(u1
.^2-v.^2.*(1-
b)./a1.^2).*(1+sigma2.*zeta./n1.^2).*E1v.*(u1.*besselj(1,u1.*a1).*besselj(0,v.*sqrt(
1-b))./besselj(1,v.*sqrt(1-b))-v.*sqrt(1-b).*besselj(0,u1.*a1)./a1);
```

```
kappa_co_co=sigma_z.*k0.*n1.^2.*b./(n2.*sqrt(1+2.*b.*deta)).*(1+besselj(0,v.*sqrt
(1-b)).^2./besselj(1,v.*sqrt(1-b)).^2);


% Paper_FiberGratingSpectra
% (5)
% Mode propagation constant
beta_co=k0.*neff_co;
beta_cl=k0.*neff_cl;


% (37)
% Detuning parameter
delta=1./2.*(beta_co-beta_cl)-pi./period;


% (36)
% Self-coupling coefficient
sigma=delta+1./2*kappa_co_co;


% (38)
% LPG transmittance at a wavelength
ka_hole=1.*kappa_cl_co;
T=(cos(sqrt(ka_hole.^2+sigma.^2).*L)).^2+(sin(sqrt(ka_hole.^2+sigma.^2).*L)).^2.*si
gma.^2./(sigma.^2+ka_hole.^2);


% Uniform dimension & superposition
t=ones(1,N);
for i_wl=1:N
    for i_num=1:mode_order
        t(1,i_wl)=T(i_num,i_wl)*t(1,i_wl);
    end
end
```

```
Transmission=10.*log10(t);

% Plot transmission figure
plot(wavelength.*1e9,Transmission,'r','linewidth',1.5);
title('The Transmission Spectrum of LPG','fontsize',18);
xlabel('Wavelength(nm)','fontsize',15);
ylabel('Transmission(dB)','fontsize',15);
axis([wl_start wl_end -inf inf]);
grid on;
```

```
clc,clear;
close all;

format long
global a1 a2 n1 n2 n3 wl nu neff_cladding_i zeta_i
wl_start=1530;
wl_end=1550;
N=2000;
wavelength=linspace(wl_start,wl_end,N).*1e-9;
n1=1.455941;
n2=1.45;
a1=4.1e-6;
a2=60e-6;
nu=1;
period=444e-6;
L=40e-3;
delta_n1=1e-4;
mode_order=7;
err=1e-10;
Array=[1.0 1.33 1.4 1.405 1.41 1.415 1.42 1.425 1.43 1.435 1.44 1.445];
% Array=[1.0 1.33]; % Test array
M=size(Array);

figure
for i_n3=1:M(2)
    n3=Array(i_n3);
    wl_sample=wavelength(N);
    n2_threshold=n2-0.005;
    while(1)
```

```
neff_cl_threshold=CladdingDichotamy(n1,n2,n3,a1,a2,wl_sample,nu,n2_threshold);
        i_mode=size(neff_cl_threshold);
        if i_mode(2)<mode_order
            n2_threshold=n2-0.005;
        else
            break;
        end
    end
    n2_threshold=neff_cl_threshold(mode_order)-1e-5;
    for i_wl=1:N
        wl=wavelength(i_wl);
        k0_i(i_wl)=2.*pi./wavelength(i_wl);
        neff_core(1,i_wl)=CoreDichotamy(n2,n1,wl,n1,n2,a1,err);
        neff_cladding=CladdingDichotamy(n1,n2,n3,a1,a2,wl,nu,n2_threshold);
        for i_num=1:mode_order
            neff_cl(i_num,i_wl)=neff_cladding(i_num);
        end
    end
    for i_num=1:mode_order
        k0(i_num,:)=k0_i;
        neff_co(i_num,:)=neff_core;
    end
    z0=377;
    sigma_z=delta_n1./n1;
    deta=(n1-n2)./n1;
    v=k0.*a1.*sqrt(n1.^2-n2.^2);
    b=(neff_co.^2-n2.^2)./(n1.^2-n2.^2);
    sigma1=i.*nu.*neff_cl./z0;
    sigma2=i.*nu.*neff_cl.*z0;
    u1=k0.*sqrt(n1.^2-neff_cl.^2);
```

```
u2=k0.*sqrt(n2.^2-neff_cl.^2);

w3=k0.*sqrt(neff_cl.^2-n3.^2);

u21=(1./u2).^2-(1./u1).^2;

u32=(1./w3).^2+(1./u2).^2;

J=(-
besselj(nu+1,u1.*a1)+nu./(u1.*a1).*besselj(nu,u1.*a1))./(u1.*besselj(nu,u1.*a1));

K=(-
besselk(nu+1,w3.*a2)+nu./(w3.*a2).*besselk(nu,w3.*a2))./(w3.*besselk(nu,w3.*a2));

pl=besselj(nu,u2.*a2).*bessely(nu,u2.*a1)-
besselj(nu,u2.*a1).*bessely(nu,u2.*a2);

ql=besselj(nu,u2.*a2).*(-
bessely(nu+1,u2.*a1)+nu./(u2.*a1).*bessely(nu,u2.*a1))-(-
besselj(nu+1,u2.*a1)+nu./(u2.*a1).*besselj(nu,u2.*a1)).*bessely(nu,u2.*a2);

rl=(-
besselj(nu+1,u2.*a2)+nu./(u2.*a2).*besselj(nu,u2.*a2)).*bessely(nu,u2.*a1)-
besselj(nu,u2.*a1).*(-bessely(nu+1,u2.*a2)+nu./(u2.*a2).*bessely(nu,u2.*a2));

sl=(-besselj(nu+1,u2.*a2)+nu./(u2.*a2).*besselj(nu,u2.*a2)).*(-
bessely(nu+1,u2.*a1)+nu./(u2.*a1).*bessely(nu,u2.*a1))-(-
besselj(nu+1,u2.*a1)+nu./(u2.*a1).*besselj(nu,u2.*a1)).*(-
bessely(nu+1,u2.*a2)+nu./(u2.*a2).*bessely(nu,u2.*a2));


zeta=1./sigma2.*(((u2.*pl.*(J.*K+sigma1.*sigma2.*u21.*u32./(n2^2*a1*a2)))+(-
K.*ql+J.*rl-sl./u2))./((-u2.*pl.*((u32./(n2^2*a2).*J-
(u21./(n1^2.*a1).*K))))+(u32.*ql./(n1^2*a2)+u21.*rl./(n1^2*a1))));

p11=neff_cl./z0-neff_cl.*z0.*zeta.^2./n1.^2+(1+neff_cl.^2./n1.^2).*imag(zeta);

p12=besselj(2,u1.*a1).^2-besselj(1,u1.*a1).*besselj(3,u1.*a1);

p13=neff_cl./z0-neff_cl.*z0.*zeta.^2./n1.^2-(1+neff_cl.^2./n1.^2).*imag(zeta);

p14=besselj(0,u1.*a1).^2+besselj(1,u1.*a1).^2;

p1=pi.*a1.^2.*u1.^2./4.*(p11.*p12+p13.*p14);

for i_num=1:mode_order

    for i_wl=1:N

        wl=wavelength(i_wl);

        zeta_i=zeta(i_num,i_wl);

        neff_cladding_i=neff_cl(i_num,i_wl);
```

```
                p2(i_num,i_wl)=real(pi.*quadl(@ElectricField_Cladding,a1,a2));
            end
        end
        F2=J-u21.*sigma2.*zeta./(n1^2.*a1);
        G2=zeta.*J+u21.*sigma1./a1;
        F3=-F2.*pl+1./u2.*ql;
        G3=-n3.^2./n2.^2.*(G2.*pl-n2.^2./n1.^2.*zeta./u2.*ql);
        p31=neff_cl.*z0.*G3.^2./n3.^2-neff_cl./z0.*F3.^2-
(1+neff_cl.^2./n3.^2).*F3.*imag(G3);
        p32=besselk(2,w3.*a2).^2-besselk(1,w3.*a2).*besselk(3,w3.*a2);
        p33=neff_cl.*z0.*G3.^2./n3.^2-
neff_cl./z0.*F3.^2+(1+neff_cl.^2./n3.^2).*F3.*imag(G3);
        p34=besselk(0,w3.*a2).^2-besselk(1,w3.*a2).^2;

p3=pi.^3.*(a1.*a2).^2.*(u1.*u2).^4.*besselj(1,u1.*a1).^2./(16.*w3.^2.*besselk(1,w3
.*a2).^2).*(p31.*p32+p33.*p34);
        E1v=1./sqrt(p1+p2+p3);

kappa_cl_co=sigma_z.*k0.*sqrt(pi.*b./(z0.*n2.*sqrt(1+2.*b.*deta))).*n1.^2.*u1./(u1
.^2-v.^2.*(1-
b)./a1.^2).*(1+sigma2.*zeta./n1.^2).*E1v.*(u1.*besselj(1,u1.*a1).*besselj(0,v.*sqrt(
1-b))./besselj(1,v.*sqrt(1-b))-v.*sqrt(1-b).*besselj(0,u1.*a1)./a1);

kappa_co_co=sigma_z.*k0.*n1.^2.*b./(n2.*sqrt(1+2.*b.*deta)).*(1+besselj(0,v.*sqrt
(1-b)).^2./besselj(1,v.*sqrt(1-b)).^2);
        beta_co=k0.*neff_co;
        beta_cl=k0.*neff_cl;
        delta=1./2.*(beta_co-beta_cl)-pi./period;
        sigma=delta+1./2*kappa_co_co;

T=(cos(sqrt(kappa_cl_co.^2+sigma.^2).*L)).^2+(sin(sqrt(kappa_cl_co.^2+sigma.^2).*
L)).^2.*sigma.^2./(sigma.^2+kappa_cl_co.^2);
        t=ones(1,N);
        for i_wl=1:N
```

```
        for i_num=1:mode_order
            t(1,i_wl)=T(i_num,i_wl)*t(1,i_wl);
        end
    end
    Transmission=10.*log10(t);
    plot(wavelength.*1e9,Transmission,'linewidth',1);
    hold on
    format short
    fprintf('Simulation completed for n3=');
    disp(n3);
    [y_min(i_n3) wl_cen(i_n3)]=min(Transmission);
end
% title(['The Peak Shifts of LPG at Mode Order ',num2str(mode_order)],'fontsize',18);
set(gca,'fontsize',15);
xlabel('Wavelength(nm)','fontsize',18);
ylabel('Transmission(dB)','fontsize',18);
%legend({'n3=1.000                                                    (Air)','n3=1.330
(Water)','n3=1.400','n3=1.405','n3=1.410','n3=1.415','n3=1.420','n3=1.425','n3=1.43
0','n3=1.435','n3=1.440','n3=1.445'},'FontSize',15);
axis([wl_start wl_end -inf inf]);
grid on
figure
% yyaxis left
plot(Array,wavelength(wl_cen)*1e9,'-o','linewidth',1);
set(gca,'fontsize',15);
xlabel('Surrounding Refractive Index','fontsize',18);
ylabel('Wavelength(nm)','fontsize',18);
ylim([1535 1545]);
% yyaxis right
% plot(Array,y_min,'-*','linewidth',1);
```

```
% ylabel('Transmission(dB)','fontsize',15);
% title(['LPG Surrounding Sensing at Mode Order ',num2str(mode_order)],'fontsize',18);
% ylim([-8.2 -7]);
```

```
clc,clear;
close all;

format long
n1=1.455;
n2=1.45;
n3=1.0;
nu=1;
a1=4.6e-6;
a2=62.5e-6;
wl=1550e-9;
n2_threshold=1.448;
neff1=n2_threshold;
neff2=n2;
neff=linspace(neff1,neff2,500);

k0=2*pi/wl;
alpha=a2/a1;
s21=(n2/n1)^2;
s23=(n2/n3)^2;
v12=k0*a1*sqrt(n1^2-n2^2);
v23=k0*a2*sqrt(n2^2-n3^2);
u1=k0.*a1.*sqrt(n1^2-neff.^2);
u2=k0.*a1.*sqrt(n2^2-neff.^2);
u3=k0.*a2.*sqrt(neff.^2-n3^2);
x1=n1.*u1.^2.*u2.^2./(nu.*v12^2.*neff);
x2=n3.*alpha^2.*u2.^2.*u3.^2./(nu.*v23^2.*neff);
J=(-besselj(nu+1,u1)+nu./u1.*besselj(nu,u1))./(u1.*besselj(nu,u1));
K=(-besselk(nu+1,u3)+nu./u3.*besselk(nu,u3))./(u3.*besselk(nu,u3));
p=besselj(nu,alpha.*u2).*bessely(nu,u2)-besselj(nu,u2).*bessely(nu,alpha.*u2);
```

```
q=besselj(nu,alpha.*u2).*(-bessely(nu+1,u2)+nu./u2.*bessely(nu,u2))-(-
besselj(nu+1,u2)+nu./u2.*besselj(nu,u2)).*bessely(nu,alpha.*u2);

r=(-
besselj(nu+1,alpha.*u2)+nu./(alpha.*u2).*besselj(nu,alpha.*u2)).*bessely(nu,u2)-
besselj(nu,u2).*(-bessely(nu+1,alpha.*u2)+nu./(alpha.*u2).*bessely(nu,alpha.*u2));

s=(-besselj(nu+1,alpha.*u2)+nu./(alpha.*u2).*besselj(nu,alpha.*u2)).*(-
bessely(nu+1,u2)+nu./u2.*bessely(nu,u2))-(-
besselj(nu+1,u2)+nu./u2.*besselj(nu,u2)).*(-
bessely(nu+1,alpha.*u2)+nu./(alpha.*u2).*bessely(nu,alpha.*u2));


L1=p.^2+2.*x1.*x2.*(n2^2/(n1*n3)).*(2./(pi.*alpha.*u2.^2)).^2;

L2=x1.^2.*x2.^2.*(J.*(r./(alpha.*u2)+K.*p)-(K.*q./u2+s./(alpha.*u2.^2)));

L3=J.*(s23.*r./(alpha.*u2)+K.*p)-s21.*(K.*q./u2+s23.*s./(alpha.*u2.^2));

L_All=L1+L2.*L3;


R1=x1.^2.*(J.*p-s21.*q./u2).*(J.*p-q./u2);

R2=x2.^2.*(K.*p+r./(alpha.*u2)).*(K.*p+s23.*r./(alpha.*u2));

R_All=R1+R2;


neff_cladding=CladdingDichotamy(n1,n2,n3,a1,a2,wl,nu,n2_threshold);

fprintf('Order of effective RI of Cladding --');

disp(neff_cladding);


neff_size=size(neff_cladding);

for i=1:168

    j=find(abs(L_All-R_All)<=0.01*i);

    j_size=size(j);

    if j_size(2)==neff_size(2)+1;

        break;

    end

end

x=j(1:end-1);
```

```
X=neff(x);
Y=L_All(x);
plot(neff,L_All,'r',neff,R_All,'b',X,Y,'k*','linewidth',1);
title('Cladding Neff Testing','fontsize',18);
xlabel('neff','fontsize',15);
axis([neff1 neff2 -inf inf]);
grid on
```

```
clc,clear;
close all;

format long
global a1 a2 n1 n2 n3 wl nu neff_cladding_i zeta_i
n1=1.455;
n2=1.45;
n3=1.0;
a1=4.6e-6;
a2=62.5e-6;
wl=1550e-9;
err=1e-10;
nu=1;
n2_threshold=1;
neff_core=CoreDichotamy(n2,n1,wl,n1,n2,a1,err);
neff_cladding=CladdingDichotamy(n1,n2,n3,a1,a2,wl,nu,n2_threshold);

% Free-space wave number
k0=2*pi/wl;
% (4)
% Electromagnetic impedance in vacuum
z0=377;
deta=(n1-n2)./n1;
% (1)
% V number of the fiber at wavelength
v=k0.*a1.*sqrt(n1.^2-n2.^2);
% Normalized effective index
b=(neff_core.^2-n2.^2)./(n1.^2-n2.^2);
% (8)(9)
% Slowly varying envelope of the grating
```

```
sigma1=i.*nu.*neff_cladding./z0;

sigma2=1.*nu.*neff_cladding.*z0;

% (10)(11)(12)(13)

% Layer phase parameters

u1=k0.*sqrt(n1^2-neff_cladding.^2);

u2=k0.*sqrt(n2^2-neff_cladding.^2);

w3=k0.*sqrt(neff_cladding.^2-n3^2);

u21=(1./u2).^2-(1./u1).^2;

u32=(1./w3).^2+(1./u2).^2;

% (14)(15)

% First-order Bessel function

J=(-besselj(nu+1,u1.*a1)+nu./(u1.*a1).*besselj(nu,u1.*a1))./(u1.*besselj(nu,u1.*a1));

% Third-order Bessel function

K=(-
besselk(nu+1,w3.*a2)+nu./(w3.*a2).*besselk(nu,w3.*a2))./(w3.*besselk(nu,w3.*a2));

% (16)(17)(18)(19)

% Cross products of Bessel function

pl=besselj(nu,u2.*a2).*bessely(nu,u2.*a1)-besselj(nu,u2.*a1).*bessely(nu,u2.*a2);

ql=besselj(nu,u2.*a2).*(-bessely(nu+1,u2.*a1)+nu./(u2.*a1).*bessely(nu,u2.*a1))-(-
besselj(nu+1,u2.*a1)+nu./(u2.*a1).*besselj(nu,u2.*a1)).*bessely(nu,u2.*a2);

rl=(-besselj(nu+1,u2.*a2)+nu./(u2.*a2).*besselj(nu,u2.*a2)).*bessely(nu,u2.*a1)-
besselj(nu,u2.*a1).*(-bessely(nu+1,u2.*a2)+nu./(u2.*a2).*bessely(nu,u2.*a2));

sl=(-besselj(nu+1,u2.*a2)+nu./(u2.*a2).*besselj(nu,u2.*a2)).*(-
bessely(nu+1,u2.*a1)+nu./(u2.*a1).*bessely(nu,u2.*a1))-(-
besselj(nu+1,u2.*a1)+nu./(u2.*a1).*besselj(nu,u2.*a1)).*(-
bessely(nu+1,u2.*a2)+nu./(u2.*a2).*bessely(nu,u2.*a2));

% (6)

% Dispersion relation left

zeta=1./sigma2.*(((u2.*pl.*(J.*K+sigma1.*sigma2.*u21.*u32./(n2^2*a1*a2)))+(-
K.*ql+J.*rl-sl./u2))./((-u2.*pl.*((u32./(n2^2*a2).*J-
(u21./(n1^2.*a1).*K))))+(u32.*ql./(n1^2*a2)+u21.*rl./(n1^2*a1))));

% (B2)
```

```
% P1
p11=neff_cladding./z0-
neff_cladding.*z0.*zeta.^2./n1.^2+(1+neff_cladding.^2./n1.^2).*imag(zeta);
p12=besselj(2,u1.*a1).^2-besselj(1,u1.*a1).*besselj(3,u1.*a1);
p13=neff_cladding./z0-neff_cladding.*z0.*zeta.^2./n1.^2-
(1+neff_cladding.^2./n1.^2).*imag(zeta);
p14=besselj(0,u1.*a1).^2+besselj(1,u1.*a1).^2;
p1=pi.*a1.^2.*u1.^2./4.*(p11.*p12+p13.*p14);
% (B3)
% P2
i_max=size(neff_cladding);
for t=1:i_max(2)
    zeta_i=zeta(t);
    neff_cladding_i=neff_cladding(t);
    p2(t)=real(pi.*quadl(@ElectricField_Cladding,a1,a2));
end
% (A7)(A8)(A15)(A16)
% Define quantities
F2=J-u21.*sigma2.*zeta./(n1^2.*a1);
G2=zeta.*J+u21.*sigma1./a1;
F3=-F2.*pl+1./u2.*ql;
G3=-n3.^2./n2.^2.*(G2.*pl-n2.^2./n1.^2.*zeta./u2.*ql);
% (B16)
% P3
p31=neff_cladding.*z0.*G3.^2./n3.^2-neff_cladding./z0.*F3.^2-
(1+neff_cladding.^2./n3.^2).*F3.*imag(G3);
p32=besselk(2,w3.*a2).^2-besselk(1,w3.*a2).*besselk(3,w3.*a2);
p33=neff_cladding.*z0.*G3.^2./n3.^2-
neff_cladding./z0.*F3.^2+(1+neff_cladding.^2./n3.^2).*F3.*imag(G3);
p34=besselk(0,w3.*a2).^2-besselk(1,w3.*a2).^2;
p3=pi.^3.*(a1.*a2).^2.*(u1.*u2).^4.*besselj(1,u1.*a1).^2./(16.*w3.^2.*besselk(1,w3
```

```
.*a2).^2).*(p31.*p32+p33.*p34);

E1v=1./sqrt(p1+p2+p3);

% (36)

% Coupling coefficient of core and cladding

kappa_cl_co=k0.*sqrt(pi.*b./(z0.*n2.*sqrt(1+2.*b.*deta))).*n1.^2.*u1./(u1.^2-
v.^2.*(1-
b)./a1.^2).*(1+sigma2.*zeta./n1.^2).*E1v.*(u1.*besselj(1,u1.*a1).*besselj(0,v.*sqrt(
1-b))./besselj(1,v.*sqrt(1-b))-v.*sqrt(1-b).*besselj(0,u1.*a1)./a1);

kappa=abs(kappa_cl_co);


for num=1:i_max(2)
    if rem(num,2)==1
        plot(num,kappa(num).*1e-6,'b*');
        hold on;
    else plot(num,kappa(num).*1e-6,'ro');
    end
end
xlabel('Cladding Mode Number \nu','fontsize',15);
ylabel('Coupling Constant/\sigma(z)(\mum^-^1)','fontsize',15);
axis([0 168 0 0.8]);
legend('\nu=odd','\nu=even')
```